Spincavitronics : repulsive and attractive energy levels in YIG bulk-microwave cavity coupled systems

Guillaume Bourcin

COLLEGES SCIENCES
BRETAGNE POUR L'INGENIEUR
LOIRE ET LE NUMERIQUE

IMT Atlantique
Bretagne-Pays de la Loire
École Mines-Télécom

THESE DE DOCTORAT DE

L'ÉCOLE NATIONALE SUPERIEURE
MINES-TELECOM ATLANTIQUE BRETAGNE PAYS DE LA LOIRE –
IMT ATLANTIQUE

ECOLE DOCTORALE N° 648
Sciences pour l'Ingénieur et le Numérique
Spécialité : *Ondes acoustiques, électromagnétisme et matériaux*

Par

Guillaume Bourcin

Spincavitronics : Repulsive and Attractive Energy Levels in YIG Bulk-Microwave Cavity Coupled Systems

Thèse présentée et soutenue à IMT Atlantique, Brest, 17/12/2024
Unité de recherche : Lab-STICC UMR 6285,
Thèse N° : 2024IMTA0447

Rapporteurs avant soutenance :

Grégoire DE LOUBENS	Directeur de recherche, CEA-SPEC
Abdelmadjid ANANE	Maître de Conférences, Université Paris-Saclay, Laboratoire Albert Fert

Composition du Jury :

Président :	David SPENATO	Professeur, Université de Bretagne Occidentale
Examinateurs :	Isabella BOVENTER	Chercheuse Thales, Thales Research and Technology
	Grégoire DE LOUBENS	Directeur de recherche, CEA-SPEC
	Abdelmadjid ANANE	Maître de Conférences, Université Paris-Saclay, Laboratoire Albert Fert
Dir. de thèse :	Vincent CASTEL	Professeur, IMT Atlantique
Co-encadrant :	Vincent VLAMINCK	Maitre de conférences, IMT Atlantique

Remerciements

La rédaction de cette thèse marque l'aboutissement d'un long parcours de recherche, qui n'aurait pas été possible sans le soutien, l'accompagnement et les encouragements de nombreuses personnes. Je tiens à leur exprimer ici toute ma gratitude.

Je souhaite tout d'abord remercier Vincent Castel pour la confiance qu'il m'a accordée en me confiant ce sujet de recherche, mais aussi pour son soutien tout au long de la thèse, ainsi que pour sa patience lors de mes moments de doute. Je le remercie également pour les moments conviviaux partagés et pour avoir transmis son goût pour le son, toujours accompagné de grosses basses

Je tiens aussi à remercier Vincent Vlaminck pour les nombreuses discussions scientifiques, les moments conviviaux, ainsi que ses apparitions dans mon bureau avec des questions de physique auxquelles je n'ai jamais su apporter de réponses. Merci aussi d'avoir partagé ton amour pour le feu lors des barbecues organisés au sein du département.

Je remercie également les membres du jury de thèse pour le temps qu'ils m'ont consacré et pour leurs remarques pertinentes, qui ont permis d'enrichir ce travail.

Je tiens à remercier l'ensemble des collègues du département Micro-Ondes, qui ont partagé mon quotidien ces trois dernières années. Je remercie particulièrement : Nicholas Attwood, toujours partant pour une faluche à la boulangerie ; Grégoire Gaudin, même si sa présence a été parfois rare ; Loïc Kom Temdie, mon camarade de bureau, beaucoup trop fort à tout type de sport (ce qui est frustrant) ; Alan Gardin, avec qui j'ai partagé mon goût pour le vin rouge et le fromage, et qui est également beaucoup trop fort en physique (ce qui est tout aussi frustrant) ; Myssipsa Mehraz, qui veut toujours que je me pousse ; Théo Dubasque, alias Legolas (même si je ne sais plus qui il est) ; Bryan Tréguer, pour ces moments de brainstorming intenses et vraiment enrichissants ; Corentin Le Lez, pour avoir partagé son café torréfié dans le Morbihan, absolument délicieux ; Achraf Sadeddine, pour m'avoir appris qu'il fallait toujours se protéger ; et enfin, Mufti Avicena, la relève, à qui je souhaite beaucoup de force et de succès.

Enfin, je remercie mes proches pour leur soutien indéfectible et pour les moments de détente et de joie qui m'ont permis de prendre du recul sur mon travail de thèse. Je remercie tout particulièrement ma conjointe, Julie Quéau, pour son soutien inconditionnel lors de mes moments de doute et pour la bonne humeur qu'elle m'apporte chaque jour. Merci également à ma belle-famille pour son soutien constant et pour l'épanouissement qu'elle m'offre. Enfin, je remercie mes amis, toujours présents, qui riaient avec moi lorsque je parlais de faire une thèse... il y a huit ans.

Contents

1 Introduction

Abstract

This chapter provides an overview of the foundational concepts and emerging fields central to this thesis, including spintronics, magnonics, cavity quantum electrodynamics (QED), and spincavitronics. We discuss the significance of each field, highlighting their applications in modern technology. Additionally, we outline my contributions to these topics and present the overall structure of the thesis.

Contents

1.1 Spintronics

Spintronics is a branch of solid-state physics that seeks to harness the electron's spin, either independently or in conjunction with its charge, to develop more efficient electronic devices [1]. The idea of using spin, an intrinsic quantum property of electrons, for information transport and processing emerged in the late 1980s following two key discoveries: spin manipulation through electric and magnetic fields by Johnson and Silsbee (1985) [2], and giant magnetoresistance (GMR), simultaneously discovered by Baibich et al. (1988) [3] and Binasch et al. (1989) [4], which earned the 2007 Nobel Prize in Physics.

The GMR effect had an immediate impact, particularly in data storage technologies such as hard drive read heads, and was essential to the development of Magnetic Random Access Memory (MRAM). MRAM devices offer advantages in speed, non-volatility (preserving data without power), and reduced energy consumption compared to conventional memory technologies [5].

Subsequent research expanded to explore additional aspects of spin manipulation [6–11], including the spin Hall effect (SHE) [12], spin-transfer torque (STT) [13, 14], the Rashba effect [15], and spin-orbit torque (SOT) [16] in topological materials [17] and interfacial systems [18].

For data storage, new spin-dependent transport phenomena have emerged, notably tunneling magnetoresistance (TMR) [19], which employs magnetic tunnel junctions (MTJs) to control current flow via electron spin [20]. The development of STT-MRAM (Spin-Transfer Torque MRAM) has further enhanced memory performance, particularly by reducing energy consumption [21].

Another growing area of application is spintronics sensors, which have found use in automotive systems, medical devices, and telecommunications [22]. In telecommunications, spin-transfer oscillators (STOs) hold promise for more compact and energy-efficient radio transmission and reception systems [23].

Spintronics also holds potential for information processing, where controlling spin could lead to improvements in energy efficiency and data density [24].

1.2 Magnonics

Magnonics is a relatively new field in solid-state physics that investigates the use of magnons - quasi-particles associated with spin waves in magnetic materials - to transport and process information. Magnons are collective excitations of electron spins in a magnetic lattice [25], and their properties can be leveraged to replace traditional charge-based currents, paving the way for a new class of low-power devices [26].

The concept of magnonics traces its origins to solid-state physics in 1932 when physicist Bloch introduced the idea of spin waves. This concept was further developed by Holstein, Primakov, and Dyson [27]. In recent years, researchers have begun exploring the potential of magnons as information carriers for technological applications, akin to the role of electrons in conventional electronics or photons in photonics [28].

Interest in magnonics has surged with the rise of spintronics and the realization that spin waves could help overcome some limitations of current electronic devices [29]. Notably, heat dissipation, a significant challenge in charge-based electronic systems, can be largely mitigated in magnonics systems since magnons carry information without requiring the movement of charge [30].

The primary applications of magnonics are focused on developing logic devices [31], and low-energy information processing systems [32]. One of the most promising areas is the creation of non-volatile and reconfigurable logic circuits based on spin waves [33]. These devices exploit spin wave interference to perform logic operations at the nanoscale [34].

An emerging application in neuromorphic computing also relies on magnonics [35]. Magnonics neural networks could mimic biological synapses and neurons, using spin waves to transmit and process analog signals, potentially leading to brain-inspired computing systems capable of handling large amounts of data with significantly lower energy consumption than traditional processors.

1.3 Cavity QED

Light-matter coupling is a fundamental phenomenon in quantum physics, describing the interactions between photons and matter particles such as atoms, electrons, or collective excitations (e.g., phonons or magnons). This concept is central to a wide range of technologies, from lasers to optical sensors, and plays a key role in areas like photonic cavities, qubits, and optomechanics [36].

Quantum electrodynamics (QED), developed by Feynman, Schwinger, and Tomonaga in the 1940s, provided a precise framework to model the interactions between electromagnetic fields and elementary particles [37]. A crucial concept in QED is strong coupling, which arises when the interactions between photons and matter become intense and exceeds individual dissipations, enough to create hybrid states known as polaritons [38, 39]. These quasi-particles result from the mixing of photon states with the energy levels of matter, and they underpin many modern applications [40, 41]. The study of light-matter coupling spans fields like cavity QED, spincavitronics, and applications in quantum communication and information processing.

In the 1980s, the development of cavity quantum electrodynamics enabled the exploration of strong coupling between a photon confined in an optical cavity and a trapped atom or molecule [42]. This phenomenon is pivotal in nonlinear optics, where high-intensity light can modify a material's optical properties [43]. More recently, the field of light-matter coupling has expanded with the advent of 2D materials and plasmonic structures, allowing for the manipulation of these interactions at the nanoscale [44].

Polaritons are also being investigated for their potential in optical transistor devices and quantum logic [45]. By controlling the propagation of polaritons in microcavities or waveguides, it is possible to design more compact integrated optical circuits with faster switching speeds and lower energy consumption compared to traditional electronic devices.

In the context of quantum information, light-matter coupling is critical for the creation and manipulation of qubits, the fundamental units of quantum information [46–48]. These are key components in the development of future quantum computers.

Furthermore, quantum teleportation and quantum networks directly benefit from advances in light-matter coupling [49]. Particularly, a network of interconnected optical cavities could enable the reliable transfer of quantum information between qubits [50], facilitating the construction of a quantum internet [51].

1.4 Spincavitronics

Spincavitronics, or cavity magnonics, is a relatively recent subfield focused on the strong coupling between magnons and photons within an electromagnetic cavity, resulting in hybrid coupled states known as cavity magnon polaritons (CMPs). This emerging field, which began to take shape in the early 2010s, lies at the intersection of spintronics, magnonics, and cavity QED.

Soykal and Flatté (2010) [52] were the first to predict that strong magnon-photon coupling is possible. Then, Huebl et al. (2013) [53] demonstrated strong magnon-photon coupling between a superconducting coplanar microwave resonator and Ga-doped YIG at 50 mK, followed by Tabuchi et al. (2014) [54], who observed this coupling below 1 K between a YIG sphere and a 3D cavity. Concurrently, Zhang et al. (2014) [55] achieved strong coupling in the same system at room temperature.

The broad frequency tunability and long lifetimes of magnons enable their coupling with other particles or quasi-particles. This system holds promise for quantum magnonics, where magnons interact with qubits mediated by cavity photons [56]. Magnons possess long coherence times, a critical feature that allows them to serve as quantum memory, thus preventing information loss due to the decoherence of quantum states in superconducting qubits [57, 58]. Additionally, this could lead to sensitive detectors for single magnon sensing, which is useful for the non-destructive detection of weak static or microwave magnetic fields, as well as for dark matter research [59, 60].

Quantum magnonics could also facilitate the development of a bidirectional quantum transducer between microwaves and optical light for superconducting circuits [61, 62]. This would enable the transfer of quantum information from a superconducting qubit to optical light via a magnon transducer, necessitating a faithful encoding of the quantum state of the qubit into a non-classical state of the magnons [63]. Such technology would pave the way for long-distance quantum communications [64]. Enhancing these techniques requires increasing the coupling strength between qubits and magnons [40].

Furthermore, spincavitronics display a broad range of applicability for radiofrequency devices, such as adjustable sensitive filters, low-noise amplifiers, isolators, circulators, and other components in communication technologies [65–73].

1.5 Contributions

Ultra-strong coupling regime:

The ultra-strong coupling regime occurs when the coupling strength exceeds 10% of the cavity frequency [74], enabling the exploration of new phenomena such as virtual excitations [75], and paving the way for exotic states like discrete time crystals [76]. This regime enhances the performance of devices operating in the strong coupling regime, particularly by accelerating control and response times within systems [77]. Certain short-lifetime systems, essential for specific quantum gates, are only observable within the USC regime, making it particularly crucial for advanced quantum applications [78, 79], including frequency conversion and dark matter detection [77, 80].

Several approaches can achieve this regime, such as coupling a large number of dipoles to a cavity or optimizing the coupling between a single dipole and the cavity mode [74]. Systems like inter-subband polaritons, superconducting circuits, and Landau polaritons have experimentally demonstrated the USC regime, reaching coupling ratios as high as 1.43 [81–83].

However, in hybrid systems, it is critical that each subsystem can couple in this regime. While the coupling regime was achieved at 60% below 10 K using superconducting/insulating/ferromagnetic multilayered microstructures [84], it has never exceeded 23% at room temperature [85].

In this study, we developed a reconfigurable hybrid system to investigate the transition between the strong coupling and ultra-strong coupling regimes at room temperature across a frequency range of 0.1 to 15 GHz within a 3D cavity, achieving a coupling strength ranging from 12% to 58% of the cavity frequency. Furthermore, our results indicate that it is necessary to incorporate an additional term in the ferromagnetic resonance equation to accurately describe the observed hybridization, particularly in the USC regime. However, questions remain regarding the most suitable model to predict USC. Our study constitutes a significant contribution to understanding these dynamics and paves the way for developing a coherent model to describe this complex system, which could have substantial implications for future advancements in this field.

Level attraction:

The phenomenon of level attraction in quantum systems paves the way for various innovative applications, particularly in the development of modern communication devices. Systems exhibiting effective non-Hermitian coupling enable nonreciprocal photon transmission, which is essential for devices such as circulators and unidirectional signal amplifiers. These components are critical for signal processing and communication [65–73]. Additionally, dissipative coupling between magnons and photons promotes applications such as magnon gradient quantum memory, enabling the encoding of quantum information and enhancing quantum computing technologies [86, 87].

Moreover, level attraction mechanisms open up avenues for advanced devices in metrology and detection. Specifically, utilizing cavity modes as damped auxiliary modes optimizes the coupling between magnons, facilitating long-range interactions that are promising for spintronics devices and spin-based technologies [88].

To this end, understanding the emergence of these level attractions is crucial. While well established for open cavity systems [67, 89–94], there have been relatively few studies on 3D cavities, and the observation of level attraction in 3D cavities has been poorly understood, largely due to the reliance on a phenomenological model that fails to provide a physical description of the system [95].

In this work, we contribute by presenting a physical model that elucidates the emergence and coupling of antiresonances in 3D cavities, validated through simulations and experimental measurements.

This thesis is structured as follows:

Chapter 2:
This chapter establishes the foundation for understanding magnetism by discussing angular momentum, from electron orbits to quantum spin. It covers the quantum description of angular momentum in static magnetic fields and provides insights into magnetic materials, particularly Yttrium Iron Garnet (YIG), which is significant for RF devices and magnon-photon coupling studies. The chapter concludes by exploring spin waves in ferromagnets, highlighting their origins in the exchange and dipolar interactions.

Chapter 3:
This chapter starts by quantizing the electromagnetic field within a cavity to establish the cavity Hamiltonian for further analysis. It draws an analogy between light-matter coupling and two coupled oscillators, providing a simplified framework to understand light-matter interactions across different systems. The discussion progresses through various coupling regimes and models, ultimately leading to the derivation of the photon-magnon coupling model while incorporating environmental factors.

Chapter 4:
This chapter details the methodological steps used in the studies, beginning with simulation considerations. It then reviews various fabrication techniques for the cavity, including traditional machining, 3D plastic printing, and metallization processes. Finally, the chapter concludes with an overview of the vector network analyzer, the primary instrument for measurements, along with details on the laboratory setup and measurement automation.

Chapter 5:
In this chapter, we discuss our studies on the strong to ultra-strong coupling regimes in frequency-reconfigurable three-dimensional reentrant cavities coupled with yttrium iron garnet slabs. The findings have been published in the Physical Review B journal [96] and can be found on arXiv.

Chapter 6:
In this chapter, we present our research on the effective coupling associated with an antiresonance in a hybrid system of a quasi-closed photonic cavity and ferrimagnetic material. The findings have been published in the Physical Review Applied journal [97] and can be found on arXiv.

2 Magnons

Abstract

In this chapter, we lay the groundwork for understanding magnetism in materials by exploring the concept of angular momentum, starting from electron orbits to the quantum phenomenon known as spin. We delve into the quantum description of angular momentum in the presence of a static magnetic field and discuss the semi-classical interpretation of measurements within such systems. Additionally, we provide an overview of various magnetic materials, focusing on Yttrium Iron Garnet (YIG), an artificial garnet known for its numerous advantages in radio frequency (RF) devices and studies involving magnon-photon coupling. Finally, we conclude with an examination of spin waves in ferromagnets, elucidating their emergence from two key interactions: the exchange interaction and the dipolar interaction.

Contents

2.1 Angular & Magnetic Momenta

To understand the origin of magnetism in materials, it is needed to go down to the atomic scale in order to visualize the behavior of electrons. The fundamental parameter of the magnetism is the angular momentum, which originates from two sources: the orbital angular momentum, and the spin angular momentum. Initially, we will explore the classical concept of orbital angular momentum, where an electron moves in a circular orbit around the nucleus, and the associated orbital magnetic momentum induced by this angular momentum. Subsequently, we will introduce the principles of quantum mechanics and discuss the angular and magnetic momenta of a single electron in motion around its nucleus, as well as in multi-electron atoms or ions. Finally, we will examine the interaction between a magnetic momentum and a static magnetic field, as well as the precession of a magnetic momentum under a uniform magnetic field, and the resulting torque exerted by a static magnetic field on an angular momentum.

2.1.1 Classical Angular & Magnetic Orbital Momenta

In classical mechanics, the electron is viewed as a particle moving in a circular orbit around its nucleus, as depicted in Fig. 2.1. Assuming the electron possesses momentum $\mathbf{p} = m\mathbf{v}$, with position $\mathbf{r}$, according to classical mechanics, the orbital angular momentum of the particle can be expressed as:

$$\mathbf{L} = \mathbf{r} \times \mathbf{p}. \tag{2.1}$$

Additionally, as an electron carries a negative charge of $-e$, its motion generates a current I, expressed as:

$$I\hat{\mathbf{u}}_\phi = -\frac{e\mathbf{v}}{2\pi r}. \tag{2.2}$$

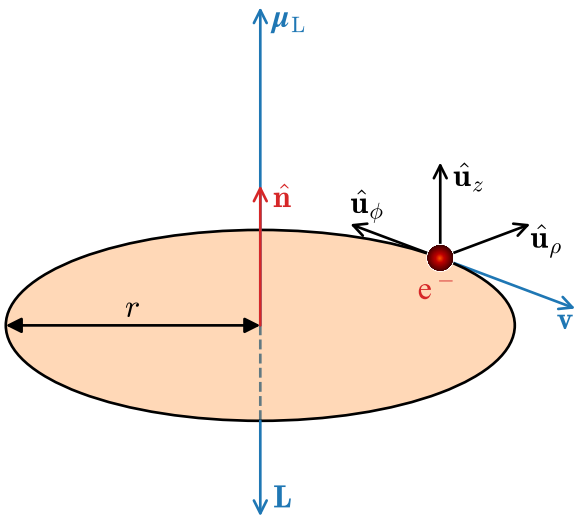

FIGURE 2.1: Schematic representation of an electron orbiting circularly around its nucleus.

Here, $\hat{\mathbf{u}}_\phi$ represents the azimuthal direction in the plane of the electron's orbit, as illustrated in Fig. 2.1. Also, it is important to note that conventionally, the direction of the current opposes the movement of the electron. According to Ampère's law [98], the orbital magnetic moment $\boldsymbol{\mu}_\mathrm{L}$ of the electron depends on the current and the surface area A enclosed by the electron's path:

$$\boldsymbol{\mu}_\mathrm{L} = IA\hat{\mathbf{n}}, \tag{2.3}$$

where $\hat{\mathbf{n}}$ is the vector normal to the orbital plane, as depicted in Fig. 2.1. The direction of the orbital magnetic moment along the z-axis is determined by the current direction and the "right-hand rule", thus $\hat{\mathbf{n}} = \hat{\mathbf{u}}_z$. Since the current and the electron velocity are opposite in direction, we observe that for an electron, the orbital magnetic moment opposes the orbital angular momentum. This relationship can be expressed by substituting I from Eq. (2.2) and $\mathbf{L}$ from Eq. (2.1) into Eq. (2.3):

$$\boldsymbol{\mu}_\mathrm{L} = \gamma_\mathrm{L}\mathbf{L}, \tag{2.4}$$

where the gyromagnetic ratio generalized for a charged particle is given by:

$$\gamma_\mathrm{L} = \frac{q}{2m}, \tag{2.5}$$

with q representing the particle's charge, which is equal to $-e$ for an electron.

2.1.2 Quantum Angular & Magnetic Momenta

Quantum mechanics is built upon six fundamental postulates [99]:

1) A quantum system is associated with a quantum state defined by a quantum wave.
2) The dynamics of a quantum system are governed by the time-dependent Schrödinger equation.
3) Measurement results in the projection of the quantum state of the system onto one of its eigenstates.
4) Prior to measurement, a quantum system can exist as a superposition of states.
5) The Heisenberg uncertainty principle states that it is impossible to precisely measure both the position and momentum of a particle simultaneously.
6) Two particles can be entangled, meaning their states are correlated even when separated by distance.

In the framework of quantum mechanics, classical quantities are reformulated as quantum operators. For instance, the classical position vector $\mathbf{r}$ is replaced by the quantum operator $\hat{\mathbf{r}}$ while classical momentum is represented by the quantum operator $\hat{\mathbf{p}} = \frac{\hbar}{i}\hat{\nabla}$, where $\hbar$ denotes the reduced Planck's constant. According to Heisenberg's uncertainty principle, the position and momentum operators do not commute, which is expressed by the commutation relation [99]:

$$[\hat{x}_i, \hat{p}_i] = \hat{x}_i\hat{p}_i - \hat{p}_i\hat{x}_i = i\hbar. \tag{2.6}$$

Here, $\hat{x}_i$ denotes $\hat{x}$, $\hat{y}$, or $\hat{z}$, and $\hat{p}_i$ represents the momentum operator along the same axis.

2.1.2.a Single Angular & Magnetic Momenta

Continuing with the discussion on orbital angular momentum, combining Eq. (2.1) and (2.6), we derive the commutation relation for orbital angular momentum:

$$[\hat{L}_{x_i}, \hat{L}_{x_j}] = i\hbar\hat{L}_{x_k}, \tag{2.7}$$

where x_i, x_j, and x_k represents x, y, z, or their cyclic permutations. This relation can be generalized for any angular momentum $\hat{\mathbf{J}}$, with the equivalent expression:

$$\hat{\mathbf{J}} \times \hat{\mathbf{J}} = i\hbar\hat{\mathbf{J}}. \tag{2.8}$$

As will be shown subsequently, it is more convenient to describe angular momentum using the lowering and raising components, defined as:

$$\hat{\mathbf{J}}_{\pm} = \hat{J}_x \pm i\hat{J}_y, \tag{2.9}$$

These operators allow for the modification of angular momentum by increasing or decreasing its projection along the z-axis, and obey the following commutation relations:

$$[\hat{J}_z, \hat{J}_{\pm}] = \pm\hbar\hat{J}_{\pm}, \tag{2.10a}$$
$$[\hat{J}_+, \hat{J}_-] = 2\hbar\hat{J}_z. \tag{2.10b}$$

Due to the non-commutativity of $\hat{J}_x$, $\hat{J}_y$, $\hat{J}_z$, $\hat{J}_+$, and $\hat{J}_-$, it is impossible to precisely determine all of these quantities through measurement within the same instance. However, simultaneous measurement of $\hat{J}_z$ and $\hat{J}^2$ is feasible. These two observables are considered as "good quantum numbers" due to their commutative nature. The operator $\hat{J}^2$ denotes the squared magnitude of the orbital angular momentum and is expressed as:

$$\hat{J}^2 = \hat{\mathbf{J}} \cdot \hat{\mathbf{J}} = \hat{J}_x^2 + \hat{J}_y^2 + \hat{J}_z^2 = \hat{J}_-\hat{J}_+ + \hat{J}_z(\hat{J}_z + \hbar). \tag{2.11}$$

If we consider an eigenstate $|m_j\rangle$ of $\hat{J}_z$ given by:

$$\hat{J}_z |m_j\rangle = m_j\hbar |m_j\rangle , \tag{2.12}$$

where m_j is a quantum number ranging from $-j$ to j, with $j\hbar$ representing the maximum value that $\hat{J}_z$ can reach, it follows that (as demonstrated in [25] p.17):

$$\hat{J}^2 |m_j\rangle = \hbar^2 j(j+1) |m_j\rangle . \tag{2.13}$$

Conversely to classical angular momentum, the quantity associated with $\hat{J}_z$ will never reach the total length value $\hbar\sqrt{j(j+1)}$, as illustrated in Fig. 2.2. However, we must be careful about this interpretation, it does not imply that the x and y components have non-zero values because $\hat{J}_z |m_j\rangle \neq \hat{J} |m_j\rangle$. This is a fundamental principle of quantum mechanics: knowing $\hat{J}_z$ does not provide information about $\hat{J}_x$ and $\hat{J}_y$. Also, for the raising

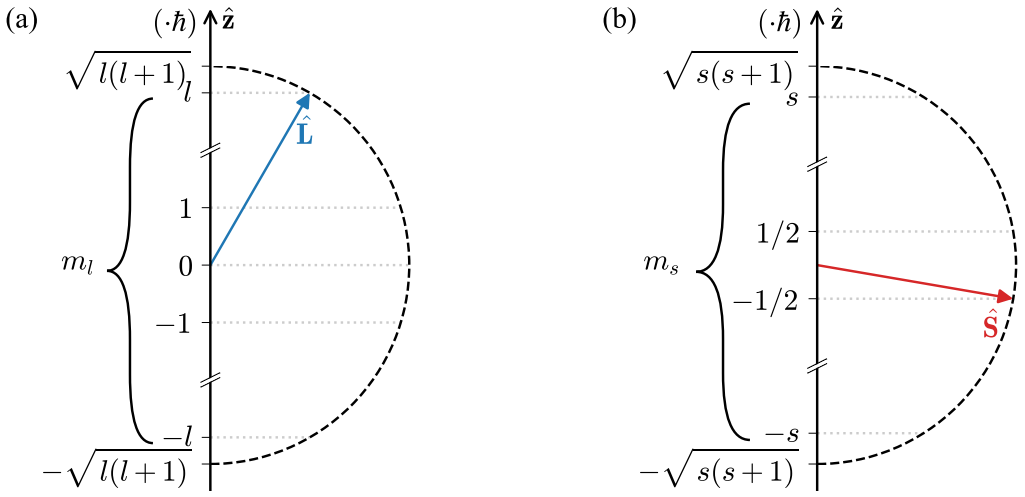

FIGURE 2.2: Schematic representation of the projection along the z-axis of the quantized values of (a) orbital and (b) spin angular momenta.

and lowering operators, applied to an eigenstate $|m_j\rangle$, it is expressed as [25]:

$$\hat{\mathbf{J}}_+ |m_j\rangle = \hbar\sqrt{j(j+1) - m_j(m_j+1)}\,|m_j+1\rangle\,, \tag{2.14a}$$

$$\hat{\mathbf{J}}_- |m_j\rangle = \hbar\sqrt{j(j+1) - m_j(m_j-1)}\,|m_j-1\rangle\,. \tag{2.14b}$$

In quantum mechanics, the orbital angular momentum, defined in Eq. (2.1) in classical mechanics, is represented by:

$$\hat{\mathbf{L}} = \hat{\mathbf{r}} \times \frac{\hbar}{i}\nabla. \tag{2.15}$$

Assuming that $|l\rangle$ is an eigenstate corresponding to the maximum eigenvalue of $\hat{L}_z$, expressed in spherical coordinates, it can be written as:

$$\hat{L}_z |l\rangle = \frac{\hbar}{i}\partial_\phi |l\rangle = \hbar l\,|l\rangle\,. \tag{2.16}$$

The solution to this equation necessitates the following condition on the eigenvalue l:

$$|l\rangle = e^{il\phi_l} = e^{il(\phi_l + 2\pi)}. \tag{2.17}$$

This implies that l is an integer, and m_l can take $2l+1$ possible values, as illustrated in Fig. 2.2 (a).

Conversely to the electron's orbital motion, the spin is a purely quantum effect with no classical analogy. The spin behaves as an angular momentum and can be conceptualized classically as the electron spinning, generating a magnetic moment. The experimental observation by Gerlach and Stern (1922) [100] revealed that the maximum quantum number for spin s is 1/2, meaning that m_s has $2s$ possible values, as depicted in Fig. 2.2 (b). According to Dirac's spin theory (1965) [101], the spin magnetic moment is described by:

$$\hat{\boldsymbol{\mu}}_{\mathrm{S}} = \gamma_{\mathrm{S}}\hat{\mathbf{S}}, \tag{2.18}$$

where $\gamma_S = 2\gamma_L$ represents the spin gyromagnetic factor.

2.1.2.b Total Angular & Magnetic Momenta in atoms and ions

Here, our aim is to determine the net magnetic momentum of atoms and ions with multiple electrons. Following Russell and Saunders (1925) [102], we introduce the weak spin-orbit coupling approximation, neglecting this effect:

$$\hat{\mathbf{S}} = \sum_i \hat{\mathbf{S}}_i, \tag{2.19a}$$

$$\hat{\mathbf{L}} = \sum_i \hat{\mathbf{L}}_i, \tag{2.19b}$$

$$\hat{\mathbf{J}} = \hat{\mathbf{S}} + \hat{\mathbf{L}}, \tag{2.19c}$$

where $\mathbf{S}_i$ and $\mathbf{L}_i$ represent the orbital and spin angular momenta of the i^{th} electron in the considered atom or ion, and $\mathbf{J}$ is the total angular momentum of the atom or ion. To be differentiated them from the angular momentum of a single electron, the quantum numbers of these operators are denoted in uppercase, i.e. $l \to L$, $s \to S$, and $j \to J$. In the same manner, $m_l \to m_L$, $m_s \to m_S$, and $m_j \to m_J$.

The total magnetic momentum is given by:

$$\hat{\boldsymbol{\mu}} = \gamma_L(\hat{\mathbf{L}} + 2\hat{\mathbf{S}}) = \gamma\hat{\mathbf{J}}. \tag{2.20}$$

γ can also be expressed as a function of γ_L as:

$$\gamma = g_L\gamma_L, \tag{2.21}$$

where g_L is the Landé factor. Deriving Eq. (2.20) leads to (see Appendix 2.A for derivation):

$$g_L = \frac{3}{2} + \frac{S(S+1) - L(L+1)}{2J(J+1)}. \tag{2.22}$$

In the particular case of an angular momentum only having a spin component, the Landé factor is $g_L = 2$. If the angular momentum only has an orbital component, the Landé factor is $g_L = 1$, retrieving the values in the previous subsections.

In atoms and ions, each electron is described by a wave function $\psi(\mathbf{r})$, which represents the probability amplitude of finding the electron at a specific position $\mathbf{r}$. This wave function depends on four different quantum numbers:

- n: the principal quantum number, which defines the shell and indicates the number $n-1$ of radial nodes of the wave function.
- l: the orbital angular momentum, which defines the subshell. Its range of possible values is given by $l \leq n-1$.
- m_l: the projection on the z-axis of the orbital angular momentum, which defines the orbital. Its range of possible values is given by $-l \leq m_z \leq +l$.
- m_s: the projection on the z-axis of the spin angular momentum, where $m_s = \pm 1/2$.

Note that the subshell is commonly written as nX, where X is s, p, d, or f if $l = 0$, 1, 2 or 3, respectively.

Several shells and subshells of an atom or an ion can be filled by several electrons. But the filling of an atom or an ion must follow two rules: the first one is the Pauli exclusion principle. This principle states that two electrons cannot occupy the same state simultaneously, meaning they cannot share the same shell, subshell, orbital, and spin. The second rule is the Hund's rule, which asserts that when an atom is in its ground state, electrons occupying a subshell that is not entirely filled are arranged in a manner that maximizes S. Once S is maximized, L is also maximized.

TABLE 2.1: Hund's rules for the ground state configuration of the Fe^{3+} ion.

m_l	2	1	0	-1	-2
m_s	↑	↑	↑	↑	↑

Let us examine the case of the Fe^{3+} ion, which will be relevant later on: its electronic configuration is $3d^5$. Despite the $3d$ subshell can accept 10 electrons, this ion only possesses 5 electrons. Following the filling rules, the Fe^{3+} ion's state has only a spin angular momentum (as the orbital angular momenta cancel each other out). Thus, the total angular momentum is $J = S = 5/2$. Since $L = 0$ for the Fe^{3+} ion, its gyromagnetic factor is that of pure spin: $|\gamma|/2\pi = 2|\gamma_{\mathrm{L}}|/2\pi = 28$ GHz.T^{-1}. Additionally, its magnetic moment is $\mu = \hbar\gamma S = -5\mu_B$. Note that it is more common to express the magnetic moment in terms of the Bohr magneton $\mu_B = \hbar|\gamma_{\mathrm{L}}|$ instead to γ_{L}.

2.1.3 Zeeman energy

The Zeeman energy arises from the interaction between an angular momentum and a static magnetic field. We will first illustrate its occurrence for orbital angular momentum from classical mechanics and then extend it to every angular momentum. First, let us recall two fundamental laws in electromagnetism: Gauss' Law and Faraday's Law, which respectively describe the behavior of electric fields and magnetic fields in vacuum.

$$\nabla \cdot \mathbf{B} = 0, \tag{2.23a}$$

$$\nabla \times \mathbf{E} = -\partial_t \mathbf{B}. \tag{2.23b}$$

From Gauss' law, it follows that there exists a vector potential $\mathbf{A}$ such that:

$$\mathbf{B} = \nabla \times \mathbf{A}. \tag{2.24}$$

Substituting into Faraday's Law, we obtain:

$$\nabla \times (\mathbf{E} + \partial_t \mathbf{A}) = 0. \tag{2.25}$$

From this condition, there exists a scalar potential ϕ such that:

$$\mathbf{E} = -\partial_t \mathbf{A} - \nabla\phi. \tag{2.26}$$

Secondly, a particle in an electromagnetic field undergoes the Lorentz force, given by:

$$\mathbf{F} = m\mathrm{d}_t\mathbf{v} = q(\mathbf{E} + \mathbf{v} \times \mathbf{B}), \tag{2.27}$$

where $\mathbf{v}$ is the velocity of the particle. Note that we did not use $\partial_t\mathbf{v}$ because we consider the center of mass of the particle in this equation, meaning that $\partial_{x_i}\mathbf{v} = 0$, where x_i represents x, y, or z. However, the material derivative of the vector potential is given by:

$$\mathrm{d}_t\mathbf{A} = \partial_t\mathbf{A} + \sum_{i=1}^{3}(\partial_t x_i)\partial_{x_i}\mathbf{A}, \tag{2.28}$$

where $\partial_t x_i = v_i$ is the velocity of the particle along the x_i-axis. The Lorentz force can be expressed as:

$$m\mathrm{d}_t\mathbf{v} = q(\mathbf{v} \times \nabla \times \mathbf{A} - \partial_t\mathbf{A} - \nabla\phi), \tag{2.29a}$$
$$\mathrm{d}_t(m\mathbf{v} + q\mathbf{A}) = q\nabla(\mathbf{v} \cdot \mathbf{A} - \phi), \tag{2.29b}$$

where we have used the following identity:

$$(\mathbf{v} \times \nabla \times \mathbf{A})\hat{\mathbf{x}}_i = v_{x_j}(\partial_{x_i}A_{x_j} - \partial_{x_j}A_{x_i}) - v_{x_k}(\partial_{x_k}A_{x_i} - \partial_{x_i}A_{x_k}), \tag{2.30a}$$
$$(\mathbf{v} \times \nabla \times \mathbf{A})\hat{\mathbf{x}}_i = \partial_{x_i}(\mathbf{v} \cdot \mathbf{A}) - \mathrm{d}_t A_{x_i} + \partial_t A_{x_i}. \tag{2.30b}$$

From the principle of least action [103], the following condition is known as the Euleur-Lagrange equation:

$$\mathrm{d}_t\partial_{\dot{x}_i}\mathcal{L} = \partial_{x_i}\mathcal{L}. \tag{2.31}$$

This equation is of the same form as Eq. (2.29b). Concerning the terms on the left-hand side, the conjugate momentum $\mathbf{p}$ is defined as:

$$\mathbf{p} = \partial_{\dot{\mathbf{x}}}\mathcal{L} = m\mathbf{v} + q\mathbf{A}. \tag{2.32}$$

Also, the Lagrangian is defined as:

$$\mathcal{L} = T - V, \tag{2.33}$$

where $T = \mathbf{p} \cdot \mathbf{v}/2$ represents the kinetic energy, and V denotes the potential energy. Considering the terms on the right-hand side of Eq. (2.29b) and (2.31), we determine the potential energy as:

$$\nabla\mathcal{L} = \frac{1}{2}\nabla(\mathbf{v} \cdot \mathbf{p}) - \nabla V = q\nabla(\mathbf{v} \cdot \mathbf{A} - \phi), \tag{2.34a}$$
$$\nabla\mathcal{L} = \frac{1}{2}q\nabla(\mathbf{v} \cdot \mathbf{A}) - \nabla V = q\nabla(\mathbf{v} \cdot \mathbf{A}) - q\nabla\phi, \tag{2.34b}$$
$$V = q\left[\phi - \frac{1}{2}(\mathbf{v} \cdot \mathbf{A})\right]. \tag{2.34c}$$

Then, the Hamiltonian describing a particle moving in an electromagnetic field is given by:

$$\mathcal{H} = T + V, \tag{2.35a}$$
$$\mathcal{H} = \frac{1}{2}\mathbf{p}\cdot\mathbf{v} + q\left[\phi - \frac{1}{2}(\mathbf{v}\cdot\mathbf{A})\right], \tag{2.35b}$$
$$\mathcal{H} = \frac{1}{2m}\mathbf{p}\cdot(\mathbf{p} - q\mathbf{A}) + q\left[\phi - \frac{1}{2m}(\mathbf{p} - q\mathbf{A})\cdot\mathbf{A}\right], \tag{2.35c}$$
$$\mathcal{H} = \frac{1}{2m}(\mathbf{p} - q\mathbf{A})^2 + q\phi. \tag{2.35d}$$

Substituting the momentum with its quantum operator, the Hamiltonian is expressed as:

$$\mathcal{H} = \frac{1}{2m}\left(\frac{\hbar}{i}\nabla - q\mathbf{A}\right)^2 + q\phi, \tag{2.36a}$$
$$\mathcal{H} = -\frac{\hbar^2}{2m}\nabla^2 + i\hbar\frac{q}{2m}\left[\nabla\cdot\mathbf{A} + \mathbf{A}\cdot\nabla\right] + \frac{q^2}{2m}A^2 + q\phi. \tag{2.36b}$$

The first term in this Hamiltonian corresponds to the momentum of a particle moving in a vacuum. The last term is related to the electric field. The third term, named the diamagnetic term, represents the electromagnetic field interacting with itself. This term, being of second order, is often neglected. The second term is of great importance and is related to the Zeeman energy, as it will be shown.

To proceed, it is more common to work in the Coulomb Gauge [98]:

$$\nabla\cdot\mathbf{A} = 0. \tag{2.37}$$

Also, we will consider the particle in a magnetic field only. In the Coulomb Gauge, and without an electric field, the scalar potential ϕ is equal to zero, regarding Eq. (2.26). Thereby, the Zeeman term in Eq. (2.36b) writes as:

$$i\hbar\frac{q}{2m}\left[\nabla\cdot\mathbf{A} + \mathbf{A}\cdot\nabla\right] = i\hbar\frac{q}{m}\mathbf{A}\cdot\nabla. \tag{2.38}$$

Because the magnetic field is considered static, the spatial derivatives of the magnetic field with respect to spatial coordinates vanish:

$$\partial_{x_i}\mathbf{B} = 0. \tag{2.39}$$

This condition allows us to write:

$$\nabla\times(\mathbf{B}\times\mathbf{r}) = \mathbf{B}\nabla\cdot\mathbf{r} - \mathbf{r}\nabla\cdot\mathbf{B} + (\mathbf{r}\cdot\nabla)\mathbf{B} - (\mathbf{B}\cdot\nabla)\mathbf{r}, \tag{2.40a}$$
$$\nabla\times(\mathbf{B}\times\mathbf{r}) = (\nabla\cdot\mathbf{r})\mathbf{B} - (\mathbf{B}\cdot\nabla)\mathbf{r}, \tag{2.40b}$$
$$\nabla\times(\mathbf{B}\times\mathbf{r}) = 2\mathbf{B}. \tag{2.40c}$$

From Eq. (2.24), we have:

$$\mathbf{A} = \frac{1}{2}(\mathbf{B}\times\mathbf{r}). \tag{2.41}$$

Hence, the Zeeman energy writes as:

$$\mathcal{H}_{\mathrm{Z}} = -\frac{\hbar}{i}\frac{q}{2m}(\mathbf{B}\times\mathbf{r})\cdot\nabla, \tag{2.42a}$$

$$\mathcal{H}_{\mathrm{Z}} = -\frac{q}{2m}(\mathbf{r}\times\frac{\hbar}{i}\nabla)\cdot\mathbf{B}, \tag{2.42b}$$

$$\mathcal{H}_{\mathrm{Z}} = -\boldsymbol{\mu}_{\mathrm{L}}\cdot\mathbf{B}. \tag{2.42c}$$

Finally, generalizing for any magnetic moment, the Zeeman Hamiltonian is expressed as:

$$\mathcal{H}_{\mathrm{Z}} = -\boldsymbol{\mu}\cdot\mathbf{B}. \tag{2.43}$$

2.1.4 Larmor Precession

The Larmor precession describes the rotation of the mean magnetic moment of a system subjected to a uniform magnetic field along the z-axis. This phenomenon can be understood semi-classically as an angular momentum precessing around the z-axis. In the Hilbert space of solutions, the system's eigenfunction is represented as:

$$|\psi\rangle = \sum_{m_J} c_{m_J}\,|m_J\rangle, \tag{2.44}$$

where m_J denotes the possible values of $\hat{S}_z$ ranging from $-J$ to J, and c_{m_J} corresponds to their probability amplitude, assumed to be real. Within the Hilbert space, the eigenvector must satisfy the following condition:

$$\langle m_J|m_{J'}\rangle = \delta_{J,J'}. \tag{2.45}$$

Additionally, the state function of the system must be normalized, ensuring that the sum of probabilities equals unity:

$$\langle\psi|\psi\rangle = \sum_{m_J} c_{m_J}^2 = 1. \tag{2.46}$$

The eigenfunction must also satisfy the time-dependent Schrödinger equation:

$$i\hbar\partial_t\,|\psi\rangle = \mathcal{H}_{\mathrm{Z}}\,|\psi\rangle\,. \tag{2.47}$$

Since the Hamiltonian in the Hilbert space of solutions is diagonal, the differential equation can be solved for each $|m_J\rangle$, resulting in:

$$c_{m_J} \to e^{i\omega_{m_J}t}c_{m_J}, \tag{2.48a}$$

$$|\psi\rangle = \sum_{m_J} c_{m_J}e^{i\omega_{m_J}}\,|m_J\rangle, \tag{2.48b}$$

where $\omega_{m_J} = m_J g_{\mathrm{L}}\mu_{\mathrm{B}}B_0$. The mean value of $\hat{J}_z$, corresponding to its measurement, is given by:

$$\langle\hat{J}_z\rangle = \langle\psi|\,\hat{J}_z\,|\psi\rangle = \hbar\sum_{m_J} c_{m_J}^2 m_J. \tag{2.49}$$

Thus, the measured value of the z-projection of the angular momentum equals the mean of the possible values. The mean values of the x and y-component are calculated as (see

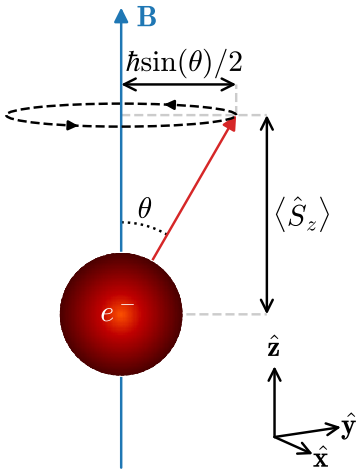

FIGURE 2.3: Schematic representation of the spin precession of an electron in the semi-classical picture.

Appendix 2.B for derivation):

$$\langle \hat{J}_x \rangle = \cos(\omega_{\mathrm{L}} t) \sum_{m_J=-J}^{J-1} c_{m_J} c_{m_J+1} J_+^{m_J}, \tag{2.50a}$$

$$\langle \hat{J}_y \rangle = \sin(\omega_{\mathrm{L}} t) \sum_{m_J=-J}^{J-1} c_{m_J} c_{m_J+1} J_+^{m_J}. \tag{2.50b}$$

From these equations, it shows that the measured values of the angular momentum in the xy-plane exhibit a precession with an angular frequency equal to:

$$\omega_{\mathrm{L}} = \frac{g_{\mathrm{L}} \mu_{\mathrm{B}}}{\hbar} B_0. \tag{2.51}$$

This is known as the Larmor angular frequency.

If a state $|m_J\rangle$ has a probability of one, then $\langle \hat{S}_x \rangle$ and $\langle \hat{S}_y \rangle$ are both 0. For a better clarification, let us examine the scenario of a single electron spin with $m_j = \pm 1/2$. We assume that $c_{1/2} = \cos(\theta/2)$, and $c_{-1/2} = \sin(\theta/2)$. In this context, the mean values of the spin angular momentum components are expressed as follows:

$$\langle \hat{S}_z \rangle = \frac{\hbar}{2}(\cos^2(\theta/2) - \sin^2(\theta/2)) = \frac{\hbar}{2}\cos(\theta), \tag{2.52a}$$

$$\langle \hat{S}_x \rangle = \hbar \cos(\omega_{\mathrm{L}} t)\cos(\theta/2)\sin(\theta/2) = \frac{\hbar}{2}\sin(\theta)\cos(\omega_{\mathrm{L}} t), \tag{2.52b}$$

$$\langle \hat{S}_y \rangle = \hbar \sin(\omega_{\mathrm{L}} t)\cos(\theta/2)\sin(\theta/2) = \frac{\hbar}{2}\sin(\theta)\sin(\omega_{\mathrm{L}} t). \tag{2.52c}$$

This scenario illustrates an angular momentum inclined at an angle θ relative to the z-axis. It mirrors the classical behavior of an angular momentum precessing around the z-axis, as depicted in Fig. 2.3. In a semi-classical picture, the electron resembles a "top" spinning around the z-axis. However, it is imperative to emphasize that while this holds true for the mean value, the quantum object itself remains time-independent, and owns an amplitude

of probabilities for each value.

2.1.5 Equation of motion of an angular momentum

In the continuation of the previous section, we will demonstrate that a static magnetic field induces a torque on an angular momentum. To illustrate this, we introduce the Ehrenfest theorem:

$$\mathrm{d}_t \langle \hat{A} \rangle = \langle \partial_t \hat{A} \rangle + \frac{1}{i\hbar} \langle [\hat{A}, \hat{\mathcal{H}}] \rangle \,, \tag{2.53}$$

where $\hat{A}$ represents operator. Each component of the angular momentum $\hat{\mathbf{J}}$ remains time-independent ($\partial_t \hat{J}_{x_i} = 0$). By considering the Zeeman Hamiltonian, it can be readily demonstrated that:

$$\mathrm{d}_t \langle \hat{J}_x \rangle = -\omega_\mathrm{L} \langle \hat{J}_y \rangle \,, \tag{2.54a}$$

$$\mathrm{d}_t \langle \hat{J}_y \rangle = \omega_\mathrm{L} \langle \hat{J}_x \rangle \,, \tag{2.54b}$$

$$\mathrm{d}_t \langle \hat{J}_z \rangle = 0. \tag{2.54c}$$

From this result, the torque exerted by a static magnetic field on an angular momentum is given by:

$$\boldsymbol{\tau} = \mathrm{d}_t \mathbf{J} = \boldsymbol{\mu} \times \mathbf{B}. \tag{2.55}$$

This equation describes the relaxation in insulators, while electrons must be taken into account to describe metals. It is worth noting that this equation does not account for precession damping rates. The damping rates are phenomenologically introduced in the equation of motion of the net magnetization by including the so-called Gilbert damping parameter α. This damping parameter arises from the energy transfer from precessing spins to lattice vibrations, a process known as magnon-phonon interaction. Its origins can be attributed to two main factors: the direct magnon-phonon coupling mediated by spin-orbit interactions (which we have neglected so far), and the intermediate spin wave states. In the latter case, the dipolar field due to the spin depends on their relative distances. If the lattice vibrates, the dipolar field associated with the spin distances changes, resulting in the creation of spin wave states.

2.2 Magnetic Materials

Magnetic materials are classified into four distinct families based on the arrangement of their magnetic moments, which results in different responses when subjected to a static magnetic field. These four families are known as diamagnetic, paramagnetic, ferromagnetic, and antiferromagnetic. It's worth noting that there is a fifth category known as ferrimagnet; however, its physics closely resembles that of antiferromagnets and can often be considered akin to ferromagnets, as will be discussed later. The investigations presented in this thesis focus on a ferrimagnetic material called Yttrium Iron Garnet (YIG), and its properties are elaborated upon in the subsequent sections.

2.2.1 Diamagnetism

A diamagnetic material consists of atoms or ions with all their subshells filled, meaning they do not possess a permanent magnetic moment. When subjected to a static magnetic field, the electron orbitals undergo significant deformation. This deformation triggers a response, known as Lenz's law, resulting in the emergence of a net magnetization $\mathbf{M}$ opposing the applied static magnetic field.

This effect is not exclusive to electronically filled atoms but applies to all types of atoms due to the deformation of electron orbitals. However, it is often negligible compared to other effects discussed subsequently. The susceptibility associated with diamagnetism is relatively weak ($|\chi_{\text{dia}}| \in [10^{-6}; 10^{-4}]$ [104]) compared to other phenomena. It is important to note that the diamagnetic susceptibility is negative because the magnetization opposes the applied magnetic field.

2.2.2 Paramagnetism

A paramagnetic material comprised of localized magnetic moments that are randomly oriented at thermal equilibrium, resulting in the absence of a net magnetic moment. However, when subjected to a static magnetic field, partial alignment of the magnetic moments with the field occurs, leading to the emergence of net magnetization. The magnitude of this net magnetization is contingent upon the temperature and the strength of the applied magnetic field.

Let us demonstrate the relationship between net magnetization, applied magnetic field strength, and temperature. The system's Hamiltonian is the Zeeman Hamiltonian, and according to statistical mechanics, the probability of an electron being in a state with energy $\mathcal{E}_{\text{Z}}(m_J)$ follows Boltzmann's statistics:

$$P(m_J) = c_{m_J}^2 = \frac{e^{\mathcal{E}_{\text{Z}}(m_J)/k_{\text{B}}T}}{\sum\limits_{m_J=-J}^{J} e^{\mathcal{E}_{\text{Z}}(m_J)/k_{\text{B}}T}}, \tag{2.56}$$

where k_B is the Boltzmann's constant. The denominator is a normalization term, which sums over all the Boltzmann's factor associated with all possible energy states. From this, the averaged value of the magnetic moment can be expressed as:

$$\langle \mu_z \rangle = \frac{\sum\limits_{m_J=-J}^{J} \mu_z(m_J) e^{-\mathcal{E}_z(m_J)/k_{\text{B}}T}}{\sum\limits_{m_J=-J}^{J} e^{-\mathcal{E}_z(m_J)/k_{\text{B}}T}}, \tag{2.57a}$$

$$\langle \mu_z \rangle = -g_{\text{L}}\mu_{\text{B}} \frac{\sum\limits_{m_J=-J}^{J} m_J e^{-m_J x}}{\sum\limits_{m_J=-J}^{J} e^{-m_J x}}. \tag{2.57b}$$

In the last equation, we defined $x = g_{\mathrm{L}}\mu_0\mu_{\mathrm{B}}H/k_{\mathrm{B}}T$. Considering the entire material, with n magnetic moments per unit volume, we can determine the average magnetization as:

$$\mathbf{M} = n\boldsymbol{\mu}. \tag{2.58}$$

After some derivations (see Appendix 2.C), the average magnetization is given by:

$$\langle M_z \rangle = M_{\mathrm{s}} B_J(y), \tag{2.59}$$

where $M_{\mathrm{s}} = ng_{\mathrm{L}}\mu_{\mathrm{B}}J$ is the saturated magnetization (i.e. all spins are aligned along the z-axis), $y = xJ$, and B_J is the Brillouin function defined as:

$$B_J(y) = \frac{2J+1}{2J}\coth\left(\frac{2J+1}{2J}y\right) - \frac{1}{2J}\coth\left(\frac{y}{2J}\right). \tag{2.60}$$

When y is low, i.e. when the temperature is sufficiently high compared to the strength of the applied magnetic field, the Brillouin function can be approximated as:

$$B_J(y) \simeq \frac{J+1}{3J}y, \tag{2.61}$$

Hence, the averaged magnetization can rewrite:

$$\langle M_z \rangle = \frac{C}{T}H, \tag{2.62}$$

where $C = \mu_0 n g_{\mathrm{L}}^2 J(J+1)\mu_{\mathrm{B}}^2/3k_{\mathrm{B}}$ is the Curie constant.

Then, we define the paramagnetic susceptibility, also known as the Curie law, as:

$$\chi_{\mathrm{para}} = \frac{\langle M_z \rangle}{H} = \frac{C}{T}. \tag{2.63}$$

Considering the value of C, the paramagnetic susceptibility is higher for materials composed of atoms with half-filled subshells (because J would be higher). Also, at high temperatures, the paramagnetism disappears, and the material behaves similarly to a diamagnetic material. Note that the paramagnetic susceptibility is positive and typically ranges from 10^{-5} to 10^{-3} [104].

2.2.3 Ferromagnetism

Ferromagnets exhibit a net magnetization because their magnetic moments are spontaneously aligned. This alignment occurs within magnetic domains, which are regions much smaller than the material sample. At equilibrium, these domains cancel each other out, resulting in no net magnetization. However, when an external magnetic field is applied, the domains tend to align with it. The magnetization is considered saturated when all the domains are perfectly aligned with the external magnetic field.

The magnetic moments within a domain spontaneously align themselves below a certain temperature known as the Curie Temperature. According to the Weiss Theory (1907) [105], there also exists an intrinsic magnetic field, historically referred to as the molecular field, due to the interaction of the magnetic moments. It has been later shown that this field

arises from exchange energy in a lattice of spins. This field is expressed as $H_{\text{ex}} = \Lambda_{\text{ex}}\mathbf{M}$, where Λ_{ex} is a material-dependent constant. In this mean field approximation, the theory remains similar to that for paramagnets, with the addition of the exchange field. The magnetization is then given by:

$$M = \frac{C}{T}H_{\text{tot}} = \frac{C}{T}(H + \Lambda_{\text{ex}}M). \tag{2.64}$$

The susceptibility is given by:

$$\chi_{\text{ferro}} = \frac{C}{T - T_{\text{C}}}, \tag{2.65}$$

where $T_{\text{C}} = \Lambda_{\text{ex}}C$ represents the Curie temperature of the material. However, this relationship holds true only when $T > T_C$. Above the Curie temperature, the ferromagnetic effect diminishes, and the material transitions to a paramagnetic state, where all magnetic moments become randomly oriented. For temperatures well below T_{C}, the magnetization follows the $T^{3/2}$ Bloch's law:

$$M \simeq M_{\text{s}}\left[1 - \left(\frac{T}{T_{\text{C}}}\right)^{3/2}\right], \tag{2.66}$$

where $M_s = M(T = 0)$ denotes the saturation magnetization. This law stems from the probability of a spin wave with wavevector $\mathbf{k}$ to exist at a temperature T, which is well demonstrated in Ashcroft and Mermin (2002) [106], p. 840.

2.2.4 Antiferromagnetism

Below the Néel temperature T_{N}, adjacent moments in an antiferromagnet are oppositely oriented, akin to two opposing ferromagnetic sublattices. The net magnetization of these sublattices cancels out in the absence of an applied magnetic field, resulting in no net magnetic moment. Similar to the Curie temperature in ferromagnets, an antiferromagnet exhibits paramagnetic behavior when the temperature exceeds the Néel temperature.

It is worth noting that ferrimagnets also consist of two sublattices, but in contrast to antiferromagnets, the moments in the sublattices do not fully cancel each other out. This discrepancy results in a net magnetization, effectively behaving like a ferromagnet in microwave frequencies and below.

2.2.5 Yttrium Iron Garnet

Yttrium Iron Garnet (YIG) stands out as an artificial insulator ferrimagnet renowned for its numerous advantages. It has secured a prominent position in RF devices and more recently in quantum research setups. One primary advantage of YIG is its remarkably low Gilbert damping rate, which typically ranges from 10^{-5} to 10^{-3} [13, 107–109]. This low damping rate results in a narrow ferromagnetic resonance line, as depicted in Fig. 2.4. YIG has two other significant advantages: a high Curie temperature ($T_{\mathbf{C}} = 560$ K), facilitating experiments at room temperature, and a dense spin population ($n_s = 4.22 \times 10^{27}$ m^{-3} [110]), which proves invaluable for magnon-photon coupling studies.

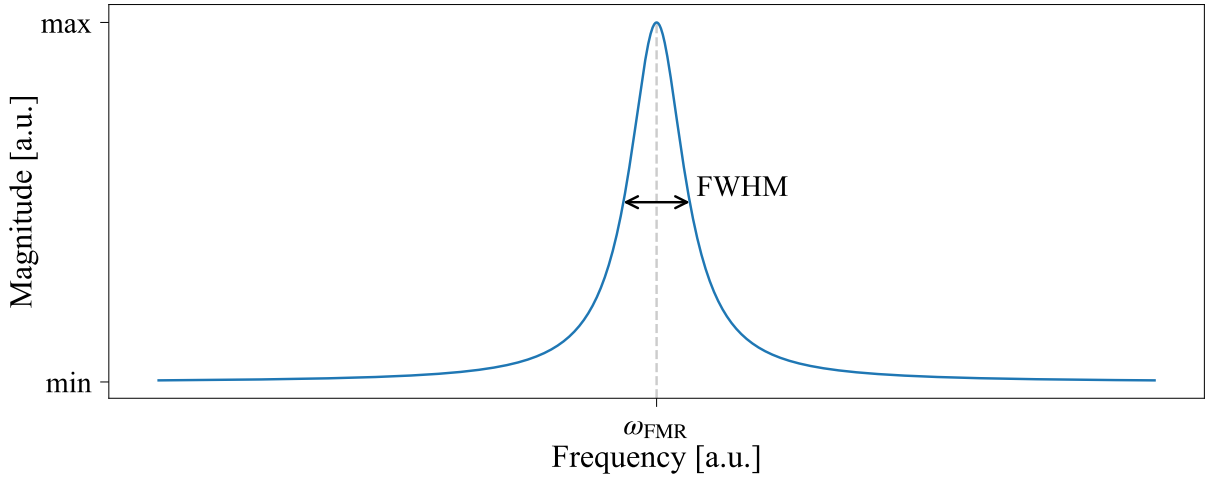

FIGURE 2.4: Schematic representation of the YIG absorption magnitude as a function of frequency. The full width at half maximum (FWHM) corresponds to the YIG losses, which are directly related to the Gilbert damping.

YIG is represented by the chemical formula $Y_3Fe_5O_{12}$. It adopts a cubic crystal structure with a body-centered cubic unit cell, akin to natural garnets, featuring a lattice constant of $a = 12.376$ Å. The unit cell comprises 160 ions organized as follows [111]:

- 16 octahedral sites occupied by Fe^{3+} ions (a-sites).
- 24 tetrahedral sites occupied by Fe^{3+} ions (d-sites).
- 24 dodecahedral sites occupied by Y^{3+} ions (c-sites).
- 96 surrounding O^{2-} ions (h-sites).

This ferrimagnet can be viewed as a ferromagnet wherein the total magnetic momentum is subtracted between the sublattices. Among the ions in this lattice, only Fe^{3+} is magnetic. Considering the subtraction of the two sublattices, the magnetic moment of one unit cell is equivalent to that of the Fe^{3+} ion, amounting to $\mu = 5\mu_B$ at $T = 0$ K.

2.3 Spin Waves

A spin wave represents the collective response of spins in a medium to a perturbation. Rather than observing a local spin reversal due to exchange interactions between nearest spins, a collective excitation of all spins in the magnetic material occurs. The nature of this excitation can vary, originating from interactions with optical waves (optical photon-magnon interaction), lattice vibrations (phonon-magnon interaction), or microwaves (microwave photon-magnon interaction). In this context, we focus on microwave photon-magnon interactions, studying spin waves in ferromagnets where interaction frequencies lie in the microwave range. As demonstrated in the following subsections, spin waves have two main origins: exchange spin waves, crucial at high wavevectors where spin spacing is significant compared to the spin wavelength; and dipole-dipole interactions arising from magnetostatics, important at low wavevectors.

2.3.1 Exchange Spin Waves

In ferromagnets, antiferromagnets, and ferrimagnets, spin alignment arises from the exchange interaction, which can take different forms depending on the material. This interaction is commonly described by the Heisenberg model, which accounts for spin alignment based on the exchange energy between neighboring spins. In metallic ferromagnets, the exchange interaction originates from the direct overlap of electronic wave functions, leading to a mechanism often referred to as direct exchange. However, in insulating magnetic oxides such as YIG, the alignment of spins is mediated by the super-exchange mechanism [112]. In this case, the interaction is indirect and occurs through non-magnetic ions like oxygen, balancing Coulomb and kinetic energy contributions to determine whether the spin alignment is parallel (ferromagnetic) or antiparallel (antiferromagnetic or ferrimagnetic).

2.3.1.a Magnon Dispersion Relation

The Heisenberg Hamiltonian, describing the exchange interaction between adjacent spins, is given by:

$$\hat{\mathcal{H}}_{\text{ex}} = -2\frac{\mathcal{J}}{\hbar^2}\sum_{j,\boldsymbol{\delta}} \hat{\mathbf{S}}_j \cdot \hat{\mathbf{S}}_{j+\boldsymbol{\delta}}, \tag{2.67}$$

where j represents the spin site of the considered spin, and $\boldsymbol{\delta}$ is the vector of the nearest neighbors of this spin site. The exchange parameter $\mathcal{J}$ is assumed to be the same for any of the nearest neighbors of the spins, hence it is factored out of the summation.

In addition to the exchange Hamiltonian, we also consider the Zeeman Hamiltonian for a complete understanding of the system's energy. Assuming a static magnetic field is applied along the z-axis, the Hamiltonian is expressed as follows:

$$\hat{\mathcal{H}} = -2\frac{\mathcal{J}}{\hbar^2}\sum_{j,\boldsymbol{\delta}} \hat{\mathbf{S}}_j \cdot \hat{\mathbf{S}}_{j+\boldsymbol{\delta}} - \frac{g_{\text{L}}\mu_{\text{B}}}{\hbar}B_0\sum_j \hat{S}_j^z. \tag{2.68}$$

Note that the total energy of the system is minimized when all spins are aligned along the z-axis. This aligned state is considered as the ground state of the system. This Hamiltonian can also be expressed as:

$$\hat{\mathcal{H}} = -\frac{\mathcal{J}}{\hbar^2}\sum_{j,\boldsymbol{\delta}} \left(S_j^- S_{j+\boldsymbol{\delta}}^+ + S_j^+ S_{j+\boldsymbol{\delta}}^- + 2S_j^z S_{j,\boldsymbol{\delta}}^z\right) - \frac{g_{\text{L}}\mu_{\text{B}}}{\hbar}B_0\sum_j S_j^z. \tag{2.69}$$

Because the ground state arises when all spins are aligned along the z-axis, it is more convenient to consider each excitation of the system, i.e. each deviation of a spin from its aligned state. To proceed, let us rewrite $\hat{S}_j^z$ as:

$$\hat{S}_j^z = \hbar(S - \hat{m}_j^\dagger \hat{m}_j), \tag{2.70}$$

where $\langle \hat{m}_j^\dagger \hat{m}_j \rangle = n_j$, and n_j represent the number of reversed spins at site j. Instead of focusing on the eigenstates of the electrons in a lattice j, we are only interested in the spin deviation at site j, which represents the number of flipped spins. In this context, we focus on the Fock states $|n_j\rangle$. Similar to a harmonic oscillator, $\hat{m}_j^\dagger$ ($\hat{m}_j$) raises (lowers) the

Fock state, as:

$$\hat{m}_j^\dagger |n_j\rangle = \sqrt{n_j + 1}\, |n_j + 1\rangle\,, \tag{2.71a}$$

$$\hat{m}_j |n_j\rangle = \sqrt{n_j}\, |n_j - 1\rangle\,. \tag{2.71b}$$

A magnon is the quasi-particle associated with the distribution of spin flips over the lattice. Therefore, a spin reversal at site j is equivalent to the presence of a magnon at site j. Additionally, $\hat{m}_j^\dagger$ ($\hat{m}_j$) creates (annihilates) a magnon on site j, and n_j represents the number of magnon on site j. This implies that multiple magnons can exist simultaneously at the same site. Magnons do not obey the Pauli exclusion principle and are bosons, exhibiting the following commutation relation:

$$[\hat{m}_j, \hat{m}_{j'}^\dagger] = \delta_{j,j'}. \tag{2.72}$$

Known as the Holstein-Primakoff transformation [113], the raising and lowering spin operators can be expressed as follows (see Appendix 2.D for derivation):

$$\hat{S}_j^+ = \hbar\sqrt{2S}\sqrt{1 - \frac{\hat{m}_j^\dagger \hat{m}_j}{2S}}\,\hat{m}_j, \tag{2.73a}$$

$$\hat{S}_j^- = \hbar\sqrt{2S}\,\hat{m}_j^\dagger\sqrt{1 - \frac{\hat{m}_j^\dagger \hat{m}_j}{2S}}. \tag{2.73b}$$

At low temperature, only a few spins are reversed across the entire lattice. Consequently, when averaging over a specific site, the number of magnons is close to zero. In the following, we consider this approximation, known as the low-temperature approximation, which allows us to retain only the first-order term of the Taylor series expansion of the square root in Eq. (2.73). This leads to:

$$\hat{S}_j^+ \simeq \hbar\sqrt{2S}\,\hat{m}_j, \tag{2.74a}$$

$$\hat{S}_j^- = \hbar\sqrt{2S}\,\hat{m}_j^\dagger. \tag{2.74b}$$

Neglecting terms in $\hat{m}$ higher than 2 (which follows the same approximation), the Hamiltonian in Eq. (2.69) becomes:

$$\begin{aligned}\hat{\mathcal{H}} = &-2\mathcal{J}S\sum_{j,\boldsymbol{\delta}}\left(\hat{m}_j^\dagger\hat{m}_{j+\boldsymbol{\delta}} + \hat{m}_j\hat{m}_{j+\boldsymbol{\delta}}^\dagger - \hat{m}_j^\dagger\hat{m}_j - \hat{m}_{j+\boldsymbol{\delta}}^\dagger\hat{m}_{j+\boldsymbol{\delta}} + S\right) \\ &- g_{\mathrm{L}}\mu_{\mathrm{B}}B_0\sum_j\left(S - \hat{m}_j^\dagger\hat{m}_j\right).\end{aligned} \tag{2.75}$$

The number of magnons on a specific site j is close to zero at low temperature. However, the total number of magnons across the lattice may not necessary be low. It only needs to be smaller than the number of sites for the approximation to hold. Therefore, it is more appropriate to consider magnons across the entire lattice rather than specific sites. To facilitate this, we define magnons in the k-space. By applying the discrete Fourier

transform to the magnon operators, we obtain:

$$\hat{m}_{\mathbf{k}} = \frac{1}{\sqrt{N}} \sum_j e^{-i\mathbf{k}\cdot\mathbf{r}_j} \hat{m}_j, \tag{2.76a}$$

$$\hat{m}^\dagger_{\mathbf{k}} = \frac{1}{\sqrt{N}} \sum_j e^{i\mathbf{k}\cdot\mathbf{r}_j} \hat{m}^\dagger_j, \tag{2.76b}$$

where $\mathbf{k}$ is the wavevector of the magnon, and $\mathbf{r}_j$ denotes the position vector of the j^{th} site. We recall that the inverse discrete Fourier transform is defined as:

$$\hat{m}_j = \frac{1}{\sqrt{N}} \sum_{\mathbf{k}} e^{\mathbf{k}\cdot\mathbf{r}_j} \hat{m}_{\mathbf{k}}, \tag{2.77a}$$

$$\hat{m}^\dagger_j = \frac{1}{\sqrt{N}} \sum_{\mathbf{k}} e^{-i\mathbf{k}\cdot\mathbf{r}_j} \hat{m}^\dagger_{\mathbf{k}}, \tag{2.77b}$$

where the summation is over all possible wavevectors $\mathbf{k}$ in the Brillouin zone. These operators satisfy the same commutation relation, given by:

$$[m_{\mathbf{k}}, m^\dagger_{\mathbf{k}'}] = \frac{1}{N} \sum_{j,l} e^{-i\mathbf{k}\cdot\mathbf{r}_j} e^{-i\mathbf{k}'\cdot\mathbf{r}_l} [m_{\mathbf{j}}, m^\dagger_{\mathbf{l}}], \tag{2.78a}$$

$$= \frac{1}{N} \sum_{j,l} e^{-i\mathbf{k}\cdot\mathbf{r}_j} e^{-i\mathbf{k}'\cdot\mathbf{r}_l} \delta_{j,l}, \tag{2.78b}$$

$$= \frac{1}{N} \sum_{j} e^{-i(\mathbf{k}'-\mathbf{k})\cdot\mathbf{r}_j}, \tag{2.78c}$$

$$= \delta_{\mathbf{k},\mathbf{k}'}, \tag{2.78d}$$

where the last line follows from the property of the discrete Fourier transform. In the k-space, the Hamiltonian is expressed as:

$$\hat{\mathcal{H}} = \mathcal{E}_0(B_0) + \hat{\mathcal{H}}_0, \tag{2.79}$$

where the ground state energy is given by:

$$\mathcal{E}_0(B_0) = -2N\mathcal{J}ZS^2 - Ng_{\text{L}}\mu_{\text{B}}B_0S. \tag{2.80}$$

The Hamiltonian $\hat{\mathcal{H}}_0$ is given by:

$$\begin{aligned}\hat{\mathcal{H}}_0 = &-2\frac{\mathcal{J}S}{N} \sum_{j,\boldsymbol{\delta},\mathbf{k},\mathbf{k}'} \Big[e^{-i(\mathbf{k}-\mathbf{k}')\cdot\mathbf{r}_j} e^{i\mathbf{k}'\cdot\boldsymbol{\delta}} \hat{m}^\dagger_{\mathbf{k}} \hat{m}_{\mathbf{k}'} + e^{i(\mathbf{k}-\mathbf{k}')\cdot\mathbf{r}_j} e^{-i\mathbf{k}'\cdot\boldsymbol{\delta}} \hat{m}_{\mathbf{k}} \hat{m}^\dagger_{\mathbf{k}'} \\ &- e^{-i(\mathbf{k}-\mathbf{k}')\cdot\mathbf{r}_j} \hat{m}^\dagger_{\mathbf{k}} \hat{m}_{\mathbf{k}'} - e^{-i(\mathbf{k}-\mathbf{k}')\cdot(\mathbf{r}_j+\boldsymbol{\delta})} \hat{m}^\dagger_{\mathbf{k}} \hat{m}_{\mathbf{k}'}\Big] \\ &+ \frac{g_{\text{L}}\mu_{\text{B}}}{N} B_0 \sum_{j,\mathbf{k},\mathbf{k}'} e^{-i(\mathbf{k}-\mathbf{k}')\cdot\mathbf{r}_j} \hat{m}^\dagger_{\mathbf{k}} \hat{m}_{\mathbf{k}'},\end{aligned} \tag{2.81a}$$

$$\hat{\mathcal{H}}_0 = -2\mathcal{J}S \sum_{\boldsymbol{\delta},\mathbf{k}} \Big[e^{i\mathbf{k}\cdot\boldsymbol{\delta}} \hat{m}^\dagger_{\mathbf{k}} \hat{m}_{\mathbf{k}} + e^{-i\mathbf{k}\cdot\boldsymbol{\delta}} \hat{m}_{\mathbf{k}} \hat{m}^\dagger_{\mathbf{k}} - 2\hat{m}^\dagger_{\mathbf{k}} \hat{m}_{\mathbf{k}}\Big] + g_{\text{L}}\mu_{\text{B}}B_0 \sum_{\mathbf{k}} \hat{m}^\dagger_{\mathbf{k}} \hat{m}_{\mathbf{k}}. \tag{2.81b}$$

As for the commutation relation in Eq. (2.78), the sum over $\mathbf{k}'$ vanishes for $\mathbf{k}' \neq \mathbf{k}$, leading to Eq. (2.81b). After this, no terms are dependent on j, hence the sum over j equals N.

By defining the normalized sum over all nearest neighbors of a spin as:

$$\gamma_{\mathbf{k}} = \frac{1}{Z}\sum_{\boldsymbol{\delta}} e^{i\mathbf{k}\cdot\boldsymbol{\delta}}, \tag{2.82}$$

where Z is the number of nearest neighbors of a spin, the Hamiltonian rewrites as:

$$\hat{\mathcal{H}}_0 = \mathcal{J}ZS\sum_{\mathbf{k}}\left[\gamma_{\mathbf{k}}\hat{m}_{\mathbf{k}}^{\dagger}\hat{m}_{\mathbf{k}} + \gamma_{-\mathbf{k}}\left(1+\hat{m}_{\mathbf{k}}^{\dagger}\hat{m}_{\mathbf{k}}\right) - 2\hat{m}_{\mathbf{k}}^{\dagger}\hat{m}_{\mathbf{k}}\right] + g_{\mathrm{L}}\mu_{\mathrm{B}}B_0\sum_{\mathbf{k}}\hat{m}_{\mathbf{k}}^{\dagger}\hat{m}_{\mathbf{k}}, \tag{2.83a}$$

$$\hat{\mathcal{H}}_0 = \sum_{\mathbf{k}}\left[\mathcal{J}ZS(2-\gamma_{\mathbf{k}}-\gamma_{-\mathbf{k}}) + g_{\mathrm{L}}\mu_{\mathrm{B}}B_0\right]\hat{m}_{\mathbf{k}}^{\dagger}\hat{m}_{\mathbf{k}}. \tag{2.83b}$$

The fact that $\sum_{\boldsymbol{\delta}} e^{\mathbf{k}\cdot\boldsymbol{\delta}} = 0$ because $\boldsymbol{\delta} \neq 0$, $\sum_{\mathbf{k}}\gamma_{\mathbf{k}} = 0$, this term is suppressed from the first to second row in the equation above. The Hamiltonian becomes analogous to that of a harmonic oscillator, with the ground state possessing an offset energy:

$$\hat{\mathcal{H}}_0 = \mathcal{E}(B_0) + \sum_{\mathbf{k}}\hbar\omega_{\mathbf{k}}\hat{m}_{\mathbf{k}}^{\dagger}\hat{m}_{\mathbf{k}}, \tag{2.84}$$

where the angular frequency of the magnons with wavevector $\mathbf{k}$ is given by:

$$\omega_{\mathbf{k}} = \left[g_{\mathrm{L}}\mu_{\mathrm{B}}B_0 - \mathcal{J}ZS(\gamma_{\mathbf{k}}+\gamma_{-\mathbf{k}}-2)\right]/\hbar. \tag{2.85}$$

The Hamiltonian in Eq. (2.84) is diagonal in the Fock space of eigenvectors $|n_{\mathbf{k}}\rangle$. We consider the system in the Fock state $|n_{\mathbf{k}}\rangle$, indicating a probability of 1 for this state and 0 for all others. Then, the mean value of a spin at lattice site j is given by:

$$\langle\hat{S}_j^z\rangle = \hbar\left\langle n_{\mathbf{k}}\right| S - \hat{m}_j^{\dagger}\hat{m}_j\left|n_{\mathbf{k}}\right\rangle = \hbar(S - \frac{n_{\mathbf{k}}}{N}), \tag{2.86}$$

where we utilized Eq. (2.77a) and (2.77b). This implies that as more spins are excited, the z-component of each spin decreases more, as expected. In the semi-classical picture, instead of observing $n_{\mathbf{k}}$ spins flipped in the lattice, it effectively reduces the z-component of all spins by $n_{\mathbf{k}}/N$. Conversely to the z-component, we find that it is impossible to determine the x and y-components of the spin angular momentum at site j:

$$\langle\hat{S}_j^x\rangle = \hbar\frac{\sqrt{2S}}{2}\left\langle n_{\mathbf{k}}\right|\hat{m}_j + \hat{m}_j^{\dagger}\left|n_{\mathbf{k}}\right\rangle = 0, \tag{2.87a}$$

$$\langle\hat{S}_j^y\rangle = \hbar\frac{\sqrt{2S}}{2i}\left\langle n_{\mathbf{k}}\right|\hat{m}_j - \hat{m}_j^{\dagger}\left|n_{\mathbf{k}}\right\rangle = 0. \tag{2.87b}$$

This does not imply the absence of components perpendicular to the applied field; rather, it indicates that in a collective spin excitation, the individual length of perpendicular components on a single site cannot be determined. To address this, it is useful to calculate

the scalar product of the perpendicular components between two adjacent spins:

$$\langle \hat{\mathbf{S}}_j^{\perp} \cdot \hat{\mathbf{S}}_{j+\boldsymbol{\delta}}^{\perp} \rangle = \langle \hat{S}_j^x \hat{S}_{j+\boldsymbol{\delta}}^x + \hat{S}_j^y \hat{S}_{j+\boldsymbol{\delta}}^y \rangle \,, \tag{2.88a}$$

$$\langle \hat{\mathbf{S}}_j^{\perp} \cdot \hat{\mathbf{S}}_{j+\boldsymbol{\delta}}^{\perp} \rangle = \hbar^2 \frac{S}{2N} \langle n_{\mathbf{k}} | \, (m_j + m_j^{\dagger})(m_{j+\boldsymbol{\delta}} + m_{j+\boldsymbol{\delta}}^{\dagger}) - (m_j - m_j^{\dagger})(m_{j+\boldsymbol{\delta}} - m_{j+\boldsymbol{\delta}}^{\dagger}) \, | n_{\mathbf{k}} \rangle \,, \tag{2.88b}$$

$$\langle \hat{\mathbf{S}}_j^{\perp} \cdot \hat{\mathbf{S}}_{j+\boldsymbol{\delta}}^{\perp} \rangle = \hbar^2 \frac{2S}{N} n_{\mathbf{k}} \cos(\mathbf{k} \cdot \boldsymbol{\delta}). \tag{2.88c}$$

In the semi-classical picture, this provides two pieces of information regarding the precessing spins: Firstly, the length of the perpendicular component at any site equals $\hbar\sqrt{2Sn_{\mathbf{k}}/N}$, which depends on the number of excited spins in the lattice with wavevector $\mathbf{k}$. Secondly, the dephasing between two nearest spins is given by $\cos(\mathbf{k} \cdot \boldsymbol{\delta})$, representing a collective spin wave, as illustrated in Fig. 2.5 (a). It is worth noting that considering the results of Eq. (2.86) and (2.88c), in the limit where $n_{\mathbf{k}} \ll N$, the precessing spins form an angle:

$$\theta \simeq \tan(\theta) = \frac{\sqrt{2Sn_{\mathbf{k}}/N}}{S - n_{\mathbf{k}}/N} \simeq \sqrt{\frac{2n_{\mathbf{k}}}{NS}}. \tag{2.89}$$

Finally, the cone angle of each spins along the z-axis widens with a higher number of excited spins.

Note that for $k = 0$, $\gamma_0 = 1$, hence the magnon angular frequency is equal to the Larmor anguler frequency:

$$\omega_0 = \frac{g_{\mathrm{L}} \mu_{\mathrm{B}}}{\hbar} B_0. \tag{2.90}$$

Let us explore the behavior of crystals with a simple cubic lattice. In a simple cubic lattice, each spin has two nearest neighbors in each direction at the same distance, denoted as a. Therefore, the Fourier coefficient can be expressed as:

$$\gamma_{\mathbf{k}} = \gamma_{-\mathbf{k}} = \frac{1}{3} \left[\cos(k_x a) + \cos(k_y a) \cos(k_z a) \right]. \tag{2.91}$$

At small k, this leads to the following quadratic dispersion relation:

$$\omega_{\mathbf{k}} = \omega_0 + \frac{4\mathcal{J}Sa^2}{\hbar} k^2. \tag{2.92}$$

Here, the first term corresponds to the precession when all the spins are in phase ($k = 0$), while the second term corresponds to the exchange energy. In this configuration, the exchange spin wave dispersion is quadratic, as illustrated in Fig. 2.5 (b).

2.3.1.b Magnon Interaction

In the previous section, we explored the magnon dispersion relation within the non-interacting spin wave approximation, where the number of magnons is negligible compared to the total number of spins in the lattice. However, when the number of magnons becomes significant, the first-order approximation in the Holstein-Primakoff transformation is no longer accurate. In such cases, it becomes necessary to expand the transformation's Taylor

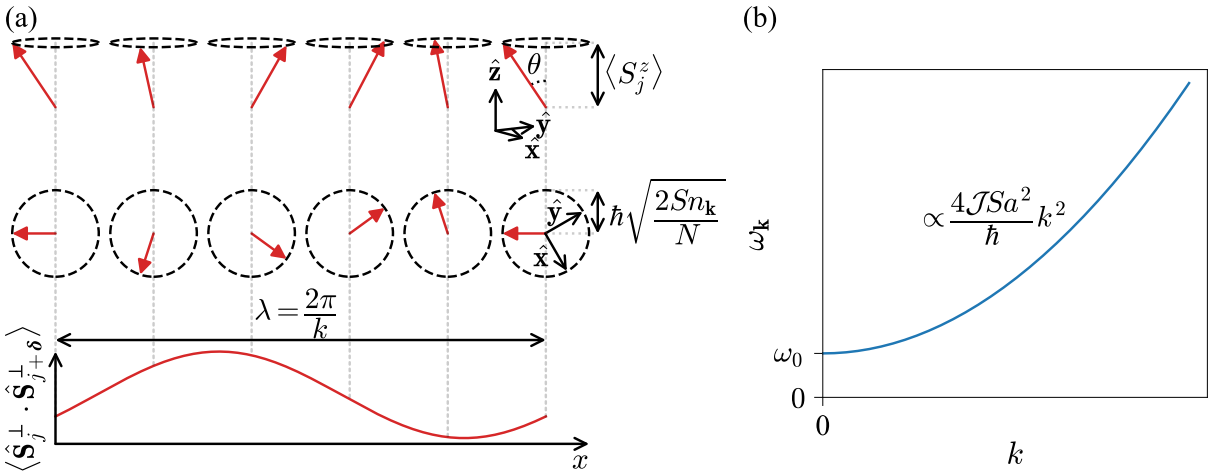

FIGURE 2.5: Illustration of (a) the precession of spin angular momenta of a spin wave in a 1D spin chain, and (b) the quadratic dispersion relation of the exchange spin wave frequency as a function of the wave vector in a crystal with a simple cubic lattice.

series to the second order:

$$\hat{S}_j^+ \simeq \hbar\sqrt{2S}\left(\hat{m}_j - \frac{\hat{m}_j^\dagger \hat{m}_j \hat{m}_j}{4S}\right), \tag{2.93a}$$

$$\hat{S}_j^- \simeq \hbar\sqrt{2S}\left(\hat{m}_j^\dagger - \frac{\hat{m}_j^\dagger \hat{m}_j^\dagger \hat{m}_j}{4S}\right). \tag{2.93b}$$

This results in the addition of a new contribution to the Hamiltonian in Eq. (2.79):

$$\mathcal{H}_1 = \frac{\mathcal{J}Z}{N} \sum_{\mathbf{k}_1,\mathbf{k}_2,\mathbf{k}_3,\mathbf{k}_4} \delta(\mathbf{k}_1 + \mathbf{k}_2 - \mathbf{k}_3 - \mathbf{k}_4)(\gamma_{\mathbf{k}_1} = +\gamma_{\mathbf{k}_3} - 2_{\mathbf{k}_1 - \mathbf{k}_3}) \hat{m}_{\mathbf{k}_1}^\dagger \hat{m}_{\mathbf{k}_2}^\dagger \hat{m}_{\mathbf{k}_3} \hat{m}_{\mathbf{k}_4}. \tag{2.94}$$

Readers can refer to Oguchi (1960) [114] for demonstration for the derivation of this Hamiltonian. It describes the nonlinear transition probability from magnon states with wavevectors $\mathbf{k}_1$ and $\mathbf{k}_2$ to magnon states with wavevectors $\mathbf{k}_3$ and $\mathbf{k}_4$. Thus, the exchange interaction allows only 4-magnon mixing to occur.

2.3.2 Dipolar Spin Waves

In the study of dipolar spin waves, we examine the behavior of magnetization, which represents the density of magnetic moments per unit volume in a sample. This implies aligning all magnetic moments along a z-axis under the influence of a static magnetic field. When a perpendicular periodic magnetic field is applied, the magnetization undergoes precession, a phenomenon described by the Polder susceptibility. It will be illustrated that the range of achievable frequencies for spin waves in a medium is restricted, forming what is known as the spin wave manifold. Additionally, the existence of certain frequencies depends on the boundary conditions and the shape of the sample. This encompasses two categories: the uniform precession modes, with $k = 0$ (also known as Kittel modes), as demonstrated in the last subsection; and the non-uniform precession, which gives rise to

backward and forward volume modes and surface modes, but will not be reviewed in this study.

2.3.2.a Polder Tensor

We consider the magnetic moments in the sample aligned along the z-axis, where a static magnetic field is applied. The resulting magnetization is expressed as:

$$\mathbf{M} = \gamma N \mathbf{J}, \tag{2.95}$$

where N represents the number of spins in the sample.

From Eq. (2.55), the equation of motion governing the magnetization, also known as the Landau-Lifshitz-Gilbert equation, is expressed as:

$$\partial_t \mathbf{M} = \gamma \mu_0 \mathbf{M} \times \mathbf{H} + \frac{\alpha}{M_\mathrm{s}} (\mathbf{M} \times \partial_t \mathbf{M}), \tag{2.96}$$

where we included the phenomenological damping term of the magnetization precession, characterized by the Gilbert damping rate α.

In addition to the static magnetic field, we consider a small time-dependent perturbation $\mathbf{h}(t)$ in the perpendicular directions of the static magnetic field (i.e. $h_z = 0$), leading to rewrites the total field and the magnetization:

$$\mathbf{H} = \mathbf{H}_\mathrm{eff} + \mathbf{h}(t), \tag{2.97a}$$
$$\mathbf{M} = \mathbf{M}_\mathrm{s} + \mathbf{m}(t). \tag{2.97b}$$

The magnetic field within the sample, denoted as $\mathbf{H}_\mathrm{eff}$, comprises three components: the applied static field $\mathbf{H}_0$, the exchange field $\mathbf{H}_\mathrm{ex}$, and the anisotropic field $\mathbf{H}_\mathrm{an}$. In the subsequent analysis, we neglect the anisotropy due to its weak influence in the structure of YIG.

It is assumed that the periodic magnetic field affects the magnetization such that it also exhibits a periodic contribution $\mathbf{m}(t)$. Given the small perturbation, the component along the z-axis remains almost equal to the saturation magnetization, hence $m_z = \mathrm{cst} \simeq 0$. The time-dependent contributions are of the form $e^{i(\mathbf{k}\cdot\mathbf{r}-\omega t)}$. Considering the exchange energy described in Eq. (2.92), from the Zeeman energy, we conclude that the exchange magnetic field has two contributions: the first one is static and proportional to the static magnetic field, $\mathbf{H}_\mathrm{ex} = \Lambda_\mathrm{ex}\mathbf{M}$; and the second one is proportional to k^2, and according to the time-dependent form of $\mathbf{m}(t)$, it can be rewritten as $\mathbf{h}_\mathrm{ex}(t) = \lambda_\mathrm{ex}\nabla^2\mathbf{m}(t) = -\lambda_\mathrm{ex}k^2\mathbf{m}(t)$, where Λ_ex and λ_ex are constant terms. Under these conditions, Eq. (2.96) can be rewritten as:

$$-i\omega\mathbf{m}(t) = \hat{\mathbf{z}} \times [(\tilde{\omega}_0 + \omega_\mathrm{M}\lambda_\mathrm{ex}k^2)\mathbf{m}(t) - \omega_\mathrm{M}\mathbf{h}(t)], \tag{2.98}$$

where we define:

$$\omega_\mathrm{M} = -\gamma\mu_0 M_\mathrm{s}, \tag{2.99a}$$
$$\tilde{\omega}_0 = \omega_0 - i\alpha\omega, \tag{2.99b}$$
$$\omega_0 = -\gamma\mu_0 H_0. \tag{2.99c}$$

Eq. (2.98) transforms into:

$$\mathbf{m} = \bar{\boldsymbol{\chi}} \cdot \mathbf{h}, \tag{2.100}$$

where $\bar{\boldsymbol{\chi}}$ is the Polder susceptibility given by [115]:

$$\bar{\boldsymbol{\chi}} = \begin{bmatrix} \chi & -i\kappa \\ i\kappa & \chi \end{bmatrix}, \tag{2.101a}$$

$$\chi = \frac{(\tilde{\omega}_0 + \omega_\mathrm{M}\lambda_\mathrm{ex}k^2)\omega_\mathrm{M}}{(\tilde{\omega}_0 + \omega_\mathrm{M}\lambda_\mathrm{ex}k^2)^2 - \omega^2}, \tag{2.101b}$$

$$\kappa = \frac{\omega_\mathrm{M}\omega}{(\tilde{\omega}_0 + \omega_\mathrm{M}\lambda_\mathrm{ex}k^2)^2 - \omega^2}. \tag{2.101c}$$

Also, the permeability tensor is given by:

$$\mathbf{b} = \bar{\boldsymbol{\mu}} \cdot \mathbf{h}, \tag{2.102a}$$

$$\bar{\boldsymbol{\mu}} = \mu_0(1 + \bar{\boldsymbol{\chi}}) = \mu_0 \begin{bmatrix} 1+\chi & -i\kappa & 0 \\ i\kappa & 1+\chi & 0 \\ 0 & 0 & 1 \end{bmatrix}. \tag{2.102b}$$

2.3.2.b Magneto-quasistatic Approximation

We will demonstrate the validity of the magneto-quasistatic approximation in the sample, which imposes certain conditions on the possible spin wavevectors. To begin, let us recall Maxwell's equations in a medium:

$$\nabla \times \mathbf{H} = \partial_t \mathbf{D} + \mathbf{J}, \tag{2.103a}$$

$$\nabla \times \mathbf{E} = -\partial_t \mathbf{B}, \tag{2.103b}$$

$$\nabla \cdot \mathbf{D} = \rho, \tag{2.103c}$$

$$\nabla \cdot \mathbf{B} = 0. \tag{2.103d}$$

Here, $\mathbf{H}$ represents the magnetic field intensity, $\mathbf{D}$ denotes the electric flux density, $\mathbf{J}$ stands for the volume electric current density, $\mathbf{E}$ is the electric field intensity, $\mathbf{B}$ represents the magnetic flux density, and ρ represents the electric volume charge density. The equations relating the electric flux density and the electric field intensity in the medium, as well as between the magnetic field intensity and the magnetic flux density in the medium, are given by:

$$\mathbf{D} = \bar{\boldsymbol{\varepsilon}} \cdot \mathbf{E}, \tag{2.104a}$$

$$\mathbf{B} = \bar{\boldsymbol{\mu}} \cdot \mathbf{H}, \tag{2.104b}$$

where $\bar{\boldsymbol{\varepsilon}}$ represents the permittivity tensor, and $\bar{\boldsymbol{\mu}}$ denotes the permeability tensor.

In the following, we consider an insulating media, which implies that $\rho = 0$, and $J = 0$. Additionally, the media is assumed to be electrically isotropic. Assuming that $\mathbf{e}$ and $\mathbf{h}$ are

periodic fields of the form $e^{i(\mathbf{k}\cdot\mathbf{r}-\omega t)}$, the Maxwell's equations are expressed as follows:

$$\mathbf{k}\times\mathbf{h} = -\omega\varepsilon\mathbf{e}, \tag{2.105a}$$
$$\mathbf{k}\times\mathbf{e} = \omega\mu_0(\mathbf{h}+\mathbf{m}), \tag{2.105b}$$
$$\mathbf{k}\cdot\mathbf{e} = 0, \tag{2.105c}$$
$$\mathbf{k}\cdot\mathbf{b} = 0. \tag{2.105d}$$

Cross-multiplying by $\mathbf{k}$ on both sides of Eq. (2.105b) yields:

$$(\mathbf{k}\cdot\mathbf{e})\mathbf{k} - k^2\mathbf{e} = \omega\mu_0\mathbf{k}\times(\mathbf{h}+\mathbf{m}). \tag{2.106}$$

Utilizing Eq. (2.105a), and (2.105c), and (2.106), the electric field is expressed as:

$$\mathbf{e} = \frac{\mu_0\omega\mathbf{k}\times\mathbf{m}}{k_0^2 - k^2}, \tag{2.107}$$

where $k_0 = \mu_0\epsilon\omega^2$. Considering Eq. (2.105a), we derive:

$$\nabla\times\mathbf{h} = -\frac{k_0^2\mathbf{k}\times\mathbf{m}}{k_0^2 - k^2}. \tag{2.108}$$

In the two limits of small k, i.e. $k \ll k_0$, and high k, i.e. $k \gg k_0$, the waves are described by the magnetostatic equations at the lowest order:

$$\nabla\times\mathbf{h} \simeq 0. \tag{2.109}$$

This is known as the magneto-quasistatic approximation, and it is verified under the conditions defined above.

From this, the magnetic field originates from a scalar potential ψ such that:

$$\mathbf{h} = -\nabla\psi. \tag{2.110}$$

From Eq. (2.105d), this also can be expressed as:

$$\nabla\cdot(\bar{\boldsymbol{\mu}}\cdot\nabla\psi) = 0. \tag{2.111}$$

This permeability, as found in Eq. (2.102b), yields the Walker's equation [116]:

$$\left[(1+\chi)(\partial_{x^2}+\partial_{y^2})+\partial_{z^2}\right]\psi = 0. \tag{2.112}$$

Let us consider a wave in the media with a propagation angle θ with respect to the applied static magnetic field along the z-axis. This implies that:

$$k_x^2 + k_y^2 = k^2\sin^2(\theta), \tag{2.113a}$$
$$k_z^2 = k^2\cos^2\theta. \tag{2.113b}$$

Substituting into the Walker's equation, we obtain the following inequality:

$$\chi\sin^2(\theta) = -1. \tag{2.114}$$

This results in the following dispersion of angular frequency in the medium:

$$\omega = \sqrt{\left[\tilde{\omega}_0 + \omega_\mathrm{M}\lambda_\mathrm{ex}k^2\right]\left[\tilde{\omega}_0 + \omega_\mathrm{M}\left(\lambda_\mathrm{ex}k^2 + \sin^2(\theta)\right)\right]}. \tag{2.115}$$

Note that this equation provides the so-called spin wave manifold in an infinite medium, where boundary conditions do not apply. Consequently, there are no constraints on the wavevector k or on the magnetization in the medium. However, this implies that all frequencies can exist within a certain frequency range relative to the wavevector, defining the spin wave manifold, as illustrated in Fig. 2.6. This spin wave manifold depends on the contributions of both the exchange interaction and the quasi-magnetostatic approximation. In the low k region, the exchange term is negligible, and this area is considered as dipolar spin waves. Conversely, at high k, the dipolar term is negligible, and this region is considered as exchange spin waves.

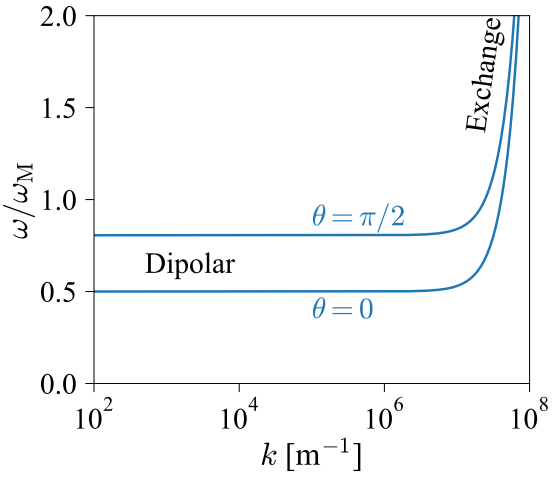

FIGURE 2.6: Spin wave manifold for the YIG, where $\omega_0 = 0.5\omega_\mathrm{M}$ and $\lambda_\mathrm{ex} = 3 \cdot 10^{-16}$ m^2, adapted from [25].

When dealing with a medium of finite size, boundary conditions come into play. This implies that the magnetization remains constant at the edges of the sample and does not precess. Consequently, certain conditions emerge regarding the uniform precession angular frequency of the magnetization, as well as the propagation of non-uniform modes.

2.3.2.c Uniform Precession Modes

The tangential component of $\mathbf{B}$ must remain continuous at the surface edges of the sample, giving rise to what is known as the demagnetizing field $\mathbf{H}_\mathrm{d}$. This field arises due to the presence of effective magnetic surface charges and is expressed as:

$$\mathbf{H}_\mathrm{d} = -\bar{\mathbf{N}} \cdot \mathbf{M}, \tag{2.116}$$

where $\bar{\mathbf{N}}$ represents the demagnetizing tensor, which is contingent upon the shape of the sample.

It has been demonstrated in the study by Schlömann (1962) [117] that for various shapes, whether ellipsoids or non-ellipsoids, the trace of the demagnetizing tensor equals

1. We will examine the same system as previously described, featuring magnetization saturated along the z-axis, which aligns with the direction of the static magnetic field. Additionally, a small periodic magnetic field is applied perpendicular to the z-axis. The total static magnetic field is given by:

$$\mathbf{H} = \mathbf{H}_0 - \bar{\mathbf{N}} \cdot \mathbf{M}_\mathrm{s}, \tag{2.117a}$$

$$\mathbf{H} = \begin{bmatrix} -N_{xz} M_\mathrm{s} \\ -N_{yz} M_\mathrm{s} \\ H_0 - N_{zz} M_\mathrm{s} \end{bmatrix}. \tag{2.117b}$$

This implies that ω_0 in Eq. (2.99c) can be expressed as:

$$\omega_0 = -\gamma \mu_0 (H_0 - N_{zz} M_\mathrm{s}). \tag{2.118}$$

Now, taking into account the periodic contributions, we obtain the following relationship:

$$\mathbf{h} = \bar{\chi}^{-1} \cdot \mathbf{m} = -\bar{\mathbf{N}} \cdot \mathbf{m}, \tag{2.119a}$$

$$\Rightarrow (\bar{\chi}^{-1} + \bar{\mathbf{N}}) \cdot \mathbf{m} = \mathbf{0}. \tag{2.119b}$$

From this equation, by calculating the determinant of $\bar{\chi}^{-1} + \bar{\mathbf{N}}$, we can determine the angular frequency of the uniform modes. Without considering the Gilbert damping rate, we find that:

$$\begin{aligned} \omega =& \frac{1}{2} \sqrt{(N_{xy} - N_{yx})^2 \omega_M^2 + 4(\omega_0 + N_{xx}\omega_M)(\omega_0 + N_{yy}\omega_M) - 4 N_{xy} N_{yx} \omega_M^2} \\ &+ \frac{i}{2} (N_{xy} - N_{yx}) \omega_M. \end{aligned} \tag{2.120}$$

In the study presented in this thesis, only two shapes are considered: a sphere and a rectangular prism. The sphere exhibits properties akin to an ellipsoidal sample: the demagnetizing field is uniform inside the sample, and the off-diagonal components of the demagnetizing tensor are zero. For a sphere, the diagonal components of the demagnetizing tensor are equal and given by:

$$N_{xx} = N_{yy} = N_{zz} = \frac{1}{3}. \tag{2.121}$$

Thus, the uniform precession of magnons in a spherical ferromagnet is reduced to [118]:

$$\omega_\mathrm{sphere} = \gamma \mu_0 H_0. \tag{2.122}$$

For the rectangular prism, the components of the demagnetization tensor are position-dependent. In the paper by Joseph and Schlömann (1965) [119], it has been shown that the diagonal components at the first order are given by:

$$\begin{aligned} N_{kk} =& \cot^{-1}[f(x_i, x_j, x_k)] + \cot^{-1}[f(-x_i, x_j, x_k)] + \cot^{-1}[f(x_i, -x_j, x_k)] \\ &+ \cot^{-1}[f(x_i, x_j, -x_k)] + \cot^{-1}[f(-x_i, -x_j, x_k)] \\ &+ \cot^{-1}[f(-x_i, x_j, -x_k)] + \cot^{-1}[f(x_i, -x_j, -x_k)] + \cot^{-1}[f(-x_i, -x_j, -x_k)], \end{aligned} \tag{2.123}$$

where:

$$f(x_i, x_j, x_k) = \sqrt{(a_i - x_i)^2 + (a_j - x_j)^2 + (a_k - x_k)^2} \frac{a_k - x_k}{(a_i - x_i)(a_j - x_j)}. \tag{2.124}$$

The off-diagonal components are expressed as:

$$N_{ik} = \log \left[\frac{G(\mathbf{r}, a_i, a_j, a_k) G(\mathbf{r}, -a_i, -a_j, a_k) G(\mathbf{r}, -a_i, a_j, -a_k) G(\mathbf{r}, a_i, -a_j, -a_k)}{G(\mathbf{r}, -a_i, a_j, a_k) G(\mathbf{r}, a_i, -a_j, a_k) G(\mathbf{r}, a_i, a_j, -a_k) G(\mathbf{r}, -a_i, -a_j, -a_k)} \right], \tag{2.125}$$

where:

$$G(\mathbf{r}, a_i, a_j, a_k) = a_j - x_j + \sqrt{(a_i - x_i)^2 + (a_j - x_j)^2 + (a_k - x_k)^2}. \tag{2.126}$$

It can be observed that the off-diagonal components are symmetric: $N_{ik} = N_{ki}$. These leads to the following angular frequency for a rectangular prism:

$$\omega_{\text{prism}} = \gamma \mu_0 \sqrt{[H_0 + (N_{xx} - N_{zz}) M_{\text{s}}][H_0 + (N_{yy} - N_{zz}) M_{\text{s}}] - N_{xy}^2 M_{\text{s}}^2}. \tag{2.127}$$

Note that for Eq. (2.127), the angular frequency exhibits spatial dependence. Depending on the geometry of the system, the angular frequency can either be evaluated by taking a spatial average of the components of the demagnetization tensor or approximated using the values at the center of the rectangular prism.

Appendices of Chapter 2

2.A Derivation of the Landé factor

To derive the Landé factor in Eq. (2.22) as discussed in Sec. 2.1.2.b, we begin with the total magnetic momentum given in Eq. (2.20). By multiplying both sides of the equation by $\hat{\mathbf{J}}$, we obtain:

$$\gamma_{\mathrm{L}}(\hat{\mathbf{L}} + 2\hat{\mathbf{S}}) \cdot (\hat{\mathbf{L}} + \hat{\mathbf{S}}) = g_{\mathrm{L}}\gamma_{\mathrm{L}}\hat{J}^2, \tag{2.128a}$$

$$\hat{L}^2 + 3\hat{\mathbf{L}} \cdot \hat{\mathbf{S}} + \hat{S}^2 = g_{\mathrm{L}}\hat{J}^2, \tag{2.128b}$$

$$\frac{3}{2}\hat{J}^2 + \frac{1}{2}(\hat{S}^2 - \hat{L}^2) = g_{\mathrm{L}}\hat{J}^2. \tag{2.128c}$$

After substituting $\hat{\mathbf{L}} \cdot \hat{\mathbf{S}}$ using the identity $\hat{J}^2 = \hat{L}^2 + \hat{\mathbf{L}} \cdot \hat{\mathbf{S}} + \hat{S}^2$, we find:

$$g_{\mathrm{L}} = \frac{3}{2} + \frac{\hat{S}^2 - \hat{L}^2}{2\hat{J}^2}. \tag{2.129}$$

Upon replacing these operators with their respective eigenvalues, we obtain the Landé factor as depicted in Eq. (2.22).

2.B Derivation of the Larmor precession of an angular momentum

The expression for the mean value of the x-component of angular momentum is derived as follows:

$$\langle \hat{J}_x \rangle = \frac{1}{2} \left(\sum_{m_J} \langle m_J | \, c_J e^{-i\omega_{m_J} t} \right) \left(\hat{J}_+ + \hat{J}_- \right) \left(\sum_{m'_J} c'_J e^{i\omega_{m'_J} t} \, |m'_J\rangle \right), \tag{2.130a}$$

$$\begin{aligned} \langle \hat{J}_x \rangle = & \frac{1}{2} \left(\sum_{m_J} \langle m_J | \, c_J e^{-i\omega_{m_J} t} \right) \\ & \left(\sum_{m'_J=-J}^{J-1} c_{m'_J} e^{i\omega_{m'_J} t} J_+^{m'_J} \, |m'_J + 1\rangle + \sum_{m'_J=-J+1}^{J} c_{m'_J} e^{i\omega_{m'_J} t} J_-^{m'_J} \, |m'_J - 1\rangle \right), \end{aligned} \tag{2.130b}$$

$$\begin{aligned} \langle \hat{J}_x \rangle = & \frac{1}{2} \left(\sum_{m_J} \langle m_J | \, c_J e^{-i\omega_{m_J} t} \right) \\ & \left(\sum_{m'_J=-J}^{J-1} c_{m'_J} e^{i\omega_{m'_J} t} J_+^{m'_J} \, |m'_J + 1\rangle + \sum_{m'_J=-J}^{J-1} c_{m'_J+1} e^{i\omega_{m'_J+1} t} J_-^{m'_J+1} \, |m'_J\rangle \right), \end{aligned} \tag{2.130c}$$

$$\langle \hat{J}_x \rangle = \frac{1}{2} \sum_{m_J=-J}^{J-1} \left(c_{m_J+1} c_{m_J} J_+^{m_J} e^{i(\omega_{m_J} - \omega_{m_J+1})t} + c_{m_J} c_{m_J+1} J_-^{m_J+1} e^{i(\omega_{m_J+1} - \omega_{m_J})t} \right), \tag{2.130d}$$

$$\langle \hat{J}_x \rangle = \cos(\omega_{\mathrm{L}} t) \sum_{m_J=-J}^{J-1} c_{m_J} c_{m_J+1} J_+^{m_J}, \tag{2.130e}$$

where $J_+^{m_J} = J_-^{m_J+1}$.

To derive the expression for the y-component of angular momentum, we follow a similar procedure:

$$\langle \hat{J}_y \rangle = \frac{1}{2i} \left(\sum_{m_J} \langle m_J | \, c_J e^{-i\omega_{m_J} t} \right) \left(\hat{J}_+ - \hat{J}_- \right) \left(\sum_{m'_J} c'_J e^{i\omega_{m'_J} t} \, | m'_J \rangle \right), \tag{2.131a}$$

$$\begin{aligned} \langle \hat{J}_y \rangle =& \frac{1}{2i} \left(\sum_{m_J} \langle m_J | \, c_J e^{-i\omega_{m_J} t} \right) \\ & \left(\sum_{m'_J=-J}^{J-1} c_{m'_J} e^{i\omega_{m'_J} t} J_+^{m'_J} \, | m'_J + 1 \rangle - \sum_{m'_J=-J+1}^{J} c_{m'_J} e^{i\omega_{m'_J} t} J_-^{m'_J} \, | m'_J - 1 \rangle \right), \end{aligned} \tag{2.131b}$$

$$\begin{aligned} \langle \hat{J}_y \rangle =& \frac{1}{2i} \left(\sum_{m_J} \langle m_J | \, c_J e^{-i\omega_{m_J} t} \right) \\ & \left(\sum_{m'_J=-J}^{J-1} c_{m'_J} e^{i\omega_{m'_J} t} J_+^{m'_J} \, | m'_J + 1 \rangle - \sum_{m'_J=-J}^{J-1} c_{m'_J+1} e^{i\omega_{m'_J+1} t} J_-^{m'_J+1} \, | m'_J \rangle \right), \end{aligned} \tag{2.131c}$$

$$\langle \hat{J}_y \rangle = \frac{1}{2i} \sum_{m_J=-J}^{J-1} \left(c_{m_J+1} c_{m_J} J_+^{m_J} e^{i(\omega_{m_J} - \omega_{m_J+1})t} - c_{m_J} c_{m_J+1} J_-^{m_J+1} e^{i(\omega_{m_J+1} - \omega_{m_J})t} \right), \tag{2.131d}$$

$$\langle \hat{J}_y \rangle = \sin(\omega_{\mathrm{L}} t) \sum_{m_J=-J}^{J-1} c_{m_J} c_{m_J+1} J_+^{m_J}. \tag{2.131e}$$

2.C Derivation of the thermal averaged value of the magnetization

Given that there are N magnetic moments per unit volume, the average of the net magnetization, as derived from equation Eq. (2.57b) in Section 2.2.2, is expressed as:

$$\langle M_z \rangle = -N g_{\mathrm{L}} \mu_{\mathrm{B}} \frac{\sum_{m_J=-J}^{J} m_J e^{-m_J x}}{\sum_{m_J=-J}^{J} e^{-m_J x}}. \tag{2.132}$$

This is analogous to taking the derivative of the natural logarithm with respect to x:

$$\langle M_z \rangle = -N g_{\mathrm{L}} \mu_{\mathrm{B}} \mathrm{d}_x \ln \left(\sum_{m_J=-J}^{J} e^{-m_J x} \right). \tag{2.133}$$

The summation over the exponential terms forms a finite geometric series, which can be expressed as:

$$\sum_{m_J=-J}^{J} e^{-mx} = \frac{e^{-(J+1/2)x} - e^{(J+1/2)x}}{e^{-x/2} - e^{x/2}}, \tag{2.134a}$$

$$\sum_{m_J=-J}^{J} e^{-mx} = \frac{\sinh[(J+1/2)x]}{\sinh[x/2]}. \tag{2.134b}$$

Substituting this expression into Eq. (2.133), the thermal average of the magnetization becomes:

$$\langle M_z \rangle = -N g_{\mathrm{L}} \mu_{\mathrm{B}} \mathrm{d}_x \left[\ln \left(\sinh[(J+1/2)x] \right) - \ln \left(\sinh[x/2] \right) \right], \tag{2.135a}$$

$$\langle M_z \rangle \simeq -N g_{\mathrm{L}} \mu_{\mathrm{B}} \mathrm{d}_x \left(\sinh[(J+1/2)x] - \sinh[x/2] \right). \tag{2.135b}$$

After considering that the static magnetic field is weak compared to thermal agitation, which implies $H \ll k_{\mathrm{B}}T \rightarrow x \ll 1$, the derived equation becomes:

$$\langle M_z \rangle = N g_{\mathrm{L}} \mu_{\mathrm{B}} J \left(\left[1 + \frac{1}{2J} \right] \coth \left[\left(1 + \frac{1}{2J} \right) Jx \right] - \left[\frac{1}{2J} \right] \coth \left[\frac{1}{2J} Jx \right] \right), \tag{2.136a}$$

$$\langle M_z \rangle = M_{\mathrm{s}} B_J(\mu_0 \mu_{\mathrm{s}} H / k_{\mathrm{B}} T), \tag{2.136b}$$

where $\mu_{\mathrm{s}} = g_{\mathrm{L}} J$ represents the saturated magnetic moment, $M_{\mathrm{s}} = N\mu_{\mathrm{s}}$ denotes the saturated magnetization, and $B_J(y)$ stands for the Brillouin function as defined in Eq. (2.60).

2.D Derivation of the Holstein-Primakoff Transformation

From equation Eq. (2.14a) and Eq. (2.14b) in Sec. 2.1.2.a, we express the raising and lowering operators for the macrospin as follows:

$$\hat{\mathbf{S}}_j^+ \left| m_S^j \right\rangle = \hbar \sqrt{S(S+1) - m_S^j (m_S^j + 1)} \left| m_S^j + 1 \right\rangle, \tag{2.137a}$$

$$\hat{\mathbf{S}}_j^- \left| m_S^j \right\rangle = \hbar \sqrt{S_j(S_j+1) - m_S^j (m_S^j - 1)} \left| m_S^j - 1 \right\rangle. \tag{2.137b}$$

Let us equate the eigenstate $|m_S^j\rangle$ to the state $|n_j\rangle$, where the eigenvalue $n_j = S - m_S^j$. When the eigenstate $|m_S^j\rangle$ rises to $|m_S^j + 1\rangle$, the eigenstate $|n_j\rangle$ must decrease to $|n_j - 1\rangle$. This implies that Eq. (2.137a) becomes:

$$\hat{\mathbf{S}}_j^+ \left| n_j \right\rangle = \hbar \sqrt{S(S+1) - [S - n_j][S - (n_j - 1)]} \left| n_j - 1 \right\rangle, \tag{2.138a}$$

$$\hat{\mathbf{S}}_j^+ \left| n_j \right\rangle = \hbar \sqrt{2S} \sqrt{1 - \frac{n_j}{2S}} \sqrt{n_j} \left| n_j - 1 \right\rangle, \tag{2.138b}$$

$$\hat{\mathbf{S}}_j^+ \left| n_j \right\rangle = \hbar \sqrt{2S} \sqrt{1 - \frac{\hat{m_j}^\dagger \hat{m_j}}{2S}} \hat{m}_j \left| n_j \right\rangle, \tag{2.138c}$$

where we have utilized the magnon lowering operator from Eq. (2.71b). In the same manner, Eq. (2.137b) transforms into:

$$\hat{\mathbf{S}}_j^- \left| n_j \right\rangle = \hbar \sqrt{S(S+1) - [S - n_j][S - (n_j + 1)]} \left| n_j + 1 \right\rangle, \tag{2.139a}$$

$$\hat{\mathbf{S}}_j^- \left| n_j \right\rangle = \hbar \sqrt{2S} \sqrt{1 - \frac{n_j}{2S}} \sqrt{n_j + 1} \left| n_j - 1 \right\rangle, \tag{2.139b}$$

$$\hat{\mathbf{S}}_j^- \left| n_j \right\rangle = \hbar \sqrt{2S} \sqrt{1 - \frac{\hat{m_j}^\dagger \hat{m_j}}{2S}} \hat{m}_j^\dagger \left| n_j \right\rangle, \tag{2.139c}$$

where we have employed the magnon raising operator from Eq. (2.71a).

3 Light-Matter Interactions

Abstract

This chapter begins with the quantization of the electromagnetic field within a cavity to establish the cavity Hamiltonian for subsequent analysis. Following this, an analogy is drawn between light-matter coupling and the physics of two coupled oscillators. This simplified model aids in comprehending the primary models describing light-matter interaction across various matter systems. After delineating the various coupling regimes, a discourse on different light-matter coupling models ensues. These models are then expanded to incorporate the system and its environment. Finally, the chapter concludes with the derivation of the photon-magnon coupling model.

Contents

3.1 Cavity Photon Quantization

This section aims to derivate the quantization of the electromagnetic field within a cavity. Beginning with classical electrodynamics, we expand the vector potential in terms of cavity modes. By utilizing the appropriate expression for the potential vector, we demonstrate that the Hamiltonian governing the cavity's photonic modes consists of a sum of oscillators. This distinctive characteristic enables us to quantify the Hamiltonian of these oscillators within the Fock state of the cavity's photonic modes, thereby achieving the quantization of the electromagnetic field within the cavity.

3.1.1 Classical Electrodynamics

It is assumed that the cavity's electromagnetic field does not interact with matter, meaning the volume electric current density $\mathbf{J}$ and the electric volume charge density ρ are both zero. As a result, Maxwell's equations, as defined in Eq. (2.103), can be rewritten as:

$$\nabla \times \mathbf{H}(\mathbf{r},t) = \varepsilon_0 \varepsilon_\mathrm{r}(\mathbf{r}) \partial_t \mathbf{E}(\mathbf{r},t), \tag{3.1a}$$
$$\nabla \times \mathbf{E}(\mathbf{r},t) = -\mu_0 \partial_t \mathbf{H}(\mathbf{r},t), \tag{3.1b}$$
$$\mu_0 \nabla \cdot \mathbf{H}(\mathbf{r},t) = 0, \tag{3.1c}$$
$$\varepsilon_0 \nabla \cdot [\varepsilon_\mathrm{r}(\mathbf{r}) \mathbf{E}(\mathbf{r},t)] = 0. \tag{3.1d}$$

Here, $\varepsilon_\mathrm{r}(\mathbf{r})$ represents the relative permittivity, which is related to the permittivity as $\varepsilon(\mathbf{r}) = \varepsilon_0 \varepsilon_\mathrm{r}(\mathbf{r})$.

From equations Eq. (3.1a) and Eq. (3.1b), we can deduce:

$$\frac{1}{\varepsilon_\mathrm{r}(\mathbf{r})} \nabla \times \nabla \times \mathbf{E}(\mathbf{r},t) = -\frac{1}{c^2} \partial_t^2 \mathbf{E}(\mathbf{r},t), \tag{3.2}$$

where c is the vacuum speed of light. This equation is known as the wave equation of the electric field, also referred to as the d'Alembert equation.

3.1.1.a Wave equation of the potential vector

We remind that the electric and magnetic fields are associated with the vector potential $\mathbf{A}$, as defined in Eq. (2.24). For all subsequent analysis, it is more convenient to work in the Coulomb gauge, as described in Eq. (2.37). It is worth noting that in this gauge, and in the absence of electric volume charge density, the scalar potential can be chosen to be zero, which simplifies calculations and leads to:

$$\mu_0 \mathbf{H}(\mathbf{r},t) = \nabla \times \mathbf{A}(\mathbf{r},t), \tag{3.3a}$$
$$\mathbf{E}(\mathbf{r},t) = -\partial_t \mathbf{A}(\mathbf{r},t). \tag{3.3b}$$

Additionally, employing the Coulomb gauge allows us to reformulate the wave equation provided in Eq. (3.2) as[1]:

$$\nabla^2 \mathbf{A}(\mathbf{r},t) = \frac{\varepsilon_\mathrm{r}(\mathbf{r})}{c^2}\partial_t^2 \mathbf{A}(\mathbf{r},t). \tag{3.4}$$

It is assumed that the potential vector can be separated into two variables: a spatial variable $\mathbf{U}(\mathbf{r})$ and a temporal variable $q(t)$. Additionally, the boundary conditions of the cavity allow only certain eigenmodes of angular frequency ω_k, which are related to the dispersion relation considering the wave number k. It is also assumed that the mode functions are real-valued. This dispersion relation depends on the cavity geometry; notably, the mode expansion of the vector potential can be expressed in the general form [120]:

$$\mathbf{A}(\mathbf{r},t) = \sum_k \mathbf{U}_k(\mathbf{r}) q_k(t). \tag{3.5}$$

Furthermore, $q(t)$ is a sinusoidal function of $\omega_k t$. Thereby, Eq. (3.4) becomes:

$$\nabla^2 \mathbf{U}_k(\mathbf{r}) = -\frac{\varepsilon_\mathrm{r}(\mathbf{r})\omega_k^2}{c^2}\mathbf{U}_k(\mathbf{r}). \tag{3.6}$$

Note that the divergence of $\mathbf{U}_k(\mathbf{r})$ is also equal to zero. In the following, it is assumed that $\mathbf{U}_k(\mathbf{r})$ is normalized. From this, it can be shown that (see Appendix 3.3):

$$\int \mathrm{d}^3\mathbf{r}\, \varepsilon_\mathrm{r}(\mathbf{r})\mathbf{U}_k(\mathbf{r})\cdot\mathbf{U}_{k'}(\mathbf{r}) = \varepsilon_{\mathrm{r},k}\delta_{k,k'}, \tag{3.7}$$

where $\varepsilon_{\mathrm{r},k}$ represents the averaged relative permittivity of mode k throughout the cavity.

3.1.1.b Hamiltonian of the photonic oscillator

Before deriving the Hamiltonian of the electromagnetic field inside the cavity, it is necessary to rewrite the vector potential in a suitable form to facilitate the solution of the Hamiltonian. Thus, the vector potential can be rewritten as [120]:

$$\mathbf{A}(\mathbf{r},t) = \sum_k \frac{q_k(t)}{\sqrt{\varepsilon_0\varepsilon_{\mathrm{r},k}}}\mathbf{U}_k(\mathbf{r}). \tag{3.8}$$

Therefore, the Hamiltonian of the electromagnetic field inside the cavity is expressed as:

$$\mathcal{H} = \frac{1}{2}\int \mathrm{d}^3\mathbf{r}\, \left[\varepsilon_0\varepsilon_\mathrm{r}(\mathbf{r})\mathbf{E}(\mathbf{r},t)\cdot\mathbf{E}(\mathbf{r},t) + \mu_0\mathbf{H}(\mathbf{r},t)\mathbf{H}(\mathbf{r},t)\right], \tag{3.9a}$$

$$\begin{aligned}\mathcal{H} = \frac{1}{2}\sum_{k,k'}\int d^3\mathbf{r}\, \Bigg[&\frac{\varepsilon_0\varepsilon_\mathrm{r}(\mathbf{r})}{\sqrt{\varepsilon_0\varepsilon_{\mathrm{r},k}}\sqrt{\varepsilon_0\varepsilon_{\mathrm{r},k'}}}\dot{q}_k(t)\dot{q}_{k'}(t)\mathbf{U}_k(\mathbf{r})\cdot\mathbf{U}_{k'}(\mathbf{r}) \\ &+\frac{1}{\mu_0}\frac{q_k(t)q_{k'}(t)}{\sqrt{\varepsilon_0\varepsilon_{\mathrm{r},k}}\sqrt{\varepsilon_0\varepsilon_{\mathrm{r},k'}}}\left(\nabla\times\mathbf{U}_k(\mathbf{r})\right)\cdot\left(\nabla\times\mathbf{U}_{k'}(\mathbf{r})\right)\Bigg].\end{aligned} \tag{3.9b}$$

[1] Utilizing the following identity: $\nabla\times\nabla\times\mathbf{A} = \nabla(\nabla\cdot\mathbf{A}) - \nabla^2\mathbf{A}$

The integration of the scalar product in the right-hand side of Eq. (3.9b) can be rewritten as[2]:

$$\int \mathrm{d}^3\mathbf{r}\,(\nabla \times \mathbf{U}_k(\mathbf{r})) \cdot (\nabla \times \mathbf{U}_{k'}(\mathbf{r})) = \frac{\varepsilon_{\mathrm{r},k}\omega_k^2}{c^2}\delta_{k,k'}. \tag{3.10}$$

This results in the following Hamiltonian:

$$\mathcal{H} = \frac{1}{2}\sum_k \left[\dot{q}_k^2(t) + \omega_k^2 q_k^2(t)\right]. \tag{3.11}$$

This Hamiltonian is analogous to that of an oscillator. Following the approach used for magnons in the previous chapter, the next section will focus on the quantization of the electromagnetic field within the cavity, beginning with this Hamiltonian.

3.1.2 Quantum Electrodynamics

To quantize the electromagnetic field inside the cavity, we need to define the following quantum operators:

$$q_k(t) \to \hat{q}_k(t), \tag{3.12a}$$
$$\dot{q}_k(t) = p_k(t) \to \hat{p}_k(t). \tag{3.12b}$$

The commutation relation postulate for these two operators is as follows [120]:

$$[\hat{q}_k(t), \hat{p}_{k'}(t)] = i\hbar\delta_{k,k'}. \tag{3.13}$$

The annihilation and creation photonic operators are defined as follows:

$$\hat{c}_k(t) = \frac{1}{\sqrt{2\hbar\omega_k}}(\omega_k\hat{q}_k(t) - i\hat{p}_k(t)), \tag{3.14a}$$
$$\hat{c}_k^\dagger(t) = \frac{1}{\sqrt{2\hbar\omega_k}}(\omega_k\hat{q}_k(t) + i\hat{p}_k(t)). \tag{3.14b}$$

The following commutation relation holds for these operators:

$$[\hat{c}_k(t), \hat{c}_{k'}^\dagger(t)] = \delta_{k,k'}. \tag{3.15}$$

The Hamiltonian expressed in Eq. (3.11) can be rewritten in terms of the annihilation and creation operators as:

$$\hat{\mathcal{H}} = \sum_k \hbar\omega_k(\hat{n}_k + \frac{1}{2}), \tag{3.16}$$

where $\hat{n}_k = \hat{c}_k^\dagger\hat{c}_k$ is the operator of photons with wavevector k. Then, n_k is the eigenvalue, i.e. the photon number, of the Fock state $|n\rangle_k$. This leads to the quantization of the vector potential as follows:

$$\hat{\mathbf{A}}(\mathbf{r}, t) = \sum_k \sqrt{\frac{\hbar}{2\omega_k\varepsilon_0\varepsilon_{\mathrm{r},k}}}(\hat{c}_k(t) + \hat{c}_k^\dagger(t))\mathbf{U}_k(\mathbf{r}). \tag{3.17}$$

[2]Using the vector identity $\mathbf{U}_k(\mathbf{r}) \cdot (\nabla \times \nabla \times \mathbf{U}_{k'}(\mathbf{r})) = (\nabla \times \mathbf{U}_k(\mathbf{r})) \cdot (\nabla \times \mathbf{U}_{k'}(\mathbf{r})) - \nabla \cdot [\mathbf{U}_k(\mathbf{r}) \times (\nabla \times \mathbf{U}_{k'}(\mathbf{r}))]$ where the last term in the right-hand side is equal to zero [120].

This implies that the quantized electric and magnetic fields can be expressed as:

$$\hat{\mathbf{E}}(\mathbf{r},t) = i\sum_k \sqrt{\frac{\hbar\omega_k}{2\varepsilon_0\varepsilon_{\mathrm{r},k}}}(\hat{c}_k(t) - \hat{c}_k^\dagger(t))\mathbf{U}_k(\mathbf{r}), \tag{3.18a}$$

$$\hat{\mathbf{H}}(\mathbf{r},t) = \frac{1}{\mu_0}\sum_k \sqrt{\frac{\hbar}{2\omega_k\varepsilon_0\varepsilon_{\mathrm{r},k}}}(\hat{c}_k(t) + \hat{c}_k^\dagger(t))\nabla\times\mathbf{U}_k(\mathbf{r}). \tag{3.18b}$$

It is worth noting that the electric and magnetic fields are $\pi/2$ out of phase. Therefore, depending on the study case, it can be more straightforward to express the electric field as proportional to $(\hat{c}_k(t) + \hat{c}_k^\dagger(t))$ instead of $i(\hat{c}_k(t) - \hat{c}_k^\dagger(t))$. Conversely, the magnetic field would then be proportional to $i(\hat{c}_k(t) - \hat{c}_k^\dagger(t))$ rather than $(\hat{c}_k(t) + \hat{c}_k^\dagger(t))$.

3.2 Coupling Models

In this section, we will delve into the primary models that describe various light-matter interactions. To gain insights, we will begin by examining the coupling of two classical harmonic oscillators, providing an intuitive introduction to coupled systems. Subsequently, we will explore two distinct types of matter systems, leading us to the four main models of light-matter interactions, along with their limitations and conditions of application.

3.2.1 A toy Model: Two coupled pendulums

This toy model serves as a simplified classical approach to gaining insights and understanding of light-matter coupling.

We can categorize the coupling into two types: coherent coupling and dissipative coupling. These two types of coupling can be effectively understood through the model of two coupled pendulums: one spring-coupled for coherent coupling and the other dashpot-coupled for dissipative coupling. Following the approach outlined in Harder et al. (2021) [121], we consider two pendulums with equal masses but different rod lengths, connected either by a spring (with spring constant k) or a dashpot and placed at a distance l from the top of the rods. Each pendulum also exhibits an intrinsic damping rate $\lambda_{1,2}$. These systems are illustrated in Fig. 3.1 (a) and (b) respectively. Each pendulum has an intrinsic eigenfrequency:

$$\omega_{1,2} = \sqrt{\frac{g}{l_{1,2}}}, \tag{3.19}$$

where g represents the gravitational acceleration.

3.2.2 Spring-coupled pendulums

For the case of the spring-coupled pendulums, the equation of motion for the two pendulums can be expressed as [121]:

$$\ddot{\phi}_{1,2} + 2\lambda_{1,2}\dot{\phi}_{1,2} + \omega_{1,2}^2\phi_{1,2} - 2J_{1,2}\omega_{1,2}(\phi_{2,1} - \phi_{1,2}) = 0, \tag{3.20}$$

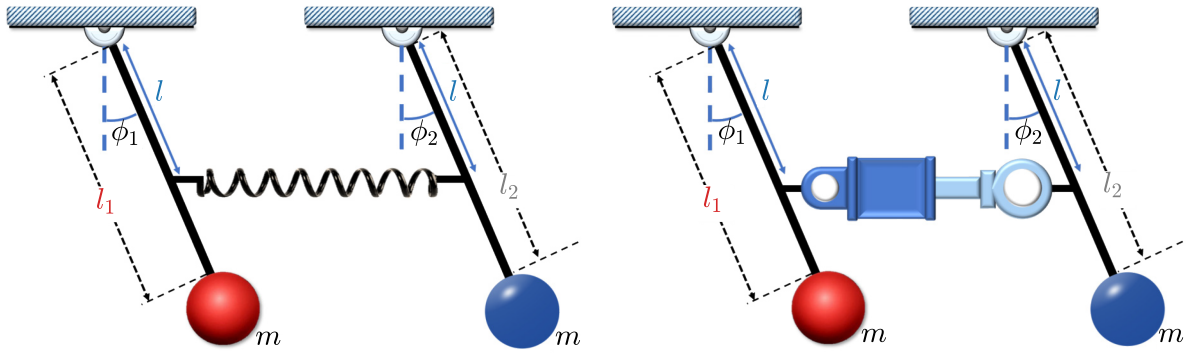

FIGURE 3.1: Schematic illustration of two coupled pendulums with (a) a string, leading to coherent coupling; and (b) a dashpot, leading to dissipative coupling, with permission from [121].

where $J_{1,2} = kl^2/(2m\omega_{1,2}l_{1,2}^2)$ represents the coherent coupling strength. In the case where $J_1 = J_2 = J$, and near zero frequency detuning $\Delta = \omega_2 - \omega_1 \simeq 0$, Eq. (3.20) simplifies to:

$$\tilde{\omega} = \frac{1}{2}\left[\tilde{\omega}_1 + \tilde{\omega}_2 + 2J \pm \sqrt{(\tilde{\omega}_1 - \tilde{\omega}_2)^2 + 4J^2}\right], \tag{3.21}$$

where $\tilde{\omega}_{1,2} = \omega_{1,2} - i\lambda_{1,2}$, represent complex eigenfrequencies due to damping. The eigenfrequencies can also be expressed as $\tilde{\omega}_\pm = \omega_\pm - i\Delta\omega_\pm$, with $\omega_\pm = \mathrm{Re}(\tilde{\omega}_\pm)$ and $\Delta\omega_\pm = -\mathrm{Im}(\tilde{\omega}_\pm)$. The coupling behavior manifests in the frequency dispersion under the condition:

$$J > \sqrt{\lambda_1\lambda_2}. \tag{3.22}$$

In Fig. 3.2 is presented the angular frequency of the hybridized modes $\omega_\pm$ in (a), and the linewidth of the hybridized modes $\Delta\omega_\pm$ in (b) versus the angular frequency detuning $\Delta = \omega_1 - \omega_2$. The coupling strength has been set to $J = 5 \cdot 10^{-2}\omega_1$, while damping parameters are $\lambda_1 = 10^{-2}\omega_1$ and $\lambda_2 = 2 \cdot 10^{-3}\omega_1$. The coherent coupling exhibits level repulsion in the dispersion frequency of the two hybridized modes, along with level attraction in the linewidth dispersion. At zero-detuning condition, the two hybridized modes are separated by $2J$, where their total deviation from the uncoupled frequencies is maximum. At this juncture, the lower branch corresponds to the pendulums oscillating in phase, while the upper branch corresponds to the pendulums oscillating out-of-phase. This observation implies that when the uncoupled frequencies of the two pendulums are equal, the two eigenfrequencies are not equal, demonstrating a degeneracy breaking scaled by the coupling strength. For a deeper understanding of the exchange energy between two coupled oscillators, it is interesting to examine the time-domain evolution. At the zero-detuning condition, the time evolution of the phase of each pendulum is given by [121]:

$$\phi_1 \simeq \phi_0 e^{-(\lambda_1+\lambda_2)t/2}\cos(Jt)\cos[(\omega_1 + J)t], \tag{3.23a}$$
$$\phi_2 \simeq \phi_0 e^{-(\lambda_1+\lambda_2)t/2}\sin(Jt)\cos[(\omega_1 + J)t], \tag{3.23b}$$

where the initial conditions are $\phi_1(t = 0) = \phi_0$ and $\phi_2(t = 0) = 0$. These initial conditions enable the observation of the so-called Rabi-like oscillations, where the two pendulums oscillate rapidly at the frequency $\omega_1 + J$, modulated by the Rabi-like frequency J, as

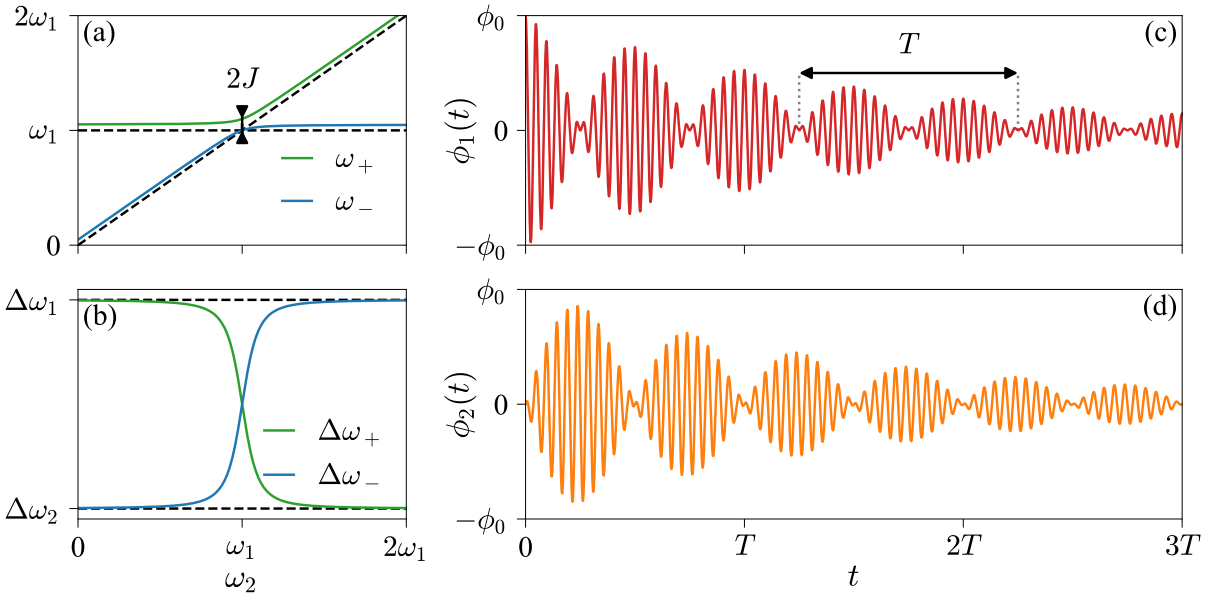

FIGURE 3.2: Coherent coupling between two spring-coupled pendulums demonstrates (a) level repulsion in the angular frequency dispersion and (b) level attraction in the linewidth dispersion, versus the angular frequency detuning $\Delta = \omega_2 - \omega_1$. At the zero-detuning condition, where $\Delta = 0$, a degeneracy breaking in angular frequency, $\omega_+ - \omega_- = 2J$, is observed, as illustrated in (a). The Rabi-like oscillations of angular position for each pendulum, shown in (c) for the first pendulum and (d) for the second pendulum, indicate a periodic exchange of energy every $t_{\text{exch}} = T/4$, with $T = 2\pi/J$. These simulations utilize $J = 5 \cdot 10^{-2}\omega_1$, $\lambda_1 = 10^{-2}\omega_1$, and $\lambda_2 = 2 \cdot 10^{-3}\omega_1$ as parameters.

illustrated in Fig. 3.2 (c) and (d), with the same parameters as given for Fig. 3.2 (a) and (b). The total energy is exchanged between the two pendulums every $t_{\text{exch}} = T/4$, where $T = 2\pi/J$ is the Rabi-like period. It is noteworthy that if the two pendulums are initially positioned in phase or out-of-phase with the same phase amplitude ϕ_0, the modulation beats would not appear.

3.2.3 Dashpot-coupled pendulums

For this case, the dashpot, due to the presence of a fluid, introduces a kinematic viscosity and adds motion resistance to the dynamics of the pendulum, representing the dissipative coupling. The equations of motion for the two pendulums then become [121]:

$$\ddot{\phi}_{1,2} + 2\lambda_{1,2}\dot{\phi}_{1,2} + \omega_{1,2}^2\phi_{1,2} - 2\Gamma_{1,2}(\dot{\phi}_{2,1} - \dot{\phi}_{1,2}) = 0, \tag{3.24}$$

where $\Gamma_{1,2} = \nu/l_{1,2}^2 \ll \omega_{1,2}$ represents the dissipative coupling strength and ν denotes the viscosity of the fluid. At near-zero frequency detuning and with $\Gamma_1 = \Gamma_2 = \Gamma$, the eigenfrequencies of the system are given by:

$$\tilde{\omega} = \frac{1}{2}\left[\tilde{\omega}_1 + \tilde{\omega}_2 - 2i\Gamma \pm \sqrt{(\tilde{\omega}_1 - \tilde{\omega}_2)^2 - 4\Gamma^2}\right]. \tag{3.25}$$

As illustrated in Fig. 3.3 (a) and (b), the coupling demonstrates level attraction

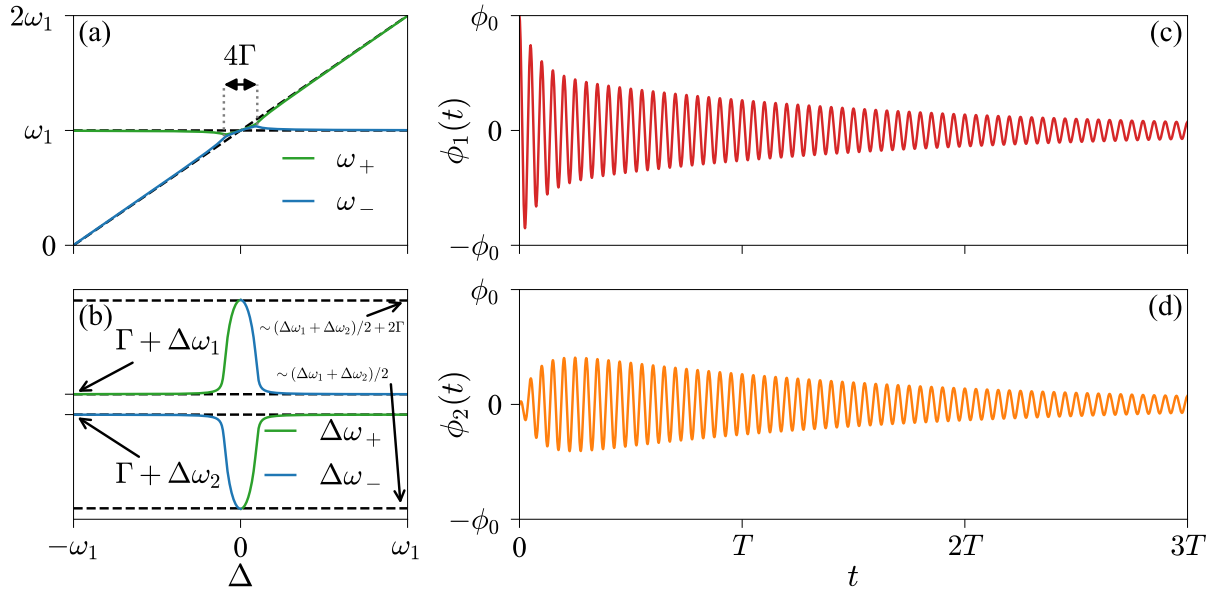

FIGURE 3.3: Dissipative coupling between two dashpot-coupled pendulums demonstrates (a) level attraction in the angular frequency dispersion and (b) level repulsion in the linewidth dispersion, versus the angular frequency detuning $\Delta = \omega_2 - \omega_1$. Near the zero-detuning condition, ranging from $\Delta = -2\Gamma$, to $\Delta = 2\Gamma$, a degeneracy in angular frequency, $\omega_+ \simeq \omega_-$, is observed, as illustrated in (a). No Rabi-like oscillations appear in the angular position of (c) the first pendulum, and (d) the second pendulum. However, the phase two pendulums synchronize themselves after a certain time, and share the same energy. These simulations utilize $J = 5 \cdot 10^{-2}\omega_1$, $\lambda_1 = 10^{-2}\omega_1$, and $\lambda_2 = 2 \cdot 10^{-3}\omega_1$ as parameters.

between the two hybridized modes in the angular frequency dispersion, while it exhibits level repulsion in the linewidth dispersion, versus the angular frequency detuning Δ. The parameters remain consistent with those specified for the two spring-coupled pendulums. The length of this degeneracy of the hybridized mode in the angular frequency detuning is proportional to the coupling strength. At zero-detuning condition, the minimum of damping represents the two pendulums being in phase, while the maximum of damping represents the two pendulums being out-of-phase. Because the out-of-phase mode is more damped than the in-phase mode, an initial state where the two pendulums are dephased (but not in the out-of-phase state) will synchronize themselves to finally be in phase after a certain time. The time evolution of the phase of each pendulum when $\Gamma \gg \sqrt{\lambda_1\lambda_2}$ is given by [121]:

$$\phi_1 \simeq \phi_0 e^{-(\lambda_1+\lambda_2)t/2} \frac{(1 + e^{-2\Gamma t})}{2} \cos(\omega_1 t), \tag{3.26a}$$

$$\phi_2 \simeq \phi_0 e^{-(\lambda_1+\lambda_2)t/2} \frac{(1 - e^{-2\Gamma t})}{2} \cos(\omega_1 t). \tag{3.26b}$$

In contrast to coherent coupling, the angular frequency is not modulated, but the damping is much larger, as depicted in Fig. 3.3 (c) and (d). The two oscillators are synchronized when $e^{-2\Gamma t} \simeq 0$, hence $\phi_1 = \phi_2$. Therefore, the amplitude and the phase of the two pendulums are equal, and the total energy is equally shared between the two

pendulums.

In the following sections, we present the various coherent coupling regimes that arise in physical models. We will then discuss different models describing light-matter interaction across various matter systems, where both coherent and dissipative coupling occur, analogous to the behavior of two coupled pendulums.

3.2.4 Coupling Regimes

The coupling strength g can be a complex value, composed of a coherent coupling part J, and a dissipative coupling part Γ, written as $g = J - i\Gamma$. When g is purely real, the hybridized modes exhibit level repulsion in the frequency spectra (as shown in Fig. 3.2 for the coherent coupling of two pendulums). Conversely, when g is purely imaginary, the hybridized modes show level attraction in the frequency spectra (as shown in Fig. 3.3 for the dissipative coupling of two pendulums).

Like classical harmonic oscillators, light-matter coupling is typically categorized into two regimes: weak coupling and strong coupling regimes.

The weak coupling (WC) regime occurs when the coupling strength is less than the intrinsic losses of each subsystem, akin to the condition in Eq. (3.22) for the pendulum. In this scenario, where losses outweigh the coupling strength, the system cannot efficiently exchange energy between light and matter.

Conversely, the strong coupling (SC) regime emerges when the coupling strength surpasses the losses of the subsystems. In this regime, an oscillatory exchange of energy quanta between light and matter becomes possible, a phenomenon known as Rabi oscillations. The strong coupling (SC) regime was first experimentally demonstrated in a collection of Rydberg atoms in a microwave cavity [122]. Soon after, it was observed in a single atom in a microwave cavity [123] and in an optical cavity [124]. Several years later, similar phenomena were demonstrated in artificial atoms such as quantum dots [125], and superconducting qubits, also known as circuit quantum electrodynamics (circuit QED) systems [126].

Beyond the SC regime, we distinguish between two additional regimes based on the ratio of the coupling strength to the eigenfrequencies of the subsystems g/ω. The system enters the Ultra-Strong Coupling (USC) regime when $g/\omega > 0.1$. The first observation of the USC regime was reported in 2009 in a microcavity embedded doped GaAs quantum well [127]. This threshold is derived from the first observation of the USC regime and does not have a specific physical significance. However, it indicates that the usual approximations may no longer be valid beyond this threshold.Chapter 5 presents our study on achieving the USC regime in a YIG/cavity system, where the distinct areas of interest and applications of the different coupling regimes are discussed.

The Deep-Strong Coupling (DSC) regime occurs when $g/\omega > 1$, meaning that the coupling strength exceeds the subsystem frequencies. It was initially explored theoretically in 2010 [128], and experimentally demonstrated in 2017 using various physical realizations [83, 129].

The differentiation of coupling regimes based on g/ω rather than intrinsic losses does not prevent the USC or DSC regimes within the WC regime. However, conventionally, the

SC regime is distinguished from the USC and DSC regimes when $g/\omega < 0.1$, assuming that the coupling strength exceeds system losses for all three regimes. Other coupling regimes exist but are beyond the scope of this thesis. Interested readers can refer to the literature for further details [74, 130–135].

Two different types of model describe light-matter coupling, depending on the description of matter. Matter can be considered either as a single two-level system or as a collective two-level system. A two-level system consists of only two possible states, such as a ground state and an excited state (for instance, the spin of a single electron). However, multiple-level systems, like atoms or artificial atoms, can be approximated as two-level systems. Similarly, collective multiple-level systems, such as YIG with a unit cell spin of 5/2, can be treated as collective two-level systems.

3.2.5 Two-levels System

3.2.5.a Quantum Rabi Model

The quantum Rabi model [136, 137] is the generic model describing the interaction of a single-mode bosonic field and a two-level system (such as a cavity mode and a single electronic spin or a qubit, for example). A two-level system can be described by the Pauli matrices, i.e. the spin operators, in the basis formed by the ground $|G\rangle$ state and the excited $|E\rangle$ state. The quantum Rabi Hamiltonian can be expressed as [39]:

$$\hat{\mathcal{H}}_{\text{Rabi}}/\hbar = \tilde{\omega}_c \hat{c}^\dagger \hat{c} + \frac{1}{2}\tilde{\omega}_q \hat{\sigma}_z + \hat{\mathcal{H}}_{\text{int}}/\hbar, \tag{3.27a}$$

$$\hat{\mathcal{H}}_{\text{int}}/\hbar = g\hat{X}\hat{\sigma}_x = g(\hat{c} + \hat{c}^\dagger)(\hat{\sigma}_- + \hat{\sigma}_+), \tag{3.27b}$$

where $\tilde{\omega}_c = \omega_c - i\kappa_c$ is the complex angular frequency of the cavity mode ω_c, represents its real value while κ_c denotes its internal damping. Meanwhile $\hat{c}$ ($\hat{c}^\dagger$) is the cavity mode creation (annihilation) operator. Also, $\tilde{\omega}_q = \omega_q - i\kappa_q$ represents the complex angular frequency associated with the transition energy between the ground state and the excited state of the two-level system, while ω_q denotes its real value, and κ_q its internal damping. $\hat{X} = \hat{c} + \hat{c}^\dagger$ represents the canonical position operator of either the electric or the magnetic field, depending of the nature of the coupling. g represents the light-matter coupling strength. Note that the ground state energy of the cavity photon and the two-level systems are neglected, being only an offset. The two-level system is described by the two Pauli operators $\hat{\sigma}_z$ and $\hat{\sigma}_x$ or the raising and the lowering Pauli operators $\hat{\sigma}_+$ and $\hat{\sigma}_-$, respectively. These operators act in the two-dimensional Hilbert space of the two-level system, in the basis defined by the ground state $|G\rangle$, and the excited state $|E\rangle$. The Pauli operators are expressed as:

$$\sigma_z = \begin{pmatrix} 1 & 0 \\ 0 & -1 \end{pmatrix}, \qquad \sigma_x = \begin{pmatrix} 0 & 1 \\ 1 & 0 \end{pmatrix}, \qquad \sigma_y = \begin{pmatrix} 0 & -i \\ i & 0 \end{pmatrix}, \tag{3.28a}$$

$$\sigma_+ = \begin{pmatrix} 0 & 1 \\ 0 & 0 \end{pmatrix}, \qquad \sigma_- = \begin{pmatrix} 0 & 0 \\ 1 & 0 \end{pmatrix}. \tag{3.28b}$$

Let us introduce an approximation to simplify calculations, particularly within the WC and SC regimes. In the interaction picture [41], the time evolution of the operators is

governed by the non-interacting Hamiltonian $\hat{\mathcal{H}}_0 = \omega_c \hat{c}^\dagger \hat{c} + \frac{1}{2}\omega_q \hat{\sigma}_z$:

$$\dot{\hat{c}}(t) = -\frac{i}{\hbar}[\hat{c}(t), \hat{\mathcal{H}}_0] \rightarrow \hat{c}(t) = \hat{c}e^{-i\omega_c t}, \tag{3.29a}$$

$$\dot{\hat{\sigma}}_\pm(t) = -\frac{i}{\hbar}[\hat{\sigma}_\pm(t), \hat{\mathcal{H}}_0] \rightarrow \hat{\sigma}_\pm(t) = \hat{\sigma}_\pm e^{\pm i\omega_q t}. \tag{3.29b}$$

In this framework, the interaction Hamiltonian in Eq. (3.27b) transforms to:

$$\hat{\mathcal{H}}_{\text{int}}/\hbar = g\left(\hat{c}\hat{\sigma}_+ e^{i(\omega_q-\omega_c)t} + \hat{c}^\dagger\hat{\sigma}_- e^{-i(\omega_q-\omega_c)t} + \hat{c}\hat{\sigma}_- e^{-i(\omega_q+\omega_c)t} + \hat{c}^\dagger\hat{\sigma}_+ e^{i(\omega_q+\omega_c)t}\right). \tag{3.30}$$

When the frequencies of light and matter are close to resonance (i.e. $\omega_c \simeq \omega_q$), the Rotating Wave Approximation (RWA) can be applied, allowing us to disregard the last two terms in Eq. (3.30). Under the resonance condition, these last two terms are considered as fast-oscillating terms, oscillating at twice the frequency of the level transition angular frequency ω_q. Analogous to a classical precessing dipole moment (representing the two-level transition), the first two terms represent a field rotating in the same direction as the dipole motion, hence termed co-rotating terms. The last two terms represent a field rotating in the opposite direction to the dipole motion, hence termed counter-rotating terms. Over one period of the dipole precession ω_q^{-1}, the co-rotating terms apply a steady torque on the dipole, while the counter-rotating terms reverse twice during this period, resulting in their average over one period being negligible [39, 41, 74, 121, 138].

3.2.5.b Jaynes-Cummings Model

Applying the RWA results in the Jaynes-Cummings Model [139] and the Hamiltonian is given by:

$$\hat{\mathcal{H}}_{\text{JC}}/\hbar = \tilde{\omega}_c \hat{c}^\dagger \hat{c} + \frac{1}{2}\tilde{\omega}_q \hat{\sigma}_z + \hat{\mathcal{H}}_{\text{int}}/\hbar, \tag{3.31a}$$

$$\hat{\mathcal{H}}_{\text{int}}/\hbar = g(\hat{c}^\dagger\hat{\sigma}_- + \hat{c}\hat{\sigma}_+). \tag{3.31b}$$

This model is applicable to systems operating in the WC and SC regimes. Beyond the SC regime, the effects of the counter-rotating terms become non-negligible, and only the Rabi model can describe the physics accurately. Additionally, it is worth noting that in the Jaynes-Cummings model, the total number of excitations in the system $\hat{N}_{\text{exc}}$ is conserved (the co-rotating terms represent the excitation and de-excitation of the two-level system, corresponding to the absorption and emission of a photon, respectively). In contrast, the Rabi model does not conserve $\hat{N}_{\text{exc}}$. However, the parity $\hat{P} = e^{i\pi\hat{N}_{\text{exch}}}$ is conserved in the Rabi model, as the counter-rotating terms changes $\hat{N}_{\text{exc}}$ by 2 [74].

3.2.6 Collective two-levels System

3.2.6.a Tavis-Cummings Model

The Tavis-Cummings model [140, 141] extends the Jaynes-Cummings model to consider collective two-level systems, while still applying the RWA. Similar to the Jaynes-Cummings model, the total number of excitations in the system $\hat{N}_{\text{exc}}$ is conserved. The collective two-level system can be generalized as a bosonic multi-mode system and represented by a

quantum oscillator, as demonstrated for magnon modes in a ferromagnet in Sec. 2.3.1.a. The Tavis-Cummings Hamiltonian is given by:

$$\hat{\mathcal{H}}_{\mathrm{TC}}/\hbar = \tilde{\omega}_c \hat{c}^\dagger \hat{c} + \tilde{\omega}_d \hat{d}^\dagger \hat{d} + \hat{\mathcal{H}}_{\mathrm{int}}/\hbar, \tag{3.32a}$$

$$\hat{\mathcal{H}}_{\mathrm{int}}/\hbar = g(\hat{c}^\dagger \hat{d} + \hat{c}\hat{d}^\dagger), \tag{3.32b}$$

where $\tilde{\omega}_d = \omega_d - i\kappa_d$ is the complex angular frequency of the bosonic mode related to the collective matter excitation, where ω_d represents its real value, and κ_d its damping. Meanwhile $\hat{d}$ ($\hat{d}^\dagger$) is the annihilation (creation) operator of the matter bosonic mode. In the Heisenberg picture, an operator $\hat{a}$ must satisfy the so-called Heisenberg equation of motion (EoM):

$$\dot{\hat{a}} = -\frac{i}{\hbar}[\hat{a}, \hat{\mathcal{H}}]. \tag{3.33}$$

For the considered system, the Heisenberg EoM becomes:

$$\mathrm{d}_t \hat{\mathbf{a}} = -i\bar{\mathbf{M}} \cdot \hat{\mathbf{a}}, \tag{3.34a}$$

$$\bar{\mathbf{M}} = \begin{bmatrix} \tilde{\omega}_c & g \\ g & \tilde{\omega}_d \end{bmatrix}, \tag{3.34b}$$

where $\hat{\mathbf{a}} = (\hat{c}, \hat{d})^{\mathrm{T}}$. Assuming that the solution of $\hat{c}$ and $\hat{d}$ are proportional to $e^{-i\omega t}$, the angular eigenfrequencies of the system are determined by solving the determinant of $\bar{\mathbf{M}} - \omega\mathbb{1}$, where $\mathbb{1}$ is the identity matrix. Subsequently, the Hamiltonian is diagonalized in the new basis of hybridized modes called polaritons, with annihilation (creation) operators

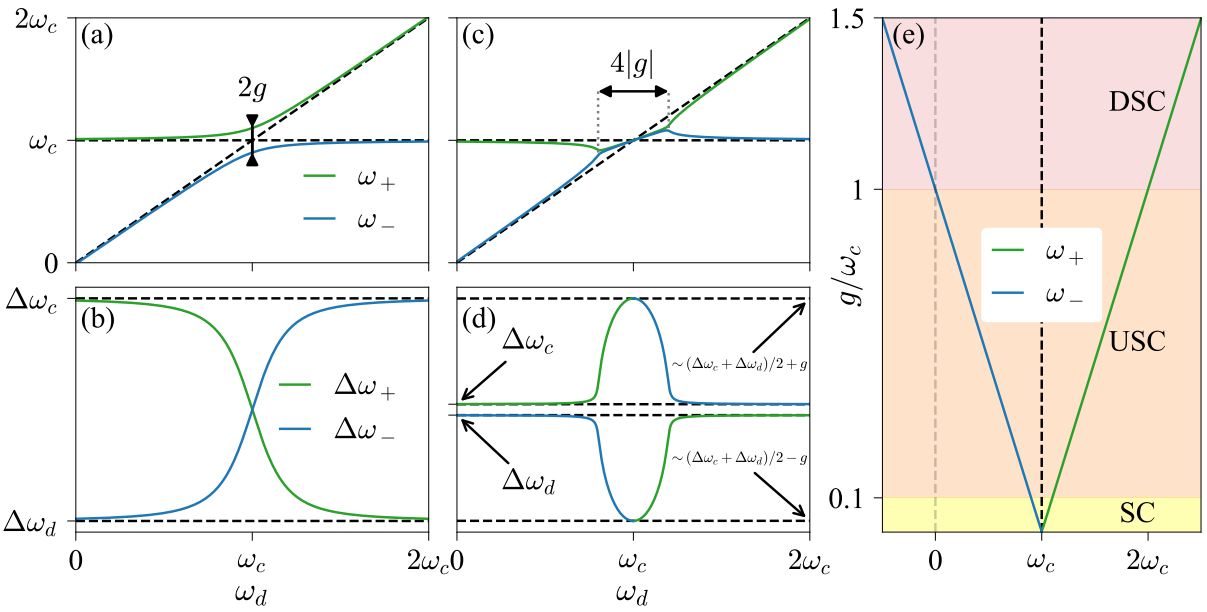

FIGURE 3.4: Coherent (dissipative) coupling of light and matter of (a) ((c)) the eigenfrequencies; and (b) ((d)) the linewidths of the polaritons versus the angular frequency detuning $\Delta = \omega_d - \omega_c$. The linear relationship of the ratio g/ω_c for the two polariton frequencies at $\omega_d = \omega_c$ in the case of level repulsion is depicted in (e). These simulations utilize $|g| = 0.1\omega_c$, $\kappa_c = 10^{-2}\omega_c$, and $\kappa_d = 2 \cdot 10^{-3}\omega_c$ as parameters.

$\hat{p}_\pm$ ($\hat{p}_\pm^\dagger$) whith satisfy the commutation relation:

$$[\hat{p}_\pm, \hat{p}_\pm^\dagger] = 1. \tag{3.35}$$

The angular eigenfrequencies of the Hamiltonian in the Fock state of the polaritons are given by:

$$\tilde{\omega}_\pm = \frac{1}{2}\left[\tilde{\omega}_c + \tilde{\omega}_d \pm \sqrt{(\tilde{\omega}_c - \tilde{\omega}_d)^2 + 4g^2}\right], \tag{3.36}$$

such as:

$$[\hat{p}_\pm, \hat{\mathcal{H}}] = \tilde{\omega}_\pm \hat{p}_\pm. \tag{3.37}$$

Similar to the Jaynes-Cummings model, the Tavis-Cummings model is applicable only for systems operating in the WC and SC regimes.

In Fig. 3.4 (a) and (b), the frequencies and linewidths of the two polaritons are depicted versus the detuning Δ in the Tavis-Cummings model when the coupling strength is purely real. Similarly, in Fig. 3.4 (c) and (d), the same quantities are shown when the coupling strength is purely imaginary. In both cases, the coupling strength is set to $|g| = 0.1\omega_c$, while the damping parameter of the cavity is $\kappa_c = 10^{-2}\omega_c$, and $\kappa_d = 2 \cdot 10^{-3}\omega_c$ for the matter damping rate. We observe similar signatures for both the eigenfrequencies and the linewidths of the polaritons as for the two cases of the coupled pendulums. When the coupling strength is real, the signatures are equivalent to the case of the spring-coupled pendulums, while when the coupling strength is imaginary, the signatures resemble those of the dashpot-coupled pendulums. In Fig. 3.4 (e), is illustrated the linear evolution of the lower (blue line) and the upper (green line) polaritons frequency at $\omega_d = \omega_c$ versus the ratio g/ω_c when the coupling is coherent. It is important to note that this evolution is invalid beyond the SC regime. Furthermore, this model is inefficace to describe the physics in the DSC regime, where the lower polariton frequency becomes negative, as depicted in Fig. 3.2.6.a (e).

3.2.6.b Dicke Model

The Dicke model [142] extends the Rabi model to account for collective two-level systems, and it can operate in the Ultra-Strong Coupling (USC) regime. Unlike the Jaynes-Cummings and Tavis-Cummings models, the total number of excitations is not conserved, but the parity remains conserved. While the Rotating Wave Approximation (RWA) is not applicable, it is still possible to find the angular eigenfrequencies, as will be shown. The Hamiltonian of the Dicke model is given by:

$$\hat{\mathcal{H}}_{\text{Dicke}}/\hbar = \tilde{\omega}_c \hat{c}^\dagger \hat{c} + \tilde{\omega}_d \hat{d}^\dagger \hat{d} + \hat{\mathcal{H}}_{\text{int}}/\hbar, \tag{3.38a}$$

$$\hat{\mathcal{H}}_{\text{int}}/\hbar = g(\hat{c} + \hat{c}^\dagger)(\hat{d} + \hat{d}^\dagger). \tag{3.38b}$$

In this model, the counter-rotating terms, i.e., $\hat{c}\hat{d}$ and $\hat{c}^\dagger\hat{d}^\dagger$, cannot be neglected. Conversely to the Tavis-Cummings model, the polaritonic operators $\hat{p}$ and $\hat{p}^\dagger$, which form the basis of the diagonalized Hamiltonian, must be expressed as linear combinations of the annihilation and creation operators of the two subsystems:

$$\hat{p}_\pm = \alpha_\pm \hat{c} + \beta_\pm \hat{d} + \gamma_\pm \hat{c}^\dagger + \delta_\pm \hat{d}^\dagger, \tag{3.39}$$

where $\alpha_\pm$, $\beta_\pm$, $\gamma_\pm$, and $\delta_\pm$ are coefficients ensuring that Eq. (3.37) remains valid. To find these coefficients, the Heisenberg equations of motion can be rewritten in terms of the new vector basis $\hat{\mathbf{a}} = (\hat{c}, \hat{d}, \hat{c}^\dagger, \hat{d}^\dagger)^{\mathrm{T}}$, known as the Hopfield-Bogolubov transformation [84, 143]:

$$\mathrm{d}_t\hat{\mathbf{a}} = -\frac{i}{2}\bar{\mathbf{M}} \cdot \hat{\mathbf{a}}, \tag{3.40a}$$

$$\bar{\mathbf{M}} = \begin{bmatrix} \tilde{\omega}_c & g & 0 & g \\ g & \tilde{\omega}_d & g & 0 \\ 0 & g & \tilde{\omega}_c & g \\ g & 0 & g & \tilde{\omega}_d \end{bmatrix}, \tag{3.40b}$$

The factor of $1/2$ and the form of $\bar{\mathbf{M}}$ arise from replacing the term $\hat{c}\hat{c}^\dagger$ with $(\hat{c}\hat{c}^\dagger + \hat{c}^\dagger\hat{c})/2 - 1$. Similar to the treatment of the term $\hat{c}\hat{c}^\dagger$, a corresponding substitution has been applied to the term $\hat{d}\hat{d}^\dagger$. While $\hat{c}$ and $\hat{d}$ are assumed to be proportional to $e^{-i\omega t}$, $\hat{c}^\dagger$ and $\hat{d}^\dagger$ naturally vary as $e^{i\omega t}$. Consequently, the angular eigenfrequencies of the system are determined by solving the determinant of $\bar{\mathbf{M}} \cdot \mathrm{diag}(1, 1, -1, -1) - \omega\mathbb{1}$[3] , resulting in:

$$\tilde{\omega}_\pm = \frac{1}{\sqrt{2}}\sqrt{\tilde{\omega}_c^2 + \tilde{\omega}_d^2 \pm \sqrt{(\tilde{\omega}_c^2 - \tilde{\omega}_d^2)^2 + 16g^2\tilde{\omega}_c\tilde{\omega}_d}}. \tag{3.41}$$

According to Eq. (3.41), when the coupling strength is higher to the critical threshold $g_c = \sqrt{\omega_c\omega_d}$, the polariton frequency ω_- becomes purely imaginary, indicating the onset of a spontaneously broken parity $\hat{P}$. This critical value in the coupling strength marks a phase transition, ushering in the superradiant phase where a new Hamiltonian emerges with a newly conserved parity [84, 144, 145]. It is worth noting that the collective oscillator operators stem from the Holstein-Primakoff transformation, as demonstrated for magnons in Sec. 2.3.1.a. Building upon Eq. (2.70), Eq. (2.73a), and Eq. (2.73b), we extend the equation describing the matter to a macroscopic angular momentum, where:

$$\hat{J}_z = \hbar(J - \hat{d}^\dagger\hat{d}), \tag{3.42a}$$

$$\hat{J}_+ = \hbar\hat{d}^\dagger(2J - \hat{d}^\dagger\hat{d}), \tag{3.42b}$$

$$\hat{J}_- = \hbar(2J - \hat{d}^\dagger\hat{d})\hat{d}. \tag{3.42c}$$

To describe the system beyond the superradiant phase, the bosonic modes are displaced as [145]:

$$\hat{c}^\dagger \to \hat{c}^\dagger + \sqrt{\alpha}, \tag{3.43a}$$

$$\hat{d}^\dagger \to \hat{d}^\dagger - \sqrt{\beta}, \tag{3.43b}$$

where α and β can be interpreted as macroscopic mean fields acquired by the two modes above g_c. We refer the reader to the derivation of the Hamiltonian in Emary and Brandes

[3] Eq. (3.40a) can also be written as $\omega\,\mathrm{diag}(1, 1, -1, -1) \cdot \hat{\mathbf{a}} = \frac{1}{2}\bar{\mathbf{M}} \cdot \hat{\mathbf{a}}$. To find the eigenvalues of the system, we need to calculate the determinant of a matrix written as $\bar{\mathbf{M}}' - \omega\mathbb{1}$. For this purpose, $\bar{\mathbf{M}}'$ needs to be equal to $\bar{\mathbf{M}} \cdot \mathrm{diag}(1, 1, -1, -1)^{-1} = \bar{\mathbf{M}} \cdot \mathrm{diag}(1, 1, -1, -1)$.

(2003) [145], where the Hamiltonian is given by [84]:

$$\begin{aligned}\hat{\mathcal{H}}/\hbar =&\tilde{\omega}_c\hat{c}^\dagger\hat{c}+\tilde{\omega}_d\frac{1+\tilde{g}^2}{2}\hat{d}^\dagger\hat{d}+g\sqrt{\frac{2}{\tilde{g}^2(\tilde{g}^2+1)}}(\hat{c}^\dagger+\hat{c})(\hat{d}^\dagger+\hat{d})\\&+\tilde{\omega}_d\frac{(\tilde{g}^2-1)(3\tilde{g}^2+1)}{8(\tilde{g}^2+1)}(\hat{d}^\dagger+\hat{d})^2,\end{aligned}\tag{3.44a}$$

where $\tilde{g}=2g/\omega_c$. The eigenfrequencies of the two polaritons in the superradiant phase are given by:

$$\tilde{\omega}_\pm=\frac{1}{\sqrt{2}}\sqrt{\tilde{\omega}_c^2+\tilde{\omega}_d^2\tilde{g}^4\pm\sqrt{(\tilde{\omega}_c^2-\tilde{\omega}_d^2\tilde{g}^4)^2+4\tilde{\omega}_c^2\tilde{\omega}_d^2}}.\tag{3.45}$$

In Fig. 3.5 (a) and (b), the frequencies and linewidths of the two polaritons are depicted versus the detuning Δ in the Tavis-Cummings model when the coupling strength is purely real. Similarly, in Fig. 3.5 (c) and (d), the same quantities are shown when the coupling strength is purely imaginary. In both cases, the coupling strength is set to $|g|=0.25$, the system performs in the USC regime. The damping parameters for both the photon and the matter are consistent with those given in the Tavis-Cummings model. The signatures for both the eigenfrequencies and the linewidths of the polaritons remain similar to the two cases of the coupled pendulums. However, a notable distinction arises when g is purely real, wherein the damping rate of the matter tends towards infinity. This indicates that only the upper polariton exists within a certain range of frequencies. In Fig. 3.5 (e), we observe that the eigenfrequencies are no longer linearly proportional to the

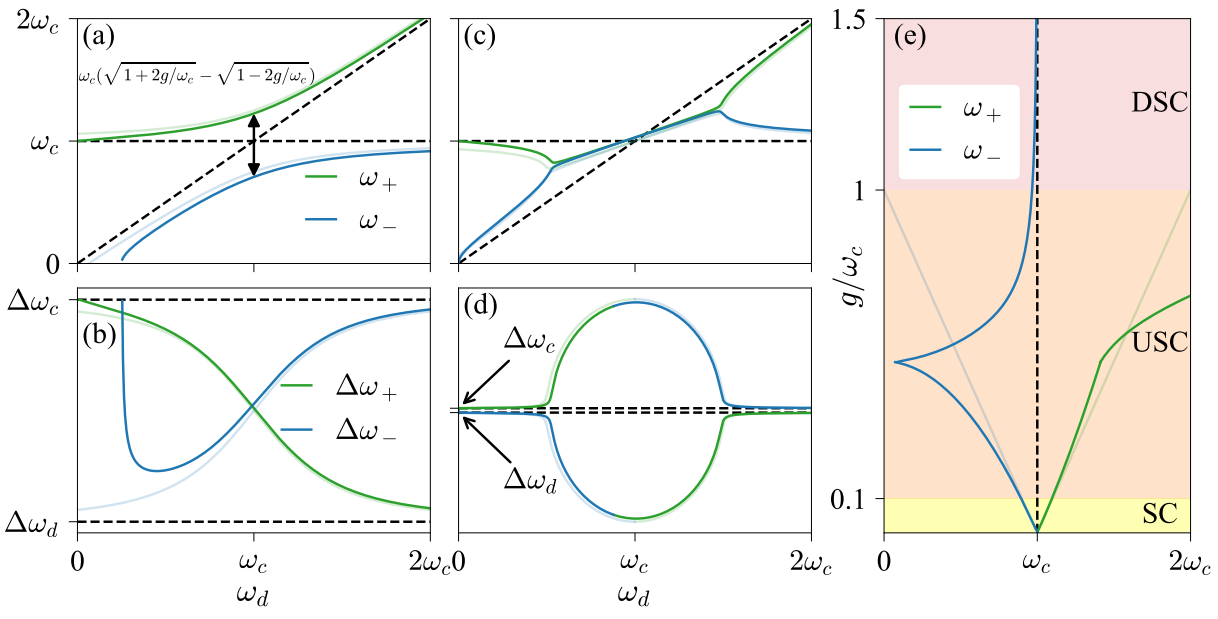

FIGURE 3.5: Coherent (dissipative) coupling of light and matter of (a) ((c)) the eigenfrequencies; and (b) ((d)) the linewidths of the polaritons versus the angular frequency detuning Δ. The linear relationship of the ratio g/ω_c for the two polariton frequencies at $\omega_d=\omega_c$ in the case of level repulsion is depicted in (e). These simulations utilize $|g|=0.25\omega_c$, $\kappa_c=10^{-2}\omega_c$, and $\kappa_d=2\cdot10^{-3}\omega_c$ as parameters. Opaque curves represent the quantities in the Dicke model, while semi-transparent curves depict quantities in the Tavis-Cummings model.

ratio g/ω_c, and we encounter a phase transition for $g/\omega_c > 0.5$. Additionally, this figure includes semi-transparent curves representing the eigenfrequencies and the linewidths in the Tavis-Cummings model for comparison.

3.2.6.c Hopfield Model

The Hopfield model is more general than the Dicke model, incorporating an additional term. Referring to Sec. 2.1.3, the diamagnetic term in Eq. (2.36b), proportional to the square root of the vector potential, was neglected. This additional is negligible for material with zero orbital angular momentum, and has been recently demonstrated for the magnon-photon coupling achieved with magnetic films and superconducting resonators [146]. However, in systems described by the Hopfield model, the diamagnetic term is no longer negligible (such as for plasmons [84, 147]). The Hopfield Hamiltonian is given by:

$$\hat{\mathcal{H}}_{\text{Hopfield}}/\hbar = \tilde{\omega}_c \hat{c}^\dagger \hat{c} + \tilde{\omega}_d \hat{d}^\dagger \hat{d} + g(\hat{c}^\dagger + \hat{c})(\hat{d}^\dagger + \hat{d}) + D(\hat{a}^\dagger + \hat{a})^2, \tag{3.46}$$

where the last term represents the diamagnetic term, where the vector potential $\hat{\mathbf{A}}$ has been substituted by its quantized field from Eq. (3.17). Using the Thomas-Reiche-Kuhn sum rule [148], it has been shown that for dipolar interaction, the diamagnetic factor is given by:

$$D = \frac{g^2}{\omega_d}. \tag{3.47}$$

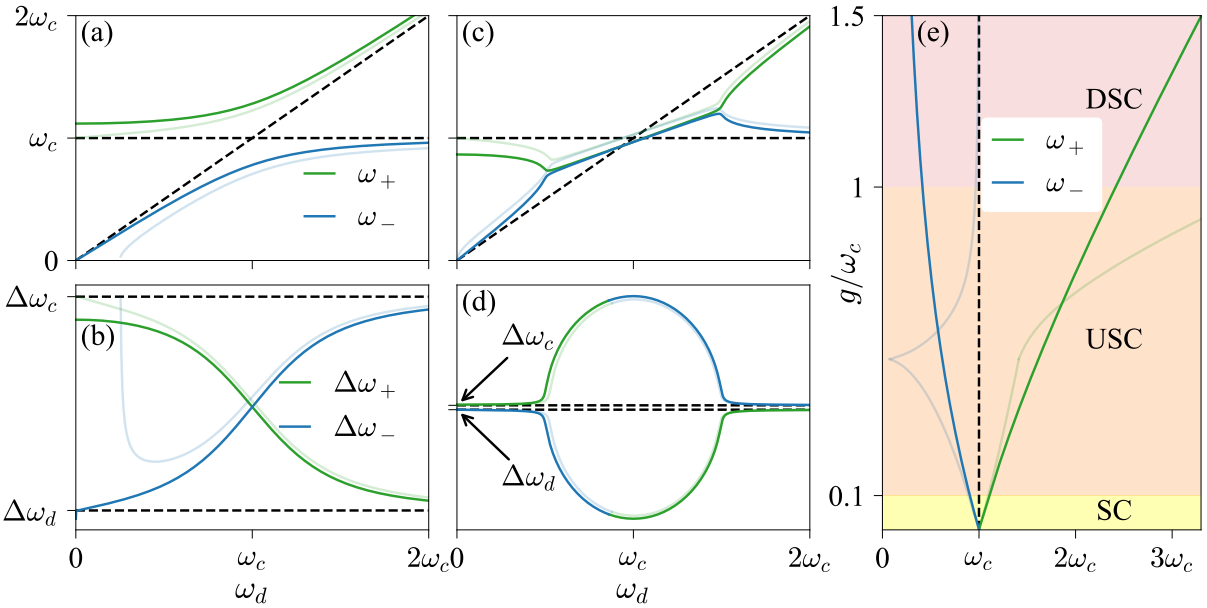

FIGURE 3.6: Coherent (dissipative) coupling of light and matter of (a) ((c)) the eigenfrequencies; and (b) ((d)) the linewidths of the polaritons versus the angular frequency detuning Δ. The linear relationship of the ratio g/ω_c for the two polariton frequencies at $\omega_d = \omega_c$ in the case of level repulsion is depicted in (e). These simulations utilize $|g| = 0.25\omega_c$, $\kappa_c = 10^{-2}\omega_c$, and $\kappa_d = 2 \cdot 10^{-3}\omega_c$ as parameters. Opaque curves represent the quantities in the Hopfield model, while semi-transparent curves depict quantities in the Dicke model.

Substituting this value into the Hamiltonian and using the Hopfield-Bogolubov transformation as shown in Sec. 3.2.6.b, and redefining the coupling strength as $g \to g\sqrt{\omega_d/\omega_c}$, we find that:

$$\tilde{\omega}_{\pm} = \frac{1}{\sqrt{2}}\sqrt{\tilde{\omega}_c^2 + \tilde{\omega}_d^2 + 4g^2 \pm \sqrt{(\tilde{\omega}_c^2 + \tilde{\omega}_d^2 + 4g^2)^2 - 4\tilde{\omega}_c^2\tilde{\omega}_d^2}}. \tag{3.48}$$

In Fig. 3.6 (a) and (b), the frequencies and linewidths of the two polaritons are depicted versus the detuning Δ in the Tavis-Cummings model when the coupling strength is purely real. Similarly, in Fig. 3.6 (c) and (d), the same quantities are shown when the coupling strength is purely imaginary. The coupling strength and the damping parameters for both the photon and the matter are consistent with those given in the Dicke model. Unlike the behavior observed in the Dicke model, the real part of ω_- does not decrease to zero when $\omega_d \neq 0$, and its linewidth never tends to infinity. In Fig. 3.5 (e), we note that the phase transition seen in the Dicke model is canceled, and the superradiant phase does not occur.

In summary, we defined the various models for light-matter coupling in two-level systems and collective two-level systems. For these two cases, a straightforward model exists to describe light-matter interaction in the strong coupling regime: the Jaynes-Cummings and Tavis-Cummings models, respectively, where the rotating wave approximation is applied. This simplifies the description of the phenomenon and aids comprehension. However, beyond the SC regime, the RWA is no longer valid. In this case, the two-level system–light interaction is better described by the Rabi model. Similarly, for collective two-level systems-light interaction beyond the SC regime is captured by more complex models. The Dicke model, for example, predicts a superradiant phase when $g_c > \sqrt{\omega_c\omega_d}$, ensuring the lower polariton frequency remains positive. Alternatively, the Hopfield model, which includes a diamagnetic term neglected in the Dicke model, does not exhibit a superradiant phase.

3.2.7 System surrounded by its environment

In the models discussed above, the assumption is that the studied system is entirely closed (excepted the fact that the intrinsic dissipation is assumed), meaning that the surrounding environment is not taken into account. However, this environment can be considered as a photon bath, wherein the electromagnetic field from outside the system can interact with it, introducing noise and dissipation [40]. Thus, the photon bath characterizes the incoming and outgoing fields in the system. This concept can be formalized through input-output theory [149, 150], which leads to the scattering matrix (S-matrix) describing the scattering through the system.

The Hamiltonian under consideration comprises three distinct components. The first one describes the closed system, encompassing its internal modes and their mutual interactions. Typically, this Hamiltonian is modeled using one of the approaches presented earlier. The second term represents the photon bath, and is characterized by a continuum of external modes of the system. This continuum implies that the environment can accommodate all frequencies (in contrast to a cavity or a resonator operating at discrete frequencies), thus necessitating a description with a continuum of modes, each associated with a specific frequency. The last component represents the coupling between the external and internal modes.

The derivation of the input-output formalism varies depending on the type of cavity involved. For instance, a cavity that traps light in one, two, or three dimensions will lead to different approaches. When light is not confined in all three dimensions, the system is considered open. In such cases, extrinsic dissipation, such as radiative losses, is comparable to or greater than intrinsic dissipation, such as conducting losses or magnon damping. Conversely, when the cavity confines light in all three dimensions, the system is deemed quasi-closed, indicating that intrinsic dissipation significantly outweighs extrinsic dissipation [121]. In the case of a cavity that doesn't confine light in all three dimensions, the frequency spectrum typically shows a dip in transmission at the resonance frequency. Conversely, in a 3D cavity, the transmission spectrum typically exhibits a peak at resonance.

3.2.8 Input-Output formalism for a quasi-closed cavity

As mentioned earlier, the Hamiltonian comprises three components and is given by:

$$\hat{\mathcal{H}} = \hat{\mathcal{H}}_{\text{sys}} + \hat{\mathcal{H}}_{\text{bath}} + \hat{\mathcal{H}}_{\text{int}}. \tag{3.49}$$

The model Hamiltonian for a closed cavity, denoted as $\hat{\mathcal{H}}_{\text{sys}}$, involves p internal bosonic modes. Although the Tavis-Cummings model has been used for this illustration, it has also been shown that the Input-Output formalism applies to systems operating in the USC regime, such as those described by the Hopfield model [151]. The Hamiltonian is expressed as follows:

$$\frac{\hat{\mathcal{H}}_{\text{sys}}}{\hbar} = \sum_p \left[\tilde{\omega}_p \hat{a}_p^\dagger(t)\hat{a}_p(t) + \frac{1}{2}\sum_{q\neq p} \left(g_{qp}\hat{a}_p^\dagger(t)\hat{a}_q(t) + \text{h.c.} \right) \right], \tag{3.50}$$

where $g_{qp}^* = g_{pq}$ is the *sine qua non* condition for expressing the equation in a compact form and ensuring that the Hamiltonian is Hermitian [152]. The first term in the parenthesis represents the unperturbed Hamiltonian of a single oscillator, where $\tilde{\omega}_p = \omega_p - i\gamma_p^{\text{int}}/2$, $\omega_p/2\pi$ is the complex free frequency of the p^{th} internal mode, where ω_p denotes its free frequency, while γ_p^{int} characterizes its intrinsic loss rate. Meanwhile, $\hat{a}_p^\dagger$ ($\hat{a}_p$) represents the creation (annihilation) operator of mode p. The second term in the parenthesis is the interaction Hamiltonian between two internal modes $\hat{a}_p$ and $\hat{a}_q$, with their mutual coupling assessed by g_{qp}, and h.c. indicating the hermitian conjugate. Note that the mode considered in the closed system are not only cavity modes, but can also represent bosonic modes (such as magnons, phonons, or excitons) of a subsystem interacting with cavity photons or other bosonic modes.

For each port n (i.e. a probe), an associated photon bath is represented by a continuum of photonic oscillators, named external modes, with angular eigenfrequency ω. The related Hamiltonian can be expressed as follows:

$$\frac{\hat{\mathcal{H}}_{\text{bath}}}{\hbar} = \sum_n \int_{\mathbb{R}} \mathrm{d}\omega\, \omega \hat{b}_{\omega,n}^\dagger(t)\hat{b}_{\omega,n}(t). \tag{3.51}$$

Here, $\hat{b}_{\omega,n}^\dagger$ ($\hat{b}_{\omega,n}$) represents the creation (annihilation) operator of the external mode associated with port n and having the angular frequency ω.

The interaction between the bath and the system can be described by the following model Hamiltonian (under the RWA):

$$\frac{\hat{\mathcal{H}}_{\text{int}}}{\hbar} = \frac{i}{\sqrt{2\pi}} \sum_{p,n} \int_{\mathbb{R}} \mathrm{d}\omega \left(\kappa_{pn}(\omega) \hat{b}^{\dagger}_{\omega,n}(t) \hat{a}_p(t) - \text{h.c.} \right), \tag{3.52}$$

where $\kappa_{pn}(\omega)$ is the external coupling strength between the external mode $\hat{b}_{n,\omega}$ and the internal mode $\hat{a}_p$. Furthermore, the unit of $\hat{b}_n(t)$ is $\text{rad}^{-1/2}.\text{s}^{1/2}$, while the unit of $\kappa_{pn}\,(\omega_k)$ is $\text{rad}^{1/2}.\text{s}^{-1/2}$. The unit of g_{qp} is $\text{rad}^{1/2}.\text{s}^{-1/2}$, and $\hat{a}_p(t)$ has no unit. In the first Markov approximation, the external coupling strength is assumed to be independent of the angular frequency:

$$\kappa_{pn}(\omega) = \kappa_{pn} \propto \sqrt{\gamma_{pn}}, \quad \gamma_{pn} \in \mathbb{R}. \tag{3.53}$$

Here, γ_{pn} is real and represents the external photonic damping rate. Note that the proportional term indicates that the external coupling strength is equal to the square root of the external damping rate, up to a phase factor, as discussed in Chapter 6.

To describe the entire system within the framework of input-output theory, we will apply the Heisenberg equations of motion, which describe the time evolution of external mode operators interacting with the system. These equations capture the interaction between incoming and outgoing photons and the electromagnetic field within the cavity. The next step is to describe the dynamics of the internal modes and their interactions with the environment (the external modes) using the Quantum Langevin equations.

3.2.8.a Heisenberg Equation of Motion

From Eq. (3.49) and considering the first Markov approximation given in Eq. (3.53), the Heisenberg EoM, given in Eq. (3.33), for the external modes reads:

$$\dot{\hat{b}}_{\omega,n}(t) = -i\omega \hat{b}_{\omega,n}(t) + \frac{1}{\sqrt{2\pi}} \sum_{p} \kappa_{pn} \hat{a}_p(t). \tag{3.54}$$

The solution of this differential equation reads as:

$$\hat{b}_{\omega,n}(t) = \hat{b}^{\tau}_{\omega,n} e^{-i\omega(t-\tau)} + \frac{1}{\sqrt{2\pi}} \sum_{p} \kappa_{pn} \int_{\tau}^{t} \mathrm{d}t'\, \hat{a}_p(t') e^{-i\omega(t-t')}, \tag{3.55}$$

where τ is a time reference.
Subsequently, we define the polychromatic bosonic operator for each port by considering all the bosonic operators of the same port across all frequencies:

$$\hat{b}^{\tau}_{n}(t) = \frac{1}{\sqrt{2\pi}} \int_{\mathbb{R}} \mathrm{d}\omega\, \hat{b}^{\tau}_{\omega,n} e^{-i\omega(t-\tau)}. \tag{3.56}$$

From this equation, we define the incoming and outgoing wave operators at each port:

$$\hat{b}^{\text{in}}_{n}(t) = \hat{b}^{t_0}_{n}(t), \quad t_0 = -\infty, \tag{3.57a}$$
$$\hat{b}^{\text{out}}_{n}(t) = \hat{b}^{t_1}_{n}(t), \quad t_1 = +\infty. \tag{3.57b}$$

3.2.8.b Input-Output Relation

Integrating over ω on both sides, Eq. (3.55) becomes [4]:

$$\frac{1}{\sqrt{2\pi}}\int_{\mathbb{R}} \mathrm{d}\omega\, \hat{b}_{\omega,n}(t) = \frac{1}{\sqrt{2\pi}}\int_{\mathbb{R}} \mathrm{d}\omega\, \hat{b}^{t_0}_{\omega,n} e^{-i\omega(t-t_0)} + \frac{1}{2\pi}\sum_p \kappa_{pn} \int_{-\infty}^{t} \mathrm{d}t'\, \hat{a}_p(t') \int_{\mathbb{R}} \mathrm{d}\omega\, e^{-i\omega(t-t')}, \tag{3.58a}$$

$$\frac{1}{\sqrt{2\pi}}\int_{\mathbb{R}} \mathrm{d}\omega\, \hat{b}_{\omega,n}(t) = \frac{1}{\sqrt{2\pi}}\int_{\mathbb{R}} \mathrm{d}\omega\, \hat{b}^{t_1}_{\omega,n} e^{-i\omega(t-t_1)} - \frac{1}{2\pi}\sum_p \kappa_{pn} \int_{t}^{+\infty} \mathrm{d}t'\, \hat{a}_p(t') \int_{\mathbb{R}} \mathrm{d}\omega\, e^{-i\omega(t-t')}, \tag{3.58b}$$

where the first term on the right-hand side of the first (second) equation is equal to $\hat{b}^{in}_n(t)$ ($\hat{b}^{out}_n(t)$), and the second term is equal to $\frac{1}{2}\sum_p \kappa_{pn}$ ($-\frac{1}{2}\sum_p \kappa_{pn}$), according to the following properties [150]:

$$\int_{\mathbb{R}} \mathrm{d}\omega\, e^{-i\omega(t-t')} = 2\pi\delta(t-t'), \tag{3.59a}$$

$$\int_{-\infty}^{t} \mathrm{d}t'\, \hat{a}_p(t')\delta(t-t') = \int_{t}^{+\infty} \mathrm{d}t'\, \hat{a}_p(t')\delta(t-t') = \frac{1}{2}\hat{a}_p(t). \tag{3.59b}$$

This results in the input-output relation:

$$\hat{b}^{\mathrm{out}}_n(t) = \hat{b}^{\mathrm{in}}_n(t) + \sum_p \kappa_{pn}\hat{a}_p(t). \tag{3.60}$$

3.2.8.c Quantum Langevin Equation

The Quantum Langevin Equation (QLE), which describes the internal modes and their associated environmental losses, reads as :

$$\dot{\hat{a}}_p(t) = -i\tilde{\omega}_p\hat{a}_p(t) - i\sum_{q\neq p} g_{qp}\hat{a}_q(t) - \frac{1}{\sqrt{2\pi}}\sum_n \int_{\mathbb{R}} \mathrm{d}\omega\, \kappa^*_{pn}(\omega)\hat{b}_{\omega n}(t). \tag{3.61}$$

Substituting the value of $\hat{b}_{\omega,n}$ from Eq. (3.55) for $\tau = t_0$ in the QLE gives rise to:

$$\begin{aligned}\dot{\hat{a}}_p(t) = &-i\tilde{\omega}_p\hat{a}_p(t) - i\sum_{q\neq p} g_{qp}\hat{a}_q(t) \\ &- \frac{1}{\sqrt{2\pi}}\sum_n \kappa^*_{pn}\left[\int_{\mathbb{R}} \mathrm{d}\omega\, \hat{b}^{t_0}_{\omega,n} e^{-i\omega(t-t_0)} + \kappa_{pn}\sum_q \int_{t_0}^{t} \mathrm{d}t' \int_{\mathbb{R}} \mathrm{d}\omega\, e^{-i\omega(t-t')}\hat{a}_q(t')\right].\end{aligned} \tag{3.62}$$

The properties given in Eq. (3.59a) and (3.59b) lead to:

$$\dot{\hat{a}}_p(t) = -i\tilde{\omega}_p\hat{a}_p(t) - i\sum_{q\neq p} g_{qp}\hat{a}_q(t) - \sum_n \kappa^*_{pn}\left(\hat{b}^{\mathrm{in}}_n(t) + \sum_q \frac{\kappa_{qn}}{2}\hat{a}_q(t)\right). \tag{3.63}$$

[4] Note that $\int_{+\infty}^{t} \mathrm{d}t'\, f(t') = -\int_{t}^{+\infty} \mathrm{d}t'\, f(t')$, where $f(t')$ is a time-dependent function.

Taking the Fourier transform[5], Eq. (3.63) can be expressed as:

$$\left(\omega - \tilde{\omega}_p + \frac{i}{2}\sum_n |\kappa_{pn}|^2\right)\hat{a}_p(\omega) + \sum_{q\neq p}\left(\frac{i}{2}\sum_n \kappa_{pn}^*\kappa_{qn} - g_{qp}\right)\hat{a}_q(\omega) = -i\sum_n \kappa_{pn}^*\hat{b}_n^{\text{in}}(\omega). \quad (3.64)$$

In matrix form:

$$\boldsymbol{\Omega}\cdot\hat{\mathbf{a}} = -i\mathbf{K}^*\cdot\hat{\mathbf{b}}_{\text{in}}, \quad (3.65a)$$

$$\Omega_{qp} = (\omega - \tilde{\omega}_p)\delta_{qp} + \frac{i}{2}\sum_n(\kappa_{pn}^*\kappa_{qn}) - g_{qp}, \quad (3.65b)$$

where $\hat{\mathbf{a}}$ is the vector containing all $\hat{a}_p(\omega)$ operator components, $\hat{\mathbf{b}}_{\text{in}}$ is the vector containing all $\hat{b}_n^{\text{in}}(\omega)$ operator components, $\mathbf{K}$ is the $p\times n$ matrix with κ_{pn} as components, Ω_{qp} are the components of the $p\times p$ matrix $\boldsymbol{\Omega}$, and δ_{qp} is the Kronecker delta.

3.2.8.d S-parameters

Substituting the solution of Eq. (3.65a) into Eq. (3.60) results in:

$$\hat{\mathbf{b}}_{\text{out}} = \mathbf{S}\cdot\hat{\mathbf{b}}_{\text{in}}, \quad (3.66)$$

where the S-matrix reads as:

$$\mathbf{S} = \mathbb{1} - i\mathbf{K}^{\text{t}}\cdot\boldsymbol{\Omega}^{-1}\cdot\mathbf{K}^*, \quad (3.67)$$

where $\mathbb{1}$ is the identity matrix.

The S-matrix simplifies the computation of reflection and transmission for complex systems with multiple internal modes and ports. As an example, Fig. 3.7 (a) depicts

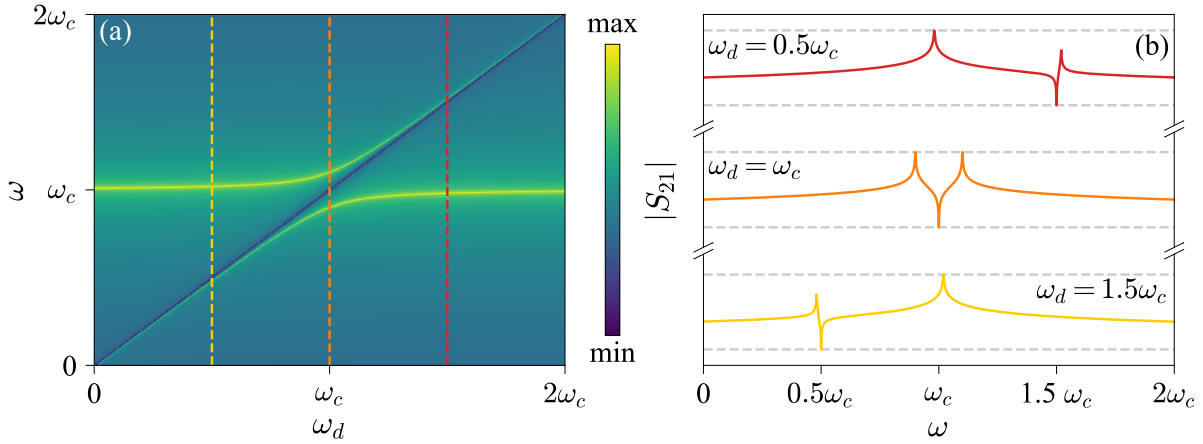

FIGURE 3.7: (a) Transmission spectrum of a system composed of a quasi-closed cavity photon and a matter boson; and (b) trace of the transmission spectra versus ω for $\omega_d = 0.5$, 1, and 1.5 in yellow, orange and red curves respectively. The intrinsic losses rate of the cavity and the magnon are $\gamma_c^{\text{int}} = 10$ MHz and $\gamma_m^{\text{int}} = 2$ MHz, and the external losses rate are $\gamma_{00} = \gamma_{01} = 5$ MHz.

[5]Reminding the Fourier Transform property: $\mathcal{F}[\dot{\hat{a}}_q(t)] = -i\omega\hat{a}_q(\omega)$

the transmission spectrum of a quasi-closed cavity composed of a cavity photon and a matter bosonic mode. It can be shown that in a quasi-closed cavity, the eigenfrequencies of the system are represented by peaks in the transmission. Fig. 3.7 (b) provides a visual representation of these peaks at $\omega_d = 0.5$, 1, and 1.5 ω_c.

It should be noted that the π-phase shift of the reflection phase has not been explicitly considered. Specifically, in Eq. (3.57b), this phase shift should be applied to the outgoing reflected wave, leading to $\hat{b}_n^{\text{out}}(t) = -\hat{b}_n^{t_1}(t)$. Consequently, this modifies the scattering matrix element to $S_{ii} \to -S_{ii}$ (the S_{ij} parameters are not considered, as the transmission does not exhibit a π-phase shift). However, since all the terms contained in S_{ii} inherently include this additional π-phase (i.e. minus sign), the interferences between these terms remain unaffected, and the underlying physics remains unchanged. Nevertheless, if we consider a system composed of cascaded scatterers, neglecting the π-phase shift in the reflection could introduce discrepancies in the model.

3.2.8.e Multi-tone driving

For multi-tone driving, the S-matrix does not normalize entrant power. To achieve this normalization, it is more convenient to use another quantity, which reads as:

$$\boldsymbol{\sigma} = \frac{\mathbf{S} \cdot \hat{\mathbf{b}}_{\text{in}}}{\sum_n |\hat{b}_n^{\text{in}}|}. \tag{3.68}$$

This quantity lies outside the scope of the studies in this thesis; however, we demonstrate that multi-tone driving can be straightforwardly expressed. For further insights into two-tone driving, readers are referred to refs [153–155].

3.2.9 Input-Output formalism for an open cavity

An open system consists of one or several waveguides that carry traveling waves. These waves can be coupled to a system comprising bosonic resonators. It is assumed that each waveguide allows waves to travel from one port at its edge to another port at the opposite edge. Consequently, a waveguide possesses two ports, and these ports cannot belong to another waveguide. With a system composed of n waveguides, there are $2n$ ports, in contrast to n ports for the case of a quasi-closed cavity.

In this scenario, the Hamiltonian of the bath is expressed in the k-space, reflecting the wave propagation within the waveguide, while no propagation occurs in a closed system, and by extension, in a quasi-closed system. The Hamiltonian of the bath for an open-cavity is given by:

$$\frac{\hat{\mathcal{H}}_{\text{bath}}}{\hbar} = \sum_n \int_{-\infty}^{+\infty} \mathrm{d}k \, c_k \tilde{\omega}_k \hat{b}_{k,n}^\dagger(t) \hat{b}_{k,n}(t). \tag{3.69}$$

Similarly, the interaction Hamiltonian is given by:

$$\frac{\hat{\mathcal{H}}_{\text{int}}}{\hbar} = \frac{i}{\sqrt{2\pi}} \sum_{p,n} \int_{-\infty}^{+\infty} \mathrm{d}k \, c_k \left(\kappa_{pn}(\omega_k) \hat{b}_{k,n}^\dagger(t) \hat{a}_p(t) - \kappa_{pn}^*(\omega_k) \hat{a}_p^\dagger(t) \hat{b}_{k,n}(t) \right). \tag{3.70}$$

In this expression, $\kappa_{pn}(\omega_k)$ denotes the coupling strength between a traveling mode n with frequency ω_k and an internal mode p. The operators $\hat{a}_p^\dagger(t)$ ($\hat{a}_p(t)$) are the creation (annihilation) operators of the mode p. Similarly, $\hat{b}_{k,n}^\dagger(t)$ ($\hat{b}_{k,n}(t)$) are the creation (annihilation) operators of the traveling mode carried by waveguide n with wave vector k. The quantity $c_k = c/\sqrt{\varepsilon_k}$ represents the speed of the traveling wave in the waveguide, where c is the vacuum speed of light, and ε_k is the electric permittivity experienced by the traveling wave in the waveguide.

In the subsequent analysis, it is assumed that all waveguides possess identical characteristics, implying that traveling waves propagate uniformly regardless of the specific waveguide. This uniformity is expressed through the consistent dependence of c_k, and ω_k on k across all waveguides. Additionally, each waveguide comprises two ports, signifying that a traveling wave with a wave vector $+k$ in waveguide n indicates electromagnetic wave propagation from the first port to the second port. Conversely, a traveling wave with a wave vector $-k$ in waveguide n signifies electromagnetic wave transmission from the second port to the first port. Consequently, due to the opposing behaviors of positive and negative k at the ports of the waveguide, the integral over k in the bath Hamiltonian of Eq. (3.69) can be partitioned into two integrals, one over positive k, and the other over negative k:

$$\frac{\hat{\mathcal{H}}_{\text{bath}}}{\hbar} = \sum_n \left(\int_0^{+\infty} \mathrm{d}k\, c_k \omega_k \hat{b}_{k,n}^\dagger(t) \hat{b}_{k,n}(t) + \int_{-\infty}^{0} \mathrm{d}k\, c_k \omega_k \hat{b}_{k,n}^\dagger(t) \hat{b}_{k,n}(t) \right), \tag{3.71}$$

where the second integral can be expressed as:

$$\int_{-\infty}^{0} \mathrm{d}k\, c_k \omega_k \hat{b}_{k,n}^\dagger(t) \hat{b}_{k,n}(t) = -\int_{0}^{-\infty} \mathrm{d}k\, c_k \omega_k \hat{b}_{k,n}^\dagger(t) \hat{b}_{k,n}(t) = \int_0^{+\infty} \mathrm{d}k\, c_{-k} \omega_{-k} \hat{b}_{-k,n}^\dagger(t) \hat{b}_{-k,n}(t). \tag{3.72}$$

In the following, we assume isotropic propagation of traveling waves, i.e. $c_k = c_{-k}$, and $\omega_k = \omega_{-k}$. Hence, the Hamiltonian of the bath is given by:

$$\frac{\hat{\mathcal{H}}_{\text{bath}}}{\hbar} = \sum_n \int_{\mathbb{R}^+} \mathrm{d}k\, c_k \omega_k \left(\hat{b}_{k,n}^\dagger(t) \hat{b}_{k,n}(t) + \hat{b}_{-k,n}^\dagger(t) \hat{b}_{-k,n}(t) \right). \tag{3.73}$$

For the same reason, $\kappa_{pn}(\omega_k) = \kappa_{pn}(\omega_{-k})$, leading to the interaction Hamiltonian in Eq. (3.70) being rewritten as:

$$\begin{aligned} \frac{\hat{\mathcal{H}}_{\text{int}}}{\hbar} = \frac{i}{\sqrt{2\pi}} \sum_{p,n} \int_{\mathbb{R}^+} \mathrm{d}k\, c_k \Big[& \kappa_{pn}(\omega_k) \left(\hat{b}_{k,n}^\dagger(t) + \hat{b}_{-k,n}^\dagger(t) \right) \hat{a}_p(t) \\ & - \kappa_{pn}^*(\omega_k) \hat{a}_p^\dagger(t) \left(\hat{b}_{k,n}(t) + \hat{b}_{-k,n}(t) \right) \Big]. \end{aligned} \tag{3.74}$$

Integrals over k, and $-k$ can be rewritten as integrals over ω_k:

$$\int_{\mathbb{R}^+} \mathrm{d}k\, c_k f(k) = \int_{\mathbb{R}^+} \mathrm{d}\omega_k\, f(k) = \int_{\mathbb{R}} \mathrm{d}\omega_k\, f(k), \tag{3.75a}$$

$$\int_{\mathbb{R}^+} \mathrm{d}k\, c_k f(-k) = \int_{\mathbb{R}^+} \mathrm{d}\omega_k\, f(-k) = \int_{\mathbb{R}} \mathrm{d}\omega_k\, f(k). \tag{3.75b}$$

The Heisenberg EoM for the traveling modes, with integral over ω_k instead of k, read as:

$$\dot{\hat{b}}_{\pm k,n}(t) = -\frac{i}{\hbar}[\hat{\mathcal{H}}, \hat{b}_{\pm k,n}(t)] = -i\omega_k \hat{b}_{\pm k,n}(t) + \frac{1}{\sqrt{2\pi}} \sum_p \kappa_{pn}(\omega_k)\hat{a}_p(t). \tag{3.76}$$

The solution to this differential equation for the traveling operators is given by:

$$\hat{b}_{\pm k,n}(t) = \hat{b}^{\tau}_{\pm k,n}(t)e^{-i\omega_k(t-\tau)} + \frac{1}{\sqrt{2\pi}} \sum_p \kappa_{pn}(\omega_k) \int_{\tau}^{t} \mathrm{d}t'\, e^{-i\omega_k(t-t')}\hat{a}_p(t'), \tag{3.77}$$

where τ is a time reference. The solution of the equations considering the direction of propagation are similar to the equations int the quasi-closed system given in Eq. (3.55).

For subsequent calculations, let's define the bosonic operators for the positive and negative polychromatic traveling waves in waveguide n. These operators account for the set of traveling waves in the positive and negative k-space, respectively:

$$\hat{b}^{\tau,\pm}_n(t) = \frac{1}{\sqrt{2\pi}} \int_{\mathbb{R}} \mathrm{d}\omega_k\, e^{-i\omega_k(t-\tau)} \hat{b}^{\tau}_{\pm k,n}(t). \tag{3.78}$$

Given the properties outlined in Eq. (3.59a) and (3.59b), we can establish the input-output relation for the positive and negative k waves similarly:

$$\hat{b}^{\mathrm{out.}\pm}_n = \hat{b}^{\mathrm{in.}\pm}_n + \sum_p \kappa_{pn}\hat{a}_p(t). \tag{3.79}$$

The QLE can be expressed as:

$$\dot{\hat{a}}_p(t) = -i\tilde{\omega}_p\hat{a}_p(t) - i\sum_{q\neq p} g_{qp}\hat{a}_q(t) - \frac{1}{\sqrt{2\pi}} \sum_n \int_{\mathbb{R}} \mathrm{d}\omega_k\, \kappa^*_{pn} \left(\hat{b}_{k,n}(t) + \hat{b}_{-k,n}(t)\right). \tag{3.80}$$

Similarly to the case of the quasi-closed cavity, we arrive at:

$$\begin{aligned}\left(\omega - \tilde{\omega}_p + i\sum_n |\kappa_{pn}|^2\right)\hat{a}_p(\omega) + \sum_{q\neq p}\left(i\sum_n \kappa^*_{pn}\kappa_{qn} - g_{qp}\right)\hat{a}_q(\omega) \\ = -i\sum_n \kappa^*_{pn}\left(\hat{b}^{\mathrm{in},+}_n(\omega) + \hat{b}^{\mathrm{in},-}_n(\omega)\right).\end{aligned} \tag{3.81}$$

In the matrix form:

$$\boldsymbol{\Omega}\cdot\hat{\mathbf{a}} = -i\mathbf{K}'\cdot\left(\hat{\mathbf{b}}^{+}_{\mathrm{in}} + \hat{\mathbf{b}}^{-}_{\mathrm{in}}\right), \tag{3.82a}$$

$$\Omega_{qp} = (\omega - \tilde{\omega}_p)\delta_{qp} + i\sum_n(\kappa^*_{pn}\kappa_{qn}) - g_{qp}, \tag{3.82b}$$

$$\kappa'_{pn} = \kappa^*_{pn}. \tag{3.82c}$$

The expression remains consistent, with $\hat{\mathbf{a}}$ representing the vector containing all $\hat{a}_p(\omega)$ operator components, $\hat{\mathbf{b}}^{\pm}_{\mathrm{in}}$ standing for the vector containing all $\hat{b}^{\mathrm{in},\pm}_n(\omega)$ operator components, $\mathbf{K}'$ representing the $p\times n$ matrix with κ'_{pn} as components, and Ω_{qp} denoting the components of the $p\times p$ matrix $\boldsymbol{\Omega}$. It is worth noting that the dissipation rates in an open cavity are twice as large as those in a quasi-closed cavity, considering Eq. (3.65b)

and Eq. (3.82b).

3.2.9.a Transmission and Reflection matrices

The input-output relation provided in Eq. (3.79) can also be expressed in matrix form as:

$$\hat{\mathbf{b}}^{\pm}_{\text{out}} = \hat{\mathbf{b}}^{\pm}_{\text{in}} - i\mathbf{K}^t \cdot \mathbf{\Omega}^{-1} \cdot \mathbf{K}' \left(\hat{\mathbf{b}}^{+}_{\text{in}} + \hat{\mathbf{b}}^{-}_{\text{in}}\right) = \mathbf{T} \cdot \hat{\mathbf{b}}^{\pm}_{\text{in}} + \mathbf{R} \cdot \hat{\mathbf{b}}^{\mp}_{\text{in}}, \tag{3.83}$$

where:

$$\mathbf{T} = \mathbb{1} - i\mathbf{K}^t \cdot \mathbf{\Omega}^{-1} \cdot \mathbf{K}', \tag{3.84a}$$

$$\mathbf{R} = -i\mathbf{K}^t \cdot \mathbf{\Omega}^{-1} \cdot \mathbf{K}'. \tag{3.84b}$$

This result differs significantly from the input-output formalism for a quasi-closed cavity. Specifically, the component T_{mn} corresponds to the $S_{2m,2n-1}$ ($S_{2m-1,2n}$) parameter when applied with $\hat{\mathbf{b}}^{+}_{\text{in}}$ ($\hat{\mathbf{b}}^{-}_{\text{in}}$), representing the transmission parameter. Conversely, R_{mn} represents the $S_{2m-1,2n-1}$ ($S_{2m,2n}$) parameter when applied with $\hat{\mathbf{b}}^{-}_{\text{in}}$ ($\hat{\mathbf{b}}^{+}_{\text{in}}$), indicating the reflection parameter. Ultimately, $\mathbf{T}$ and $\mathbf{R}$ are the transmission and reflection matrices of the waves propagating in the positive or negative direction in the waveguide. It is noteworthy that the off-diagonal components of $\mathbf{T}$ and $\mathbf{R}$ are identical, indicating that the waveguides behave similarly regardless of their input ports.

As an example, Fig. 3.8 (a) depicts the transmission spectrum of an open cavity composed of a cavity photon and a matter bosonic mode. It can be shown that in an open cavity, the eigenfrequencies of the system are represented by dips in the transmission. Fig. 3.8 (b) provides a visual representation of these dips at $\omega_d = 0.5$, 1, and 1.5 ω_c.

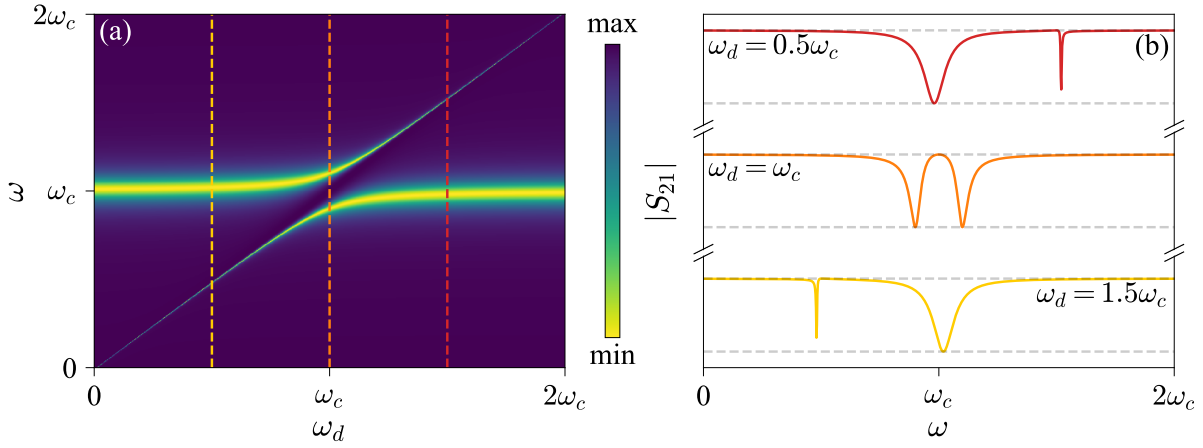

FIGURE 3.8: (a) Transmission spectrum of an open system composed of a cavity photon and a matter boson; and (b) trace of the transmission spectra versus ω for $\omega_d = 0.5$, 1, and 1.5 in yellow, orange and red curves respectively. The intrinsic losses rate of the cavity and the magnon are $\gamma_c^{\text{int}} = 10$ MHz and $\gamma_m^{\text{int}} = 2$ MHz, and the external losses rate are $\gamma_{00} = \gamma_{01} = 400$ MHz.

3.2.9.b Multi-tone driving

For multi-tone driving in an open cavity, the normalized parameter can be expressed as:

$$\boldsymbol{\sigma}^{\pm} = \frac{\mathbf{T} \cdot \hat{\mathbf{b}}_{\text{in}}^{\pm} + \mathbf{R} \cdot \hat{\mathbf{b}}_{\text{in}}^{\mp}}{\sum_n \left(|\hat{b}_n^{\text{in},+}| + |\hat{b}_n^{\text{in},-}| \right)}. \tag{3.85}$$

3.3 Microwave photon-magnon coupling

In this section, we derive the Hamiltonian that arises from physical considerations in the case of photon-magnon coupling. From this, we will define the coupling strength as a function of a so-called filling factor.

As demonstrated earlier, both the Hamiltonians governing the magnon mode, denoted as $\hat{\mathcal{H}}_m$, and the cavity photonic mode, denoted as $\hat{\mathcal{H}}_c$, can be described by quantum harmonic oscillators:

$$\hat{\mathcal{H}}_m = \hbar\omega_m \hat{m}^\dagger \hat{m}, \tag{3.86a}$$

$$\hat{\mathcal{H}}_c = \hbar\omega_c \hat{c}^\dagger \hat{c}. \tag{3.86b}$$

Both equations stem from Eq. (2.84) for the magnon mode and Eq. (3.16) for the cavity photonic mode. Notably, the ground states of the magnon, denoted by $\mathcal{E}(B_0)$, and the cavity photon, represented by $1/2\hbar\omega_c$, are omitted as they merely serve as energy offsets and are not pertinent to the subsequent calculations. Additionally, only the Kittel mode, corresponding to $k = 0$, is considered as the magnon mode.

In the ensuing analysis, we examine a ferromagnetic material coupled with the cavity electromagnetic field. It is also assumed that the angular momentum of the ferromagnet is solely due to the spin-one. Furthermore, we posit the presence of a static magnetic field oriented along the z-axis, facilitating the alignment of all spins along this axis. Since we focus solely on the uniform precession magnon mode, we can interpret all spins in the sample as constituting a single macrospin.

$$\hat{\mathbf{S}} \to N_S \hat{\mathbf{S}}, \tag{3.87}$$

where N_S represents the total number of spins within the sample. As outlined in Sec. 2, the interaction between magnons and photons arises via the Zeeman interaction. Referring to Eq. (2.43) and Eq. (2.58), the interaction Hamiltonian governing the magnetization of the entire ferromagnet can be expressed as:

$$\hat{\mathcal{H}}_{\text{int}} = -\mu_0 \int_{V_m} \mathrm{d}^3\mathbf{r}\, \hat{\mathbf{M}} \cdot \hat{\mathbf{h}}. \tag{3.88}$$

Here, $\hat{\mathbf{M}} = n_S \hat{\boldsymbol{\mu}}$, where $n_S = N_S/V_m$ represents the spin density within the ferromagnet, with V_m being the volume of the ferromagnetic material. Since the magnetic moment solely arises from the spin angular momentum, the number of spins corresponds to the number of magnetic moments within the material. From Eq. (2.20), the macrospin can

also be expressed as:

$$\hat{\mathbf{S}} = \frac{N_S}{\gamma}\hat{\boldsymbol{\mu}} = \frac{V_m}{\gamma}\hat{\mathbf{M}}. \tag{3.89}$$

Moreover, the total length of the macrospin is given by:

$$S = N_S\frac{\mu}{\hbar\gamma} = -N_S\frac{\mu}{g_{\mathrm{L}}\mu_{\mathrm{B}}}. \tag{3.90}$$

Substituting the magnetization operator with the macrospin operator using Eq. (3.89), and the cavity magnetic field with its value in Eq. (3.18b), the interaction Hamiltonian in Eq. (3.88) can be expressed as:

$$\hat{\mathcal{H}}_{\mathrm{int}} = -\frac{\gamma}{V_m}\sqrt{\frac{\hbar}{2\omega_c\varepsilon_0\varepsilon_{\mathrm{r},c}}}\int_{V_m}\mathrm{d}^3\mathbf{r}\,\hat{\mathbf{S}}\cdot(\hat{c}^\dagger+\hat{c})\nabla\times\mathbf{U}. \tag{3.91}$$

Applying the Holstein-Primakoff transformation to replace the macrospin operator with the magnon operator using Eq. (2.70), Eq. (2.74a), and Eq. (2.74b), we derive:

$$\int_{V_m}\mathrm{d}^3\mathbf{r}\,\hat{S}_x\hat{h}_x = \frac{\hbar}{2}\sqrt{2S}(\hat{m}^\dagger+\hat{m})(\hat{c}^\dagger+\hat{c})\int_{V_m}\mathrm{d}^3\mathbf{r}\,\nabla\times\mathbf{U}\cdot\mathbf{x}, \tag{3.92a}$$

$$\int_{V_m}\mathrm{d}^3\mathbf{r}\,\hat{S}_y\hat{h}_y = i\frac{\hbar}{2}\sqrt{2S}(\hat{m}^\dagger-\hat{m})(\hat{c}^\dagger+\hat{c})\int_{V_m}\mathrm{d}^3\mathbf{r}\,\nabla\times\mathbf{U}\cdot\mathbf{y}, \tag{3.92b}$$

$$\int_{V_m}\mathrm{d}^3\mathbf{r}\,\hat{S}_z\hat{h}_z = \hbar(S-\hat{m}^\dagger\hat{m})(\hat{c}^\dagger+\hat{c})\int_{V_m}\mathrm{d}^3\mathbf{r}\,\nabla\times\mathbf{U}\cdot\mathbf{z}. \tag{3.92c}$$

Referring to the supplementary information of Flower et al. (2019) [156], the expression above can be rewritten as a function of the ratio of the magnetic field within the ferromagnet to the total energy field associated with the total h-field in the entire cavity. Initially, we consider the Hamiltonian of the magnetic field component in Eq. (3.9b). The energies of the magnetic field within the magnetic material and the entire cavity are expressed as:

$$\mathcal{H}_{V_m} = \frac{1}{2\mu_0}\int_{V_m}\mathrm{d}^3\mathbf{r}\,\mathbf{h}\cdot\mathbf{h} = \frac{1}{2\mu_0}\frac{q^2(t)}{\varepsilon_0\varepsilon_{\mathrm{r},c}}\int_{V_m}\mathrm{d}^3\mathbf{r}\,\left(\nabla\times\mathbf{U}(\mathbf{r})\right)\cdot\left(\nabla\times\mathbf{U}(\mathbf{r})\right), \tag{3.93a}$$

$$\mathcal{H}_{V_c} = \frac{1}{2\mu_0}\int_{V_c}\mathrm{d}^3\mathbf{r}\,\mathbf{h}\cdot\mathbf{h} = \frac{1}{2\mu_0}\int_{V_c}\mathrm{d}^3\mathbf{r}\,|\mathbf{h}|^2 = \frac{1}{2\mu_0}\frac{q^2(t)}{\varepsilon_0\varepsilon_{\mathrm{r},c}}\frac{\varepsilon_{\mathrm{r},c}\omega_c^2}{c^2}. \tag{3.93b}$$

Combining these two equations, the energy ratio is expressed as:

$$\frac{\mathcal{H}_{V_m}}{\mathcal{H}_{V_c}} = \frac{\int_{V_m}\mathrm{d}^3\mathbf{r}\,\mathbf{h}\cdot\mathbf{h}}{\int_{V_c}\mathrm{d}^3\mathbf{r}\,|\mathbf{h}|^2} = \frac{\int_{V_m}\mathrm{d}^3\mathbf{r}\,\left(\nabla\times\mathbf{U}(\mathbf{r})\right)\cdot\left(\nabla\times\mathbf{U}(\mathbf{r})\right)}{\varepsilon_{\mathrm{r},c}\omega_c^2/c^2}. \tag{3.94}$$

This implies that the rotational of $\mathbf{U}(\mathbf{r})$ can be parametrized as a function of the magnetic field:

$$\nabla\times\mathbf{U}(\mathbf{r}) = \frac{\sqrt{\varepsilon_{\mathrm{r},c}}\omega_c}{c}\frac{\mathbf{h}}{\sqrt{\int_{V_c}\mathrm{d}^3\mathbf{r}\,|\mathbf{h}|^2}}. \tag{3.95}$$

Finally, the interaction Hamiltonian, can be expressed as:

$$\hat{\mathcal{H}}_{\mathrm{int}}/\hbar = g_x(\hat{m}^\dagger+\hat{m})(\hat{c}^\dagger+\hat{c}) + ig_y(\hat{m}^\dagger-\hat{m})(\hat{c}^\dagger+\hat{c}) + g_z\hat{m}^\dagger\hat{m}(\hat{c}^\dagger+\hat{c}) + \Omega_z(\hat{c}^\dagger+\hat{c}). \tag{3.96}$$

Here, g_x and g_y represent the coupling strengths in the two directions perpendicular to the static magnetic field. These are the couplings of interest in the studies presented in this thesis, and are given by:

$$g_x = -\frac{\gamma\sqrt{\hbar\mu_0\omega_c S}}{2V_m}\frac{\int_{V_m} \mathrm{d}^3\mathbf{r}\, \mathbf{h}\cdot\mathbf{x}}{\sqrt{\int_{V_c} \mathrm{d}^3\mathbf{r}\, |\mathbf{h}|^2}}, \tag{3.97a}$$

$$g_y = -\frac{\gamma\sqrt{\hbar\mu_0\omega_c S}}{2V_m}\frac{\int_{V_m} \mathrm{d}^3\mathbf{r}\, \mathbf{h}\cdot\mathbf{y}}{\sqrt{\int_{V_c} \mathrm{d}^3\mathbf{r}\, |\mathbf{h}|^2}}. \tag{3.97b}$$

The two terms g_z and Ω_z represent the coupling strength along the z-axis and the effective field associated with the spins aligned along the z-axis, respectively. They are expressed as:

$$g_z = \frac{\gamma\sqrt{\hbar\mu_0\omega_c}}{\sqrt{2}V_m}\frac{\int_{V_m} \mathrm{d}^3\mathbf{r}\, \mathbf{h}\cdot\mathbf{z}}{\sqrt{\int_{V_c} \mathrm{d}^3\mathbf{r}\, |\mathbf{h}|^2}}, \tag{3.98a}$$

$$\Omega_z = \frac{\gamma\sqrt{\hbar\mu_0\omega_c S}}{\sqrt{2}V_m}\frac{\int_{V_m} \mathrm{d}^3\mathbf{r}\, \mathbf{h}\cdot\mathbf{z}}{\sqrt{\int_{V_c} \mathrm{d}^3\mathbf{r}\, |\mathbf{h}|^2}}. \tag{3.98b}$$

It is worth noting that g_z is negligible when a periodic magnetic field is applied along the z-axis. This is because it is not proportional to the square root of S, and hence not directly related to the number of spins N_S in the material, unlike the perpendicular coupling strengths g_x and g_y. Furthermore, in the studies undertaken in this thesis, the periodic magnetic field is applied perpendicular to the static magnetic field, resulting in only g_x and g_y being considered in all subsequent analyses.

It is noteworthy that Equation Eq. (3.96) represents the Dicke model, wherein there exists a coupling phase between the Cartesian directions, as highlighted in Gardin et al. (2023) [157]. Then, by considering only the coupling strengths in the perpendicular direction, the Hamiltonian in Equation Eq. (3.96) can be simplified to:

$$\hat{\mathcal{H}}_{\mathrm{int}}/\hbar = g(e^{i\phi}\hat{m}^\dagger + e^{-i\phi}\hat{m})(\hat{c}^\dagger + \hat{c}) + \mathrm{h.c.} \tag{3.99}$$

Here, the coupling strength is expressed as:

$$\frac{g}{2\pi} = \eta\sqrt{\omega_c}\frac{|\gamma|}{4\pi}\sqrt{\frac{|\mu|}{g_{\mathrm{L}}\mu_{\mathrm{B}}}\mu_0\hbar n_{\mathrm{S}}}. \tag{3.100}$$

for YIG, the constant terms on the right-hand side of ω_c are provided in Sec. 2.2.5, and are equal to $16.5493 \cdot 10^3$ $\mathrm{Hz}^{1/2}$. In the coupling strength expression, we introduced the filling factor, expressed as:

$$\eta = \frac{\sqrt{\left(\int_{V_m} \mathrm{d}^3\mathbf{r}\, \mathbf{h}\cdot\mathbf{x}\right)^2 + \left(\int_{V_m} \mathrm{d}^3\mathbf{r}\, \mathbf{h}\cdot\mathbf{y}\right)^2}}{\sqrt{V_m \int_{V_c} \mathrm{d}^3\mathbf{r}\, |\mathbf{h}|^2}}. \tag{3.101}$$

The filling factor quantifies the proportion of the effective magnetic field perpendicular to the static magnetic field within the volume of the magnetic material V_m, relative to the total field within the entire volume of the cavity V_c. Regarding the coupling phase, it

varies depending on the direction of the magnetic field and is expressed as:

$$\phi = \arg\left[\int_{V_m} \mathrm{d}^3\mathbf{r}\, \mathbf{h}\cdot\mathbf{x} + i\int_{V_m} \mathrm{d}^3\mathbf{r}\, \mathbf{h}\cdot\mathbf{y}\right]. \tag{3.102}$$

When dealing with a single cavity mode in one-tone driving, the coupling phase does not exert any influence. Consequently, the polariton frequencies adhere to those of the Dicke model in Eq. (3.45) without applying the RWA or align with the Tavis-Cummings model's frequencies when the RWA is implemented, as outlined in Eq. (3.36).

Appendix of Chapter 3

To demonstrate orthogonality, we start with the wave equation for $\mathbf{U}k(\mathbf{r})$ in Eq. (3.6). Multiplying both sides by $\mathbf{U}_{k'}(\mathbf{r})$ and integrating across the entire cavity volume yields:

$$\int \mathrm{d}^3\mathbf{r}\, \mathbf{U}_{k'}(\mathbf{r}) \cdot \nabla^2 \mathbf{U}_k(\mathbf{r}) = \frac{\omega_k^2}{c^2} \int \mathrm{d}^3\mathbf{r}\, \varepsilon_\mathrm{r}(\mathbf{r}) \mathbf{U}_{k'}(\mathbf{r}) \cdot \mathbf{U}_k(\mathbf{r}). \tag{3.103}$$

After performing two integrations by parts on the left-hand side[6], we get:

$$\int \mathrm{d}^3\mathbf{r}\, \mathbf{U}_{k'}(\mathbf{r}) \cdot \nabla^2 \mathbf{U}_k(\mathbf{r}) = \int \mathrm{d}^3\mathbf{r}\, (\nabla^2 \mathbf{U}_{k'}(\mathbf{r})) \cdot \mathbf{U}_k(\mathbf{r}), \tag{3.104}$$

Given that the Coulomb gauge applies to $\mathbf{U}_k$, it follows that:

$$\frac{\omega_k^2}{c^2} \int \mathrm{d}^3\mathbf{r}\, \varepsilon_\mathrm{r}(\mathbf{r}) \mathbf{U}_{k'}(\mathbf{r}) \cdot \mathbf{U}_k(\mathbf{r}) = \frac{\omega_{k'}^2}{c^2} \int \mathrm{d}^3\mathbf{r}\, \varepsilon_\mathrm{r}(\mathbf{r}) \mathbf{U}_{k'}(\mathbf{r}) \cdot \mathbf{U}_k(\mathbf{r}) \tag{3.105a}$$

$$\frac{\omega_k^2 - \omega_{k'}^2}{c^2} \int \mathrm{d}^3\mathbf{r}\, \varepsilon_\mathrm{r}(\mathbf{r}) \mathbf{U}_{k'}(\mathbf{r}) \cdot \mathbf{U}_k(\mathbf{r}) = 0 \tag{3.105b}$$

The last equation establishes the orthogonality relation between $\mathbf{U}_k(\mathbf{r})$ and $\mathbf{U}_{k'}(\mathbf{r})$ when $k \neq k'$:

$$\int \mathrm{d}^3\mathbf{r}\, \varepsilon_\mathrm{r}(\mathbf{r}) \mathbf{U}_{k'}(\mathbf{r}) \cdot \mathbf{U}_k(\mathbf{r}) = 0, \qquad \forall k \neq k'. \tag{3.106}$$

It is also assumed that $\mathbf{U}_k(\mathbf{r})$ is normalized throughout the cavity:

$$\int \mathrm{d}^3\mathbf{r}\, \mathbf{U}_k(\mathbf{r}) \cdot \mathbf{U}_k(\mathbf{r}) = 1. \tag{3.107}$$

These two equations enable us to express:

$$\int \mathrm{d}^3\mathbf{r}\, \varepsilon_\mathrm{r}(\mathbf{r}) \mathbf{U}_{k'}(\mathbf{r}) \cdot \mathbf{U}_k(\mathbf{r}) = \varepsilon_{\mathrm{r},k} \delta_{k',k} \tag{3.108}$$

where $\varepsilon_{\mathrm{r},k}$ is the averaged relative permittivity of mode k throughout the cavity.

[6] First integration: $\int \mathrm{d}^3\mathbf{r}\, \mathbf{U}_{k'}(\mathbf{r}) \cdot \nabla^2 \mathbf{U}_k(\mathbf{r}) = \int_\mathrm{surf} d\mathbf{S}\, \mathbf{U}_{k'}(\mathbf{r}) \cdot \nabla \mathbf{U}_k(\mathbf{r}) - \int \mathrm{d}^3\mathbf{r}\, \nabla \mathbf{U}_{k'}(\mathbf{r}) \cdot \nabla \mathbf{U}_k(\mathbf{r})$. Second integration: $\int \mathrm{d}^3\mathbf{r}\, \nabla \mathbf{U}_{k'}(\mathbf{r}) \cdot \nabla \mathbf{U}_k(\mathbf{r}) = \int_\mathrm{surf} d\mathbf{S}\, \nabla \mathbf{U}_{k'}(\mathbf{r}) \cdot \mathbf{U}_k(\mathbf{r}) - \int \mathrm{d}^3\mathbf{r}\, \nabla^2 \mathbf{U}_{k'}(\mathbf{r}) \cdot \mathbf{U}_k(\mathbf{r})$. Note that the surface integrals cancel, using the equalities $\int_\mathrm{surf} d\mathbf{S}\, \mathbf{U}_{k'}(\mathbf{r}) \cdot \nabla \mathbf{U}_k(\mathbf{r}) = -\int_\mathrm{surf} d\mathbf{S}\, \mathbf{U}_k(\mathbf{r}) \nabla \cdot \mathbf{U}_{k'}(\mathbf{r})$ and $\int_\mathrm{surf} d\mathbf{S}\, \nabla \mathbf{U}_{k'}(\mathbf{r}) \cdot \mathbf{U}_k(\mathbf{r}) = -\int_\mathrm{surf} d\mathbf{S}\, (\nabla \cdot \mathbf{U}_k(\mathbf{r})) \mathbf{U}_{k'}(\mathbf{r})$. This cancellation occurs because the modes $\mathbf{U}_k$ are confined within the cavity and vanish at infinity (see [158] p.163), and the divergences are equal to zero due to the Coulomb gauge.

4 Methodology

Abstract

This chapter outlines the various methodological steps employed in the studies. It begins with a discussion of the simulation considerations, including the use of perfect electric conductors for the cavity walls, the mesh grid, and the incorporation of the magnetic properties of the ferrimagnet in both the EigenModes and Frequency Domain solvers. Following this, the chapter covers the different fabrication techniques for the cavity, ranging from traditional machining to 3D plastic printing, including metallization processes. The chapter concludes with an overview of the functionality of the vector network analyzer, the primary instrument used in the measurement campaign, and details the laboratory setup and measurement automation.

Contents

4.1 Simulations

The simulations presented in this thesis were conducted using COMSOL Multiphysics®, specifically employing Finite Element Modeling (FEM). This numerical method is widely utilized to address complex physics problems and to simulate the behavior of physical systems under various conditions. FEM works by dividing the spatial domain of interest into finite elements that form a mesh. Each of these elements is interconnected by nodes, and for each element, differential equations are formulated (in this case, based on the wave equation). These local equations are then assembled into a global matrix equation that represents the entire mesh. Boundary conditions and initial conditions are also incorporated to simulate environmental interactions and initial states. The resulting matrix equation is solved using various numerical techniques, such as iterative or direct methods. FEM is capable of modeling both 2D and 3D systems, with the latter requiring significantly more computational power, memory, and time to solve [159].

In the following subsections, we will focus on the RF module, which simulates electromagnetic phenomena in the radio frequency (RF) domain. This module is particularly useful for designing and simulating RF devices such as antennas, waveguides, filters, integrated circuits, and resonant cavities. The simulations are based on Maxwell's equations and can be solved in either the time domain or the frequency domain. The studies presented in this thesis focus on solving the frequency domain equations, assuming sinusoidal excitations and linear media, leading to the following time-harmonic field representation [160]:

$$\mathbf{E}(x,y,z,t) = \mathbf{E}(x,y,z)e^{i\omega t}, \tag{4.1a}$$

$$\mathbf{H}(x,y,z,t) = \mathbf{H}(x,y,z)e^{i\omega t}. \tag{4.1b}$$

From the Maxwell's equations given in Eq. (2.103) and the relations in Eq. (2.104), where the permittivity tensor $\bar{\boldsymbol{\varepsilon}}$ is complex-valued, we derive the time-independent wave equation for the electric field as follows:

$$\nabla \times (\bar{\boldsymbol{\mu}}^{-1}\nabla \times \mathbf{E}) - \omega^2 \bar{\boldsymbol{\varepsilon}}\mathbf{E} = \mathbf{0}. \tag{4.2}$$

We assume the complex permittivity is expressed as:

$$\bar{\boldsymbol{\varepsilon}} = \varepsilon_0 \left[\bar{\boldsymbol{\varepsilon}}' - i\left(\frac{\bar{\boldsymbol{\sigma}}}{\omega\varepsilon_0} + \bar{\boldsymbol{\varepsilon}}'' \right) \right], \tag{4.3}$$

where the first term in the parentheses represents conduction losses (with $\bar{\boldsymbol{\sigma}}$ being the electrical conductivity), and $\bar{\boldsymbol{\varepsilon}}''$ accounts for dielectric losses. Substituting this into Eq. (4.2), we obtain the reduced wave equation:

$$\nabla \times \bar{\boldsymbol{\mu}}_{\mathrm{r}}^{-1}(\nabla \times \mathbf{E}) - k_0^2 \bar{\boldsymbol{\varepsilon}}'[1 - i\tan(\delta)]\mathbf{E} = \mathbf{0}, \tag{4.4}$$

where the loss tangent $\tan(\delta)$ is defined as:

$$\tan(\delta) = \frac{\dfrac{\bar{\boldsymbol{\sigma}}}{\omega\varepsilon_0} + \bar{\boldsymbol{\varepsilon}}''}{\bar{\boldsymbol{\varepsilon}}}, \tag{4.5}$$

and k_0 is the wave number in a vacuum, given by:

$$k_0 = \frac{\omega}{c_0}, \tag{4.6}$$

with c_0 being the speed of light in a vacuum.

Furthermore, the solutions to these equations are obtained by applying the following boundary conditions between two dielectric media:

$$\hat{\mathbf{n}}_2 \times (\mathbf{E}_1 - \mathbf{E}_2) = \mathbf{0}, \tag{4.7a}$$
$$\hat{\mathbf{n}}_2 \times (\mathbf{H}_1 - \mathbf{H}_2) = \mathbf{J}_\mathrm{s}, \tag{4.7b}$$

where $\mathbf{E}_i$ and $\mathbf{H}_i$ are the electric and magnetic fields in medium i (for $i = 1, 2$), $\hat{\mathbf{n}}_2$ is the outward normal from medium 2, and $\mathbf{J}_\mathrm{s}$ represents the surface current density.

4.1.1 Perfect Electric Conductor

In simulations, all the physics is restricted within a finite volume space. For instance, when simulating a cavity, the boundaries of the cavity also define the boundaries of the simulation space. By default, these boundaries are treated as Perfect Electric Conductors (PEC), which leads to the following boundary conditions:

$$-\hat{\mathbf{n}}_2 \times \mathbf{E}_2 = \mathbf{0}, \tag{4.8a}$$
$$-\hat{\mathbf{n}}_2 \times \mathbf{H}_2 = \mathbf{J}_\mathrm{s}, \tag{4.8b}$$

where the subscript 2 denotes the inner medium in the cavity.

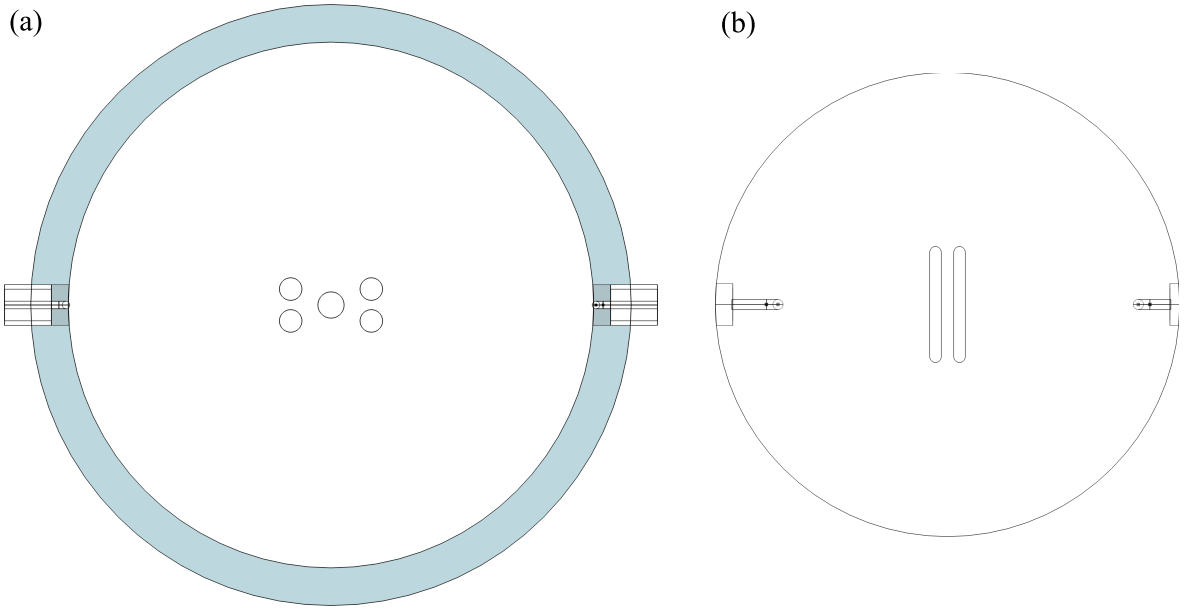

FIGURE 4.1: Sketch of two different cavities: Multi-re-entrant cavity from [161] with modeled copper walls in blue and PEC conditions for the outer cavity boundary; and double re-entrant cavity presented in Chapter 5 with PEC conditions for the inner cavity boundary.

Fig. 4.1 illustrates two different approaches to cavity simulation. In panel (a), the multi-re-entrant cavity discussed in [161] is shown. Here, the cavity walls are modeled as a conductive material (copper with $\sigma = 58.7 \cdot 10^6$ S.m^{-1}), and the outer boundaries are treated as PEC. This setup more accurately reflects real-world conditions by accounting for conductive losses and the effect of probe placement within the cavity wall. However, this approach incurs high computational costs due to the detailed modeling of wall conductivity and probe placement.

In contrast, panel (b) depicts a double re-entrant cavity from the study presented in Chapter 5. In this case, the simulation space boundaries are defined by the inner cavity walls, with the conductive losses of the cavity walls excluded from the model. This simplification significantly reduces computational time while still providing useful insights into the cavity's behavior.

4.1.2 Mesh

An essential aspect of FEM simulations is the mesh, which discretizes the entire system for analysis. A coarser mesh accelerates computation but may lack precision or

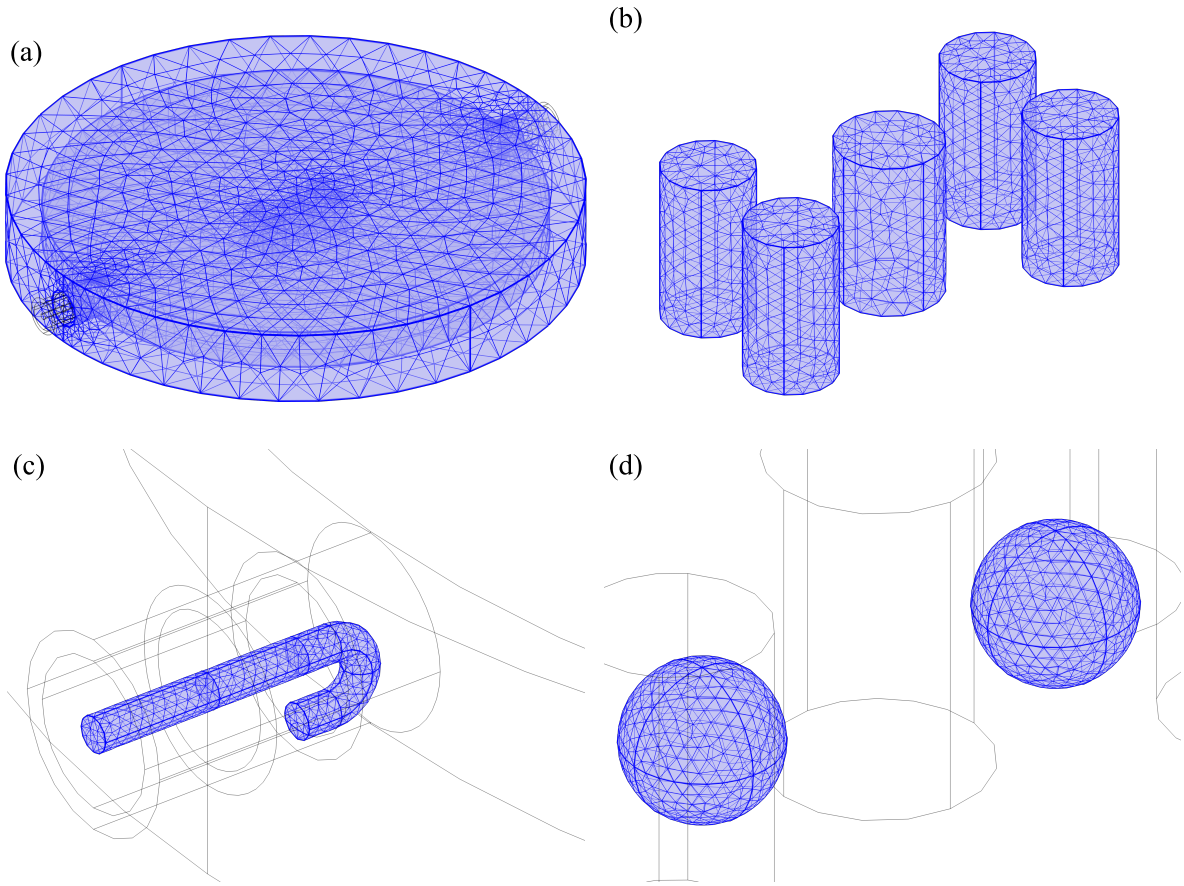

FIGURE 4.2: Illustration of the different meshing strategies for the cavity elements: (a) a *fine* mesh applied to the cavity air and walls; (b) and (c) a *finer* mesh used for the cavity posts and probe elements; and (d) a *extremely fine* mesh dedicated to the YIG elements.

fail to capture important details. Conversely, a finer mesh provides greater accuracy but significantly increases computational time.

To balance accuracy and efficiency, it is crucial to adapt the mesh to different regions of the system. COMSOL Multiphysics® offers a range of predefined mesh sizes, from *extremely coarse* to *extremely fine*, with varying maximum and minimum element sizes, and growth rates.

In the simulations discussed in this thesis, we employed a strategy of using different mesh sizes for different components of the cavity. The aim was to achieve a mesh fine enough to ensure convergence of the results while minimizing computational time. Specifically:

- **Cavity Air and Walls:** The mesh for the air and wall regions was set to *fine*, providing a balance between computational speed and accuracy.
- **Probes and Posts:** For elements involving probes and other components where the boundaries are not modeled as PEC, the mesh was set to *finer* to ensure detailed resolution.
- **YIG Elements:** The YIG slabs or spheres, which are critical for accurate results, were assigned an *extremely fine* mesh.

These mesh calibrations are illustrated in Fig. 4.2, with (a) and (b) showing the mesh for the cavity air and walls, (c) for the posts and probes, and (d) for the YIG elements. This approach ensures that the mesh is adequately refined in regions of interest while optimizing the overall computational efficiency.

4.1.3 EigenModes Simulation

To illustrate this section, we will discuss the simulations presented in [161]. This study highlights the significance of coupling phases in creating synthetic gauge fields in "loop coupled system" as described by Eq. (3.102).

In the appendix of [161], it is presented the design of a cavity that introduces a non-trivial phase shift between two consecutive cavity modes and two magnons, while operating in the strong coupling regime. A non-trivial phase is defined as a total effective phase Φ that deviates from 0 or $\pi/4$ radians and is expressed as:

$$\Phi = \phi_{22} - \phi_{21} - (\phi_{12} - \phi_{11}), \tag{4.9}$$

where ϕ_{ij} denotes the coupling phase between a cavity mode j and a magnon i. For further details on coupling phases and their implications, the reader can refer to [161].

To achieve this, the study involved developing a re-entrant cavity equipped with five posts, which also ensures uniform coupling strength across multiple YIG spheres. This configuration allows precise control over the coupling phases and facilitates the exploration of synthetic gauge field phenomena.

In Eigenmodes (EM) analyses, we seek the complex solutions of the eigenfrequency λ_p, where the time-dependence term of the electric field is expressed as $e^{\lambda_p t}$. The complex eigenfrequency λ_p is written as:

$$\lambda_p = -i\omega_p + \delta_p, \tag{4.10}$$

where ω_p represents the eigenfrequency, and δ_p accounts for the damping.

Eigenmodes (EM) simulations are employed to determine the mode frequencies and its quality factor Q_p for the study presented in Chapter 3. The quality factor is given by:

$$Q_p = \frac{\omega_p}{2|\delta_p|}. \tag{4.11}$$

Here, δ_p represents the total damping in the system. This damping depends on several factors: dielectric losses $\bar{\bar{\varepsilon}}''$ (which are not considered in our studies), conduction losses (as described in Eq. (4.3), considered only when PEC conditions are not applied to the inner cavity walls), and the damping rates associated with the probes γ_{pn}, where p denotes a cavity mode and n the port number, as given in Eq. (3.53). Thus, the quality factor can be rewritten as:

$$Q_p = \frac{\omega_p}{\gamma_p^{\text{int}} + \sum_n \gamma_{pn}}, \tag{4.12}$$

where γ_p^{int} represents the intrinsic losses of the internal mode, encompassing conduction losses, dielectric losses, and magnetic losses when a magnetic material is considered (Gilbert damping in the case of a ferrimagnet). Consequently:

$$|\delta_p| = \frac{1}{2}\left(\gamma_p + \sum_n \gamma_{pn}\right). \tag{4.13}$$

The factor 1/2 accounts for a quasi-closed cavity, as mentioned in Eq. (3.65b). It is important to note that the quality factor Q_p is used exclusively in the study presented in Chapter 6, where the inner cavity walls are considered as PEC and the permittivity of the dielectric and YIG materials are assumed to be purely real (i.e., no losses). Additionally, in EM simulations, the Polder tensor is not considered, implying that YIG is assumed fully saturated ($\mu_\text{r} = 1$), and thus magnetic damping is not accounted for. Consequently, losses are attributed solely to the external damping rates, and the damping term is given by $|\delta_p| = \sum_n \gamma_{pn}/2$.

In all studies presented in this thesis, the filling factor η has been estimated from the EM simulations based on the proportion of the RF magnetic field within the ferrimagnet relative to the entire cavity, as described in Eq. (3.101). The electric and magnetic field solutions from these simulations are phasors, as EM solutions are obtained in the frequency domain and are time-independent. To interpret these phasor solutions in the time domain, we consider the fields at $t = 0$. The real part of the electric field represents its maximum amplitude, since the differential equations are solved for the electric field. The magnetic field, which is $\pi/2$ out of phase with the electric field, has its maximum amplitude represented by the imaginary part.

The filling factor in simulations is described by:

$$\eta = \frac{\sqrt{\left(\int_{V_m} \mathrm{d}^3\mathbf{r}\, \mathcal{I}\{h_x\}\right)^2 + \left(\int_{V_m} \mathrm{d}^3\mathbf{r}\, \mathcal{I}\{h_y\}\right)^2}}{\sqrt{V_m \int_{V_c} \mathrm{d}^3\mathbf{r}\ (\mathcal{I}\{h_x\}^2 + \mathcal{I}\{h_y\}^2 + \mathcal{I}\{h_z\}^2)}}. \tag{4.14}$$

Here, $\mathcal{I}\{h_x\}$, $\mathcal{I}\{h_y\}$, and $\mathcal{I}\{h_z\}$ denote the imaginary parts of the magnetic field components h_y, h_z, and h_x, respectively.

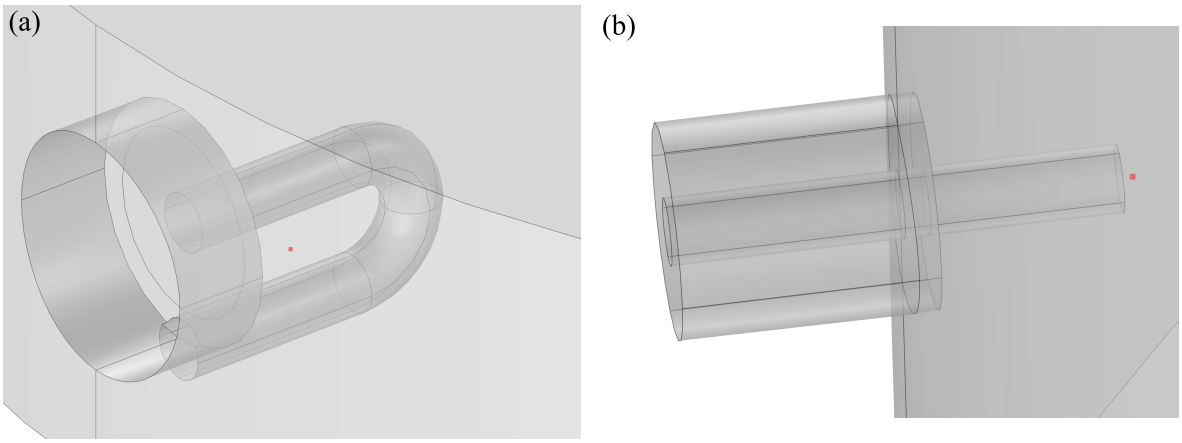

FIGURE 4.3: Sketch of (a) the magnetic probe, and (b) the electric probe. The red marker indicates the *domain point probe* used in COMSOL Multiphysics®. The magnetic field is *probed* along the axis perpendicular to the normal "loop" probe direction, while the electric field is *probed* along the axis of the probe.

In COMSOL Multiphysics®, scalar-valued quantities can be monitored and analyzed using *probes* [162]. These probes allow for detailed examination of various physical quantities throughout the simulation domain. Specifically, domain probes are used to extract the RF magnetic field in any direction and integrate it over the volume of the system's components. This capability facilitates the calculation of coupling strengths and the ratio g/ω using *global variable probes*.

Additionally, the effective coupling phase, as defined in Eq. (4.9), was determined by averaging the RF magnetic fields in each of the YIG spheres. For each eigenmode, the angle of a cavity mode is calculated using the *domain probes* with the formula:

$$\phi_{pn} = \text{atan2}\left[\mathcal{I}(h_y), \mathcal{I}(h_x)\right]. \tag{4.15}$$

This method enabled the design of a cavity that introduces a non-trivial phase between modes, with detailed information about the cavity dimensions and features provided in Appendix 4.A.

For the study in Chapter 6, *domain point probe* were utilized to determine the sign of the RF magnetic field $\mathbf{h}$ at the center of the magnetic probe. This was done along the normal direction to the plane formed by the probe's loop, as shown in Fig. 4.3 (a) by the red maker. Similarly, for an electric probe, the RF electric field E close to the probe along the probe's axis was used to identify the sign, illustrated in Fig. 4.3 (b) by the red maker.

The EM simulations also allow for the extraction of field mappings at various plane coordinates, which are essential for mode analysis in subsequent chapters. For example, Fig. 4.4 shows the norm of the RF magnetic field in a color plot within the (x, y) plane at the z-coordinate of the YIG sphere centers. This visualization provides insights into the spatial distribution of the field for different cavity modes.

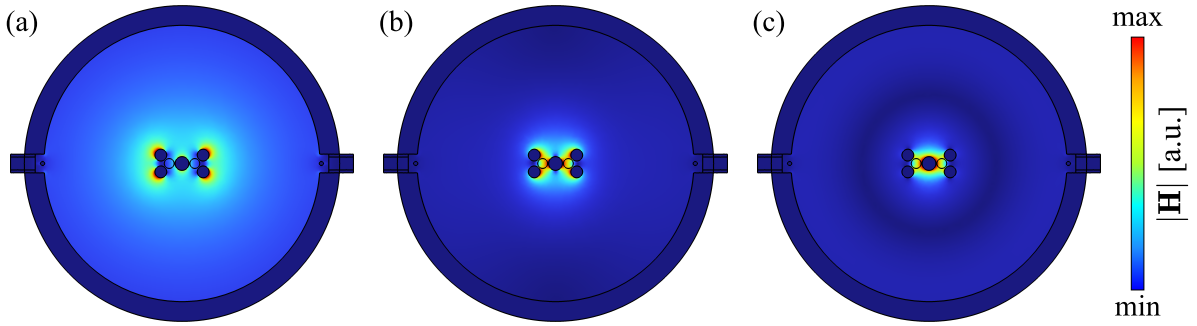

FIGURE 4.4: Representation of the $|\mathbf{H}|$-field of the first three cavity modes in the (x, y) plane at the z-coordinate corresponding to the center of the YIG spheres.

4.1.4 Frequency Domain Simulation

4.1.4.a *S*-parameters

In Frequency Domain (FD) simulations, scattering parameters (S-parameters) are used to characterize the behavior of a system in terms of transmitted and reflected voltage waves at the ports of the cavity. The S-parameters are computed by analyzing the electric field $\mathbf{E}_i$ at the fundamental mode of the i^{th} port and the electric field $\mathbf{E}_\mathrm{c}$ inside the cavity. The ports are typically modeled as matching loads (e.g., 50 Ω as a standard value [163]) to minimize reflections and accurately represent real-world conditions. In this thesis, the ports are assumed to be coaxial cables operating in the Transverse ElectroMagnetic (TEM) mode.

For a coaxial transmission line, the TEM mode is characterized by specific electric and magnetic field distributions. The scalar potential Φ in the coaxial line is given by [163]:

$$\Phi = V_0 \frac{\ln(b/\rho)}{\ln(b/a)}, \tag{4.16}$$

where V_0 is the potential of the inner conductor, a and b are the radii of the inner and outer conductors, respectively. The coordinate system used here is cylindrical with ρ representing the radial direction and θ the azimuthal direction, as depicted in Fig. 4.5. Given the electric field $\mathbf{E}$ can be derived from the gradient of the scalar potential:

$$\mathbf{E} = -\nabla\Phi, \tag{4.17}$$

the components of the electric and magnetic fields are calculated as follows:

$$E_\rho = \frac{V_0}{\rho \ln(b/a)}, \tag{4.18a}$$

$$H_\theta = \frac{V_0}{\rho Z \ln(b/a)}, \tag{4.18b}$$

where Z is the characteristic impedance of the coaxial line. The other components of the electric and magnetic fields are zero. In the coaxial line, the electric field is oriented along the radial axis ρ and the magnetic field is oriented along the azimuthal axis θ, as shown in Fig. 4.5 (a) and (b) from the COMSOL Multiphysics® simulation.

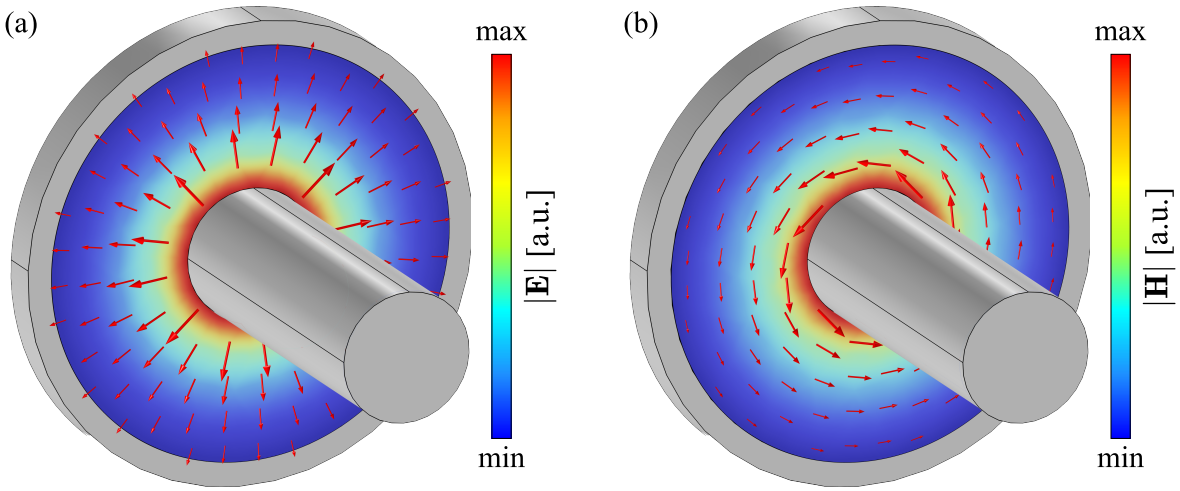

FIGURE 4.5: Sketch of the simulated (a) electric field, and (b) magnetic field of the TEM mode in a coaxial line.

In simulations, ensuring that the electric fields at the port boundaries match in terms of their power is crucial for accurate analysis of S-parameters. The Poynting vector, which represents the power flow in an electromagnetic field, is used to compute the power at the port boundary. The power P at a port boundary surface area Ω is given by:

$$P = \int_{\Omega} \mathrm{d}\Omega\, \hat{\mathbf{n}} \cdot \mathbf{S} = \frac{1}{2} \int_{\Omega} \mathrm{d}\Omega\, \hat{\mathbf{n}} \cdot \mathcal{R}\{\mathbf{E} \times \mathbf{H}^*\}, \tag{4.19}$$

where $\hat{\mathbf{n}}$ is the normal vector to the surface Ω.

For a TEM mode, the magnetic field $\mathbf{H}$ can be expressed as [163]:

$$\mathbf{H} = \frac{1}{Z_{\mathrm{TEM}}} (\hat{\mathbf{n}} \times \mathbf{E}), \tag{4.20}$$

where Z_{TEM} is the impedance of the TEM wave, given by [163]:

$$Z_{\mathrm{TEM}} = \sqrt{\frac{\mu}{\varepsilon}}. \tag{4.21}$$

Substituting Eq. (4.20) into Eq. (4.19), the total power at the port boundary becomes:

$$P = \frac{1}{2Z_{\mathrm{TEM}}} \int_{\Omega} \mathrm{d}\Omega\, |\mathbf{E}|^2 \tag{4.22}$$

In the cavity, the electric field at the port boundary is the sum of the incoming wave (if the port is excited) and the transmitted or reflected waves. The power at these boundaries must be consistent with the port modes, which represent their excitations. Therefore, the equality of power at the boundary can be expressed as:

$$\delta_{ij} \frac{1}{2Z_{\mathrm{TEM}}} \int_{\Omega_i} \mathrm{d}\Omega_i\, \mathcal{R}\{\mathbf{E}_j \cdot \mathbf{E}_i^*\} = \frac{1}{2Z_{\mathrm{TEM}}} \int_{\Omega_i} \mathrm{d}\Omega_i\, \mathcal{R}\{\mathbf{E}_{\mathrm{c}} \cdot \mathbf{E}_i^*\} - \frac{1}{2Z_{\mathrm{TEM}}} \int_{\Omega_i} \mathrm{d}\Omega_i\, \mathcal{R}\{S_{ij}\mathbf{E}_i \cdot \mathbf{E}_i^*\}. \tag{4.23}$$

Here, Ω_i represents the surface area of the i^{th} port boundary. The term on the left-hand side represents the power of the excited port, where δ_{ij} is the Kronecker delta indicating orthogonality between port modes when $i \neq j$. The first term on the right-hand side accounts for the coupling between the electric fields of the port mode and the cavity at the port boundary, while the last term represents the power associated with the transmitted or reflected port mode.

From Eq. (4.23), the S-parameters can be derived as:

$$S_{ij} = \frac{\int_{\Omega_i} \mathrm{d}\Omega_i \ (\mathbf{E}_\mathrm{c} - \delta_{ij}\mathbf{E}_j) \cdot \mathbf{E}_i^*}{\int_{\Omega_i} \mathrm{d}\Omega_i \, \mathbf{E}_i \cdot \mathbf{E}_i^*} \tag{4.24}$$

When the S-parameters are defined in decibels (dB), the convention used is:

$$|S_{ij}|(\mathrm{dB}) = 10\log(|S_{ij}|^2) = 20\log(|S_{ij}|). \tag{4.25}$$

This dB representation is employed in this thesis as well.

4.1.4.b Physics convention

COMSOL Multiphysics® is a versatile tool for simulating electromagnetic fields based on solving Maxwell's equations. However, it does not directly support micromagnetic simulations, which are essential for accurately modeling phenomena such as photon-magnon coupling in magnetic materials. To address this limitation when simulating photon-magnon coupling in a ferrimagnetic domain, a workaround involves incorporating the demagnetizing field into the applied static magnetic field.

When a static magnetic field H_0 along the z-axis, the total static magnetic field H_tot within the ferrimagnetic domain is affected by the demagnetizing field. Considering Eq. (2.117b), this total static magnetic field is given by:

$$H_\mathrm{tot} = H_0 - N_{zz}M_\mathrm{s}, \tag{4.26}$$

where N_{zz} is the demagnetizing factor along the z-axis. For different geometries, this factor takes specific forms, and is defined by Eq. (2.121) for a sphere, and by Eq. (2.123) for a slab.

In the software, the magnetic dynamics of a YIG material is represented using the permeability tensor $\bar{\boldsymbol{\mu}}$. When dealing with electromagnetic waves in COMSOL Multiphysics®, the time dependence is conventionally expressed as $e^{i\omega t}$, as defined in Eq. (4.1). However, in condensed matter physics, and throughout this thesis, the convention is $e^{-i\omega t}$. This difference in sign convention affects the formulation of the permeability tensor. Following a similar derivation as in Sec. 2.3.2.a , but adapting it to software's convention, the permeability tensor $\bar{\boldsymbol{\mu}}$ given in Eq. (2.102b) becomes:

$$\mathbf{b} = \bar{\boldsymbol{\mu}} \cdot \mathbf{h}, \tag{4.27a}$$

$$\bar{\boldsymbol{\mu}} = \mu_0(1 + \bar{\boldsymbol{\chi}}) = \mu_0 \begin{bmatrix} 1+\chi & i\kappa & 0 \\ -i\kappa & 1+\chi & 0 \\ 0 & 0 & 1 \end{bmatrix}. \tag{4.27b}$$

Here, the components χ and κ are defined similarly to the expressions in Eq. (2.101b) and (2.101b), at the exception that $\tilde{\omega}_0 = \omega_0 + i\alpha\omega$.

In Chapter 6, the phases obtained from the input-output model are compared to those derived from FD simulations. Due to the differences in conventions, the transmission phases and the smooth phase transitions observed at resonances or antiresonances are inverted between the two approaches. This inversion results from the time-dependent term of the solution, which, in the context of the Schrödinger equation, is expressed as $e^{-i\omega t}$ (as derived in [164] on p.38-39). This convention is crucial for maintaining a positive frequency in the system.

To align with the software's convention, where the time-dependence is expressed as $e^{i\omega t}$, it is necessary to change the sign of one of the terms in the Schrödinger equation. After making this adjustment, the time derivative of an operator $\hat{\mathcal{A}}$ in the Heisenberg picture is expressed as:

$$\partial_t \hat{\mathcal{A}} = \frac{i}{\hbar}[\hat{\mathcal{A}}, \hat{\mathcal{H}}]. \tag{4.28}$$

This expression is derived similarly to the conventional quantum mechanics approach, as demonstrated [99] on p.321-322. This consistency in phase convention is crucial when comparing the results from quantum models with those from simulations.

Based on the adjustments for the phase convention, the S-matrix for a quasi-closed cavity is now expressed as:

$$\mathbf{S} = \mathbb{1} + i\mathbf{K}^{\mathrm{t}} \cdot \mathbf{\Omega}^{-1} \cdot \mathbf{K}^{*}, \tag{4.29}$$

The components of the matrix $\mathbf{\Omega}$, which were initially defined in Eq. (3.65b), must also be rewritten as:

$$\Omega_{qp} = (\omega - \tilde{\omega}_p)\delta_{qp} - \frac{i}{2}\sum_n (\kappa^*_{pn}\kappa_{qn}) - g_{qp}. \tag{4.30}$$

Additionally, the complex frequency of the p^{th} internal mode is given by $\tilde{\omega}_p = \omega_p + i\gamma_p^{\mathrm{int}}/2$. The derivation of the input-output model for a quasi-closed cavity under the software convention is detailed in Appendix 4.B. To illustrate this, consider a system comprising a single cavity mode with positive external coupling phases at two probes. In both conventions, we introduce the complex frequency of the cavity mode as $\tilde{\omega}_p = \omega_p - i\gamma_p^{\mathrm{int}}/2$. The transmission in the two conventions is then expressed as follows:

$$S_{21} = -i\frac{\sqrt{\gamma_{00}\gamma_{01}}}{\omega - \omega_0 + \frac{i}{2}(\gamma_{00} + \gamma_{01} + \gamma_0^{\mathrm{int}})}, \tag{4.31a}$$

$$S_{21}^{\mathrm{soft}} = i\frac{\sqrt{\gamma_{00}\gamma_{01}}}{\omega - \omega_0 - \frac{i}{2}(\gamma_{00} + \gamma_{01} - \gamma_0^{\mathrm{int}})}, \tag{4.31b}$$

where ω_0 denotes the cavity mode frequency, γ_{00} and γ_{01} represent the dissipation loss rates at the two probes. In Eq. (4.31a), γ_0^{int} corresponds to the intrinsic loss rate of the cavity mode and shares the same sign as the other dissipation rates. However, in Eq. (4.31b), the sign of γ_0^{int} is opposed to that of the dissipation rates, indicating a gain in the COMSOL convention.

In Fig. 4.6 (a), we illustrate the transmission magnitude for a cavity mode with $\omega_0 = 5$

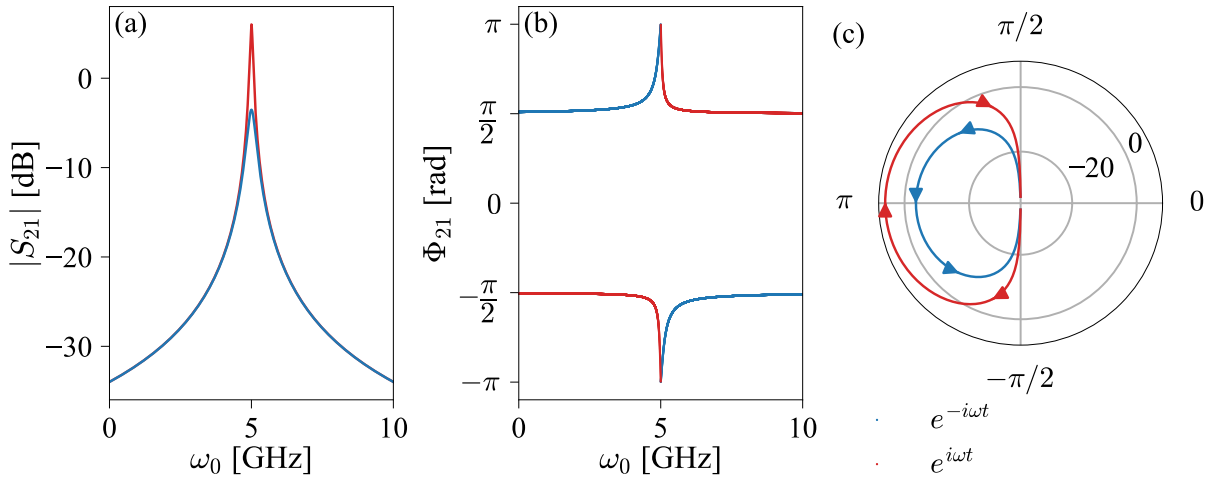

FIGURE 4.6: Modeled transmission of a single cavity mode using the input-output formalism with two conventions: $e^{-i\omega t}$ shown in blue and $e^{i\omega t}$ shown in red, with intrinsic loss rates treated as negative in both models. The transmission magnitude is presented in (a), the phase in (b), and the phase trajectories in a polar representation in (c).

GHz, $\gamma_{00} = \gamma_{01} = \gamma_0^{\text{int}} = 0.1$. To emphasize the importance of the sign convention in the imaginary part, the transmission calculated using the input-output model from Eq. (4.31a) is shown in blue. Here, the minus sign of the complex cavity frequency effectively represents a loss, as indicated by the fact that the transmission at the resonance frequency does not reach 0 dB. Conversely, the transmission obtained following the simulation convention described in Eq. (4.31b) is depicted in red. In this case, the minus sign for the imaginary part of the complex cavity frequency corresponds to a gain, resulting in the transmission at the resonance frequency exceeding 0 dB. This highlights that in COMSOL Multiphysics®, special attention must be paid to the signs of the imaginary parts when incorporating losses, as it directly impacts the interpretation of the simulation results.

The phases corresponding to these transmissions are given by:

$$\Phi_{21} = \tan2^{-1}\left[-2(\omega-\omega_0), -(\gamma_{00}+\gamma_{01}+\gamma_0^{\text{int}})\right], \tag{4.32a}$$

$$\Phi_{21}^{\text{soft}} = \tan2^{-1}\left[2(\omega-\omega_0), -(\gamma_{00}+\gamma_{01}-\gamma_0^{\text{int}})\right]. \tag{4.32b}$$

Here, the $\tan2^{-1}$ function is used, which correctly accounts for the signs of both the real and imaginary components of S_{21} to yield the correct phase.

In Fig. 4.6 (b), the transmission phases corresponding to the two conventions are shown in blue and red, as defined by Eq. (4.32a) and (4.32b), respectively. The figure illustrates that the phases before and after the resonance are inverted between the two conventions. Additionally, both conventions show a phase jump at the resonance passing through the value π. However, the phase trajectory exhibits a counter-clockwise (CCW) behavior for the $e^{-i\omega t}$ convention, while it shows a clockwise (CW) behavior for the software convention, as depicted in Fig. 4.6 (c).

In the following analysis, we compare the magnitude and phase transmission obtained from a FD simulation with those derived from the input-output model under both phase

conventions. The FD simulations were conducted on a double re-entrant cavity loaded with a dielectric slab, as detailed in Sec. 6.7, with the corresponding magnitude and phase transmission shown in Fig. 6.9.

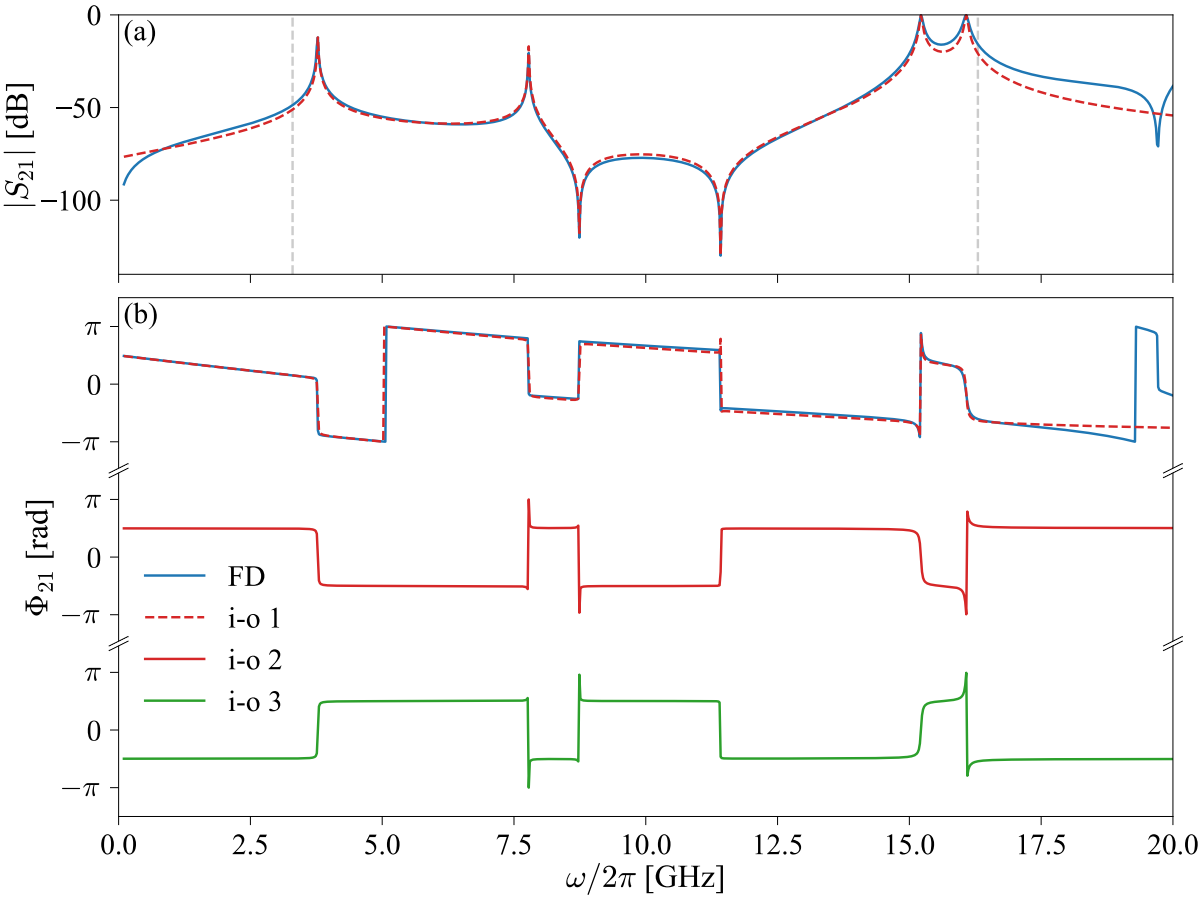

FIGURE 4.7: FD simulations are shown in solid blue lines and compared to the input-output model in red for a double re-entrant cavity loaded with a dielectric slab. The magnitude of the transmission is presented in (a), and the phases in (b). The dashed and solid red lines correspond to the input-output model using two software conventions, denoted as "i-o 1" and "i-o 2", with the exception that a phase $\Phi = \alpha\omega + \beta\omega^2$ is added to the S-parameter for "i-o 1". The green solid line, labeled "i-o 3", represents the modeled phase using the $e^{-i\omega t}$ convention.

By fitting the dissipation rates at the two probes for four different cavity modes, as well as the intrinsic losses, both phase conventions accurately reproduce the simulated transmission. This is demonstrated in Fig. 4.7 (a), where the FD simulation results are shown by the solid blue line, and the modeled transmission is represented by the dashed red line.

Fig. 4.7 (b) illustrates the phase comparison: the simulated phase is depicted in blue, the phase modeled using the software convention in red (labeled "i-o 2"), and the phase modeled with the $e^{-i\omega t}$ convention in green (labeled "i-o 3"). The dashed red line (labeled "i-o 1") represents the input-output model using the software convention with an additional polynomial phase term, $\Phi = \alpha\omega + \beta\omega^2$, where α and β are fitted parameters, to better match the simulated phase. This polynomial phase correction accounts for phase variations not captured by the standard input-output model but does not alter the underlying physics.

Notably, when examining the phase at $\omega \simeq 0$, where the added phase term equals zero, the input-output model derived using the software convention aligns with the FD simulations, while the phase is inverted for the $e^{-i\omega t}$ convention. Additionally, the smooth phase jumps observed in the software convention exhibit the same trajectory as those in the FD simulations, in contrast to the trajectory in the $e^{-i\omega t}$ convention, which is opposed.

Therefore, in chapter 6, the input-output model is utilized with the same convention as COMSOL Multiphysics® to ensure that the phase calculations are consistent across with simulations.

4.2 Cavity Conception

4.2.1 Design

Once the cavity optimized with simulations software, and before fabrication, the cavity must be modelized with a computer aided design (CAD) software. In this thesis, the cavities were designed on SolidWorks CAD 3D®.

The conception of the cavity has to respond to two constraints: The cavity has to be adapted to the utilized SMA connector in measurement, where the data sheet is given in Appendix 4.C. As depicted in Fig. 4.8 (a), the cavity is mounted of two rectangular symmetrical pieces of both sides of the cavity. A central hole enables to pass the probe

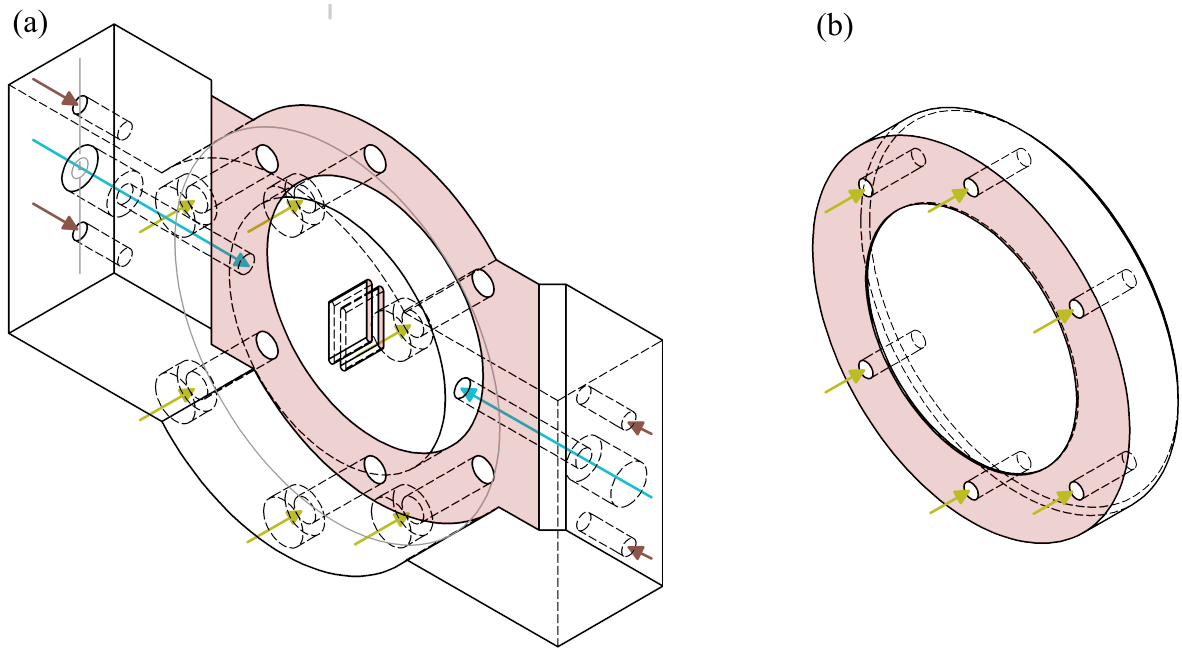

FIGURE 4.8: Design of the double reentrant cavity (presented in Chapter 5) on SolidWorks CAD 3D®. Blue arrows present the probed insertions in the cavity holes, and brown arrows the hole for the screws to maintain probes. Green arrows represent holes to assemble (a) the base of the cavity and (b) the lid of the cavity. Red areas represent the same plane height once the cavity assembled.

throughout the cavity after fabrication (represented by blue arrows), and are maintained by two screws, where insertions are represented by brown arrows.

A second design requirement was to create a cavity capable of adjusting the distance between the tops of the posts and the top of the cavity (see Chapter 5 for more details). It has been chosen that the cavity would be divided into two distinct pieces: the base of the cavity, referred in Fig. 4.8 (a); and the lid of the cavity, referred in Fig. 4.8 (b). These two pieces are assembled with six screws, and represented by green arrows. From this, top of the posts and the top of the base of the cavity are at the same plane height (represented by red areas). When assembled with the lid, the distance between the top of the posts and the top of the lid in the cavity are determined by the extrusion on the lid (the blank area in the center of the red area). Different cavity lid with different extrusion height were fabricated for the study in Chapter 5.

4.2.2 Fabrication

Two methods were employed for the fabrication of the cavities. One is the 3D printing, making possible to create some complex cavity design at least cost, but with weak accuracy. The second one is the aluminum or copper machining with higher accuracy. However, the second method is more expensive and does not enable to fabricate the more complex cavities. The double re-entrant cavity has been machined by Protolabs 3D Hubs®. This cavity is made of aluminum and presents a surface roughness of 3.2 µm. The cylindrical cavity from [95] and presented in Chapter 6 has been machined at IMT Atlantique. The machining tool used is the Hurco VM10i®, which offers a positioning accuracy of 10 µm. It should be noted that the cavity discussed in Sec. 5.6.0.b will soon be machined using this equipment. In Fig. 4.9 is presented the double reentrante cavity fabricated by both methods, were the printed cavity is shown in Fig. 4.9 (a), and metalized in (b), and the machined cavity is illustrated in Fig. 4.9 (c).

The 3D printing is elaborated with a Form 3B+® utilizing a liquid based process, named stereolithography (SLA). This process uses a liquid photopolymer resin, which is a light-sensitive material that hardens when exposed to ultraviolet (UV) light, of 405 nm. This resin is placed in a vat. The object is fabricated on the plate of a build platform which can displace on the vertical z-axis. A laser beam with a beam size of 85 µm, guided

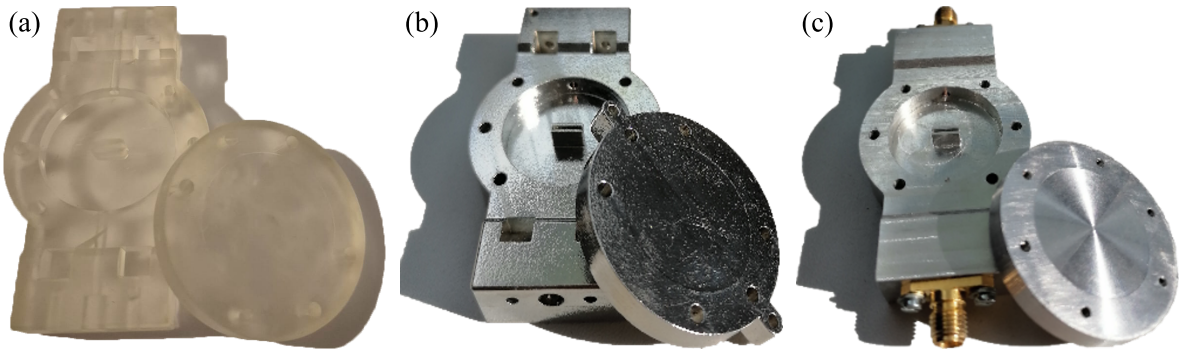

FIGURE 4.9: Rendering of the double reentrante cavity after (a) 3D printing, (b) metallization, and (c) machining.

by a set of mirrors (named as galvanometer), selectively cures the resin by tracing a cross-sectional layer of the desired object on the surface of the liquid. The displacement on the (x, y) plane is of 25 µm. After one layer is cured, the build platform uppers by a small increment of 25 µm, to allow for the next layer of liquid resin to be exposed and cured. This process repeats, building the object layer by layer from the bottom up. Once the printing is complete, the object is washed with alcohol isopropyl (IPA) to remove excess resin. An additional curing in a UV oven to ensure full polymerization and enhance mechanical properties. The utilized resin is the High Temp Resin® from FormLabs® being highly resistant. This resin enables that the weak structure, such as posts in reentrante cavities, does not flex during fabrication. The cavities fabricated with this resin were post-polymerized in a UV bath at 60°C during 60 minutes.

A preliminary surface treatment of a plastic material is essential to ensure the chemical and mechanical compatibility of the metallization layer to be deposited (see Fig. 4.10 (a)). The most commonly used techniques for 3D metallization are mechanical and chemical treatments. Mechanical treatment significantly increases surface roughness by creating micro-cavities, typically through high-pressure sandblasting [165]. While this method can be applied to various geometries (from 2D to 3D), the resulting metallization quality is often suboptimal due to the high initial roughness. Additionally, the directional nature of sandblasting makes it challenging to reach certain areas of the structure. The most effective method for surface preparation is a chemical treatment using chromic acid [166]. This technique is widely adopted at the industrial scale because it simultaneously creates both chemical and mechanical affinity (through increased roughness) between the substrate and the deposited metal. Moreover, since the process is conducted in immersion, it can be applied to all geometries, including the most complex ones, ensuring comprehensive surface modification.

Following surface modification using one of the two techniques described above, the next step is to activate the surface. The most common method involves incorporating palladium (Pd) nanoparticles onto the plastic surface, as depicted in Fig. 4.10 (b). The activation process occurs in two steps [167]. First, the surface is immersed in a solution of tin chloride ($SnCl_2$), where the tin ions Sn^{2+} is adsorbed by the substrate S, as shown in Eq. (4.33a). This step is followed by immersion in a solution of palladium chloride ($PdCl_2$). During immersion, the tin is completely removed from the surface as shown in Eq. (4.33b), and the amount of Pd deposited corresponds exactly to the quantity of oxidized tin. As a result of this reaction, nanometric particles ranging from 1 to 4 nm are dispersed across the substrate surface. These Pd particles serve as catalytic sites for

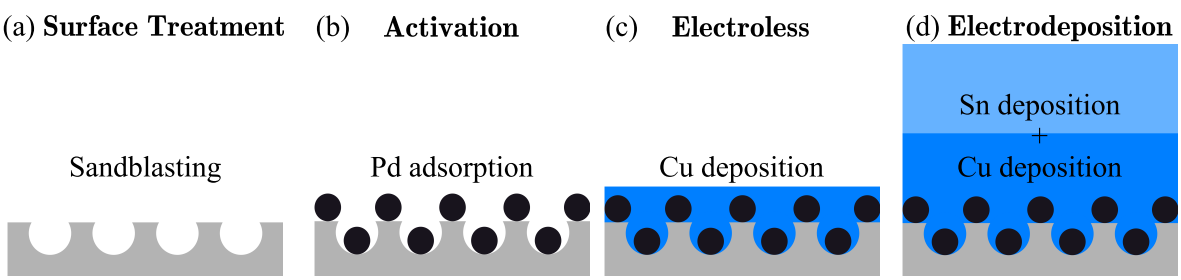

FIGURE 4.10: Metallization steps of a 3D printed cavity.

the subsequent electroless deposition process (or autocatalytic deposition), which occurs without an external electron source.

$$S + Sn_{sol}{}^{2+} \longrightarrow S \cdot Sn_{ads}{}^{2+} \tag{4.33a}$$

$$S \cdot Sn_{ads}{}^{2+} + Pd_{sol}{}^{2+} \longrightarrow S \cdot Pd_{ads} + Sn_{sol}{}^{4+} \tag{4.33b}$$

The distinctive feature of autocatalytic deposition is its ability to metallize electrically insulating surfaces. The mechanism of autocatalytic deposition can be understood through the fundamental principles of electrochemical deposition [167, 168]. As the name suggests, electroless deposition is a chemical process that does not require electrodes, meaning no external electric current is supplied, as sketched in Fig. 4.11 (a). Nevertheless, the insulating surface to be metallized, which contains the catalyst, will subsequently be referred to as the electrode. Without activation, i.e. without the catalyst, metallization cannot begin. The solution contains metal in ionic form, $M_{sol}{}^{Z+}$ (such as copper ions, Cu^{2+}), and a reducing agent Red_{sol}. The overall reaction of the autocatalytic bath can be described as follows:

$$M_{sol}{}^{Z+} + Red_{sol} \xrightarrow{\text{catalytic surface}} M_{lat} + Ox_{sol}, \tag{4.34}$$

where Ox_{sol} represents the oxidation product of the reducing agent. This reaction occurs exclusively on the activated surface due to the presence of Pd nanoparticles, which act as the catalyst. The metal initially present in the solution is then deposited onto the surface of the substrate, referred to as M_{lat}, as illustrated in Fig. 4.10 (c). Additionally, the solution contains stabilizers that help maintain a relatively constant pH and stabilize the reaction, preventing the metallic ions in the solution from reducing and forming metal

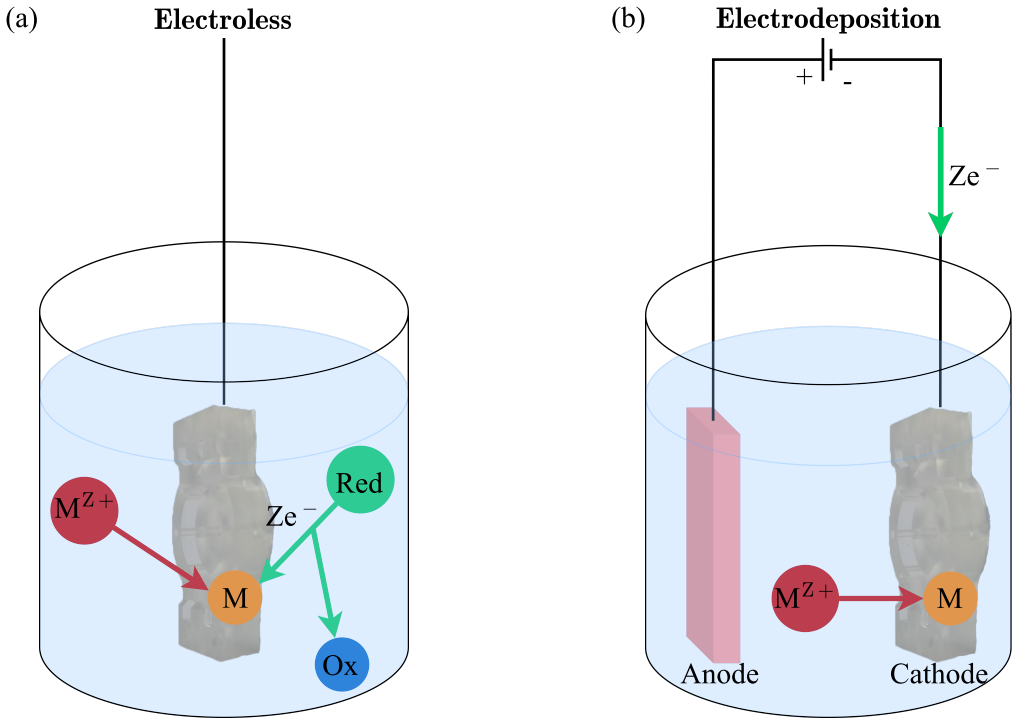

FIGURE 4.11: Sketch of (a) the electroless and (b) the electrodeposition techniques.

precipitates. Consequently, the reaction concludes spontaneously once the metal layer on the substrate reaches approximately 3 µm in thickness [169].

After the electroless plating stage, the metallic layer is further thickened using electrodeposition [170] (see Fig. 4.10 (d)). Electrodeposition involves the chemical deposition of metal onto a conductive substrate (the cathode) through an electric current. The procedure, illustrated in Fig. 4.11 (b), involves applying a current between the anode and a cathode, both immersed in an electrolyte solution containing the metal to be deposited in ionic form (M^{Z+}):

$$M_{sol}{}^{Z+} + Ze^{-} \xrightarrow{\text{electrode}} M_{lat}. \tag{4.35}$$

This equation describes the reaction that occurs once electrons (Ze^{-}) are supplied by the external power source. When the current is inactive, the reaction ceases. The process is divided into two stages: the first stage increases the copper layer thickness to 5–10 µm, while the second stage deposits an additional 8 µm of tin to ensure high electrical conductivity [169]. The final metallic layer deposited on each cavity has a total thickness of 16–21 µm, which corresponds to at least seven skin depths[1], at 1 GHz [171].

The metallization of the cavities was subcontracted to Elliptika®, a company based in Brest, France, specializing in the design and development of RF and microwave products and solutions. The mechanical approach described above for surface pretreatment was employed in the fabrication of the cavities presented in this thesis.

The YIG slab and spheres were fabricated by Ferrisphere, Inc®, a company specialized in YIG fabrication. As mentioned in [172], the sharpness of the magnetic resonance linewidth of the YIG spheres depends on their surface roughness, meaning that the YIG material needs to be polished. Here, we outline the procedure for YIG sphere polishing.

Initially, YIG is produced as large single-crystal YIG cylinders, measuring a few centimeters in length and a few millimeters in diameter. The cylinder is then cut into

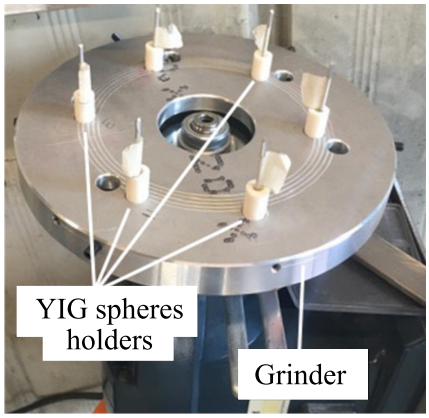

FIGURE 4.12: Grinder used to polish YIG spheres, with permission from [172].

cubes, which are subsequently ground to form spheres. The grinding process involves mounting a sandpaper sheet onto a rotating grinder plate, which operates at a high

[1]The skin depth determines, in first approximation, the width of the region where the current is concentrated within a conductor. It is used to calculate the effective resistance at a given frequency and is given by [163]: $\delta = \sqrt{2/(\omega\mu\sigma)}$.

frequency. The YIG cubes are placed in a holder (as shown in Fig. 4.12), allowing them to be abraded into spherical shapes. Throughout the process, different grades of sandpaper are used, progressing from coarser to finer grains to achieve the desired polished finish.

4.3 Experimental Setup

4.3.1 Vector Network Analyser

The Vector Network Analyzer (VNA) is the primary instrument used in our measurements, enabling us to probe the physical properties of the device under test (DUT). The VNA computes the scattering parameters (S-parameters) by measuring the reflected and transmitted voltage waves at each port. Let V_i^+ denote the amplitude of the incident voltage wave at port i, and V_j^- denotes the amplitude of the transmitted or reflected voltage wave at port j. The S-parameters are defined as:

$$S_{ij} = \left.\frac{V_i^-}{V_j^+}\right|_{V_k^+=0 \ \forall \ k\neq j} . \tag{4.36}$$

To better understand the systematic errors inherent to the VNA and characterize its performance, we outline its operation. Although various VNA architectures exist, we focus on the architecture of the two-port R&S® ZNB40 from Rohde & Schwarz®. , used in our laboratory. Each port of the VNA shares the same structure, which consists of three key components: the RF signal source, the reference block, and the test block, as depicted in Fig. 4.13.

The VNA source is tunable in both RF frequency and power. In our measurements, only the RF frequency is swept. A switch positioned after the source allows automatic selection of the port to be excited, enabling sequential measurement of S_{11}, S_{21}, S_{22}, and S_{12}.

Both the reference and test blocks consist of a directional coupler and a receiver. In the reference block, the coupler directs a small portion of the forward wave to the receiver while allowing the majority to propagate toward the DUT. Conversely, in the test block, the coupler is arranged to direct the backward wave toward the receiver, while allowing the forward wave to continue toward the DUT. Thus, the couplers in the reference and test blocks are mounted inversely, as depicted in Fig. 4.13. For each coupler, we define the incident wave as the wave to be diverted (the forward wave in the reference block and the backward wave in the test block), and the reverse wave as the wave that passes through.

However, couplers are not ideal and introduce losses within the VNA. A key characteristic is the coupler's directivity, which quantifies the error introduced by reverse waves passing through the coupling device. The following terms describe the various losses contributing to the directivity error [173]:

- **Insertion loss**: This loss represents the attenuation of waves passing through the coupler. It is expressed as:

$$\text{Insertion Loss (dB)} = -10\log_{10}\left(\frac{\text{output power}}{\text{input power}}\right), \tag{4.37}$$

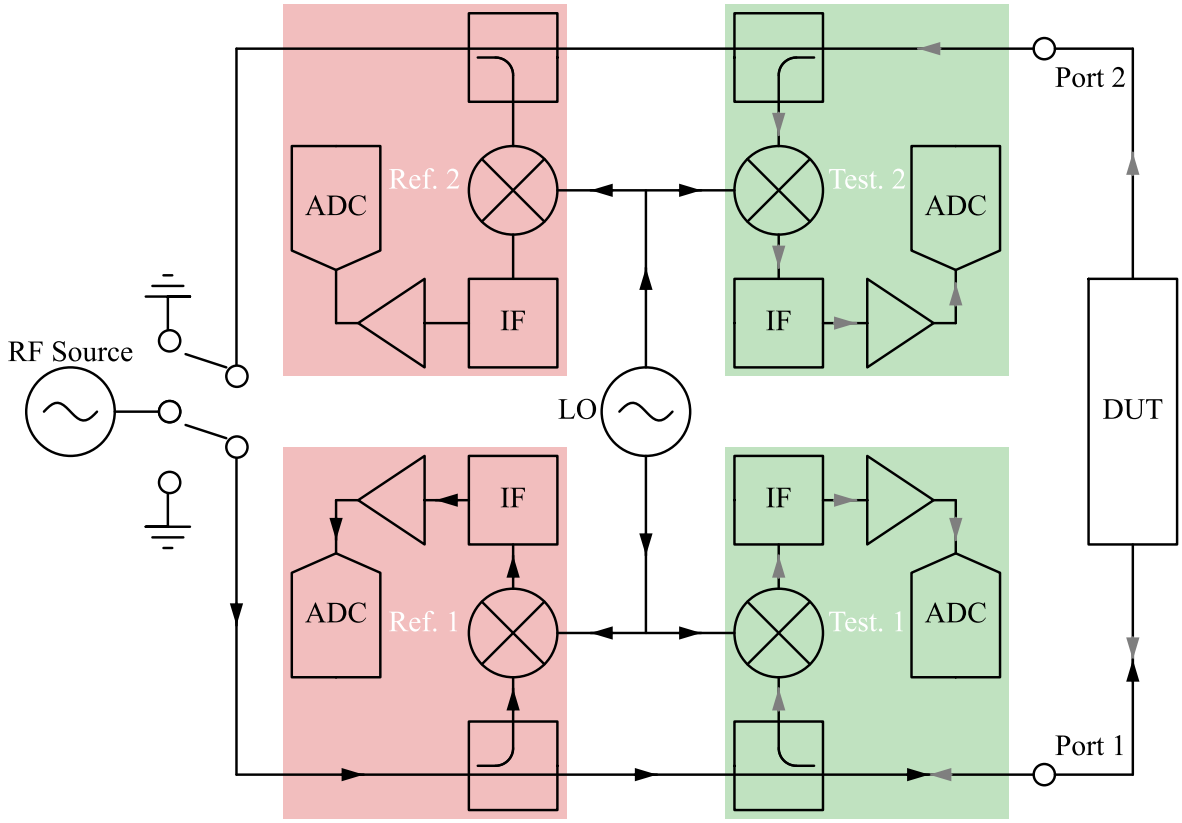

FIGURE 4.13: Vector Network Analyzer block diagram.

where lower insertion loss corresponds to less signal attenuation. Typically, insertion loss is about 1 dB.

- **Coupling Factor**: This describes the fraction of the incident wave that is coupled. The uncoupled portion is effectively lost. It is given by:

$$\text{Coupling Factor (dB)} = -10 \log_{10} \left(\frac{\text{incident coupled power}}{\text{incident power}} \right), \tag{4.38}$$

where a higher coupled power results in a lower coupling factor. The typical coupling factor ranges from 10 to 20 dB.

- **Isolation**: Ideally, no reverse wave should be coupled, but in practice, some reverse waves are coupled, leading to errors. Isolation is expressed as:

$$\text{Isolation (dB)} = -10 \log_{10} \left(\frac{\text{reverse coupled power}}{\text{reverse power}} \right), \tag{4.39}$$

where better isolation (higher dB) indicates fewer errors. Accurate VNAs typically require a minimum isolation of 30 dB.

- **Directivity**: This metric characterizes the ability of the VNA to distinguish between incident and reverse waves within the coupler. It is given by:

$$\text{Directivity (dB)} = \text{Isolation (dB)} - \text{Coupling Factor (dB)} - \text{Insertion Loss (dB)}, \tag{4.40}$$

  Higher directivity indicates lower measurement errors.

Due to the broad frequency range of a VNA, implementing a receiver capable of detecting all frequencies directly would be both expensive and space-prohibitive, as it would require specialized electronics for each frequency band. Instead, a more efficient approach is employed using a heterodyne downconversion receiver. In this method, all frequencies are downconverted to a fixed Intermediate Frequency (IF), allowing the receiver to be optimized for this single frequency. This is achieved through the use of a tunable local oscillator (LO) that adjusts its frequency to match the RF signal. When the incident wave and LO are mixed, two new frequencies are produced: the sum and difference of the two input frequencies. Since lower-frequency electronics are more cost-effective, a filter is used to retain only the difference frequency, which corresponds to the IF. This filter has a defined bandwidth, known as the IF bandwidth (IFBW).

Moreover, to avoid the high cost associated with an LO that covers the entire VNA frequency range, the LO signal is clipped to generate a square wave. A square wave contains the odd harmonics of the fundamental LO frequency. By mixing these harmonics with the incident wave and filtering the result, the desired IF signal is obtained. However, broadband noise and spurious signals can also be downconverted through these harmonics, producing unwanted components within the IFBW. This is why users can select the IFBW. A wider IFBW enables faster measurements but introduces more noise, while narrower IFBW offers a higher signal-to-noise ratio (SNR) but results in longer measurement times due to the filter's stabilization time, which is inversely proportional to the IFBW.

The receiver is also equipped with an anti-aliasing low-pass filter, a low-noise amplifier (LNA) to improve the SNR, and an analog-to-digital converter (ADC) that samples the IF signal. Once digitized, digital signal processing (DSP) is used to extract the magnitude and phase of the signal. Finally, any additional processing or error corrections are handled by the central processing unit (CPU).

Before utilizing the VNA, calibration is necessary to obtain accurate S-parameter measurements. The calibration is essential because, once cables or other RF components are added to connect the VNA to the device under test (DUT), the S-parameters must be adjusted to account for these additional components. Furthermore, internal elements of the VNA can introduce systematic errors, such as imperfect RF-source switching or limited coupler directivity, as mentioned earlier [174]. Various calibration procedures exist to correct these errors. Here, we describe the widely used 12-term Short-Open-Load-Thru (SOLT) calibration method for two-port VNAs [175, 176]. This method is sometimes referred to as TOSM (Thru-Open-Short-Match).

The SOLT calibration method is conducted in two stages: first, the error terms for each port are determined individually using the Short-Open-Load (SOL) technique; then, the remaining error terms between the two ports are identified using the Thru method.

4.3.1.a 1-Port Error Model

In this model, we consider only one port of the VNA connected to the DUT. In our measurements, the DUT corresponds to the cavity. However, during calibration, the DUT corresponds to reference devices from the calibration kit provided with the instrument, specifically Short, Open, and Load (SOL) circuits with well-known ideal values.

Fig. 4.14 illustrates the cascaded S-parameters schemes for each port. The E (E') matrix, with components e_{ij} (e'_{ij}), represent the S-matrix of the systematic errors for port 1 (port 2). The variables a_0 and b_0 (a'_3 and b'_3) denote the incident and reflected waves at the port 1 receiver, while a_1 and b_1 (a'_2 and b'_2) represents the incident and reflected waves at the DUT connectors, which we aim to quantify. The terms without primes refer to waves and errors when port 1 is excited, while those with primes represent waves and errors when port 2 is excited.

It is crucial to distinguish between the errors depending on which port is excited, as the VNA uses an RF-source switch to toggle between ports. Any imperfections in this switch can result in non-reciprocal errors between forward (port 1 excitation) and reverse (port 2 excitation) measurements. Specifically, e_{00} (e'_{33}) represents the directivity of port 1 (port 2), e_{10} and e_{01} (e'_{23} and e'_{32}) account for transmission and reflection tracking for port 1 (port 2), and e_{11} (e'_{22}) describes the match for port 1 (port 2). In the literature, S_{ii} is commonly referred to as Γ when considering a single port. For clarity in this subsection and the next, we will continue using the notation S_{ii}.

Referring to Fig. 4.14 (a), the measured reflection coefficient $S_{11}^{\mathrm{m}} = b_0/a_0$ at port 1 can be expressed as follows. The incident and reflected waves at the DUT port are described by:

$$a_1 = e_{11}b_1 + e_{10}a_0, \tag{4.41a}$$
$$b_1 = S_{11}a_1. \tag{4.41b}$$

From these, the incident wave at the DUT can be written as:

$$a_1 = \frac{e_{10}}{1 - e_{11}S_{11}}a_0. \tag{4.42}$$

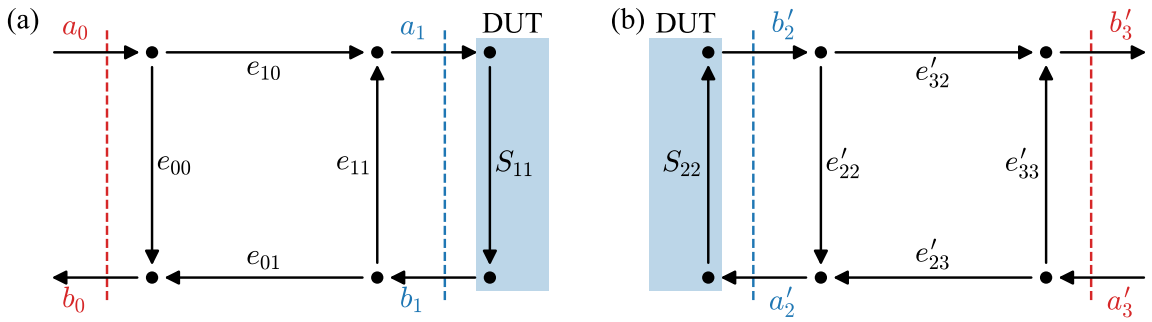

FIGURE 4.14: 1-Port Error Model Scheme

Next, referring again to Fig. 4.14 (a), , the reflected wave b_0 is given by:

$$b_0 = e_{00}a_0 + e_{01}b_1 = \frac{e_{00} - \Delta_e S_{11}}{1 - e_{11}S_{11}}a_0, \tag{4.43}$$

where $\Delta_e = \det\{E\} = e_{00}e_{11} - e_{01}e_{10}$. Finally, we obtain the measured reflection coefficient as:

$$S_{11}^{\mathrm{m}} = \frac{b_0}{a_0} = \frac{e_{00} - \Delta_e S_{11}}{1 - e_{11}S_{11}}. \tag{4.44}$$

From transmission line theory, the reflection coefficient S_{11} for short, open, and load circuits is known [163]. These can be expressed as:

$$S_{11}^{\mathrm{short}} = -1 \quad \rightarrow \quad S_{11}^{\mathrm{m,short}} = \frac{\Delta_e - e_{00}}{1 - e_{11}}, \tag{4.45a}$$

$$S_{11}^{\mathrm{open}} = 1 \quad \rightarrow \quad S_{11}^{\mathrm{m,open}} = \frac{e_{00} - \Delta_e}{1 - e_{11}}, \tag{4.45b}$$

$$S_{11}^{\mathrm{load}} = 0 \quad \rightarrow \quad S_{11}^{\mathrm{m,load}} = e_{00}. \tag{4.45c}$$

From Eq. (4.45a) and (4.45b), the error terms can be derived as:

$$e_{11} = \left(1 + \frac{S_{11}^{\mathrm{m,open}} - e_{00}}{e_{00} - S_{11}^{\mathrm{m,short}}}\right)\left(1 + S_{11}^{\mathrm{m,open}} - e_{00}\right)^{-1}, \tag{4.46a}$$

$$e_{01}e_{10} = (1 - e_{11})S_{11}^{\mathrm{m,open}} - e_{00} + e_{00}e_{11}. \tag{4.46b}$$

Similarly, at port 2, the parameters can be expressed as follows:

$$S_{22}^{\mathrm{m}} = \frac{b_3'}{a_3'} = \frac{e_{33}' - \Delta_e' S_{22}}{1 - e_{22'}S_{22}}, \tag{4.47a}$$

$$S_{22}^{\mathrm{load}} = e_{33}', \tag{4.47b}$$

$$e_{22}' = \left(1 + \frac{S_{22}^{\mathrm{m,open}} - e_{33}'}{e_{33}' - S_{22}^{\mathrm{m,short}}}\right)\left(1 + S_{22}^{\mathrm{m,open}} - e_{33}'\right)^{-1}, \tag{4.47c}$$

$$e_{23}'e_{32}' = (1 - e_{22}')S_{22}^{\mathrm{m,open}} - e_{33}' + e_{33}'e_{22}'. \tag{4.47d}$$

With these equations, 6 out of the 12 error terms are determined. It is noteworthy that knowing the cross terms $e_{01}e_{10}$ and $e_{23}'e_{32}'$ is sufficient for error correction, thus reducing the total number of independent terms needed from 14 to 12.

4.3.1.b 2-Ports Error Model

For the 2-port error model, additional errors not accounted for in the 1-port error model, as illustrated in Fig. 4.15, are considered. These include errors E_2 from port 2 when port 1 is excited, and E_1' when port 2 is excited. Additionally, leakage errors e_{30} and e_{03}' account for cross-talk between ports 1 and 2, where the waves do not pass through the DUT.

Applying a similar derivation as in Sec. 4.3.1.a, the measured S-parameters are expressed as (see Appendix 4.D for derivations):

$$S_{11}^{\mathrm{m}} = \frac{b_0}{a_0} = e_{00} + e_{01}e_{10}\frac{S_{11} - e_{22}\Delta_S}{1 - e_{11}S_{11} - e_{22}S_{22} + e_{11}e_{22}\Delta_S}, \tag{4.48a}$$

$$S_{21}^{\mathrm{m}} = \frac{b_3}{a_0} = e_{30} + e_{10}e_{32}\frac{S_{21}}{1 - e_{11}S_{11} - e_{22}S_{22} + e_{11}e_{22}\Delta_S}, \tag{4.48b}$$

$$S_{22}^{\mathrm{m}} = \frac{b'_3}{a'_3} = e'_{33} + e'_{23}e'_{32}\frac{S_{22} - e'_{11}\Delta_S}{1 - e'_{11}S_{11} - e'_{22}S_{22} + e'_{11}e'_{22}\Delta_S}, \tag{4.48c}$$

$$S_{12}^{\mathrm{m}} = \frac{b'_0}{a'_3} = e'_{03} + e'_{01}e'_{23}\frac{S_{12}}{1 - e'_{11}S_{11} - e'_{22}S_{22} + e'_{11}e'_{22}\Delta_S}, \tag{4.48d}$$

where $\Delta_S = \det\{S\} = S_{11}S_{22} - S_{12}S_{21}$.

The remaining errors can be determined through a two-step process. The first step involves testing the isolation of the system to identify the leakage terms e_{30} and e'_{03}. By using matched loads at both ports, the following relations are obtained:

$$S_{21}^{\mathrm{load}} = 0 \quad \rightarrow \quad S_{21}^{\mathrm{m,load}} = e_{30}, \tag{4.49a}$$

$$S_{12}^{\mathrm{load}} = 0 \quad \rightarrow \quad S_{12}^{\mathrm{m,load}} = e'_{03}. \tag{4.49b}$$

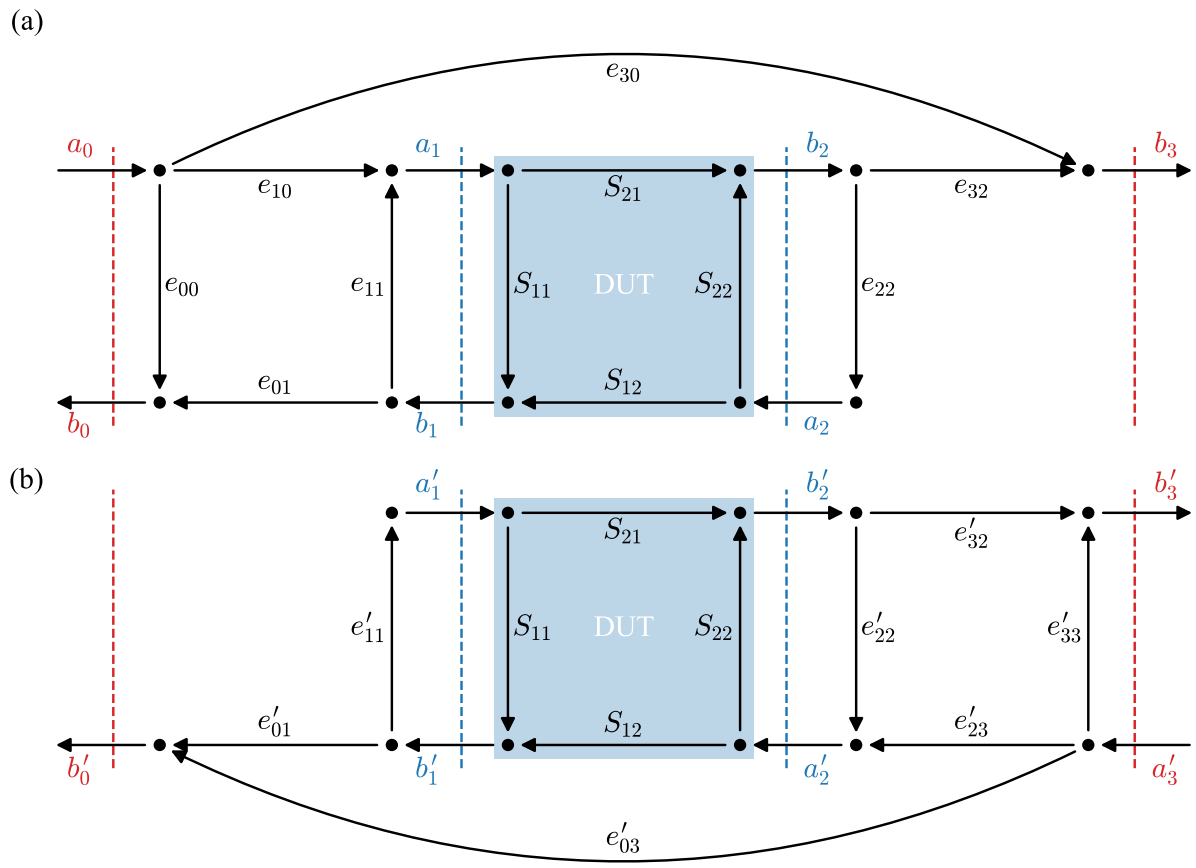

FIGURE 4.15: 2-Ports Error Model Scheme.

Typically, this isolation step is optional and primarily necessary for very low power signals. In many cases, the leakage terms are assumed to be zero by default.

The final four components are derived using the Thru calibration method, where:

$$\mathbf{S}^{\text{thru}} = \begin{bmatrix} 0 & 1 \\ 1 & 0 \end{bmatrix}. \tag{4.50}$$

From this, the remaining terms are calculated as follows:

$$S_{11}^{\text{m,thru}} = e_{00} + e_{01}e_{10}\frac{e_{22}}{1 - e_{11}e_{22}} \quad \Rightarrow \quad e_{22} = \frac{e_{00} + S_{11}^{\text{m,thru}}}{e_{01}e_{10} + e_{11}(e_{00} + S_{11}^{\text{m,thru}})}, \tag{4.51a}$$

$$S_{21}^{\text{m,thru}} = e_{30} + e_{10}e_{32}\frac{1}{1 - e_{11}e_{22}} \quad \Rightarrow \quad e_{10}e_{32} = (1 - e_{11}e_{22})(S_{21}^{\text{m,thru}} - e_{30}), \tag{4.51b}$$

$$S_{22}^{\text{m,thru}} = e'_{33} + e'_{23}e'_{32}\frac{e'_{11}}{1 - e'_{11}e'_{22}} \quad \Rightarrow \quad e'_{11} = \frac{e'_{23} + S_{22}^{\text{m,thru}}}{e'_{23}e'_{32} + e'_{11}(e'_{33} + S_{22}^{\text{m,thru}})}, \tag{4.51c}$$

$$S_{12}^{\text{m,thru}} = e'_{03} + e'_{01}e'_{23}\frac{1}{1 - e'_{11}e'_{22}} \quad \Rightarrow \quad e'_{01}e'_{23} = (1 - e'_{11}e'_{22})(S_{21}^{\text{m,thru}} - e'_{03}). \tag{4.51d}$$

With the SOLT calibration, all error terms affecting the measurement setup are identified and can be corrected. This involves computing the DUT's S-parameter by isolating the S_{ij} parameters in Eq. (4.48). For detailed expressions and further explanations, the reader can refer to [176].

4.3.2 Measurement & automation

In this section, we present the experimental setup and the Python program developed for automating measurements. The program is available on GitHub. and provides a graphical user interface (GUI) for convenient control of measurement instruments. The instruments are managed using the PyVisa Python package, which interfaces with devices following the Virtual Instrument Software Architecture (VISA) standard. This allows control of various instruments and communication protocols such as GPIB, USB, and Ethernet.

As shown in Fig. 4.16, the interface consists of several blocks, with each block representing a specific instrument type that may or may not be part of the measurement setup. The GUI provides standard commands linked to the laboratory's available instrument brands, and the program automates the measurement process differently based on the selected instruments.

In this example, we focus on the operation of the program when using the Vector Network Analyzer (VNA), the power supply (PS) for the electromagnet (EM), and the gaussmeter (GM). Although the source meter is included in the program for potential future measurements, it was not used for the experiments presented in this thesis. The source meter could apply current or detect weak signals by filtering them to the modulation frequency, which is useful for generating the Spin Hall Effect (SHE) or detecting Hall voltage via inverse SHE (iSHE) [7, 8, 11, 12, 17].

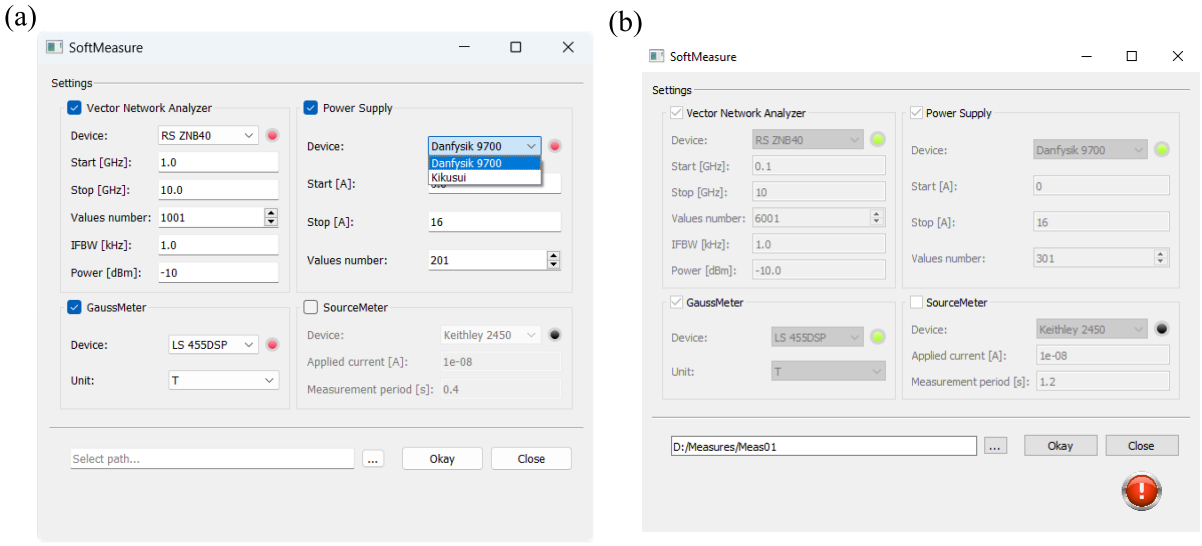

FIGURE 4.16: Automation measurements interface showing the user settings configuration for defining measurement parameters.

As illustrated in Fig. 4.16, the interface allows the user to define key parameters for the VNA, including start and stop frequencies, the number of points in the sweep, the IFBW, and the input power. For the power supply, the user specifies the start and stop current values and the number of steps, while the gaussmeter settings enable selection of the magnetic field units. Before starting measurements, the user must define a folder path where the data will be saved, including files for the applied current, magnetic field, and each S-parameter (both in magnitude, dB, and phase). As shown in Fig. 4.16 (b), the user can stop the measurement at any time, at which point the instruments reset (with the power supply returning to $I = 0$) and disconnect, allowing the instruments to be used locally rather than remotely. The interface is designed with safety in mind: it prevents application of current values exceeding 38 A and reminds the user to activate the electromagnet cooling system prior to measurement. Any errors, such as missing file paths or connection issues, are reported via the interface, along with detailed error messages and tracebacks.

As depicted in Fig. 4.17, the measurement process begins with instrument connection and initialization. During initialization, the power supply sets the current to $I = 0$ to ensure no current is applied. Once initialized, the system enters a measurement loop, where measurements continue until the target current is reached. In each iteration, the system

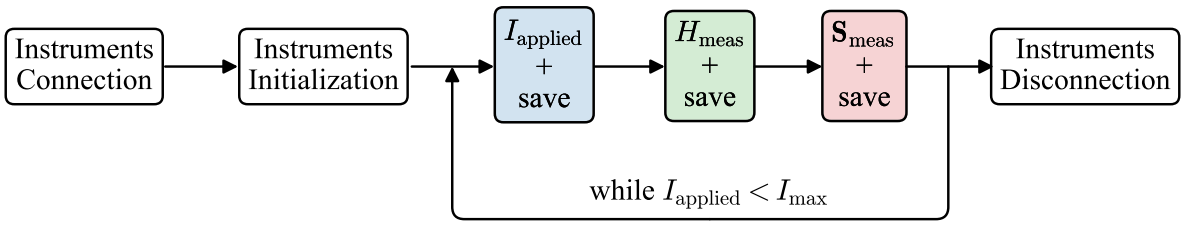

FIGURE 4.17: Flowchart of a measurement campaign illustrating the sequential steps involved in conducting measurements.

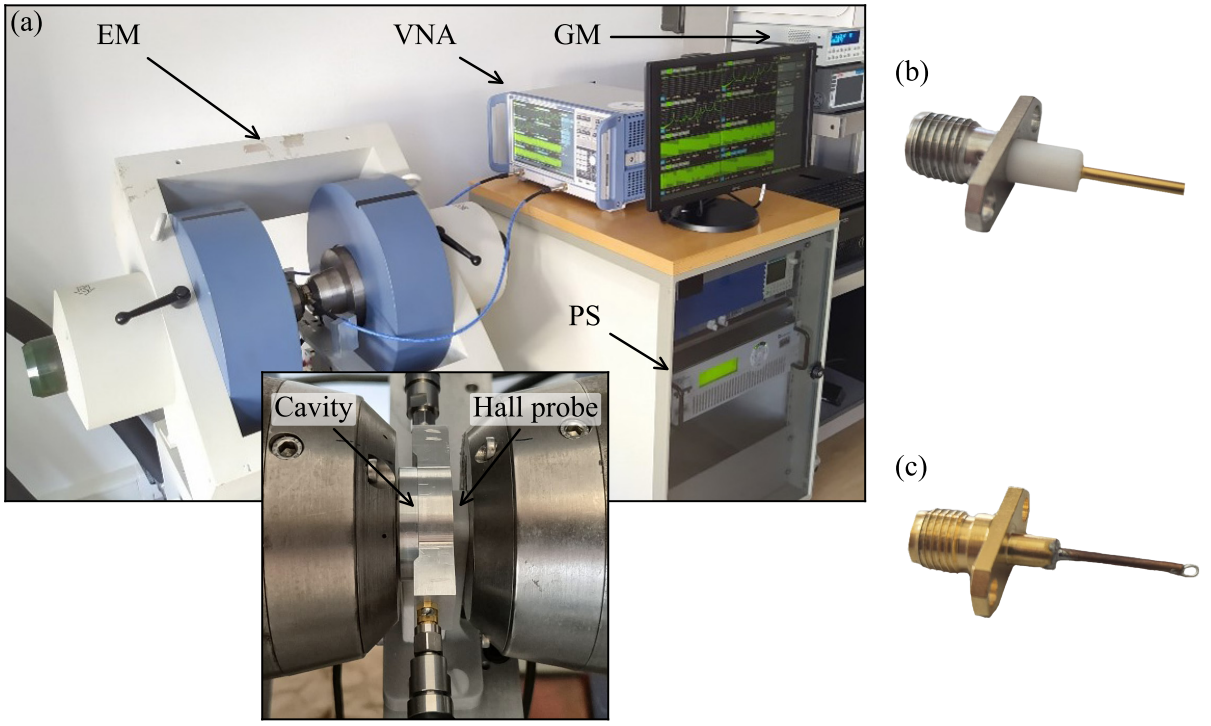

FIGURE 4.18: (a) Laboratory setup with the cavity shown in the inset. (b) and (c) SMA connectors for probing the electric E- and magnetic H-fields, respectively.

applies the next current value and records it. Subsequently, the gaussmeter measures and logs the corresponding magnetic field. Finally, the VNA performs a frequency sweep, recording the S-parameters. After the loop completes, the instruments reset and disconnect, with the power supply returning to $I = 0$ before disconnection.

The experimental setup comprises the following instruments, as shown in Fig. 4.18 (a):

- **VNA**: The two-ports R&S® ZNB40 from Rohde & Schwarz® is employed, covering a frequency range from 100 kHz to 40 GHz. It provides a wide dynamic range of up to 135 dB with an IF bandwidth from 1 Hz to 10 MHz, and an adjustable power input between -60 dBm and 10 dBm. After calibration, the VNA achieves an effective directivity of approximately 42 dB, source match of 38 dB, load match of 40 dB, reflection tracking of 0.05 dB, and transmission tracking of 0.02 dB [177].
- **Gaussmeter (GM)**: The Lake Shore Cryotronics, Inc® Model 455 DSP gaussmeter is used to measure magnetic flux density, with a range from 35 µT to 35 T. In DC mode, the accuracy is ± 0.075 % [178].
- **Power Supply (PS)**: The electromagnet is powered by the SYSTEM 9700 from Danfysik®, which includes a polarity switch enabling current up to ± 50 A at 60 V DC [179]. Its accuracy specifications are listed in Table 4.1. The power supply can be controlled through either voltage or current.

TABLE 4.1: Accuracy characteristics of the Danfysik® SYSTEM 9700 [179]

Current setting resolution	20 bits DAC
Current reproducibility	±10 ppm
Absolute current calibration	$-0/+400$ ppm at $I_{\max}$
Current read-back resolution	16 bits ADC
Voltage read-back resolution	16 bits ADC

- **Electromagnet (EM)**: The EM7-HV electromagnet from Lake Shore Cryotronics, Inc® is utilized, with an air gap between the poles of up to 178 mm and pole cap diameters of 51 mm. The coils have a resistance of 1.0 Ω, allowing a maximum continuous operating current of ±67.5 A at ±75 V. The coil temperature limit is 45°C, and the water inlet temperature must be maintained between 15°C and 25°C [180].

Fig. 4.18 show the SMA connectors used as electric and magnetic field probes, respectively. The magnetic field probes are custom-made in the laboratory. The power supply and electromagnet enable magnetic fields of up to 2 T, with a gap of approximately 2 cm between the poles, while the VNA can measure frequencies up to 40 GHz. As an example, Fig. 4.19 illustrates the magnitude of the transmission spectrum as a function of both the magnetic field and the applied RF frequency.

For data post-processing, the polariton frequencies were extracted from the transmission spectra, as shown in Fig. 4.20 (a) by identifying transmission maxima within specific regions (indicated by red squares in Fig. 4.20 (b)). Selecting specific regions helps to avoid maxima from other cavity modes or polaritons resulting from coupling with additional magnonic modes, which could otherwise reduce the accuracy of the fitting results. The extracted frequency values as a function of the applied magnetic field were then fitted to

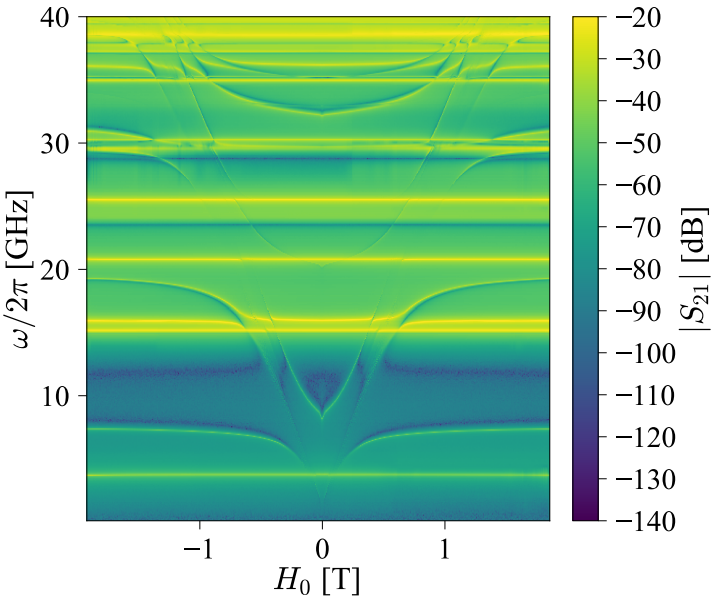

FIGURE 4.19: Measurement of the transmission spectrum as a function of the applied static magnetic field H_0 and the RF field frequency.

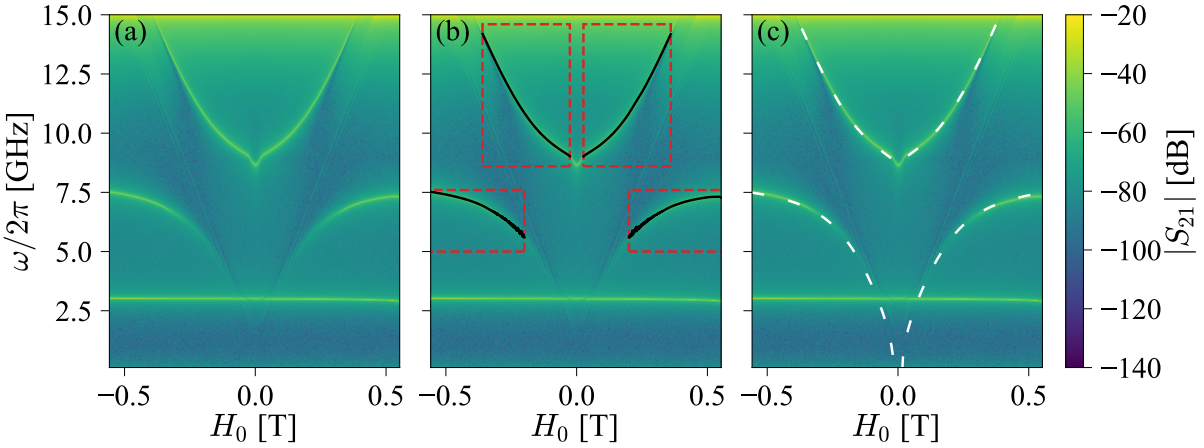

FIGURE 4.20: Data post-processing steps: (a) transmission spectrum; (b) extraction of the maxima in defined regions corresponding to the polariton frequencies; (c) fitting results of the extracted data values.

the theoretical model using the least squares method, which minimizes the sum of squared errors between the observed data and the model predictions [181].

Appendices of Chapter 4

4.A Engineering arbitrary physical phases through a quintuple reentrante cavity

The objective of this investigation is to design a cavity capable of introducing a non-trivial phase between consecutive modes while performing in the strong coupling regime. Re-entrant cavities have demonstrated a favorable ease of design for observing various phenomena, and are more detailed in Chapter 5.

In this study, we developed a quintuple re-entrant cavity tailored to achieve several key objectives. This cavity design facilitates the observation of a non-trivial phase difference between consecutive modes, ensures uniform coupling strength across multiple YIG spheres, and performing within the strong coupling regime. Furthermore, the phase relationship between the two modes is contingent upon the positioning of four posts within the cavity, as demonstrated in our analysis. By manipulating the positions of these posts, it is feasible to fine-tune the coupling phase by adjusting the gap between the top of the post and the cavity lid.

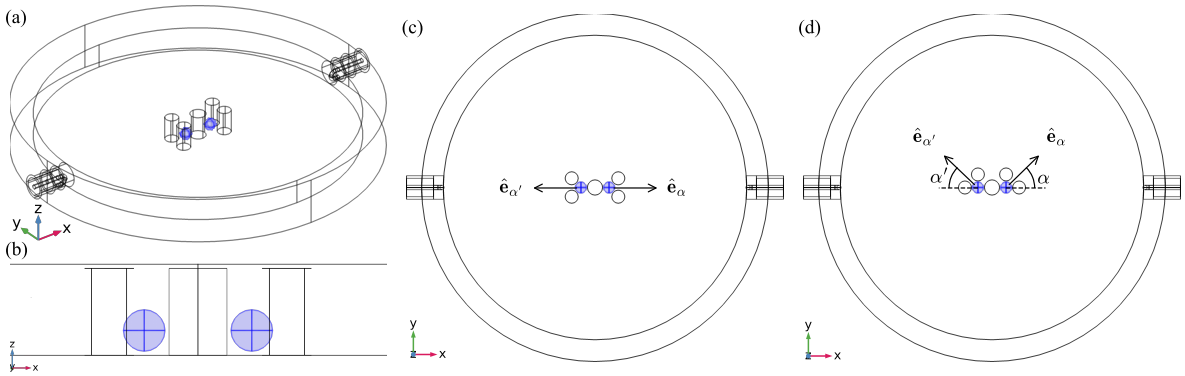

FIGURE 4.21: Representation of the quintuple reentrante cavity (a) in the three dimensions; (b) in the (z, x) plane zoomed to view the gap d between the top of the posts and the lid; (c) in the (x, y) plane with represented the direction $\hat{\mathbf{e}}_\alpha$ and the direction $\hat{\mathbf{e}}_{\alpha'}$ being the symetric to $\hat{\mathbf{e}}_\alpha$ versus the y-axis passing throughout 0; (d) in the (x, y) plane with the direction $\hat{\mathbf{e}}_\alpha$ making an angle α versus the x-axis representing the angle forming by the two peripherical posts at the right-hand side of the cavity where the center of the azimuthal displacement is the center of the YIG sphere of the right-hand side. The two YIG spheres are represented in blue.

The cavity dimensions were optimized to maximize the coupling strength for each YIG sphere and to ensure that the phase falls within a range $[n\pi/4, (n+1)\pi/4]$ with $n \in \mathbb{Z}$ relative to a free dimension variable α, as detailed below. As depicted in Fig. 4.21, the cavity is cylindrical and features five cylindrical posts. The cavity has a radius of 14 mm and a height of 2.25 mm. All posts have the same height, which depends on the value of the gap d; thus, the post height is $2.25 - d$. Positioned at the center of the cavity is a fixed post with a radius of 0.7 mm. The two YIG spheres are located on either side of

the center post along the x-axis, with a spacing of 0.1 mm from the center post. Four additional posts are situated at the periphery of each YIG sphere, spaced 0.1 mm from the spheres. These peripheral posts are symmetrically positioned with respect to the y-axis, which passes through the center of the cavity. The radius of the peripheral posts is 0.6 mm. Relative to the direction $\hat{e}_\alpha$, the two peripheral posts on the right-hand side of the cavity are positioned at $\pm 45°$. Additionally, the direction $\hat{e}_\alpha$ forms an angle α with the x-axis, ranging from 0° to 45°, allowing for tuning of the coupling phases.

The H-field distributions are depicted in Fig. 4.4 for the first three modes of the cavity. Our focus lies on the second and third modes due to their high filling factor values η, which are quite similar for both modes and spheres, as illustrated in Table 4.2. This table presents the eigenfrequencies f of the first three modes of the cavity, along with the filling factors η_L and η_R for the YIG spheres on the left and right-hand sides, respectively. Additionally, the associated coupling strengths g_L and g_R are provided. The values are given for an angle $\alpha = 0°$ and a gap $d = 50$ µm.

Table 4.3 presents similar characteristics for the two modes of interest, along with the averaged H-field direction inside each YIG sphere and the phase coupling. It is observed that the coupling strength slightly decreases from $\alpha = 0$ř to $\alpha = 45$ř, while the difference in coupling strength between mode 1 and mode 2 slightly increases. However, the coupling strength remains relatively constant, ranging from 4.2% to 5.7%. The phase coupling varies between 129° and 180° for α ranging from 45° to 0°, allowing for measurements with a non-trivial phase between 135° and 180°.

TABLE 4.2: Cavity Modes characteristics of the 3 first modes for $d = 50$ µm.

Mode	**f [GHz]**	$\boldsymbol{\eta_L}$	$\boldsymbol{\eta_R}$	$\boldsymbol{g_L/\omega}$	$\boldsymbol{g_R/\omega}$
0	4.02	0.018	0.019	0.011	0.012
1	8.29	0.125	0.123	0.055	0.056
2	12.03	0.144	0.145	0.055	0.055

Table 4.4 presents the same information for a fixed angle of 45° while varying the gap d from 100 µm to 5 µm. It demonstrates that measurements with a non-trivial phase can be conducted within the range of 90° to 135°.

TABLE 4.3: Cavity Modes characteristics versus α for $d = 50$ µm

$\boldsymbol{\alpha}$ [°]	f [GHz]	$\boldsymbol{\eta_L}$	$\boldsymbol{\eta_R}$	$\boldsymbol{g_L/\omega}$	$\boldsymbol{g_R/\omega}$	$\boldsymbol{\phi_L}$ [°]	$\boldsymbol{\phi_R}$ [°]	$\boldsymbol{\theta}$ [°]
0	8.29	0.125	0.123	0.057	0.056	90	90	180
	12.03	0.144	0.145	0.055	0.055	-90	90	
5	8.29	0.125	0.122	0.057	0.056	-91	-88	170
	12.09	0.141	0.142	0.053	0.053	-86	87	
10	8.27	0.125	0.122	0.057	0.055	-92	-87	160
	12.07	0.139	0.140	0.053	0.053	-82	83	
15	8.33	0.124	0.122	0.056	0.055	86	95	151
	12.09	0.134	0.134	0.050	0.051	-79	80	
20	8.38	0.124	0.120	0.056	0.055	85	96	144
	12.07	0.130	0.130	0.049	0.049	-76	78	
25	8.48	0.122	0.121	0.055	0.054	-97	-83	139
	12.05	0.126	0.125	0.047	0.047	-76	77	
30	8.54	0.122	0.119	0.055	0.054	83	98	133
	12.03	0.121	0.121	0.046	0.046	-74	75	
35	8.62	0.121	0.119	0.054	0.053	-98	-81	131
	11.99	0.119	0.119	0.045	0.045	106	-105	
40	8.74	0.121	0.118	0.054	0.052	81	99	130
	11.97	0.115	0.115	0.044	0.044	-73	74	
45	8.90	0.120	0.118	0.053	0.052	-99	-80	128
	11.96	0.112	0.112	0.042	0.042	-74	74	

TABLE 4.4: Cavity Modes characteristics versus d for $\alpha = 45°$

$\boldsymbol{d}$ [µm]	f [GHz]	$\boldsymbol{\eta_L}$	$\boldsymbol{\eta_R}$	$\boldsymbol{g_L/\omega}$	$\boldsymbol{g_R/\omega}$	$\boldsymbol{\phi_L}$ [°]	$\boldsymbol{\phi_R}$ [°]	$\boldsymbol{\theta}$[°]
5	3.34	0.123	0.116	0.088	0.083	80	102	146
	4.67	0.154	0.157	0.093	0.095	97	-95	
10	4.63	0.124	0.115	0.075	0.070	-100	-78	147
	6.45	0.155	0.158	0.080	0.082	97	-94	
25	6.88	0.122	0.118	0.061	0.059	-100	-79	144
	9.61	0.156	0.158	0.066	0.067	98	-97	
50	8.90	0.120	0.118	0.053	0.052	-99	-80	129
	11.95	0.112	0.112	0.043	0.043	-74	74	
100	10.84	0.112	0.110	0.045	0.044	82	98	90
	12.77	0.051	0.051	0.019	0.019	-53	53	

4.B Input-Output formalism for a quasi-closed cavity with COMSOL Multiphysics® convention

4.B.0.a Heisenberg Equation of Motion

From Eq. (3.49) and considering the first Markov approximation given in Eq. (3.53), the Heisenberg EoM, given in Eq. (3.33), for the external modes reads:

$$\dot{\hat{b}}_{\omega,n}(t) = i\omega\hat{b}_{\omega,n}(t) - \frac{1}{\sqrt{2\pi}}\sum_p \kappa_{pn}\hat{a}_p(t). \tag{4.52}$$

The solution of this differential equation reads as:

$$\begin{aligned}\hat{b}_{\omega,n}(t) =& \hat{b}^{\tau}_{\omega,n}e^{i\omega(t-\tau)} \\ &- \frac{1}{\sqrt{2\pi}}\sum_p \kappa_{pn}\int_t^{\tau} \mathrm{d}t'\,\hat{a}_p(t')e^{i\omega(t-t')},\end{aligned} \tag{4.53}$$

where τ is a time reference.
Subsequently, we define the polychromatic bosonic operator for each port by considering all the bosonic operators of the same port across all frequencies:

$$\hat{b}^{\tau}_n(t) = \frac{1}{\sqrt{2\pi}}\int_{\mathbb{R}} \mathrm{d}\omega\,\hat{b}^{\tau}_{\omega,n}e^{i\omega(t-\tau)}. \tag{4.54}$$

From this equation, we define the incoming and outgoing wave operators at each port:

$$\hat{b}^{\mathrm{in}}_n(t) = \hat{b}^{t_0}_n(t), \quad t_0 = +\infty, \tag{4.55a}$$
$$\hat{b}^{\mathrm{out}}_n(t) = \hat{b}^{t_1}_n(t), \quad t_1 = -\infty. \tag{4.55b}$$

4.B.0.b Input-Output Relation

Integrating over ω on both sides, Eq. (4.53) becomes:

$$\begin{aligned}\frac{1}{\sqrt{2\pi}}\int_{\mathbb{R}} \mathrm{d}\omega\,\hat{b}_{\omega,n}(t) =& \frac{1}{\sqrt{2\pi}}\int_{\mathbb{R}} \mathrm{d}\omega\,\hat{b}^{t_0}_{\omega,n}e^{i\omega(t-t_0)} \\ &- \frac{1}{2\pi}\sum_p \kappa_{pn}\int_t^{+\infty} \mathrm{d}t'\,\hat{a}_p(t')\int_{\mathbb{R}} \mathrm{d}\omega\,e^{i\omega(t-t')},\end{aligned} \tag{4.56a}$$

$$\begin{aligned}\frac{1}{\sqrt{2\pi}}\int_{\mathbb{R}} \mathrm{d}\omega\,\hat{b}_{\omega,n}(t) =& \frac{1}{\sqrt{2\pi}}\int_{\mathbb{R}} \mathrm{d}\omega\,\hat{b}^{t_1}_{\omega,n}e^{i\omega(t-t_1)} \\ &+ \frac{1}{2\pi}\sum_p \kappa_{pn}\int_{-\infty}^{t} \mathrm{d}t'\,\hat{a}_p(t')\int_{\mathbb{R}} \mathrm{d}\omega\,e^{i\omega(t-t')},\end{aligned} \tag{4.56b}$$

where the first term on the right-hand side of the first (second) equation is equal to $\hat{b}^{in}_n(t)$ ($\hat{b}^{out}_n(t)$), and the second term is equal to $-\frac{1}{2}\sum_p \kappa_{pn}$ ($\frac{1}{2}\sum_p \kappa_{pn}$), according to the following

properties [150]:

$$\int_{\mathbb{R}} \mathrm{d}\omega\, e^{i\omega(t-t')} = 2\pi\delta(t-t'), \tag{4.57a}$$

$$\int_{-\infty}^{t} \mathrm{d}t'\, \hat{a}_p(t')\delta(t-t') = \int_{t}^{+\infty} \mathrm{d}t'\, \hat{a}_p(t')\delta(t-t') = \frac{1}{2}\hat{a}_p(t). \tag{4.57b}$$

This results in the input-output relation:

$$\hat{b}_n^{\mathrm{out}}(t) = \hat{b}_n^{\mathrm{in}}(t) - \sum_p \kappa_{pn}\hat{a}_p(t). \tag{4.58}$$

4.B.0.c Quantum Langevin Equation

The Quantum Langevin Equation (QLE) reads as:

$$\dot{\hat{a}}_p(t) = i\tilde{\omega}_p\hat{a}_p(t) + i\sum_{q\neq p} g_{qp}\hat{a}_q(t) + \frac{1}{\sqrt{2\pi}}\sum_n \int_{\mathbb{R}} \mathrm{d}\omega\, \kappa_{pn}^*(\omega)\hat{b}_{\omega n}(t). \tag{4.59}$$

Substituting the value of $\hat{b}_{\omega,n}$ from Eq. (4.53) for $\tau = t_0$ in the QLE gives rise to:

$$\begin{aligned}\dot{\hat{a}}_p(t) =& i\tilde{\omega}_p\hat{a}_p(t) + i\sum_{q\neq p} g_{qp}\hat{a}_q(t) \\ &+ \frac{1}{\sqrt{2\pi}}\sum_n \kappa_{pn}^* \left[\int_{\mathbb{R}} \mathrm{d}\omega\, \hat{b}_{\omega,n}^{t_0} e^{i\omega(t-t_0)} - \kappa_{pn}\sum_q \int_t^{t_0} \mathrm{d}t' \int_{\mathbb{R}} \mathrm{d}\omega\, e^{i\omega(t-t')}\hat{a}_q(t')\right].\end{aligned} \tag{4.60}$$

The properties given in Eq. (4.57a) and (4.57b) lead to:

$$\dot{\hat{a}}_p(t) = i\tilde{\omega}_p\hat{a}_p(t) + i\sum_{q\neq p} g_{qp}\hat{a}_q(t) + \sum_n \kappa_{pn}^*\left(\hat{b}_n^{\mathrm{in}}(t) - \sum_q \frac{\kappa_{qn}}{2}\hat{a}_q(t)\right). \tag{4.61}$$

Taking the Fourier transform[2], Eq. (4.61) can be expressed as:

$$\left(\omega - \tilde{\omega}_p - \frac{i}{2}\sum_n |\kappa_{pn}|^2\right)\hat{a}_p(\omega) - \sum_{q\neq p}\left(\frac{i}{2}\sum_n \kappa_{pn}^*\kappa_{qn} + g_{qp}\right)\hat{a}_q(\omega) = -i\sum_n \kappa_{pn}^*\hat{b}_n^{\mathrm{in}}(\omega). \tag{4.62}$$

In matrix form:

$$\boldsymbol{\Omega}\cdot\hat{\mathbf{a}} = -i\mathbf{K}^*\cdot\hat{\mathbf{b}}_{\mathrm{in}}, \tag{4.63a}$$

$$\Omega_{qp} = (\omega - \tilde{\omega}_p)\delta_{qp} - \frac{i}{2}\sum_n(\kappa_{pn}^*\kappa_{qn}) - g_{qp}, \tag{4.63b}$$

where $\hat{\mathbf{a}}$ is the vector containing all $\hat{a}_p(\omega)$ operator components, $\hat{\mathbf{b}}_{\mathrm{in}}$ is the vector containing all $\hat{b}_n^{\mathrm{in}}(\omega)$ operator components, $\mathbf{K}$ is the $p\times m$ matrix with κ_{pm} as components, Ω_{qp} are the components of the $p\times p$ matrix $\boldsymbol{\Omega}$, and δ_{qp} is the Kronecker delta.

[2]Reminding the Fourier Transform property: $\mathcal{F}[\dot{\hat{a}}_q(t)] = i\omega\hat{a}_q(\omega)$

4.B.0.d S-parameters

Substituting the solution of Eq. (4.63a) into Eq. (4.58) results in:

$$\hat{\mathbf{b}}_{\text{out}} = \mathbf{S} \cdot \hat{\mathbf{b}}_{\text{in}}, \tag{4.64}$$

where the S-matrix reads as:

$$\mathbf{S} = \mathbb{1} + i\mathbf{K}^{\text{t}} \cdot \mathbf{\Omega}^{-1} \cdot \mathbf{K}^{*}, \tag{4.65}$$

where $\mathbb{1}$ is the identity matrix.

4.C SMA connector data sheet

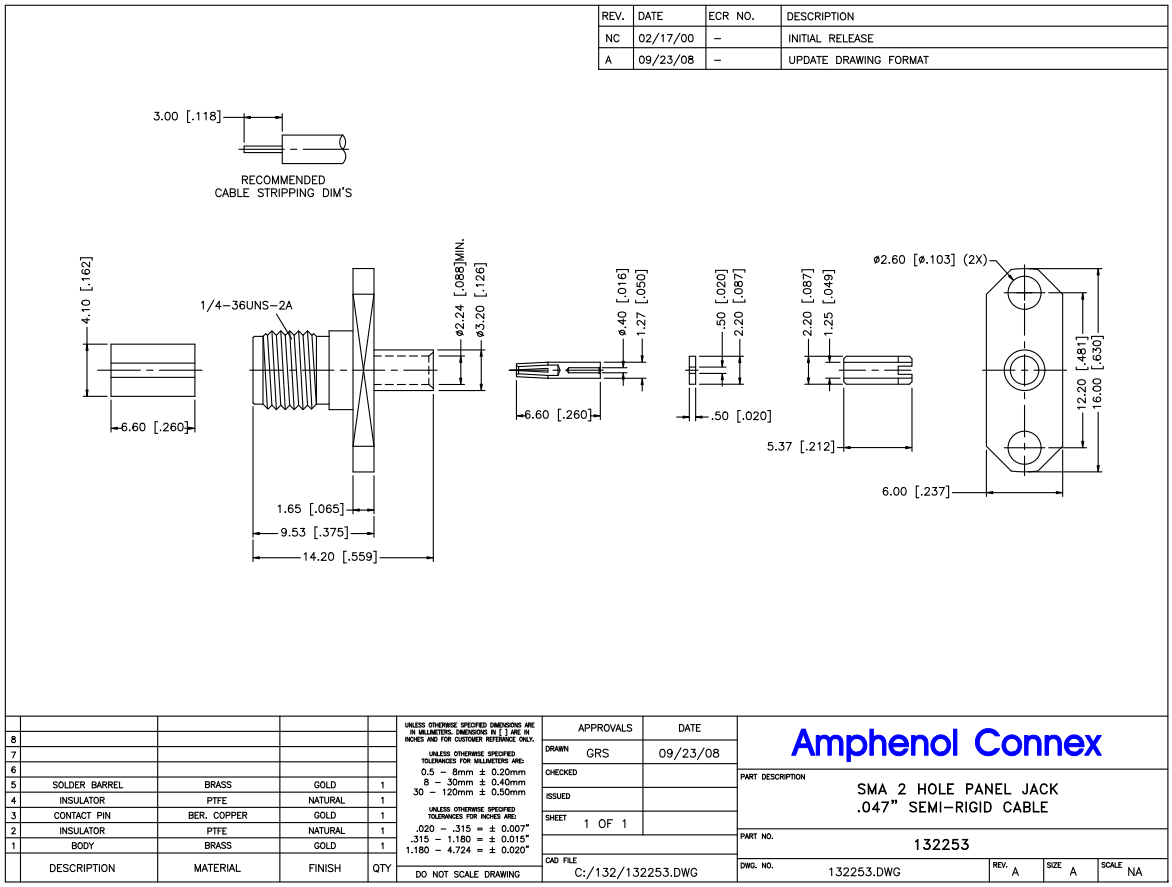

FIGURE 4.22: Data sheet of the utilized SMA connector

4.D 2-Ports Error Model

Here, we aim to derivate the S-parameters in the 2-Port Error Model from Sec. 4.3.1.b.

4.D.1 S_{11}^{m} calculation

Referring to Fig. 4.15 (a), we have:

$$\begin{aligned} a_2 &= e_{22}b_2 \\ b_2 &= S_{21}a_1 + S_{22}a_2 \end{aligned} \quad \Rightarrow \quad \begin{aligned} b_2 &= \frac{S_{21}}{1 - e_{22}S_{22}}a_1 \\ a_2 &= \frac{e_{22}S_{21}}{1 - e_{22}S_{22}}a_1 \end{aligned}. \tag{4.66}$$

Moreover, we have:

$$\begin{aligned} a_1 &= e_{10}a_0 + e_{11}b_1 \\ b_1 &= S_{12}a_2 + S_{11}a_1 \end{aligned}. \tag{4.67}$$

Substituting a_2 into the expression of b_1 we have:

$$b_1 = \left(\frac{e_{22}S_{21}}{1 - e_{22}S_{22}} + S_{11}\right)a_1 \tag{4.68}$$

Substituting a_1, b_1 is expressed as:

$$b_1 = e_{10}\frac{S_{11} - e_{22}\Delta_S}{1 - e_{11}S_{11} - e_{22}S_{22} + e_{11}e_{22}\Delta_S}a_0. \tag{4.69}$$

Furthermore, we have:

$$b_0 = e_{00}a_0 + e_{01}b_1. \tag{4.70}$$

We finally arrive at the expression of the measured reflection S_{11}^{m} at port 1 given in Eq. (4.48a) by substituting b_1 into the expression of b_0. The same derivation referring to Fig. 4.15 (b) permits to find the measured reflection S_{22}^{m} at port 2, given in Eq. (4.48c).

4.D.2 S_{21}^{m} calculation

Substituting b_1 given in Eq. (4.67) into the expression of a_1, it reads that:

$$a_1 = e_{10}a_0 + e_{11}(S_{12}a_2 + S_{11}a_1). \tag{4.71}$$

By substituting a_2 from Eq. (4.66), the expression of a_1 is given by:

$$a_1 = e_{10}\frac{e_{22}S_{22}}{1 - e_{11}S_{11} - e_{22}S_{22} + e_{22}\Delta_S}a_0 \tag{4.72}$$

Moreover, referring to Fig. 4.15 (a), we have:

$$b_3 = e_{30}a_0 + e_{32}b_2. \tag{4.73}$$

By substituting b_2 from Eq. (4.66) into this expression, it becomes that:

$$b_3 = e_{30}a_0 + e_{32}\frac{S_{21}}{1 - e_{22}S_{22}}a_1. \tag{4.74}$$

We finally arrive at the expression of the measured transmission S_{21}^{m} at port 1 given in Eq. (4.48b) by substituting a_1 into the expression of b_3. The same derivation referring to

Fig. 4.15 (b) permits to find the measured transmission S_{12}^{m} at port 2 given in Eq. (4.48d).

5 Strong to ultra-strong coherent coupling measurements in a YIG/cavity system at room temperature

Abstract

We present an experimental study of the strong to ultra-strong coupling regimes at room temperature in frequency-reconfigurable three-dimensional reentrant cavities coupled with a yttrium-iron-garnet slab. The observed coupling rate, defined as the ratio of the coupling strength to the cavity frequency of interest, ranges from 12% to 59%. We show that certain considerations must be taken into account when analyzing the polaritonic branches of a cavity spintronic device where the RF field is highly focused in the magnetic material. Our observations are in excellent agreement with electromagnetic finite-element simulations in the frequency domain. This study has been published in the Physical Review B journal [96] and can be found on arXiv. The section titled *Further Work* includes additional studies, particularly simulations approaching the deep-strong coupling regime.

Contents

5.1 Introduction

As mentioned in Sec. 3.2.4, the Ultra-Strong Coupling (USC) regime is achieved when the coupling strength exceeds 0.1 times the cavity frequency. Similar to the Strong Coupling (SC) regime, the USC regime also presents significant interest for various applications. For instance, devices that operate efficiently in the SC regime could potentially achieve enhanced performance in the USC regime. This is because the coupling, which facilitates the exchange between two subsystems, would enable faster control and response times [77]. Additionally, specific short-lifetime systems, such as those required for certain quantum gates [78], might only be observable in the USC regime [79]. More broadly, achieving the USC regime allows the exploration of novel phenomena, including new stable states of matter. For example, recent predictions indicate the potential existence of discrete time crystals in the USC regime for systems described by the Dicke model [76]. Furthermore, the ground state in the USC regime presents light and matter excitations, due to the counter-rotating term. This means that all excited states are dressed by multiple states containing different numbers of excitations, i.e. virtual excitations. Virtual excitations are known in non-linear optics, by analogy the virtual excitations in the USC regime could lead to higher order processes [75], such as higher-harmonic and sub-harmonic generation, multiphoton absorption [182], parametric amplification, Raman scattering [183], and Kerr effect to name a few.

Two methods can be employed to achieve the USC regime in a system [74]. The first approach involves coupling many dipoles to the same cavity mode. Although each dipole individually has a small coupling strength, the cumulative effect of a large number of dipoles results in a macroscopically increased effective coupling. The second approach optimizes the different degrees of freedom to enhance the coupling strength between a single dipole and the cavity mode.

The USC regime was first predicted in 2005 [184] and experimentally demonstrated in 2009 [127] using intersubband polaritons. Intersubband polaritons are hybrid quasi-particles formed from the interaction between an optical microcavity and doped quantum wells. The dipole moment of these polaritons is oriented along the growth axis, and they couple with transverse magnetic polarized waves. Quantum wells, created by layering different semiconductor materials at the nanoscale, confine carriers in a potential well, leading to the splitting of electronic bands into discrete and parallel subbands. Electrons in the conduction band can be collectively excited in the THz and mid-infrared regions. This system holds promise for applications in quantum key distribution, quantum teleportation, and quantum repeater technologies [185, 186]. The highest coupling strength achieved so far is a ratio of $g/\omega = 0.45$ [81].

Similar to other systems with many dipoles, Landau polaritons have exhibited a coupling ratio of $g/\omega = 1.43$ [129]. These quasi-particles result from the hybridization between a microcavity and doped quantum wells under a transverse magnetic field, with the in-plane dipole coupling to transverse electric-polarized radiation. The USC regime has been observed in various cavity types, including split-ring resonators [82], photonic crystal cavities [187], and coplanar microresonators [188]. Researchers have investigated several phenomena within the USC regime, such as the Bloch-Siegert shift, which occurs when anti-resonant terms are considered [189], and phenomena associated with the Deep Strong Coupling (DSC) regime, including light-matter decoupling [129].

Superconducting circuits are considered the most promising platform for achieving artificial atoms (composed of Josephson junctions) coupled to LC resonators, such as lumped-element circuits or transmission lines [190, 191]. Operating at GHz frequencies and cooled to millikelvin temperatures, these systems allow for easy design and in situ tuning of properties like coupling strength and frequency. They have been extensively used to engineer quantum states and realize quantum gates [192]. This platform also marked the first experiment to reach the DSC regime, achieving a coupling ratio of $g/\omega = 1.34$ [83].

In recent years, Cavity-Magnon Polaritons (CMPs) have garnered significant interest for various applications in quantum information, including frequency conversion, quantum memories, and quantum communication. Additionally, CMPs have shown promise in metrology for high-accuracy and stability clocks [156, 193–195], as well as in the detection of dark matter [77, 80]. So far, the USC regime in cavity spintronics has been experimentally achieved at low [84, 156, 196–198] and room [55, 85] temperatures, and investigated theoretically [109, 199].

Very recently, Golovchanskiy et al. (2021) [198] proposed an approach to achieve on-chip USC hybrid magnonic systems reaching $g/\omega = 0.6$ and based on superconducting/insulating/ferromagnetic multilayered microstructures operating below 10 K. They highlighted in particular the drastic failure of currently adopted models in the USC regime.

Here, we present measurements and simulations of a reconfigurable hybrid system that allows the study of the transition from the SC to USC regimes at room temperature in the 0.1-15 GHz frequency range. We utilize a magnetic field-focusing double-post reentrant cavity first described by Goryachev et al. (2014) [196]. A set of three different resonators (by their dimensions and post shapes) allow us to follow the evolution of the coupling strength through USC regime (starting from the SC/USC limit). With these results we confirm that it is necessary to add an extra term in the expression of the ferromagnetic resonance (FMR) frequency equation to accurately describe the observed hybridization (measurements and simulations) with the commonly used Dicke model [142]. We show that this additional term does not depend on the coupling rate but on the level of confinement of the rf magnetic field in the magnetic material. Moreover, this added term can be negligible in the SC regime, while it is essential in the USC regime.

5.2 Hybrid System Description

The multiple post re-entrant cavity [200] is a unique type of microwave cavity. Within the simple cylindrical cavity, can exist several metallic posts, presenting a potentially tunable gap between the top of the gap, and the lid of the cavity, as illustrated in Fig. 5.1 for a double re-entrant cavity.

Assuming the whole cavity as a lumped LC-circuit, it as been shown that each post can be considered as a microwave resonator owing the following capacitance C and inductance

L [200–203]:

$$C = \frac{\varepsilon \pi r^2}{d}, \tag{5.1a}$$

$$L = \frac{\mu_0 (H-d)}{2\pi} \ln\left(\frac{R}{r}\right), \tag{5.1b}$$

where ε is the permittivity, r is the post radius, d is the gap length, H is the cavity height ($H-d$ is then the post height), and R is the cavity radius. Then, each post has a intrinsic resonance frequency writing as:

$$\omega_c = \frac{1}{\sqrt{LC}} = \frac{\sqrt{2}}{\sqrt{\mu_0 \varepsilon (H/d-1) r^2 \ln(R/r)}}. \tag{5.2}$$

Noteworthily, the cavity frequencies are proportional to the intrinsic frequencies of the posts [200], meaning that decreasing (increasing) the gap d or increasing (decreasing) the post's surface will decrease (increase) the cavity frequencies.

The double re-entrant cavity proposed in [196] is loaded with a YIG sphere in order to reach a filling factor to 3%, and a ratio g/ω of 0.1. The hybrid system presented here is made of a modified re-entrant cavity and a commercial single crystal of YIG. The YIG is a slab of 3.82×6.09×0.61 mm^3. The choice of a millimetric slab allows to focus uniformly the magnetic field throughout the YIG volume in a much simpler way than with a YIG sphere, with adapting the post shapes.

The two first-order resonant modes of the double re-entrant cavity are termed the Dark Mode (DM) and the Bright Mode (BM). Both contain the electric field of the mode between the top of the post and the lid of the cavity. For the DM (as shown in Fig. 5.2 (a)), the RF electric fields (**e**-fields) focused above the two posts are in-phase, resulting in the circulating RF magnetic fields (**h**-fields) destructively interfering in the region between the posts (hence "dark"), whilst the opposite is true for the BM (as shown in Fig. 5.2 (b)). The advantages of such a cavity are three-fold: first, the highly localized electric field results in extremely large frequency sensitivity to any perturbations inside this region (displacement of the containment area or modification of the dielectric material). Secondly, the physical separation of the electric and magnetic fields permits separate interaction with both magnetic and electrically sensitive devices at different locations, potentially

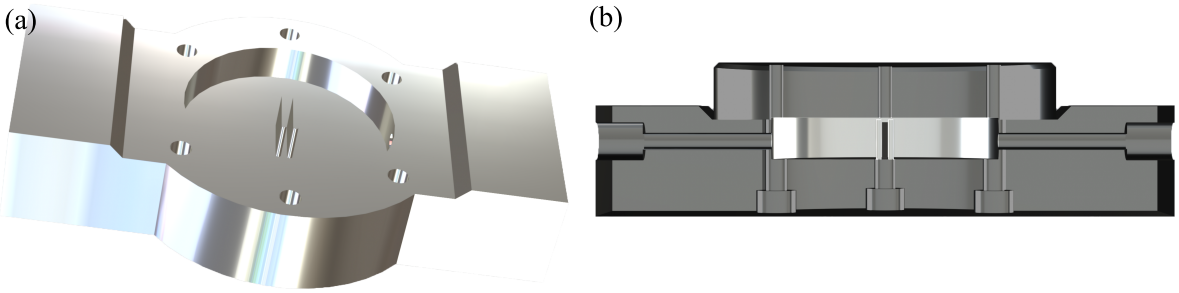

FIGURE 5.1: Double re-entrant cavity (a) without the lid; and (b) profile cut where a YIG slab is positioned between the two posts.

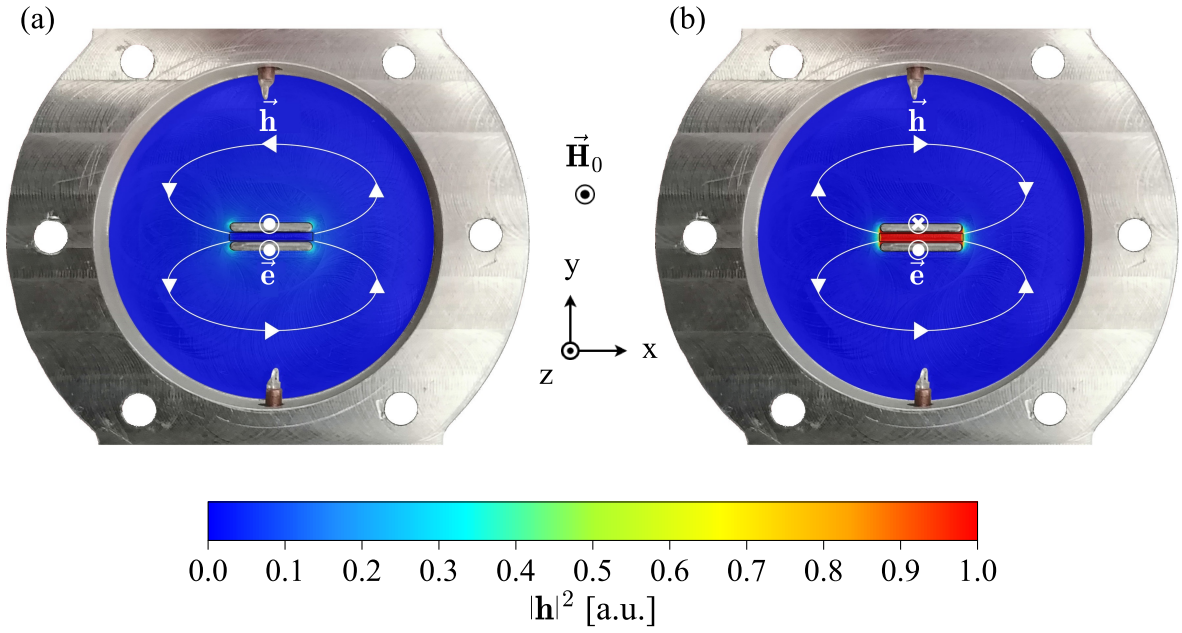

FIGURE 5.2: Re-entrant cavity with electromagnetic simulation using COMSOL Multiphysics® overlay where $|\mathbf{h}|^2$ is displayed for the first two photonic modes: (a) the DM; and (b) the BM.

simultaneously. Finally, the magnetic field focusing between the posts results in extremely strong interactions with any magnetically susceptible material placed there.

5.3 Optimization

An appropriate optimization of the cavity allows one to maximize the coupling and to obtain a quasi-homogeneous **h**-field inside the YIG slab. With the use of Finite Element Modeling (FEM) and following the procedure described by Bourhill et al. (2020) [110], we were able to precisely predict and therefore optimize prior to construction, the cavity frequency, frequency tuning range, and the coupling strength, we recall writes as (see Sec. 3.3):

$$\frac{g}{2\pi} = \eta\sqrt{\omega_c}\frac{\gamma}{4\pi}\sqrt{\frac{\mu}{g_{\mathrm{L}}\mu_{\mathrm{B}}}\mu_0\hbar n_{\mathrm{S}}}, \tag{5.3}$$

where $\gamma = 2\pi$ 28 GHz.T^{-1} is the gyromagnetic ratio for YIG, $g_{\mathrm{L}} = 2$ is the Landé g-factor for an electron spin, μ_0 is the vacuum permeability, μ_{B} is the Bohr magneton, $\mu = 5\mu_{\mathrm{B}}$ is the magnetic moment at each Fe atom site, $n_s = 4.22 \times 10^{27}$ m^{-3} is the spin density for YIG [110]. It is worth noting that the spin density value has been a point of confusion in the literature. Bourhill et al. (2020) [110] provides the exact value based on lattice considerations, where $n_s = (a^3/8)^{-1}$ with $a = 12.376$ Å, as the spin is shared by eight distinct unit cells in the cubic crystal lattice (hence the 1/8 factor) [204]. The filling factor η is expressed as:

$$\eta = \frac{\sqrt{\left(\int_{V_m} \mathrm{d}^3\mathbf{r}\, \mathbf{h}\cdot\mathbf{x}\right)^2 + \left(\int_{V_m} \mathrm{d}^3\mathbf{r}\, \mathbf{h}\cdot\mathbf{y}\right)^2}}{\sqrt{V_m \int_{V_c} \mathrm{d}^3\mathbf{r}\, |\mathbf{h}|^2}}. \tag{5.4}$$

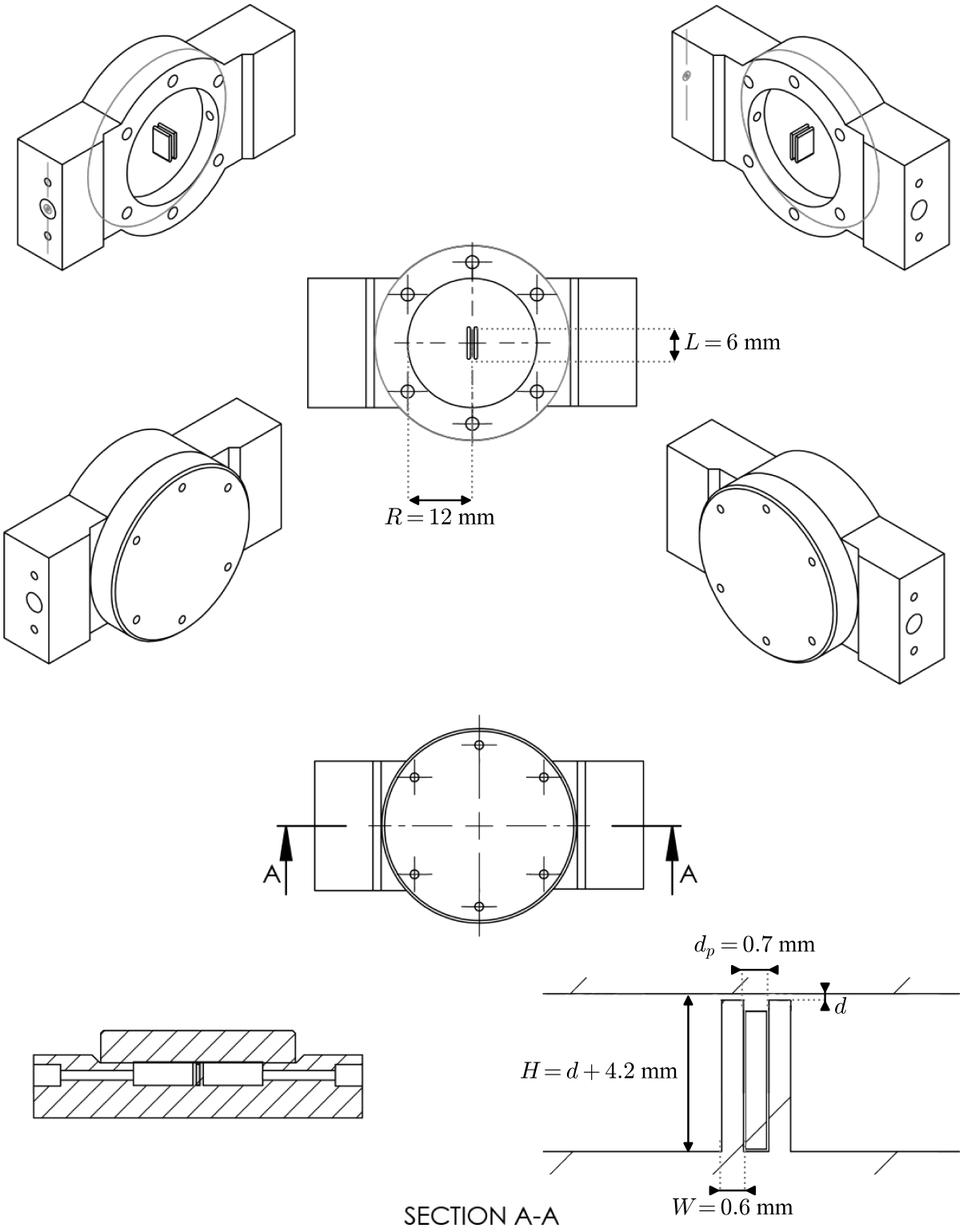

FIGURE 5.3: Technical drawing of the double re-entrant cavity with the optimized parameter values.

The optimization of the cavity design was based on the maximization of the filling factor η and the **h**-field homogeneity at the first BM inside the YIG slab. For a correct distribution of the RF field inside the cavity (seen as a Perfect Electric Conductor, PEC), it is necessary to consider the electrical property of the YIG, namely a relative dielectric permittivity of 15. Dynamic magnetic properties are not useful at this stage and the material is treated as a simple dielectric, with the Polder tensor being neglected.

The optimization was carried out for a fixed value of the distance d between the posts and the lid of the cavity ($d = 50$ μm). Then, there exist only three free parameters for the optimization of the hybrid system, two for the size of the posts, the width W and the length L, and one for the cavity, the radius R. The other parameters such as the height of the posts ($H = 4.2$) mm and the distance between the posts ($d_p = 0.7$) mm were fixed by the constraints imposed by the YIG dimension and the cavity manufacturing accuracy. The cavity parameters with their optimized values are given in the technical drawing in Fig. 5.3.

As depicted in Fig. 5.4, the containment of the **h**-field inside the YIG is at its maximum when the post dimensions are of the slab dimensions. Hence, the width of the posts has been optimized over a range from 0.1 mm to 2 mm, and their lengths from 4 mm to 8 mm. The radius of the cavity does not have a big impact on η. The cavity radius has been optimized over a range from 10 mm to 14 mm. Each contour represents the value of η with respect to W and L. The hashed contour delimits the surface where $\eta \geq 78.5\%$. For better feasibility, we choose the largest values of W and L. This leads to an optimal value of η for $W = 0.6$ mm, $L = 6$ mm, and $R = 12$ mm.

The simulated evolution of the two eigenmodes (DM and BM) are shown in the inset of Fig. 5.5 (a) with respect to the distance d, with a range from 1 to 100 μm. Decreasing d will decrease the frequency of the eigenmodes and the frequency difference between the BM and the DM. Fig. 5.5 (a) shows electromagnetic simulation results for η (right y-axis) and g/ω (left y-axis) versus d for a cavity with the optimized dimensions, where

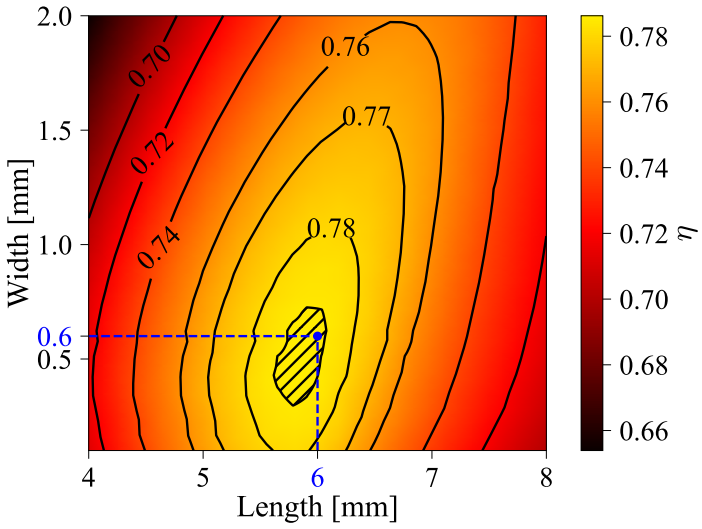

FIGURE 5.4: Filling factor η function of the width (W) and the length (L) of the two posts.

$\omega = \omega_{\mathrm{BM}}$ the frequency mode of interest in our study. η is maximized for $d = 9$ μm. The variation of η over this range of d values is only 2.7%, therefore we may consider it more or less invariant. The tuneability of the distance d plays a role on the g/ω ratio as shown in Fig. 5.5 (a). Indeed, $\omega/2\pi$ is decreasing with d, and η is remaining almost constant. Considering Eq. (5.3), $g/2\pi$ is a function of η and the square root of ω. Therefore, the ratio g/ω will increase with the inverse of the square root of ω from 36.8 to 80.5% as d decreases from 100 to 1 μm.

Fig. 5.5 (b) illustrates the SC to DSC transition for YIG with the frequency dependence of g/ω. The blue dots correspond to the values extracted from EM simulation already discussed in Fig. 5.5 (a) and the solid line dependencies are based on Eq. (5.3) for two constant values of η, 0.79 (blue) and 1 (green). The magnetic properties of YIG require working in a specific frequency range in order to explore the DSC. For the maximum reachable value of η (green line), which corresponds to the entire **h**-field perpendicular to $\mathbf{H}_0$ and fully confined to $\mathbf{V}_m$, DSC is possible when the magnons are coupled to a microwave mode below 1.72 GHz [110]. In our case (with η close to 0.79), DSC is achievable but at a smaller resonant frequency (1.07 GHz). Note that the optimized cavity configuration of this work does not allow to reach the DSC due to the presence of the dark mode which

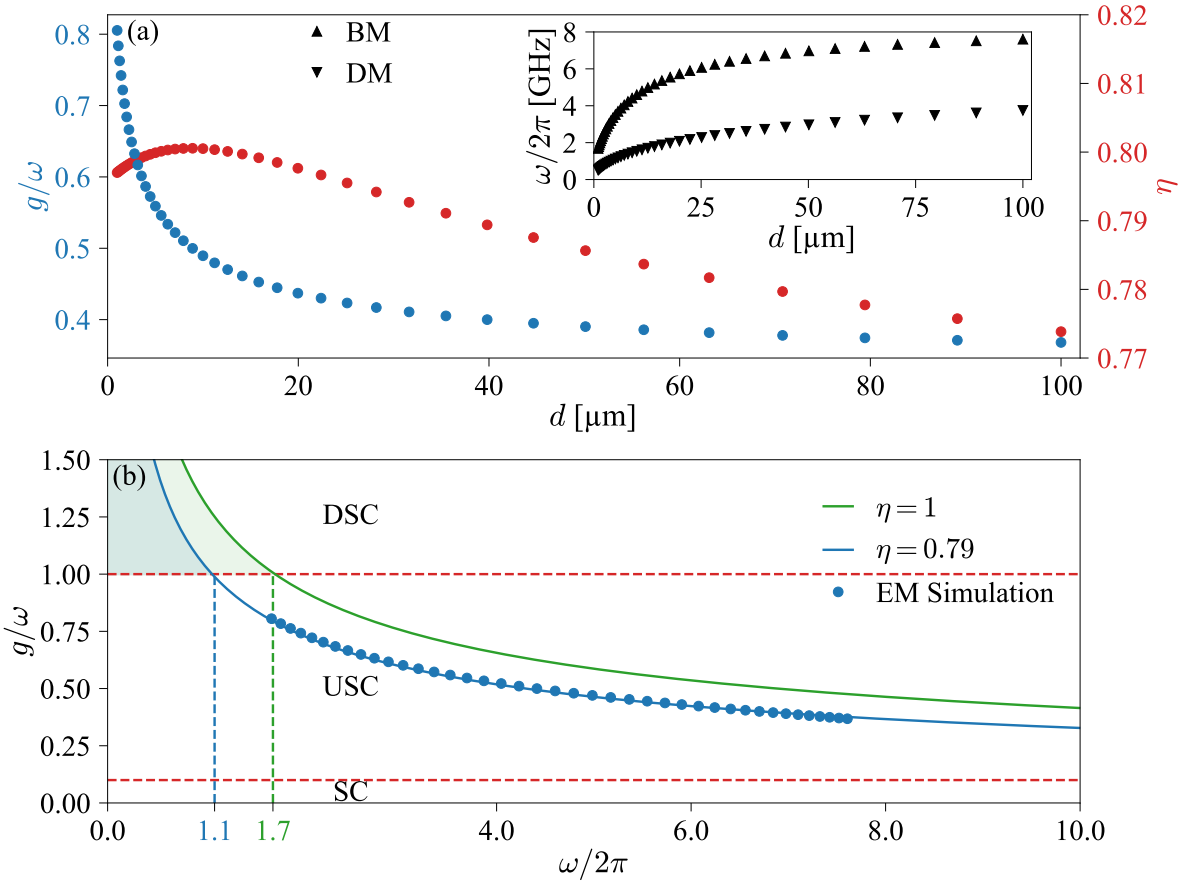

FIGURE 5.5: (a) Evolution of the ratio g/ω (with $\omega = \omega_{BM}$) in blue and η in red versus d for Eigen-Mode simulations (EM). Inset: Evolution of simulated DM and BM frequencies versus d. (b) Evolution of g/ω versus the BM frequency for $\eta = 1$ and $\eta = 0.79$.

prevents clear identification of the coupling signature in the spectra when the DM and BM are close, and the difficulty to control distance d lower than 4 μm.

5.4 Results and Discussion

5.4.1 Simulation Details

To compare the experimental results, simulations in the frequency domain (FD), solving for the S_{21} scattering parameter were conducted for different values of d from 2 to 100 µm. For these simulations, we considered the excitation probes and hence the coupling losses. Losses due to finite conductivity of the cavity walls are also taken into consideration.

The static and dynamic magnetic properties of YIG are used to solve the frequency response of the entire system as a function of the applied magnetic field. The spin dynamics of ferrimagnetic systems can be described by the Landau-Lifshitz-Gilbert (LLG) equation and the frequency dependence of the coupled dynamics can be accurately estimated by using a linear solution of the LLG equation in solving Maxwell's equations. Some consideration regarding the shape of the YIG sample must be taken into account. As mentioned in Sec. 2.3.2.c, the FMR dispersion for a relatively thick slab geometry requires careful consideration. Based on the works of Kittel (1948) [118], Schlömann (1962) [117], the demagnetizing field expression has been adapted to our non-ellipsoidal sample of YIG. From these results, it is determined that the demagnetizing field is significantly different from the thin-film form, and therefore for accurate simulations proper consideration of this difference must be taken into consideration.

Hence, considering Eq. (2.117a) the effective static magnetic field in the YIG is different from the applied one and read as:

$$H_i = H_0 - N_{zz}(x, y, z)M_s, \tag{5.5}$$

where H_i is the internal static magnetic field along the z-axis, and N_{zz} is the spatially dependent demagnetizing component along the z-axis, given in Eq. (2.123). Note that the off-diagonal components of the demagnetizing tensor are equal to zero for the considered slab dimensions, leading the effective field H_i to be only in the z-axis. More details about the simulations are given in Sec. 4.1.

5.4.2 Experimental Setup

To reach the specifications described above, an aluminum cavity with an accuracy of 20 µm has been machined. For the applied static magnetic field, we used an electromagnet where the produced field is aligned along the z-axis (see Fig. 5.2), in the direction of the height of the posts. H_0 aligns all the spin moments along the z-axis and to saturate the macroscopic YIG magnetization. With the shape of the cavity, the h-field for the BM, considered as the perturbative field, is only along the x-axis inside the YIG slab between the two posts, as shown in Fig. 5.2 (b) due to the constructive interference of the two h-fields around each post. A gaussmeter allows one to measure in situ H_0 magnitudes. S-parameters are measured with a two-port Vector Network Analyzer (VNA), with the

magnitude and phase of the scattering parameters recorded between 0.1 to 15 GHz with an input power of −10 dBm. All measurements are conducted at RT. The magnitude of the S_{21} transmission spectra as a function of H_0 are displayed in Fig. 5.6 for measurement and simulation with differing sized gaps between the top of the posts and the roof of the cavity. Experimentally, this is varied by using different cavity lids which had recesses of differing heights machined into them. More details about the experimental setup are given in Sec. 4.3.

5.4.3 Results

Measurement and simulation results of magnetic spectroscopy of the cavity magnon system are shown in Fig. 5.6 as the first and second column, respectively, for different values of d. Each row represents a comparison between a measurement and a simulation with a distance close to the measured value. The latter can be determined by the unperturbed value of f_{DM}, which acts as a calibration for d.

The external magnetic field was always applied symmetrically for negative and positive values. This allows to improve the fit accuracy on measurements, because we have twice as many data points. All measurements with complete frame are shown in Appendix 5.A.

We can easily distinguish the two hybrid eigenfrequencies $f_+ = \omega_+/2\pi$ (for the higher branch) and $f_- = \omega_-/2\pi$ (for the lower branch) from either side of the BM frequency. It should be noted that at low H_0 values the BM is not visible, whilst we can clearly see the DM which is the lowest frequency mode and has a negligible coupling with the magnon mode, hence is constant versus H_0.

Some minor discrepancies between simulation and experiment should be pointed out:

(i) an inflection point on the curvature of the upper CMP in frequency at low H_0 (observed only in the USC regime) for measurements, appearing neither in simulation nor analytic fits;

(ii) anti-resonances only appearing either in measurement, the horizontal one around 4.3 GHz in Fig. 5.6 (a) and (e), or in simulation with a S-like shape, around 10, 4, and 2 GHz in respectively Fig. 5.6 (b), (d) and (f). Let us notice that this anti-resonance does not appear in measurements when a cavity mode is overlapping with this transmission dip, as shown for $d = 11$ µm in Fig. 5.6 (c) and Fig. 5.19 (e), and for $d = 116$ µm in Fig. 5.19 (a). However, the study on antiresonances in Chapter 6 allows for a clear identification of two behaviors: the first involves a cavity antiresonance coupling with magnons, mediated by the magnon's interaction with different cavity modes; the second describes a non-coupled cavity antiresonance, which depends on the various cavity mode frequencies and their associated dissipations;

(iii) another magnon mode exists near the upper CMP in simulations. It is clear that it is another magnon mode because its **H**-field's frequency dependence does not change as d is varied.
Differences given in the two last points could be explained by the fact that the YIG sample is a perfect rectangular prism in simulation whereas the real sample is not. The imperfections of the YIG geometry could result in a weak transmission, which could be not detected in measurement.

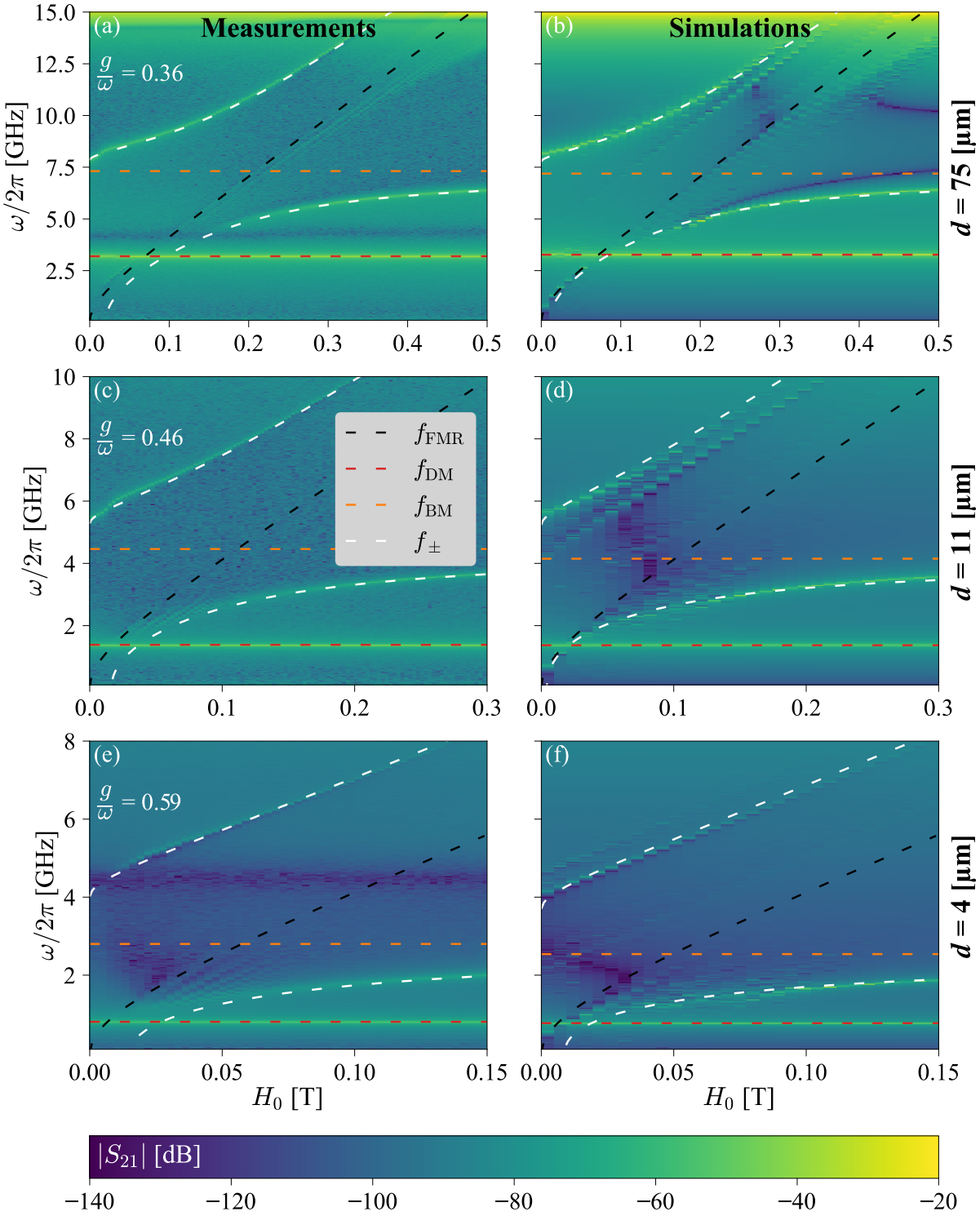

FIGURE 5.6: Transmission spectra versus frequency and H_0 for (a), (c), (e) measurements at RT, and (b), (d), (f) simulations. Comparison spectra between measurement and simulations are shown for different distances d as labelled. A fit with the Dicke model with a shifted magnon frequency is shown superimposed on (c) and (d) where the FMR frequency ($f_{\mathrm{FMR}} = \omega_{\mathrm{FMR}}/2\pi$) is shown in black, the DM frequency ($f_{\mathrm{DM}} = \omega_{\mathrm{DM}}/2\pi$) in red, the BM frequency ($f_{\mathrm{BM}} = \omega/2\pi$) in orange and the two polariton frequencies ($f_{\pm} = \omega_{\pm}/2\pi$) in white.

Despite these minor deviations, the agreement between simulations and measurements on the magnon-photon coupling and the resulting CMPs is excellent. In particular, we validated the spatial distribution of the demagnetizing field, hence the expression of the FMR for a slab, and the ability of the Maxwell's equations to describe the system. This permits one to conduct a simulation with a magnetic field larger than experimentally possible in order to extract the BM frequency. Indeed, it is impossible to measure the unperturbed BM frequency f_{BM} in the USC regime even when applying a high magnetic field near to 2 T.

5.4.4 Model Description

In the USC regime, the Tavis-Cummings model becomes no longer applicable [127, 190], as $g/\omega > 0.1$ leads to a failure of the rotating wave approximation as the interaction term of the Hamiltonian can no longer be assumed to be "slowly rotating" compared to the system terms. As mentioned in Sec. 3.3, the standard model for cavity magnonics is the Dicke model, with polariton angular frequency given by (c.f. Sec. 3.2.6.b):

$$\omega_{\pm} = \frac{1}{\sqrt{2}}\sqrt{\omega_c^2 + \omega_m^2 \pm \sqrt{(\omega_c^2 - \omega_m^2)^2 + 16g^2\omega_c\omega_m}}. \tag{5.6}$$

Additionally, as explained in Sec. 3.2.6.b, the system enters in the superradiant phase when $g \geq \sqrt{\omega_c\omega_m}$. In this phase, the eigenfrequencies of the two polaritons become:

$$\omega_{\pm} = \frac{1}{\sqrt{2}}\sqrt{\omega_c^2 + \omega_m^2\tilde{g}^4 \pm \sqrt{(\omega_c^2 - \omega_m^2\tilde{g}^4)^2 + 4\omega_c^2\omega_m^2}}. \tag{5.7}$$

where $\tilde{g} = 2g/\omega_c$.

We notice that the Dicke model in its normal and superradiant phase cannot describe observed polariton frequency dispersion for measurements and simulations. Indeed, in

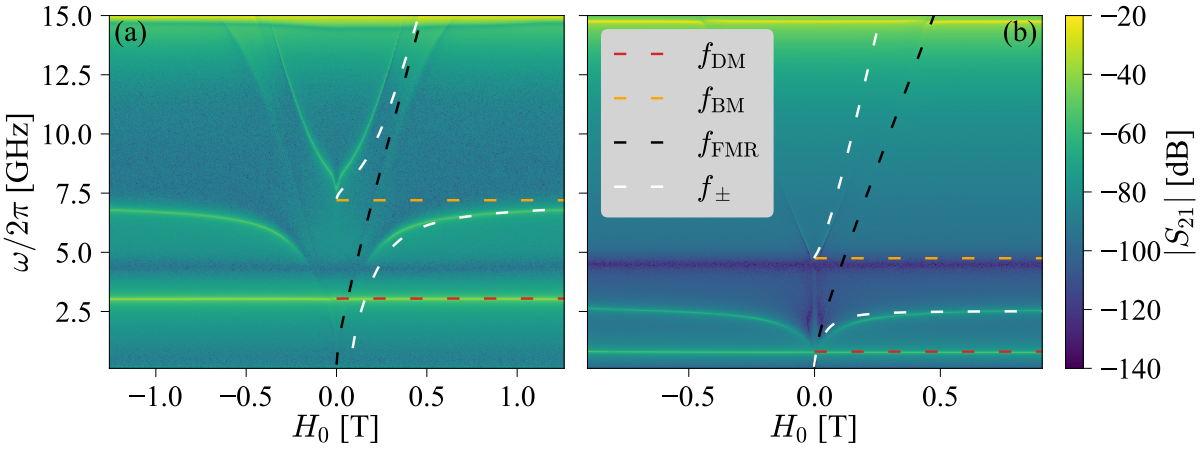

FIGURE 5.7: Transmission spectra versus the RF frequency and the **H**-field for (a) $d = 65$ µm and (b) $d = 4$ µm. The DM frequency is shown in red while the FMR frequency is shown in black. The BM (in orange) and the CMP frequencies (in white) were fitted with the Dicke model in its (a) normal phase and (b) superradiant phase.

Fig. 5.7, is depicted two measured transmission spectra at (a) $d = 65$ µm and (b) $d = 4$ µm. According to the results from the EM simulation illustrated in Fig. 5.5, these two spectra would depict a system performing in the normal phase in Fig. 5.7 (a), and superradiant phase in Fig. 5.7 (b). In Fig. 5.7 (a), the two eigen-modes of the fit with the Dicke model in its normal phase shown in dotted white line which are not consistent with the measurement, and prove the inability to fit with the standard Dicke model.

Moreover, in Fig. 5.7 (b), the fit with the superradiant phase, seems to be consistent with the measured transmission spectrum. However, the fitted parameters are $\omega_c = 4.75$ GHz, and $g = 2.58$ GHz conversely to $\omega_c \sim 3.2$ GHz and $g \sim 1.9$ GHz considering results from EM simulation. This mismatch means that the superradiant phase does not occur, and that the Dicke model is not able to describe the physics of the system in the USC regime.

As mentioned in Sec. 3.2.6.c, the diamagnetic term D is negligible for the magnon-photon coupling. Indeed, it has been recently shown in Ghirri et al. (2023) [146] that in the USC regime (here for a system composed of a magnetic film in contact with superconducting resonator) the magnon-photon coupling does not follow the Hopfield model. For the sake of completeness, we decided to follow the methodology used in Keller et al. (2020) [205], where it was demonstrated that the physics of Landau polaritons is described by a Hopfield-like model where the diamagnetic term is scaled by a parameter ξ. In this study, it has been found that the parameter ξ is lower than one for Landau polaritons. Then, the angular eigenfrequencies in the Hopfield model given in Eq. (3.48) become:

$$\omega_{\pm} = \frac{1}{\sqrt{2}}\sqrt{\omega_c^2 + \omega_m^2 + 4\xi g^2 \pm \sqrt{(\omega_c^2 - \omega_m^2 + 4\xi g^2)^2 + 4g^2\omega_c\omega_m}}. \tag{5.8}$$

In Fig. 5.8 is depicted the transmission spectrum for $d = 65$ µm, and also a fit with the Hopfield-like model with ξ being (a) less, (b) equal (leading to the standard Hopfield model), and (c) more than one. As illustrated, the only effect of this prefactor is equivalent to increase (for $\xi < 1$) or decrease (for $\xi > 1$) the BM frequency, whereas it is needed to

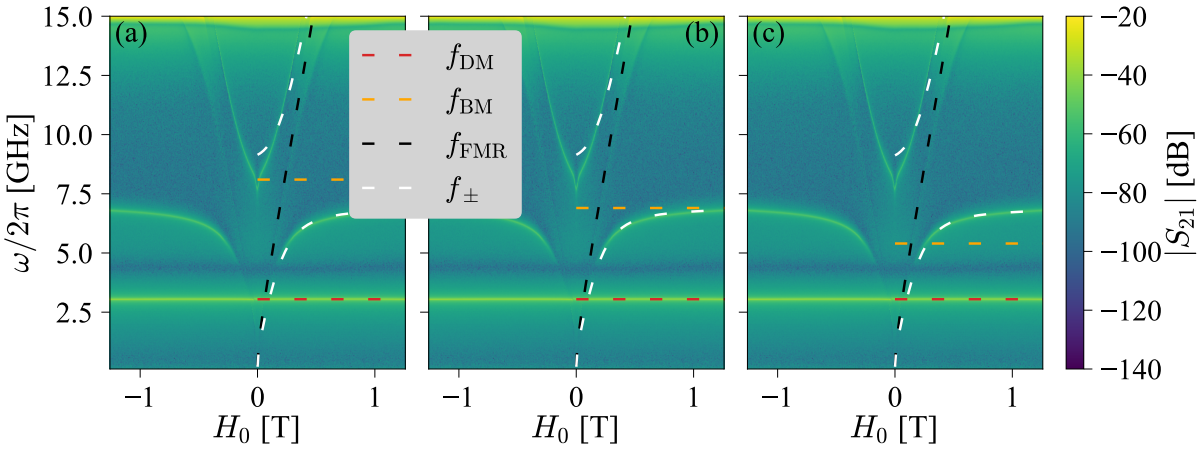

FIGURE 5.8: Transmission spectra versus the RF frequency and the **H**-field for $d = 65$ µm. The DM frequency is shown in red while the FMR frequency is shown in black. The BM (in orange) and the CMP frequencies (in white) were fitted with the Hopfield-like model where the prefactor is (a) $\xi < 1$, (b) $\xi = 1$, (c) $\xi > 1$.

have a model which affects the FMR. Finally, the Hopfield model, even modified, is not able to describe the physics of the magnon-photon coupling in the USC regime.

To remedy these issues, it has been proposed by Golovchanskiy et al. (2021) [84] to modify the Dicke model with the addition of a **H**-field in the FMR dispersion equation. We also modified the term of the FMR frequency dependence in Eq. (2.127) to:

$$\omega_m \rightarrow \omega_m + \Delta_m \tag{5.9}$$

here $\Delta_m = 2\pi f_\Delta$ is a frequency shift, which will be further discussed in Sec. 5.4.5. This modified Dicke model was found to fit best the experimental and simulation spectra, as seen in the white dashed lines of Fig. 5.6 for $d = 75$ μm in (a) and (b), $d = 11$ μm in (c) and (d), and $d = 4$ μm in (e) and (f). Measurement fit, shown in Fig. 5.6 (a), (c), and (e), is achieved with the BM frequency f_{BM} (in orange), the coupling strength $g/2\pi$, and the added frequency f_Δ as fitting parameters. For simulation fit, shown in Fig. 5.6 (b), (d), and (f), the BM frequency is considered as fixed parameter. Indeed, simulations were performed at an artificial high **H**-field ($H_0 = 10$ T), in order to tune the magnon mode many orders of coupling strength away, and clearly distinguish the two photonic modes.

All values of fit parameters for measurements are available in Appendix 5.A, and are pooled with simulations in Fig. 5.9. For the measurements (shown in blue), the distance d has been estimated from the measured DM frequency. The fitted BM frequencies of the measurements are in good agreement with simulations (shown in black in the inset of Fig. 5.9). Regarding the coupling strength g/ω, we achieve a ratio g/ω ranging from 0.35 to 0.59, corresponding to $d = 116$ μm to $d = 4$ μm, respectively. As mentioned in Sec. 5.2, the values of g/ω are different from the optimization step ones (dotted red curve), mainly due to the different estimated frequencies, shown in the inset. Once again, the correlation between fitted simulations and measurements for the ratio g/ω are also good. This clearly demonstrates the validity of the simulations.

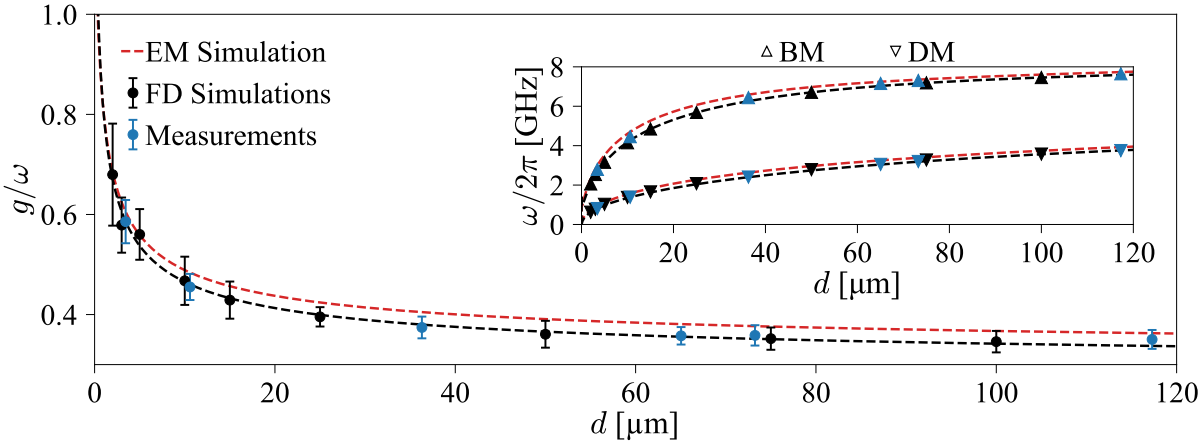

FIGURE 5.9: g/ω versus d for fitted FD simulations (in black) and for fitted measurements (in blue). The simulation trend is plotted in the black dashed line. Inset: DM and BM frequencies versus the distance d, in the black dashed line are shown DM and BM reading values from simulations at extremely high applied **H**-field. Eigen-Mode (EM) simulations are shown as the red dashed line.

5.4.5 Discussion

We discuss here the physical meaning of the frequency shift in the modified Dicke model. For a deeper understanding of the behavior of this added term, we investigated the transition between the SC and the USC regimes. In order to study a wide range or g/ω values, we have used two other cavities with the same YIG sample. The first described machined cavity will be named "CAV_{01}" in the following. This cavity operates in a g/ω range from 0.35 to 0.59, as mentioned in the Table 5.2 in Appendix 5.A.

The second cavity, "CAV_{02}", has been 3D printed and has the same shape as CAV_{01}, but with smaller height posts. This cavity is performing in a certain range of g/ω, from 0.28 to 0.32 (see Table 5.3 in Appendix 5.B).

The third cavity, "CAV_{03}'", is also a double re-entrant 3D printed cavity with cylinder posts, adjustable in height. This cavity was used in a previous work [110] to experimentally verify a reworked theory that predicts coupling values from simulations alone. The cavity has radius $R_{cav} = 20$ mm and height $H_{cav} = 4.6$ mm, whilst the posts have radius $R_{post} = 2.05$ mm and are spaced to 2.7 mm. The operating ratio g/ω is lower than the two other cavities and enables to have experimental results at the SC/USC threshold, with g/ω comprised between 0.12 and 0.25 (see Table 5.4 in Appendix 5.C).

The operating range in BM frequencies, coupling strengths, and added frequencies for the three cavities are summarized in Table 5.1.

TABLE 5.1: Operating range of the cavities

Cavity	f_{BM} [GHz]	$g/2\pi$ [GHz]	$\Delta_m/2\pi$ [GHz]
CAV_{01}	2.80 - 7.65	1.64 - 2.68	2.27 - 2.59
CAV_{02}	7.63 - 9.79	2.42 - 2.72	1.63 - 1.74
CAV_{03}	2.35 - 5.53	0.58 - 0.69	0.29 - 0.50

Thanks to the validation of the FD simulations, we were able to simulate the CAV_{01} design for different dimensions of the YIG slab, while keeping the aspect ratio of the slab constant. Since the demagnetizing components described in Eq. (2.123) are only dependent on this aspect ratio, the FMR remains unchanged. However, still decreasing the YIG slab dimensions decrease the filling factor η, therefore the coupling strength and g/ω from 0.36 to 0.05 with $d = 50$ μm.

We plotted Δ_m/ω versus g/ω in Fig. 5.10 (a) which clearly display a quadratic dependence. For $g/\omega \leq 0.1$, Δ_m/ω is more or less negligible. This description agrees with the commonly situated transition point (shown as the red dotted line) between the SC and USC regimes where all models converge. Our simulations show the need for the $\Delta_m/2\pi$ parameter to properly fit the data. Fig. 5.10 (b) shows that $\Delta_m/2\pi$ is linearly proportional to η^2. According to this observation and the definition of η, we noticed that the more this energy is confined in the YIG, the larger the shift in the magnon frequency will be. In the literature, the parameter η is not so often considered or estimated. In ref [110], we had the opportunity to test the model of Eq. (5.3) and (5.4) on multiple published experimental results, and η rarely exceeds 0.05 in any of them. As a reminder, and in view of the description in Fig. 5.5, our system (CAV_{01}) proposes a η of about 0.79.

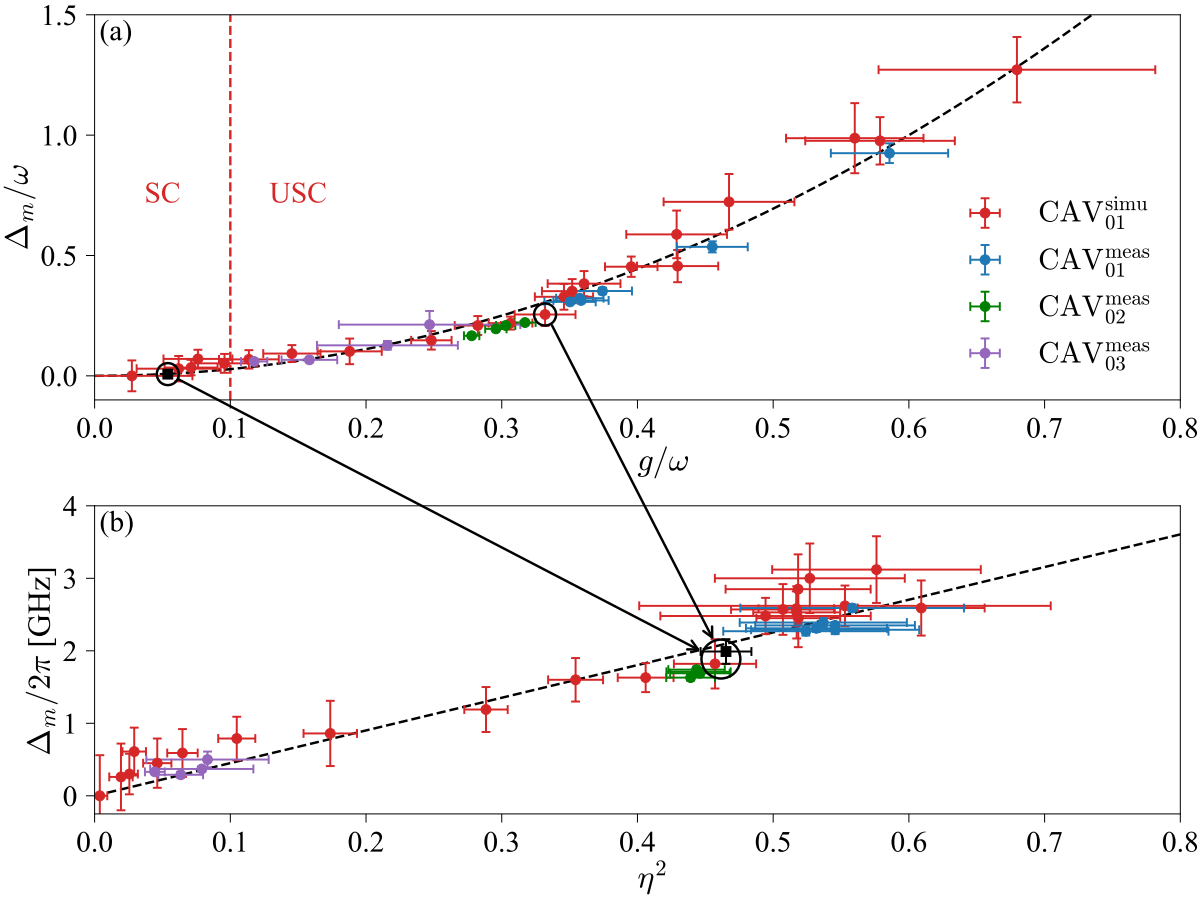

FIGURE 5.10: (a) Δ_m/ω versus g/ω and (b) $\Delta_m/2\pi$ versus η^2. Shown are the FD simulations on CAV_{01} in red and measurements in blue, in green for CAV_{02}, and in purple for CAV_{03}. In (a) and (b), fitted values for a reduced CAV_{01} with an aspect ratio equal to 0.025 as the black square. The two data points circled in (a) correspond to the same value of $\Delta_m/2\pi$ in (b).

In Fig. 5.10 is represented by square marker a simulation where dimensions of the cavity and the YIG are reduced by a ratio equal to 0.025 for $d = 50$ μm. By decreasing the dimensions of the entire cavity CAV_{01} by this ratio, the BM frequency is increased to 275 GHz. Then, this cavity operates in the SC regime. However, the proportion of the **h**-field in the YIG remains the same, hence also η.

In Fig. 5.10 (a), are circled the reduced system performing in the SC regimes, and the unmodified cavity in the USC regime presenting the same η value. In Fig. 5.10 (b), it is shown that the frequency shift $\Delta_m/2\pi$ is the same for both cavities, and for the same value of η^2. It is then important to note that this effect is not bounded to the coupling strength and hence to the coupling regime, but instead to the filling factor, something that has never been discussed so far.

Considering Eq. (5.3), $\Delta_m/2\pi$ is also linearly proportional to g^2/ω which is a dependent function of the magnetic properties of the YIG and η^2. As a physical mechanism, we have identified two nonlinear processes that could be involved in the appearance of $\Delta_m/2\pi$ in this study, due to their similar behavior: the multi-photon Rabi oscillations [74, 75, 182] for its effective coupling being proportional to g^2/ω. When the coupling between an artificial

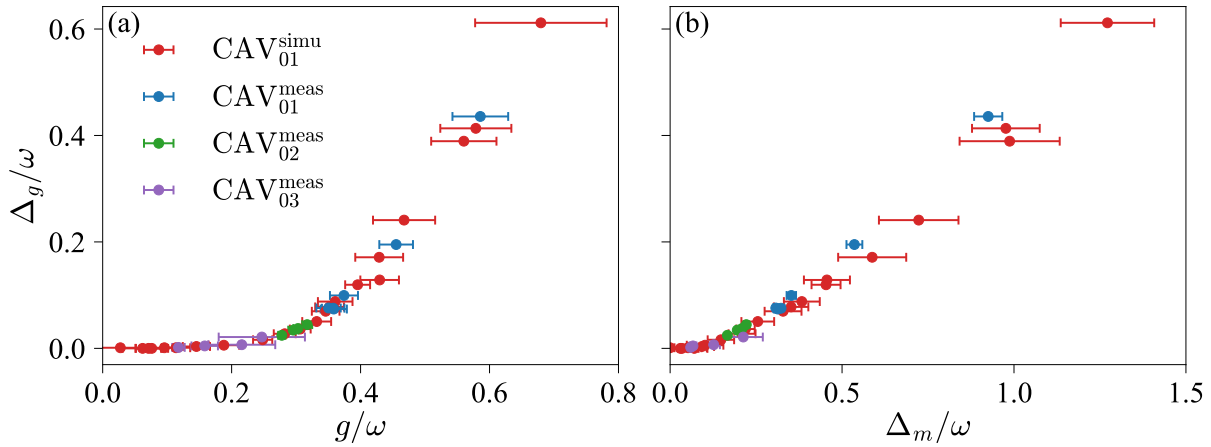

FIGURE 5.11: Δ_g/ω versus (a) g/ω; and (b) Δ_m/ω. Shown are the FD simulations on CAV_{01} in red and measurements in blue, in green for CAV_{02}, and in purple for CAV_{03}.

single atom and a cavity is in the USC regime, the system can exchange several photons (and undergo multi-photon Rabi oscillations) instead to a single one (commonly known as Rabi oscillation); and the self-Kerr, and the cross-Kerr effects [206–210] presenting a frequency shift of the magnon, due to magnetocrystalline anisotropy and magnon-magnon interactions, respectively.

As a remark, we note an offset far detuned from the BM frequency at a zero **H**-field arising for high g/ω when the FMR is shifted. This offset in frequency, when the FMR is shifted, leads to a forbidden gap in frequency, noted Δ_g, where there is no resonance linked to the CMP. Without adding the shift Δ_m to the FMR in the Dicke model, and without applied **H**-field, the frequency of the upper polariton is equal to the cavity one. Considering Fig. 5.11, Δ_g/ω is not observable when g/ω is equal or lower to 0.2. For higher g/ω values, Δ_g/ω is quadratic, as shown in (a). In (b) is shown the evolution of Δ_g/ω versus Δ_m/ω.

5.5 Conclusion

In conclusion, we proposed a double re-entrant cavity design to achieve USC magnon-photon coupling at microwave frequencies, which was supported by both experimental data and electromagnetic simulations. To the best of our knowledge, this is the only demonstration of USC magnon-photon coupling at room temperature so far. Noteworthily, reaching the USC without cryogenic temperatures is promising for the development of RF applications based on cavity spintronics.

We explained the importance of optimizing the filling-factor η for reaching the USC, aside from just the frequency of the resonator and the spin density. Importantly, the cavity we proposed is parametrized by the distance d between the posts and the lid. We showed that tuning this parameter allowed to continuously go from the regular SC to the USC regime. The ability to study the transition from the SC to USC regime is a significant step towards understanding the physics of USC magnon-photon coupling.

Indeed, we showed that the standard models describing the coupling of a single resonator mode to many dipoles (e.g. the Dicke and Hopfield models) failed to properly describe our experimental data. Nevertheless, thanks to the validation of our electromagnetic simulations, we showed that a frequency shift in the magnon frequency adequately modelled our data, which we note is fully captured by the classical Maxwell's equations. Furthermore, we showed that this frequency shift only depended on the filling-factor η, highlighting its importance for hybrid magnon-photon systems. While the physical origin of the magnon's frequency shift is still unknown, we hope that its relation with η will motivate further research into deriving a proper theoretical model for USC magnon-photon coupling.

5.6 Further Works

In this section, is presented a study which could help to the understanding of the physical meaning of the added shifted magnonic frequency term. This section outlines two different approaches to achieving the DSC regime. These methods are similar to those employed in the initial study. After maximizing the filling factor η, and consequently the coupling strength g, we explored various strategies to reduce the cavity frequency ω, with the aim of increasing the ratio g/ω.

The first method in the study aimed to maximize g/ω by reducing the distance d between the top of the posts and the lid in the double re-entrant cavity. Experimentally, the minimum achievable distance was 4 µm, resulting in $g/\omega = 0.59$. An untested approach involves depositing a thin dielectric layer (several hundred of nanometers) on the top of the posts using chemical vapor deposition (CVD). According to Fig. 5.5 (a), this could increase g/ω to 0.81 with $d = 1$ µm, and even higher for $d < 1$ µm. However, increasing the coupling strength could cause the lower polariton to overlap with the DM, potentially complicating the observation of the coupling in the transmission spectra.

5.6.0.a 1 post connected

Considering the work by [110], it has been demonstrated that the DM and BM frequencies can be independently tuned by adjusting the distances d_1 and d_2 of the posts (refer to Fig. 5.12 (c) for the schematic). Specifically, the BM is only slightly affected by tuning one of the post distances, whereas the DM is primarily influenced by the post with the smaller distance.

In Fig. 5.12 (a), the distance d_1 of one post is kept constant at 50 µm, while the distance d_2 of the other post is tuned from 100 µm to 0 µm. We observe that the DM exhibits a behavior similar to when both posts have the same distance d (c.f. Fig. 5.5 (a)), approaching zero when one of the posts is connected to the lid. However, the BM only slightly decreases with decreasing d_2, and does not exhibit the same behavior as when both posts have the same distance. When both distances are equal, i.e. $d_1 = d_2 = 50$ µm, the ratio g/ω is 0.39, while it reaches $g/\omega \simeq 0.41$ whith $d_1 = 50$ µm and $d_2 = 0$ µm as illustrated in Fig. 5.12 (b). This slight increase is due to the small decrease in the BM frequency.

When one post is connected to the lid of the cavity, the electric field is focused at the top of the other post. This configuration causes the magnetic field to circulate around

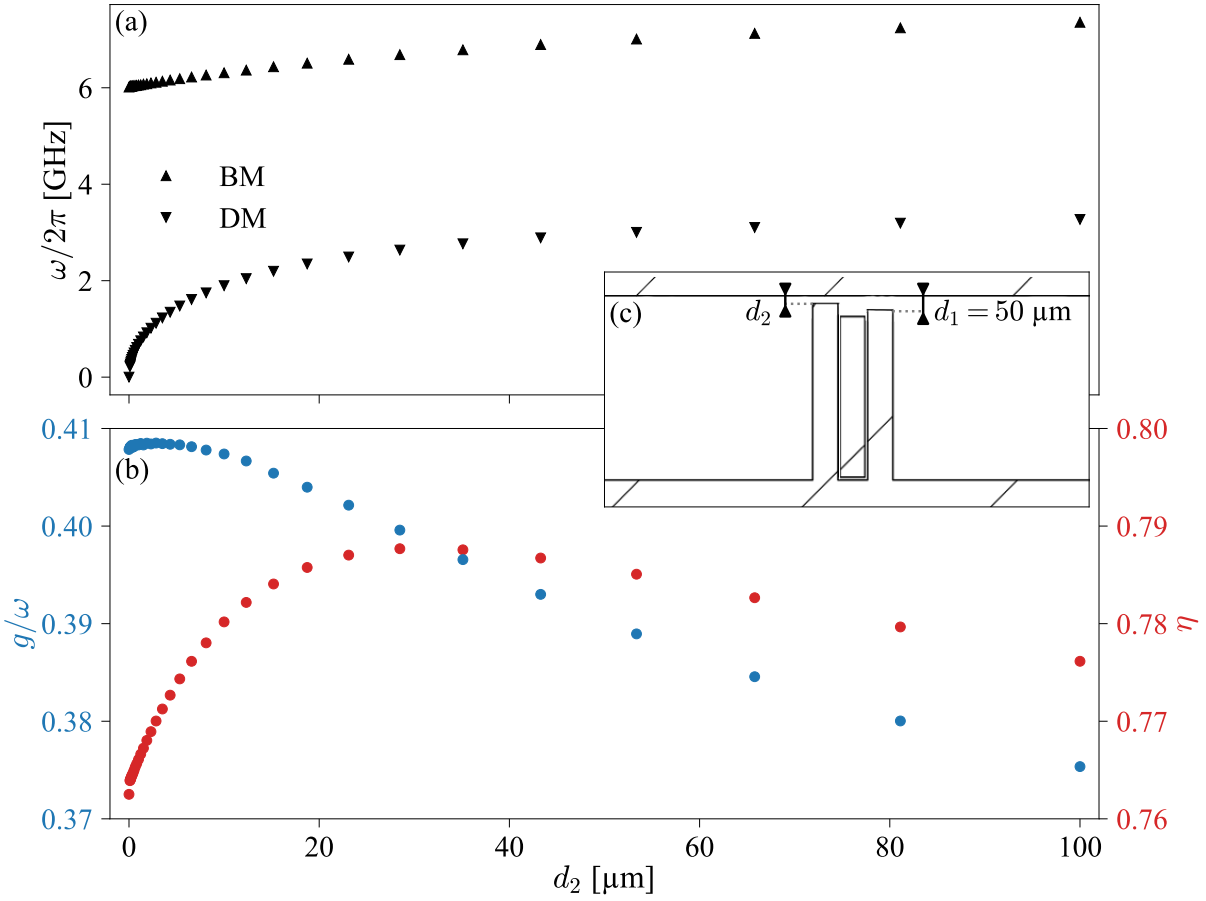

FIGURE 5.12: Evolution of (a) the DM and BM frequencies, and (b) the ratio g/ω (in blue) and η (in red) of the BM versus d_2, with $d_1 = 50$ µm for EM simulations. (c) A scheme of the parameters d_1 and d_2 in the cavity.

the post where the electric field is focused. The connected post acts as a node for the magnetic field within the cavity. Since there is no second source of focused electric field, the magnetic field around the second post is necessarily in phase with the magnetic field generated by the first post. Consequently, only the BM occurs when one post is connected to the lid, while the DM does not appear.

Connecting one post to the lid allows for the maximization of g/ω. Based on this observation, EM simulations were conducted to visualize its evolution with varying d_2, swept from 100 µm to 1 µm, while keeping $d_1 = 0$ µm. As shown in Fig. 5.13, g/ω reached 0.65 at $d_2 = 4$ µm, compared to $g/\omega = 0.59$ when both posts are $d = 4$ µm from the lid. Compared to the scenario where $d_2 = d = 50$ µm, the coupling ratio increased by 5%, while at $d_2 = d = 4$ µm, it grew by 10%. The coupling ratio would reach 0.90 at $d_2 = 1$ µm, representing an increase of 11%. However, without a new method to experimentally decrease the gap, connecting a post to the cavity does not allow for significant progress into the USC regime, nor does it enable reaching the DSC regime. Nevertheless, connecting a post suppresses the DM in the experiments and results in a slightly higher g/ω. In the following cavity design ideas aimed at reaching the DSC regime, one of the two posts remains connected to the lid of the cavity.

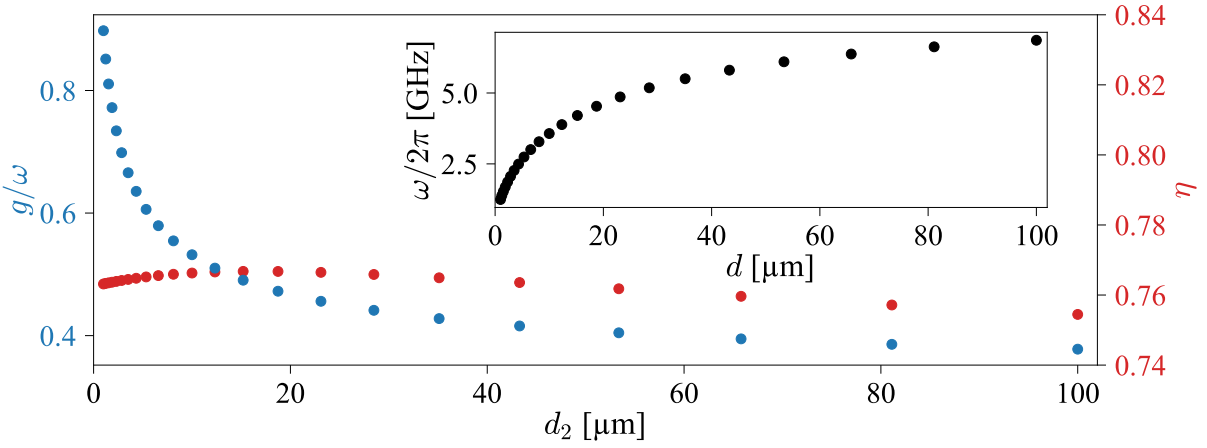

FIGURE 5.13: Evolution of the ratio g/ω (in blue) and η (in red) versus d_2, with the other post connected to the lid, for EM simulations. The inset shows the cavity mode frequency.

5.6.0.b Enlarge the post/plate

In this section, we develop a new design of cavity post in order to theoretically reach the DSC regime. We remind that the cavity frequencies are inversely proportional to the post surface S_2, due to its effective capacitance (c.f. Eq. (5.2) and (5.1a)). This means that by increasing the surface of the top of the posts would enable to increase the coupling ratio. We decided to keep the length of the post equal to $L = 0.6$ mm, with $d_2 = 10$ µm, while the width W_2 of the unconnected post is tuned from 0.6 mm to 6 mm, as illustrated in Fig. 5.14 (c). This means that the post surface is tuned from $S_2 = 3.52$ to $S_2 = 35.91$ mm^2. Fig. 5.14 (a) and (b) show the conducted EM simulations.

As depicted in Fig. 5.14 (a), the value of g/ω increases from 0.53 at a post width $W_2 = 0.6$ mm to 0.76 at $W_2 = 6$ mm (square markers). Regarding Fig. 5.14 (b), this increase in g/ω is effectively due to the decrease in the cavity frequency $\omega/2\pi$, which drops from 3.58 GHz to 1.41 GHz. However, η decreases from 0.77 to 0.69, indicating that the DSC would not be reached at $\omega/2\pi = 1.1$ GHz, as mentioned in Fig. 5.5. The thicker the post, the greater its impact on the internal electromagnetic field, hence on η.

To remedy on the decrease of the η value, and to still grew the ratio g/ω, we thought about a new post design. As depicted in Fig. 5.14 (c), the cavity on the right kept a thin post ($W = 0.6$) as in the previous subsection, but is mounted of a thin plate (presenting a height of 0.5 mm) at its top in order to keep the same surface as the post S_2, and also function of the plate width W_2. By comparison, the newly designed post presents value of η (with circle markers) more or less constant, where $\eta \simeq 0.76$. From this, the ratio g/ω reaches 0.88 at $W_2 = 6$ mm (with $\omega/2\pi = 1.28$ GHz). As a remark, the frequencies of both the two designed posts are nearly similar, indicating that the capacitive effect dominates the frequency evolution. At this stage, two cavities were designed in order to follow the ratio g/ω from 0.6 to more than 1 in the DSC regime experimentally, and are presented in Appendix 5.D. The EM values of one of these cavities, named $\text{CAV}_{01}^{\text{must}}$ are presented in Fig. 5.14 (in diamante markers) at $d_2 = 10$ µm. The second cavity is not reported because it presents a larger surface plate value. However, these cavities do not show interpretable results. Indeed, in these measurements, only the lower CMP occurs, while the upper CMP

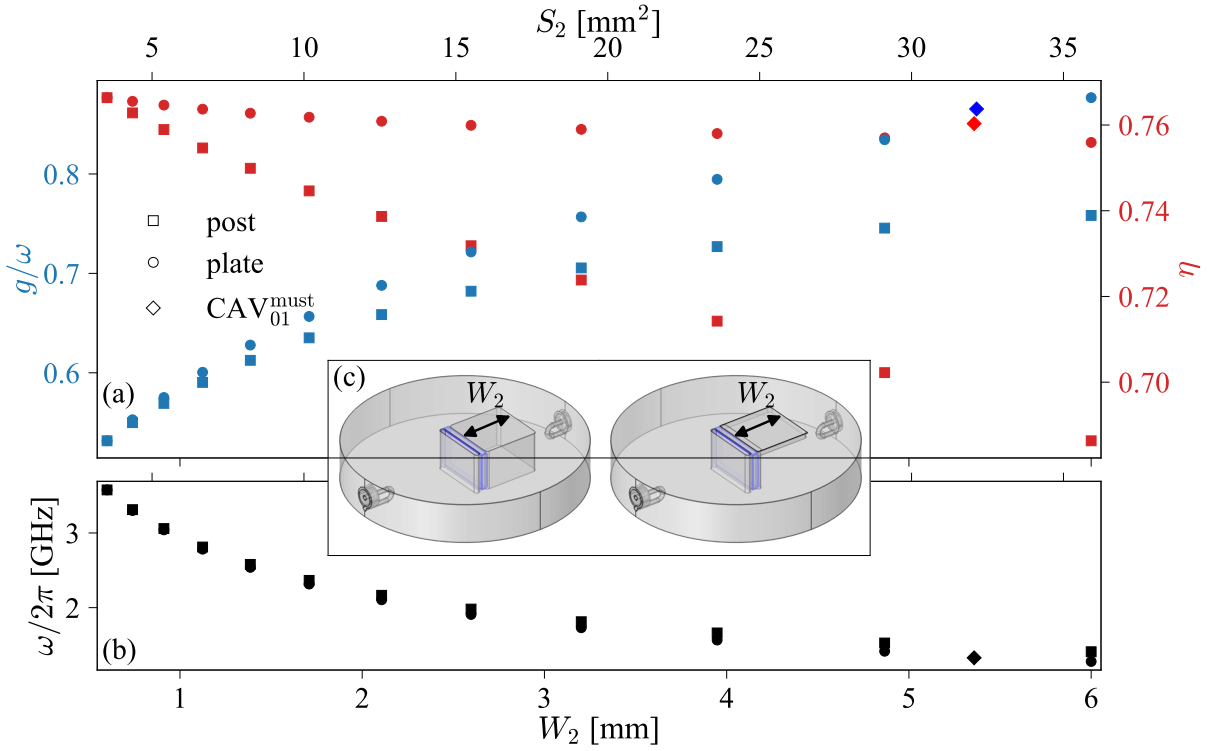

FIGURE 5.14: Evolution of the (a) the ratio g/ω (in blue) and η (in red) of the cavity mode, and (b) its frequency for the cavity with enlarged post (in square marker) or plate (in circle marker) versus d_2, with $d_1 = 10$ µm for EM simulations. The two cavities are illustrated in (c). Values of CAV$_{01}^{\text{must}}$ are presented in diamante marker.

seems to not appear. To understand, FD simulations were performed on the two cavities presented in Fig. 5.14 (c), for different values of W_2 (0.6, 1, 2, and 3 mm), on a frequency range from 0 to 6 GHz with a step of 10 MHz, and at two values of the applied static magnetic field: H_{sat} ($H = 100$ T to discard any magnonic modes from the coupling frame), and at $H = 0.01$ T, at the coupling frame.

These simulations are presented in Fig. 5.15. Fig. 5.15 (a) and (b) illustrate the transmission versus the post or plate widths. In Fig. 5.15 (a), with a saturated applied static magnetic field, we observe the cavity frequency decreasing from 3.5 GHz at $W_2 = 0.6$ mm to 1.8 GHz at $W_2 = 6$ mm. In Fig. 5.15 (b), with a static magnetic field applied at 0.01 T, a split resonance is observed where the lower polariton frequency shifts from 1.2 GHz at $W_2 = 0.6$ mm to 0.9 at $W_2 = 6$ mm. The peak at higher frequency, representing the upper CMP, is less defined for $W_2 < 6$ mm but becomes better defined at $W_2 = 6$ mm. Nevertheless, the coupling remains observable for all values of W_2 mm. The upper CMP decreases from approximately 5.2 GHz at $W = 0.6$ mm to 4.3 GHz at $W = 6$ mm.

In Fig. 5.15 (c) and (d), the transmission versus the plate width for different widths is presented. At H_{sat}, the cavity frequency decreases from 3.5 GHz at $W_2 = 0.6$ mm to 1.7 GHz at $W_2 = 6$ mm, as illustrated in Fig. 5.15 (c). This indicates that the plate allows achieving a lower cavity frequency at higher widths compared to a large post. However, referring to Fig. 5.15 (d), the upper CMP is almost not visible at $W_2 > 2$ mm, whereas it remains clear for the post configuration. At $W_2 = 2$ mm, the upper CMP is still visible,

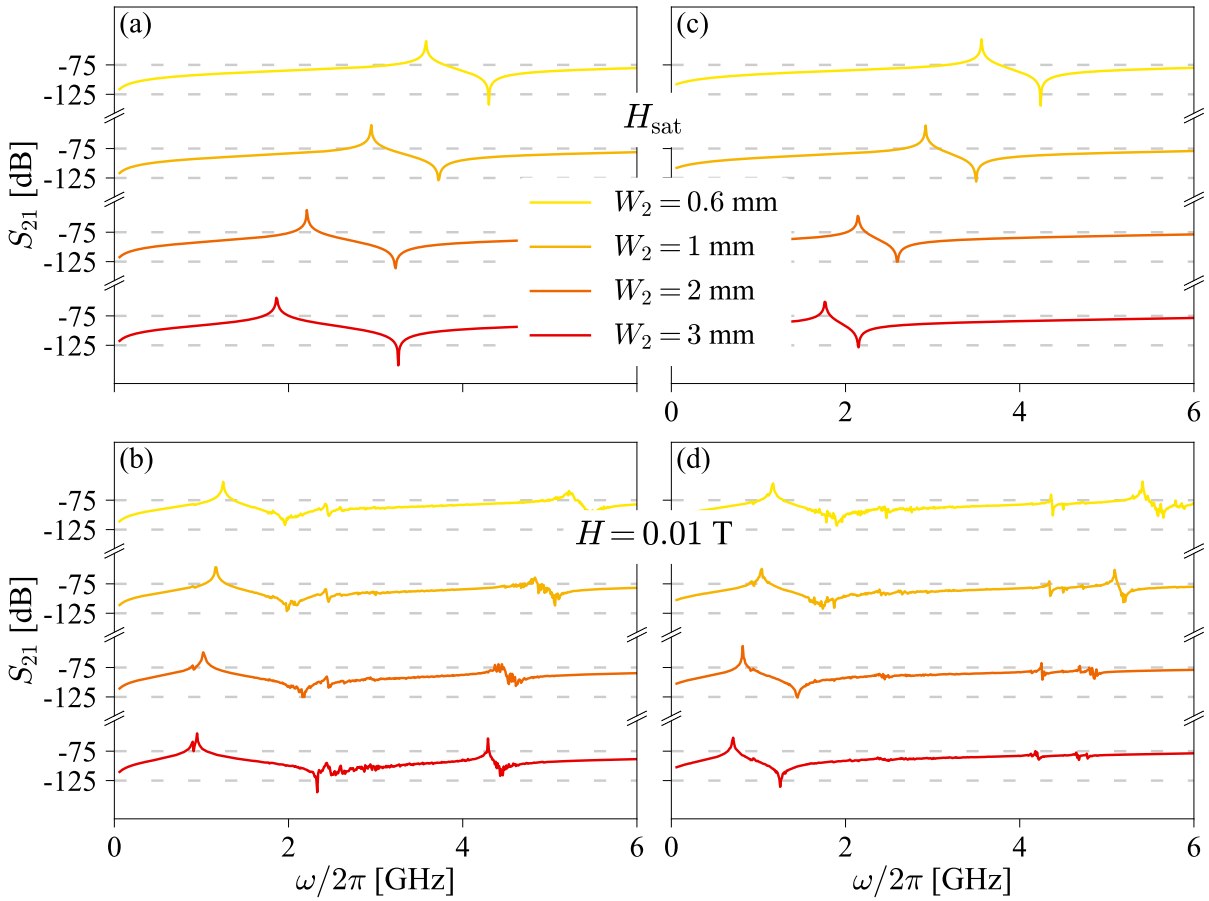

FIGURE 5.15: Transmission S_{21} versus $\omega/2\pi$ for different post (plate) widths at (a) ((c)) H_{sat} and (b) ((d)) $H = 0.01$ T, from FD simulations.

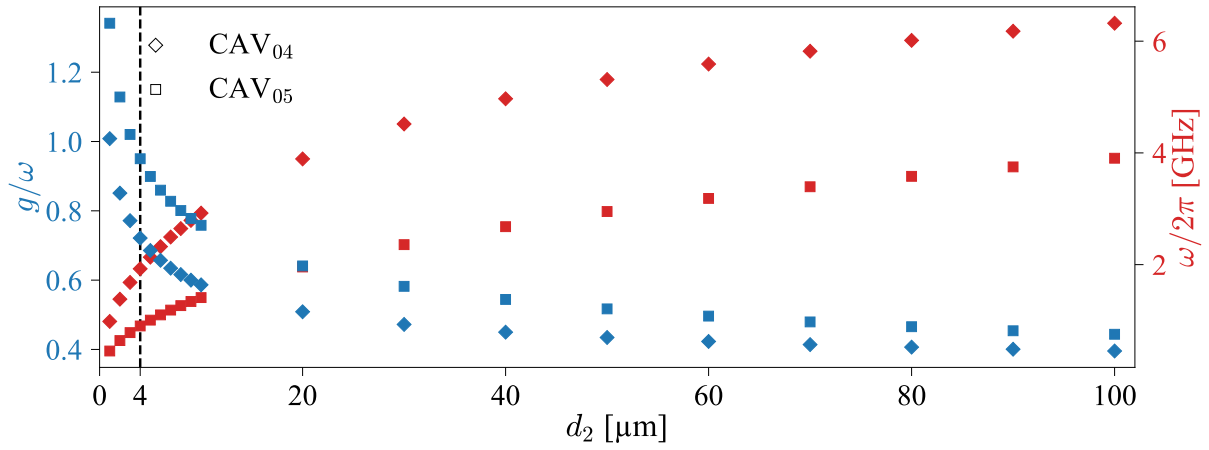

FIGURE 5.16: Evolution of the ratio g/ω (in blue) and the cavity frequency $\omega/2\pi$ (in red) versus d_2 for EM simulations. Diamante markers represent the cavity with plate, named CAV$_{04}$, and the square markers represent the cavity without plate, named CAV$_{05}$.

but its magnitude is weak enough and would likely disappear in simulations at $d = 4$ µm or less.

The cavity with a plate width of $W_2 = 1$ mm and the cavity without a plate but with a width of $W_2 = 6$ mm were selected for further study. These cavities are respectively named CAV_{04} and CAV_{05}. In Fig. 5.16 the ratio g/ω (in blue) and the cavity frequency $\omega/2\pi$ (in red) are shown as a function of d_2 from 1 to 100 µm, based on EM simulations. The cavity CAV_{04} could potentially achieve a ratio of $g/\omega = 1.0$ at $d_2 = 1$ µm, while CAV_{05} could reach $g/\omega = 1.34$ at the same d_2, primarily due to its larger post surface area compared to the plate surface area. However, at $d_2 = 4$ µm the DSC regime is not yet reached. The cavity CAV_{05} is very close to the DSC regime with $g/\omega = 0.95$, while CAV_{04} achieves a ratio of 0.72.

To determine the magnon shift for both cavities, finite-difference (FD) simulations were conducted over a frequency range of 10 GHz with a step size of 10 MHz, and for 8 different values of the applied magnetic field H_0 ranging from 0 to 150 mT. In Fig. 5.17 (a), the transmission versus $\omega_2\pi$ for various H_0 values is shown for cavity CAV_{04}. While the lower CMP is clearly observable, the upper CMP rapidly diminishes with increasing H_0. Due to the limited number of H_0 values and the disappearance of the upper CMP resonance at higher H_0 values, the fit of the CMP was performed using only one variable, the magnon frequency shift Δ_m. The cavity frequency and coupling strength values were derived from the EM simulation results. The fitted CMP frequencies are depicted as blue dashed lines in Fig. 5.17 (a), with a cavity frequency $\omega_c = 1.93$ GHz, coupling strength $g = 1.39$ GHz, and resulting magnon frequency shift $\Delta_m = 2.54 \pm 0.36$ GHz. In Fig. 5.17 (a), the transmission versus $\omega_2\pi$ for various H_0 values is shown for cavity CAV_{05}. The fitted CMP frequencies are illustrated as blue dashed lines in Fig. 5.17 (b), with a cavity frequency $\omega_c = 0.90$ GHz, coupling strength $g = 0.86$ GHz, and resulting magnon frequency shift $\Delta_m = 2.50 \pm 0.37$ GHz.

These values were compared to previous cavity simulation and measurement data, as depicted in Fig. 5.18, where Δ_m/ω is plotted against g/ω. The two added values (grey diamond for CAV_{04} and black square for CAV_{05}) align well with the quadratic dependence of Δ_m/ω on g/ω. In this section, we confirmed that the dependence of Δ_m/ω in the USC regime remains consistent, even approaching the DSC regime. These new simulations also demonstrated that the cavity geometry has no impact on this dependence. However, we have shown that connecting one post can suppress the DM and slightly increase the g/ω ratio of the BM. It was also demonstrated that adding a plate on top of the post is theoretically the best method to avoid decreasing η, thereby achieving a higher g/ω ratio for the same surface area as a larger post. However, it was observed that the upper CMP vanishes with a plate surface larger than 2 mm.

To conclude, the optimal 3D cavity design to achieve the DSC regime involves connecting one post to the lid and increasing the surface area of the unconnected post. Future simulations could explore which post designs might further optimize the coupling ratio; for instance, a semi-circular post might outperform the rectangular base used in this study. Such a cavity could be readily machined, potentially enabling the first experimental measurements of a 3D cavity operating in the DSC regime.

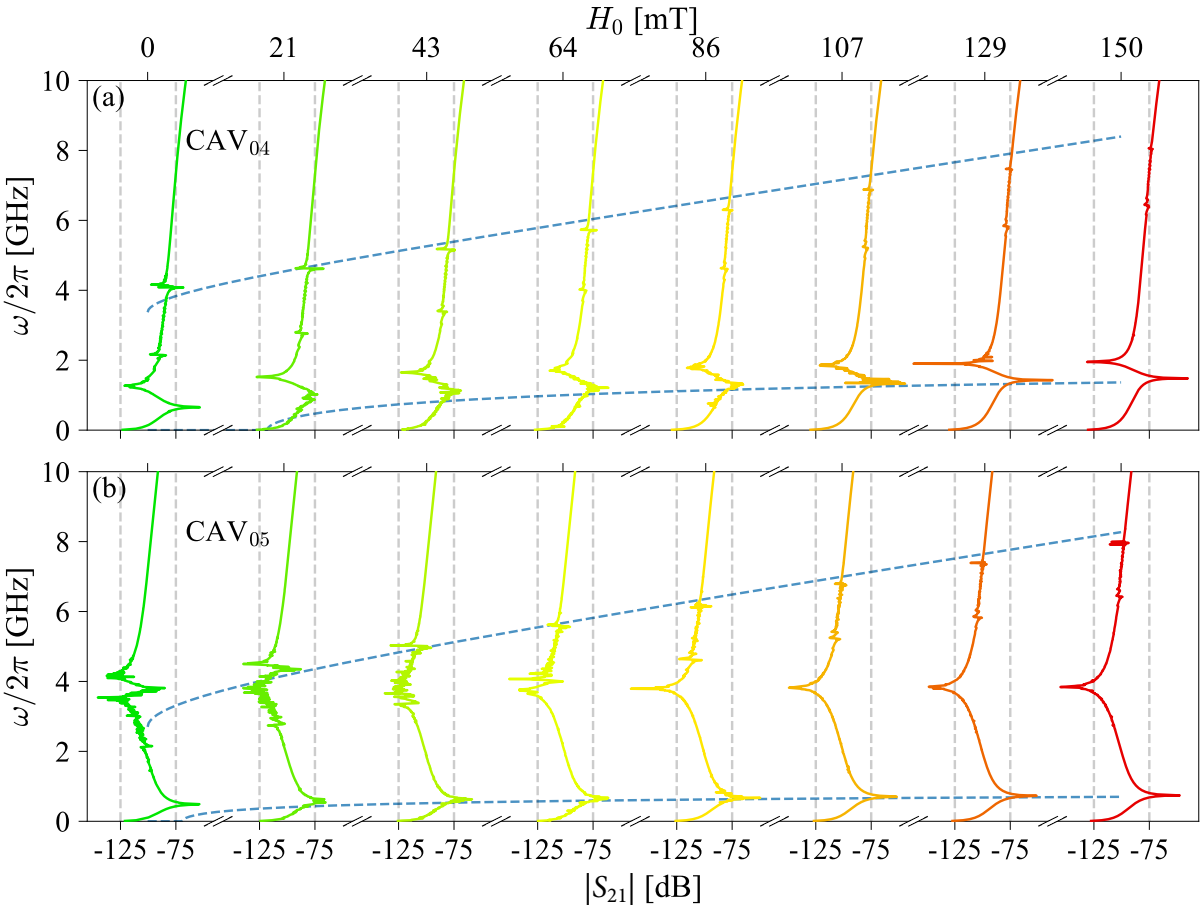

FIGURE 5.17: Transmission S_{21} versus $\omega/2\pi$ at different static magnetic field H_0 values for (a) CAV_{04} and (b) CAV_{05}, from FD simulations. Blue dashed lines correspond to fitted CMP frequency values.

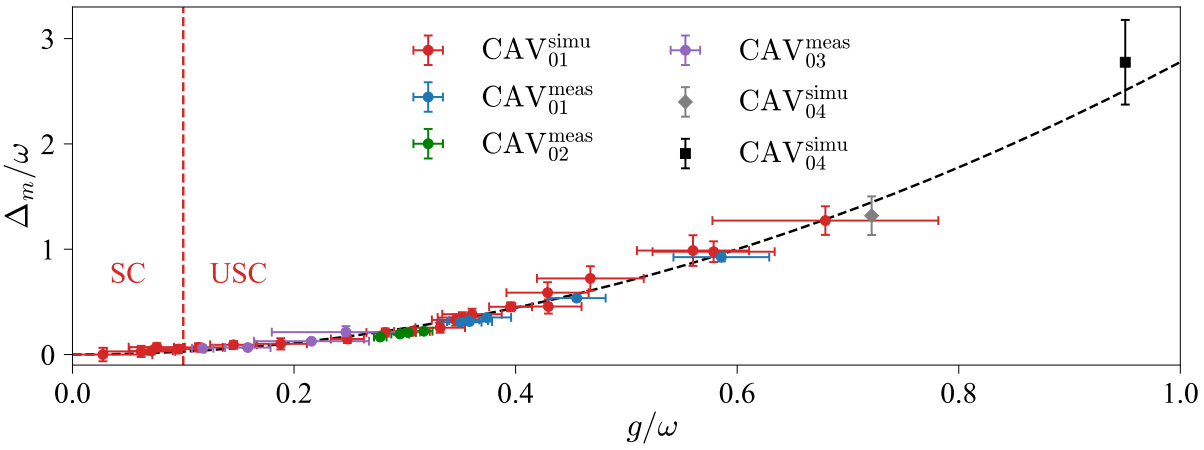

FIGURE 5.18: Δ_m/ω versus g/ω. Shown are the FD simulations on CAV_{01} in red and measurements in blue, in green for CAV_{02}, in purple for CAV_{03}, in grey diamante for CAV_{04}, and in black square for CAV_{05}.

Appendices of Chapter 5

5.A Measurements of CAV_{01}

TABLE 5.2: The parameters associated with measurements at different values of distance d between the post and the lid of the machined cavity. The numbering refers to the spectra shown in Fig. 5.19. f_{DM} and f_{BM} represent the frequencies of the dark and bright modes, respectively; g is the coupling strength of the bright mode; $\Delta_m/2\pi$ is the observed frequency shift of the magnon; and f_{gap} refers to the forbidden frequency gap between the two polaritons.

Numbering	d [μm]	f_{DM} [GHz]	f_{BM} [GHz]	$g/2\pi$ [GHz]	g/ω	$g^2/2\pi\omega$ [GHz]	$\Delta_m/2\pi$ [GHz]	f_{gap} [GHz]
(a)	116	3.75	7.65	2.68	0.35	0.94	2.35	0.58
(b)	75	3.19	7.31	2.62	0.36	0.94	2.29	0.54
(c)	65	3.05	7.16	2.56	0.36	0.92	2.31	0.54
(d)	36	2.40	6.44	2.41	0.37	0.90	2.27	0.64
(e)	11	1.38	4.46	2.03	0.46	0.92	2.39	0.87
(f)	4	0.81	2.80	1.64	0.59	0.96	2.59	1.22

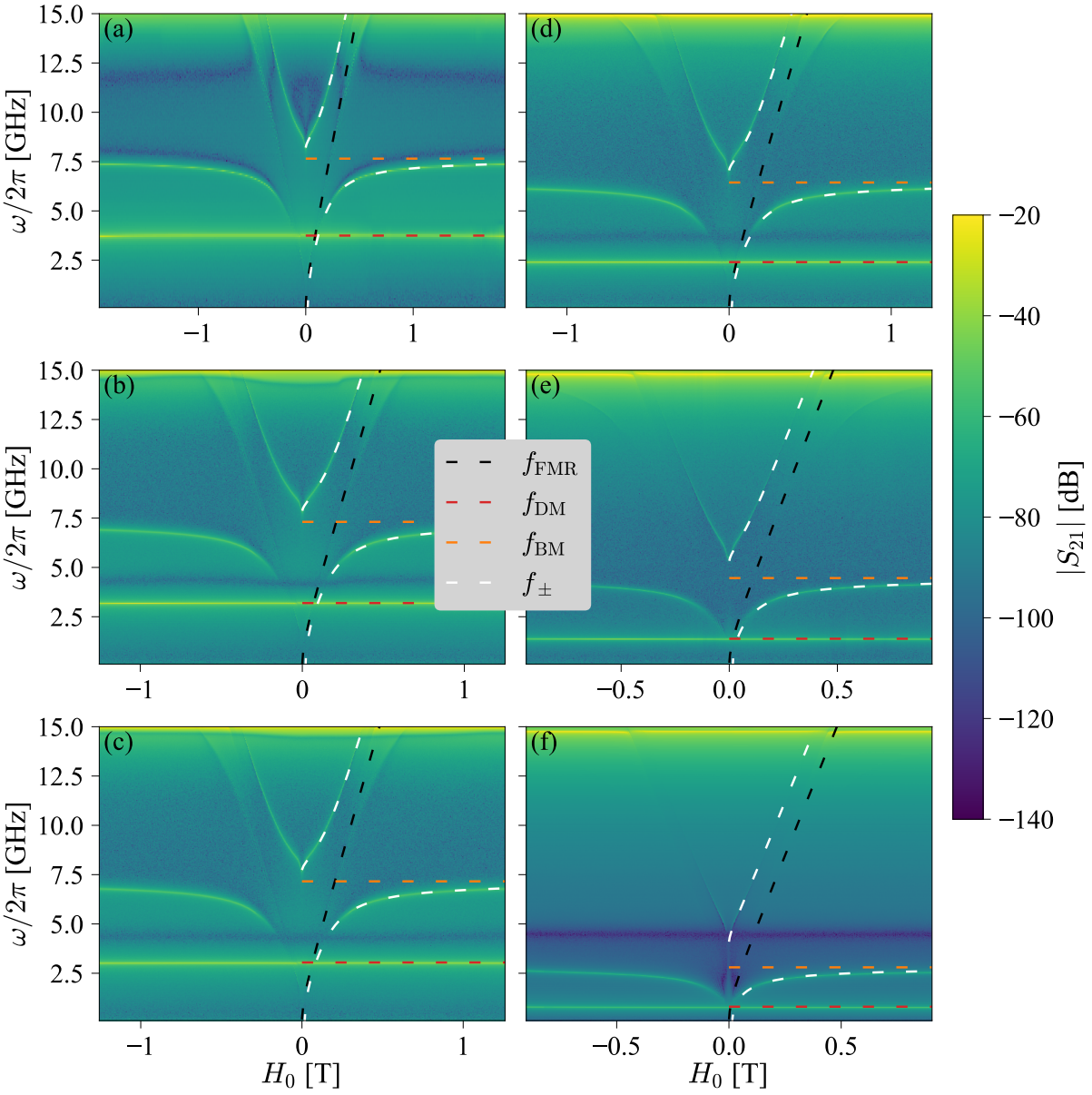

FIGURE 5.19: Transmission spectra versus the RF frequency and the **H**-field. The DM frequency f_{DM} is shown in red while the FMR frequency f_{FMR} is shown in black. The BM frequency f_{BM} (in orange) and the CMP frequencies $f_{\pm}$ (in white) were fitted with the modified Dicke model with parameters shown in Table 5.2.

5.B Measurements of CAV_{02}

TABLE 5.3: The parameters associated with measurements at different values of distance d between the post and the lid of the printed cavity. The numbering refers to the spectra shown in Fig. 5.20. f_{DM} and f_{BM} represent the frequencies of the dark and bright modes, respectively; g is the coupling strength of the bright mode; $\Delta_m/2\pi$ is the observed frequency shift of the magnon; and f_{gap} refers to the forbidden frequency gap between the two polaritons.

Numbering	f_{DM} [GHz]	f_{BM} [GHz]	$g/2\pi$ [GHz]	g/ω	$g^2/2\pi\omega$ [GHz]	$\Delta_m/2\pi$ [GHz]	f_{gap} [GHz]
(a)	4.06	9.79	2.72	0.28	0.76	1.63	0.24
(b)	3.26	8.76	2.59	0.30	0.77	1.71	0.30
(c)	3.01	8.32	2.52	0.30	0.76	1.74	0.31
(d)	2.64	7.63	2.42	0.32	0.77	1.69	0.34

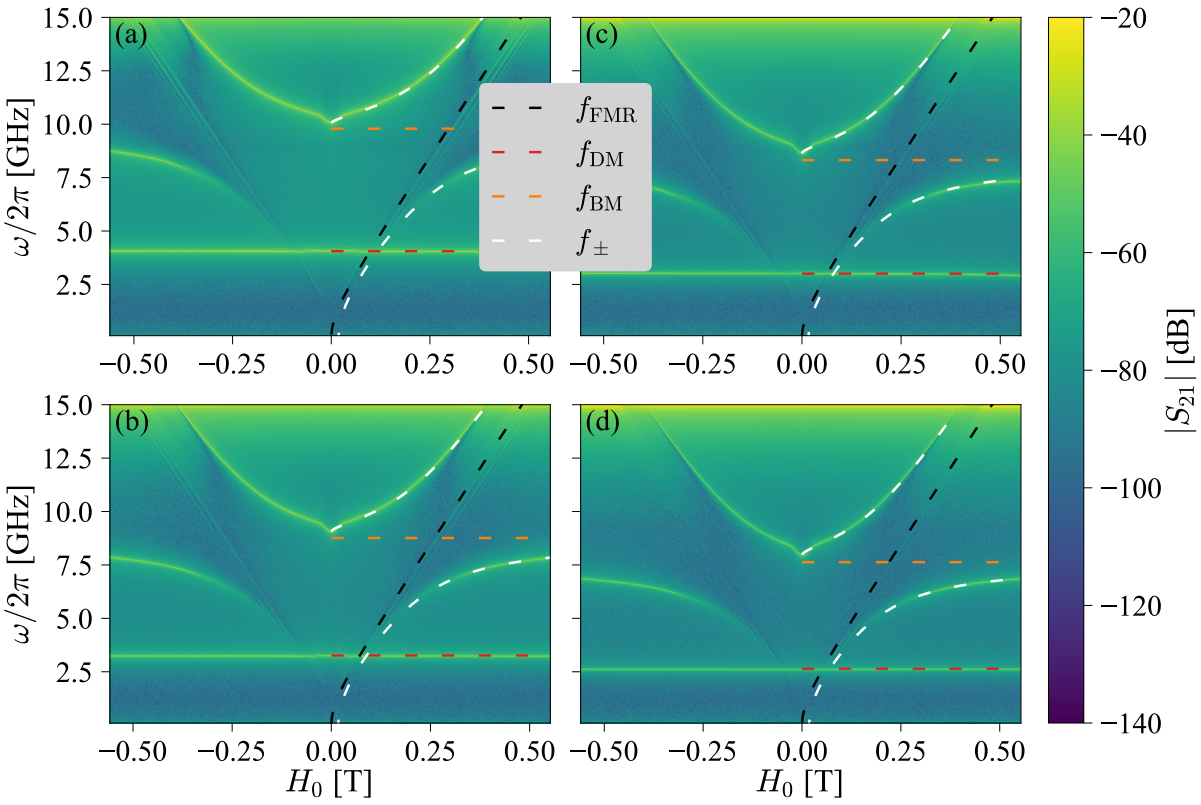

FIGURE 5.20: Transmission spectra versus the RF frequency and the **H**-field. The DM frequency f_{DM} is shown in red while the FMR frequency f_{FMR} is shown in black. The BM frequency f_{BM} (in orange) and the CMP frequencies $f_\pm$ (in white) were fitted with the modified Dicke model with parameters shown in Table 5.3.

5.C Measurements of CAV_{03}

TABLE 5.4: The parameters associated with measurements at different values of distance d between the post and the lid of the printed cavity. The numbering refers to the spectra shown in Fig. 5.21. f_{DM} and f_{BM} represent the frequencies of the dark and bright modes, respectively; g is the coupling strength of the bright mode; $\Delta_m/2\pi$ is the observed frequency shift of the magnon; and f_{gap} refers to the forbidden frequency gap between the two polaritons.

Numbering	f_{DM} [GHz]	f_{BM} [GHz]	$g/2\pi$ [GHz]	g/ω	$g^2/2\pi\omega$ [GHz]	$\Delta_m/2\pi$ [GHz]	f_{gap} [GHz]
(a)	3.02	5.53	0.65	0.12	0.08	0.33	0.01
(b)	2.29	4.36	0.69	0.16	0.11	0.29	0.02
(c)	1.44	2.92	0.63	0.22	0.14	0.37	0.02
(d)	1.30	2.35	0.58	0.25	0.14	0.50	0.05

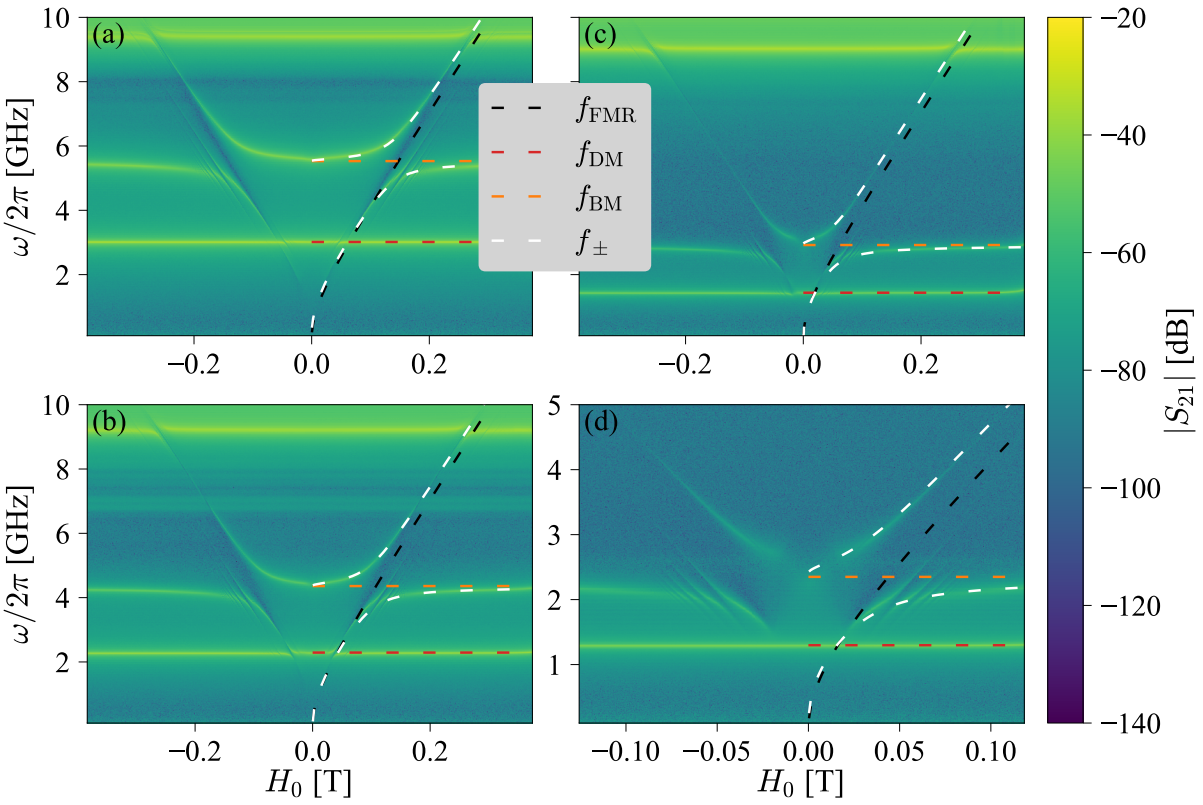

FIGURE 5.21: Transmission spectra versus the RF frequency and the **H**-field. The DM frequency f_{DM} is shown in red while the FMR frequency f_{FMR} is shown in black. The BM frequency f_{BM} (in orange) and the CMP frequencies $f_{\pm}$ (in white) were fitted with the modified Dicke model with parameters shown in Table 5.4.

5.D Cavities with post-mounted plate

As explained in the main text, the post-mounted plate is the most efficient design and was selected for measurement. However, this design is particularly challenging to machine. 3D printing offers the capability to create such complex post shapes. Nevertheless, one of the printing steps involves heating the newly printed object to harden the resin. Thin and wide structures, such as the plate, can bend during this process. To address this issue, we designed a new shape for the plate, featuring a "mustache"-like form to better distribute the surface area and weight around the post, as depicted in Fig. 5.22. These two cavities were designed to experimentally follow the ratio g/ω from 0.6 to above 1 in the DSC regime. The first cavity, named $\mathrm{CAV}_{01}^{\mathrm{must}}$ and depicted in Fig. 5.22 (a), has a post surface area of 32.14 mm^2. Referring to Fig. 5.22 (d), the plate dimensions are $L_1 = 14$ mm, $W_{p,1} = 2$ mm, and $W_{p,2} = 1$ mm. The fillets defining the radius of the corners, as given in Fig. 5.22 (b), have the following dimensions: $F_1 = 2$ mm, $F_2 = 1$ mm, $F_3 = 0.5$ mm, and $F_4 = 0.5$ mm.

The ratio g/ω for this cavity ranges from 0.51 at $d = 100$ µm to 1.08 at $d = 4$ µm, as illustrated in Fig. 5.23 (a). Its values at 10 µm are reported in Fig. 5.14.

The second cavity, named $\mathrm{CAV}_{02}^{\mathrm{must}}$, is depicted in Fig. 5.22 (c). This cavity is designed to allow deeper exploration into the DSC regime. The dimensions of the cavity are: $L_1 = 18$ mm, $W_{p,1} = 8$ mm, and $W_{p,2} = 4$ mm, $F_1 = 8$ mm, $F_2 = 2$ mm, $F_3 = 2$ mm, and $F_4 = 1$ mm. The ratio g/ω for this cavity ranges from 0.70 at $d = 100$ µm to 1.57 at $d = 4$ µm, as illustrated in Fig. 5.23 (b).

Unfortunately, we were unable to observe the coupling in the transmission spectra during measurements for the two cavities, CAV_{04} and CAV_{05}. The reasons for this failure are provided in the main text.

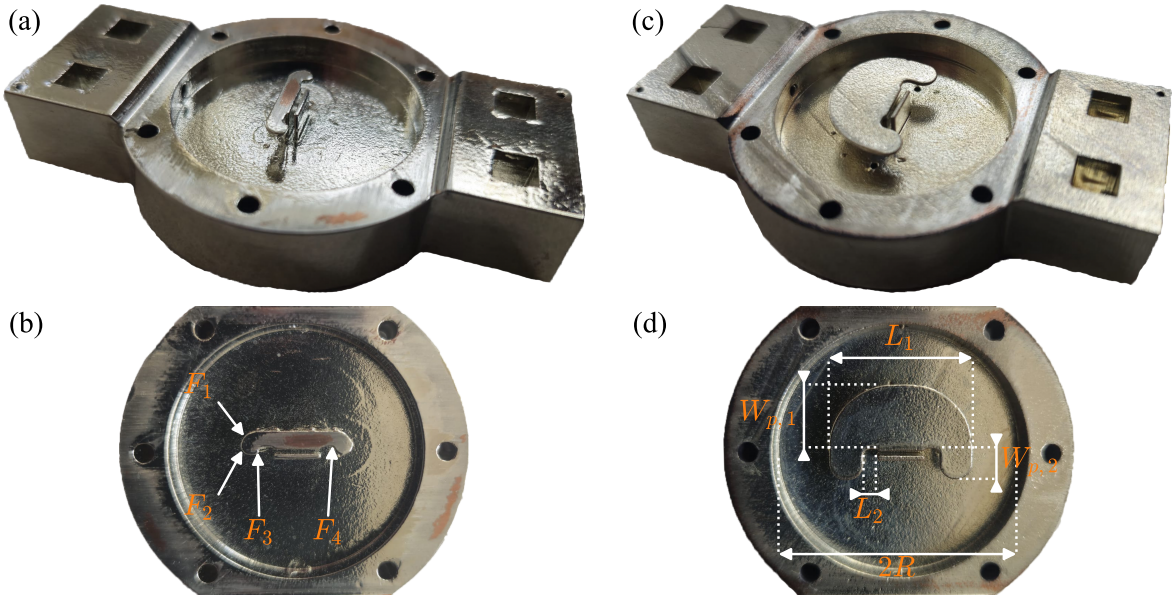

FIGURE 5.22: (a) ((c)) 3/4 and profile (b) ((d)) views of the cavity $\mathrm{CAV}_{01}^{\mathrm{must}}$ ($\mathrm{CAV}_{02}^{\mathrm{must}}$).

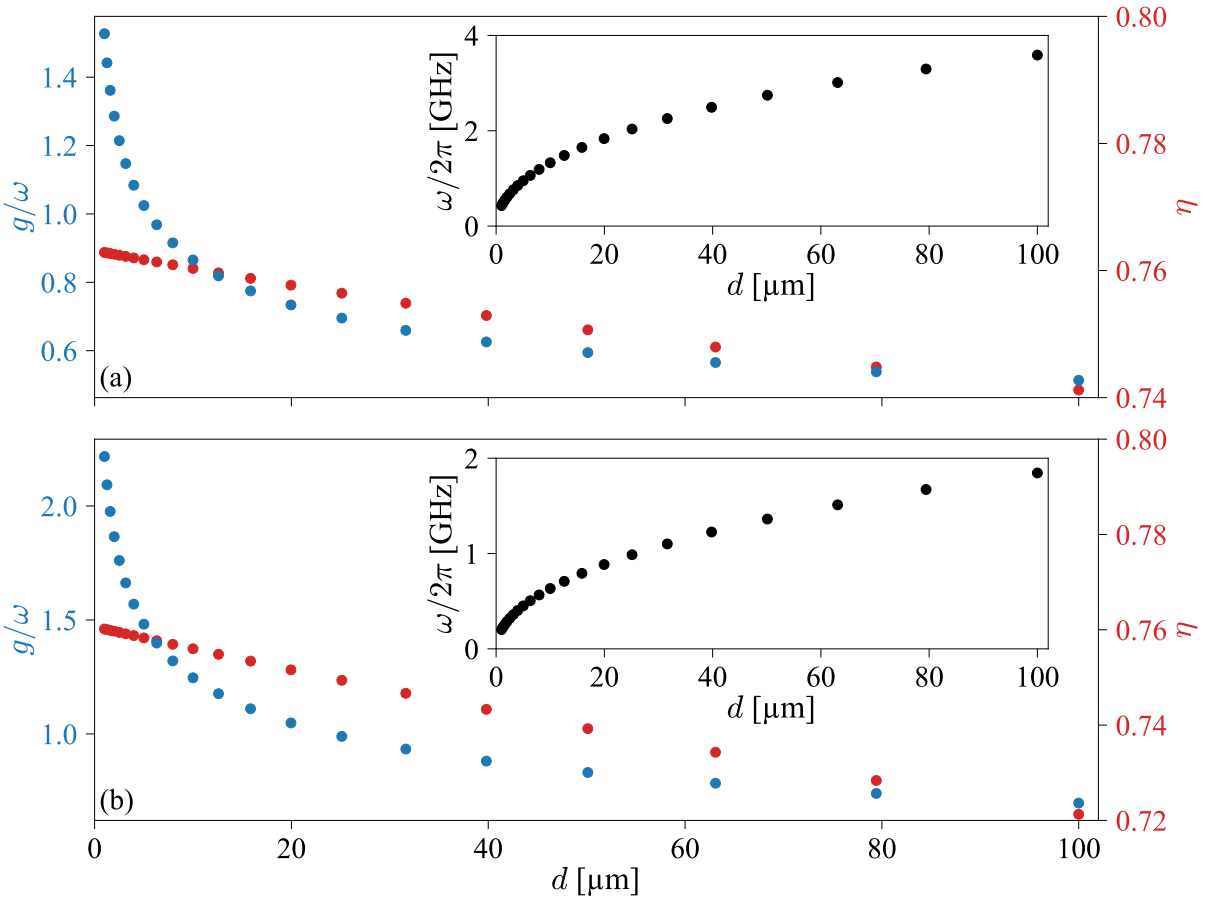

FIGURE 5.23: Evolution of ratio g/ω (in blue) and η (in red) versus d_2, with $d_1 = 10$ µm for EM simulations for (a) $\text{CAV}_{01}^{\text{must}}$, and (b) $\text{CAV}_{02}^{\text{must}}$. In inset is shown the cavity frequency $\omega/2\pi$.

6 Level attraction in a quasi-closed cavity

Abstract

We provide a comprehensive analytical description of the coupling associated with an antiresonance within a hybrid system comprised of a quasi-closed photonic cavity and a ferrimagnet. Whilst the level attraction between a resonant system inside an open cavity is well understood, the physical underpinnings of this phenomena within quasi-closed cavities have remained elusive. Leveraging the input-output theory, we successfully differentiate between the repulsive and attractive aspects of this coupling. Our model demonstrates that by understanding the phase-jump at the resonances and the antiresonance, we can predict the nature of the coupling of the antiresonance for a given position of the ferrimagnet in the cavity. This study has been published in the Physical Review Applied journal [97] and can be found on arXiv. The section titled *Further Work* includes additional studies, particularly measurements on a double reentrant cavity.

Contents

6.1 Introduction

The level attraction of modes has garnered significant interest over the past decade, offering new opportunities for the development of microwave and quantum devices. In particular, level attraction has gained attention for its potential to give rise to two distinct types of singularities, as illustrated in Fig. 6.1 (c) and (d). One of these is the exceptional point (EP), which leads to the coalescence of polariton frequencies [35, 40, 211]. EPs enable several intriguing applications, including topological energy transfer [212], which involves the robust transfer of energy between systems that are resistant to both thermal and quantum fluctuations - a feature of great interest for quantum communication. Moreover, a small perturbation near an EP can induce a measurable frequency splitting, thereby enhancing the sensitivity of devices designed for sensing applications [213–215].

The second singularity emerging in systems exhibiting level attraction is the bound state in the continuum (BIC). At this point, the hybridized modes remain perfectly embedded within the radiation continuum without radiating energy [216], resulting in an exceptionally long lifetime [217] i.e. one of the eigenfrequencies has no imaginary part, as shown in Fig. 6.1. The presence of BICs holds promise for applications in slow-light devices, sensing, and quantum memory technologies [40, 217].

Furthermore, the level attraction of photons and magnons can had to spontaneously break the parity-time-symmetry (PT-symmetry), and can form a high-fidelity Bell state [218]. Bell states are a particular kind of entanglement between two particles, with a strong

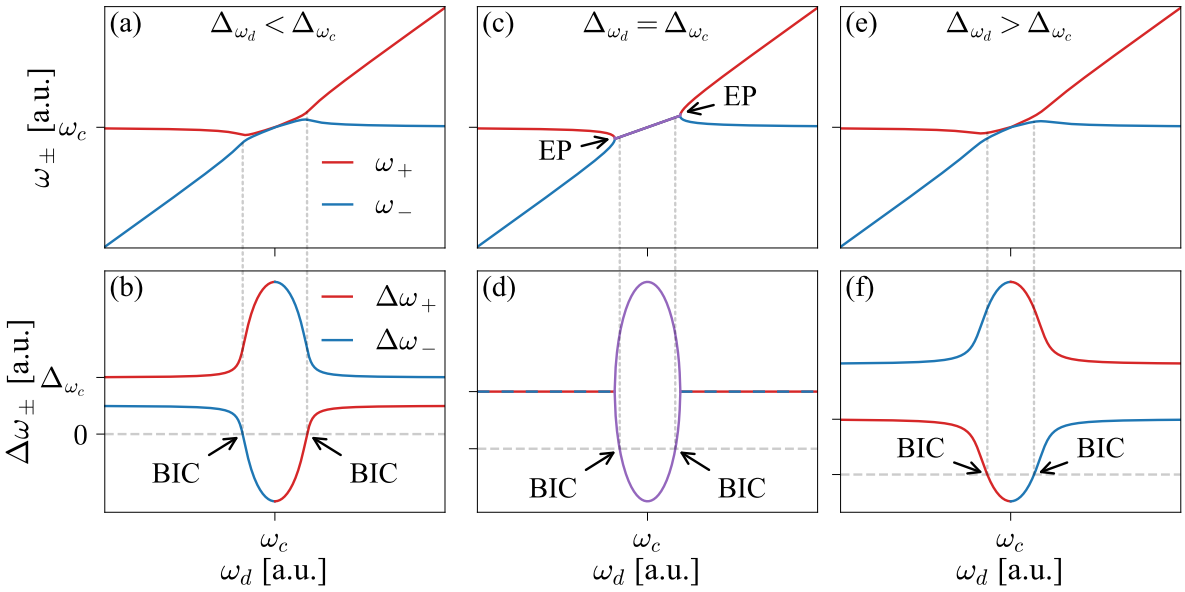

FIGURE 6.1: Dissipative coupling between light and matter shown in the eigenfrequencies (a), (c), (e), and the polariton linewidths (b), (d), (f) as a function of the angular frequency ω_d. Bound states in the continuum (BICs) correspond to real eigenvalues with no imaginary components, while exceptional points (EPs) appear in systems exhibiting level attraction, where the linewidths of the two bosonic modes converge to equality, where Δ_{ω_d} and Δ_{ω_c} represent the matter and the light dissipation, respectively.

correlation, even spatially separated, hence are fundamental in quantum information such as quantum teleportation, quantum cryptography, and quantum error correction [219]. Hence, it is important that the entanglement is steady and robust against perturbation of the environment, which can lead to instability [218].

Systems described by an effective non-Hermitian Hamiltonian can exhibit non-reciprocal photon transmission [65–73]. This property is valuable for devices such as circulators, backscattering isolators, and unidirectional signal amplifiers, which are critical components in modern communication and signal processing technologies.

Level attraction can manifest in both dissipative or coherent systems. In dissipative systems, the effective Hamiltonian is non-Hermitian, leading to dissipative coupling characterized by the spectral signature of mode level attraction. It has been demonstrated that in open cavities - identified by an antiresonance (dip) in the transmission spectra at their mode frequencies - dissipative coupling can occur when both the cavity mode and the magnon (in the case of cavity magnonics) are coupled to the same traveling wave, i.e., the same waveguide [67, 89–94].

Dissipative coupling also arises in mediated coupling scenarios, where traveling waves serve as a medium for coupling between two systems. Alternatively, this coupling can be mediated by an intermediate dissipative mode. Theoretical studies have demonstrated that a dissipative reservoir, which may include traveling waves or a damped auxiliary mode, can mediate coupling between two oscillators [121, 220]. Initially predicted by Metelmann and Clerk (2015) [65] and later refined by Yu et al. (2019) [221], this framework has been used to explain the first experimental observation of dissipative magnon-photon coupling [222].

Beyond effective dissipative magnon-photon coupling, it has been experimentally shown that a cavity mode can function as a damped auxiliary mode, facilitating mediated dissipative magnon-magnon coupling [223]. In this case, the cavity can couple to magnons either coherently or dissipatively [224]. This type of dissipative coupling holds considerable promise for applications such as magnon gradient memory, which could enable quantum information encoding [86], as well as for quantum computation [87, 224]. Furthermore, mediated coupling has been shown to enable long-distance interactions, enhancing the control and manipulation of cavity spintronic devices, with significant potential for advancing spin-based technologies [88].

In coherent systems, two primary mechanisms can lead to level attraction. Theoretically, it has been shown that coherent coupling between systems with positive and negative energies can result in level attraction [225]. A negative energy system refers to one that has been previously pumped to its highest excited state [226, 227]. For instance, a collective spin ensemble can exhibit both effective positive and negative energy: when the ensemble is polarized along the direction of the static magnetic field, the spin precession carries positive energy. In contrast, when the polarization opposes the static magnetic field, the precession is reversed, and the energy becomes negative [228]. In a ferromagnetic system, the quasi-particle associated with this negative energy corresponds not to the magnon - typically associated with a distribution of spins flipped opposite to the applied magnetic field, as discussed in Sec. 2.3.1.a - but to a distribution of spins flipped in the same direction as the magnetic field.

Level attraction in coherent systems can also arise from interference effects. While level attraction as been predicted [229] and experimentally observed [153, 154] in two-tone driven systems, where both cavity modes and magnons are driven, we recently demonstrated through an analytical model and simulations that this coupling signature originates from interference phenomena [155]. Furthermore, a recent study showed that interference between a magnon coupled to different cavity modes can lead to level attraction [230].

In contrast, the attractive character of the coupling between an antiresonance cavity mode and a magnon in a quasi-closed cavity was solely experimentally identified by Rao et al. (2019) [95]. To explain this observation, a phenomenological model based on RLC circuits was employed. However, this approach did not provide a clear understanding of the mechanisms underlying the emergence of level attraction. A more comprehensive understanding of the origins of this phenomenon is a valuable insight for the design of cavities in the various applications detailed above.

In this chapter, we focus on the coupling between an antiresonance and a magnon mode by applying input-output theory. This approach provides a deeper understanding of the parameters that govern the coupling behavior, whether it is repulsive or attractive. We begin by introducing the general S-matrix derived from input-output theory and proceed to explore the two distinct pathways leading to the occurrence of antiresonance. This analysis provides significant insight into the factors contributing to the antiresonance coupling phenomenon, particularly focusing on the phase-jump, which is the key feature of the effective antiresonance coupling behavior.

Finally, the agreement between finite element method (FEM) simulations and our proposed model prove the possibility to precisely control the coupling behavior when positioning a ferrimagnetic sphere at different locations in a quasi-closed cavity.

6.2 Physical Model

As a reminder of Sec. 3.2.8, the model Hamiltonian for a closed cavity, denoted as $\hat{\mathcal{H}}_{\text{sys}}$, encompasses p internal bosonic modes, which can be either photons or magnons in the context of this study. The Hamiltonian is expressed as follows:

$$\frac{\hat{\mathcal{H}}_{\text{sys}}}{\hbar} = \sum_p \left[\tilde{\omega}_p \hat{a}_p^\dagger(t)\hat{a}_p(t) + \frac{1}{2}\sum_{q\neq p} \left(g_{qp}\hat{a}_p^\dagger(t)\hat{a}_q(t) + \text{h.c.} \right) \right]. \tag{6.1}$$

The first term represents the unperturbed Hamiltonian of a single oscillator, where $\tilde{\omega}_p = \omega_p - i\gamma_p^{\text{int}}/2$, $\omega_p/2\pi$ is the eigenfrequency, γ_p^{int} represents the intrinsic loss rates, and $\hat{a}_p^\dagger$ ($\hat{a}_p$) is the creation (annihilation) operator of mode p. The second term is the interaction Hamiltonian between two internal modes $\hat{a}_p$ and $\hat{a}_q$, with their mutual coupling assessed by g_{qp}, and h.c. indicating the hermitian conjugate. Note that the factor 1/2 on the intrinsic losses term can be derived from the input-output theory [40]. It is worth noting that the fast oscillating terms (i.e. $\hat{a}_p^\dagger\hat{a}_q^\dagger$ and $\hat{a}_p\hat{a}_q$) are neglected in this approximation, which is known as the Rotating Wave Approximation (RWA) [231]. Indeed, this study follows the work of Rao et al. (2019) [95], where various couplings were investigated in the strong-coupling regime. Additionally, using the RWA simplifies the calculations and offers a comprehensive understanding of the antiresonances and coupling effects that arise.

In a quasi-closed cavity, the cavity modes are coupled to a common photon bath [150, 152]. For each port n (i.e. a probe), an associated photon bath is represented by a continuum of photonic oscillators, named external modes, with eigenfrequency ω. The related Hamiltonian can be expressed as follow:

$$\frac{\hat{\mathcal{H}}_{\text{bath}}}{\hbar} = \sum_n \int_{\mathbb{R}} \mathrm{d}\omega\, \omega \hat{b}^\dagger_{\omega,n}(t)\hat{b}_{\omega,n}(t). \tag{6.2}$$

Here, $\hat{b}^\dagger_{\omega,n}$ ($\hat{b}_{\omega,n}$) represents the creation (annihilation) operator of the external mode associated with port n and having the frequency ω.

The interaction between the bath and the system can be described by the following model Hamiltonian (under the RWA):

$$\frac{\hat{\mathcal{H}}_{\text{int}}}{\hbar} = \frac{i}{\sqrt{2\pi}} \sum_{p,n} \int_{\mathbb{R}} \mathrm{d}\omega \left(\kappa_{pn}(\omega)\hat{b}^\dagger_{\omega,n}(t)\hat{a}_p(t) - \text{h.c.}\right), \tag{6.3}$$

where $\kappa_{pn}(\omega)$ is the external coupling strength between the external mode $\hat{b}_{n,\omega}$ and the internal mode $\hat{a}_p$.

In the first Markov approximation, the external coupling strength is assumed to be independent of the frequency:

$$\kappa_{pn}(\omega) = \kappa_{pn} = \sqrt{\gamma_{pn}} e^{i\phi_{pn}}, \quad \gamma_{pn} \in \mathbb{R}. \tag{6.4}$$

Here, γ_{pn} is real and represents the external photonic damping rate. Additionally, a phase contribution ϕ_{pn} is introduced to the external coupling κ_{pn}, as previously discussed in [232, 233]. The coupling phase is contingent on the phase of the electric (magnetic) field injected or probed within the cavity. At a given time t, the first probe injects a field with a certain phase. Consequently, each excited cavity mode shares the same phase at this location in their field distribution within the cavity. However, the phase of the modes at the second probe may differ, according to their field distribution, giving rise to both constructive and destructive interferences. A probe senses the field only along one axis, thereby resulting in an external coupling phase of either 0 or π.

The complete Hamiltonian is given by:

$$\hat{\mathcal{H}} = \hat{\mathcal{H}}_{\text{sys}} + \hat{\mathcal{H}}_{\text{bath}} + \hat{\mathcal{H}}_{\text{int}}. \tag{6.5}$$

It is important to note that, owing to the RWA, this Hamiltonian is no longer applicable to systems operating beyond the Strong-Coupling (SC) regime, where $g_{qp}/\sqrt{\omega_q\omega_p} < 0.1$ and $\kappa_{pn}(\omega)/\sqrt{\omega_p} < 0.1$ [74, 77, 151]. It is important to note that the input-output theory in the USC regime has already been explored in prior work by [151]. Further investigations into the antiresonance behavior within this regime would provide valuable insights and could be an interesting direction for future research. Both internal and external modes obey to the bosonic relation[3]. The derivation of the S-matrix using the input-output theory is given in Sec. 3.2.8.d.

[3] $[\hat{a}_i(t), \hat{a}^\dagger_j(t)] = \delta_{ij}, \quad [\hat{b}_{\omega,i}(t), \hat{b}^\dagger_{\omega',j}(t)] = \delta_{ij}\delta(\omega - \omega')$, where δ_{ij} and $\delta(\omega - \omega')$ are the Kronecker symbols.

6.3 Physics of an antiresonance

The following section will discuss the two contributions to the existence of an antiresonance with two internal modes: when both modes are hybridized Cavity-Magnon Polaritons (CMP), and when both modes are photonic modes. These scenarios are illustrated in the two system schemes in Fig. 6.2 (a), and (b), respectively. Fig. 6.2 (c), a combination of Fig. 6.2 (a) and (b), will be discussed in Sec. 6.4. In the rest of the study, the magnonic loss rates correspond to $\gamma_m = \alpha\omega$, where $\alpha = 2.10^{-4}$ is the Gilbert damping of YIG [8], while the intrinsic photonic loss rates are neglected. Neglecting the photonic loss rates (i.e. from 0 to $10\gamma_m$) has no impact on the physics of the antiresonance except on its linewidth; however, its frequency and coupling behavior remain unaffected.

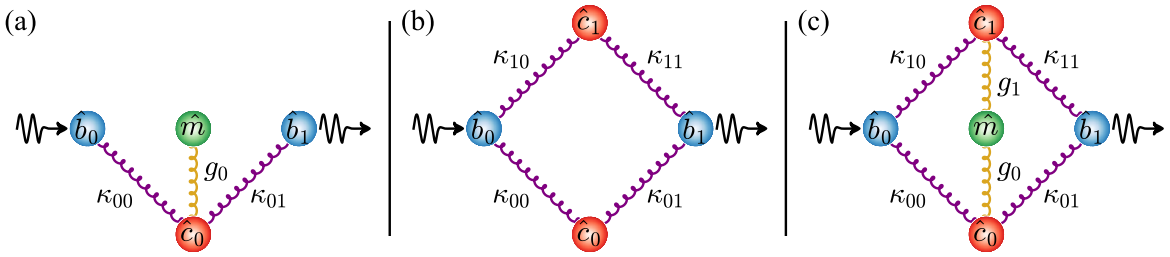

FIGURE 6.2: Schemes of classical oscillators representing a quasi-closed cavity composed of (a) a photonic mode $\hat{c}_0$ coupled with strength g_0 to a magnon mode $\hat{m}$; (b) two photonic modes $\hat{c}_0$ and $\hat{c}_1$; and (c) two photonic modes $\hat{c}_0$ and $\hat{c}_1$ coupled with strength g_0 and g_1 respectively to a magnon mode $\hat{m}$. $\hat{b}_0$ and $\hat{b}_1$ are the ports, and $\kappa_{ij} = \sqrt{\gamma_{ij}}e^{i\phi_{ij}}$ the external couplings.

6.3.1 One photon mode & one magnon mode

The depicted system in Fig. 6.2 (a) consists of a single photonic mode $\hat{c}_0$ with a frequency ω_0, interacting with two ports (i.e. two probes) denoted as $\hat{b}_0$ and $\hat{b}_1$. The coupling strengths for these interactions are characterized by κ_{00} and κ_{01}, respectively. Additionally, the magnon $\hat{m}$ with a frequency of ω_m is only coupled to the photonic mode with a coupling strength of g_0. According to Eq. (3.65) and (4.65), the transmission of this system is expressed as follows:

$$S_{21} = -i\frac{\sqrt{\gamma_{00}\gamma_{01}}\tilde{\Delta}_m e^{i\Phi_0}}{\tilde{\Delta}_0\tilde{\Delta}_m - g_0^2}, \tag{6.6}$$

where $\tilde{\Delta}_m = \omega - \tilde{\omega}_m$, $\tilde{\omega}_m = \omega_m - \frac{i}{2}\alpha$, $\tilde{\Delta}_0 = \omega - \tilde{\omega}_0$, $\tilde{\omega}_0 = \omega_0 - \frac{i}{2}(\gamma_{00} + \gamma_{01})$, and $\Phi_0 = \phi_{01} - \phi_{00}$.
Minimizing the denominator in Eq. (6.6) gives rise to the complex polaritonic frequencies:

$$\tilde{\omega}_\pm = \frac{1}{2}\left[\tilde{\omega}_0 + \tilde{\omega}_m \pm \sqrt{(\tilde{\omega}_m - \tilde{\omega}_0)^2 + 4g_0^2}\right], \tag{6.7}$$

where $\omega_\pm = \mathcal{R}\{\tilde{\omega}_\pm\}$ represents the polaritonic frequencies, and $\gamma_\pm = \mathcal{I}\{\tilde{\omega}_\pm\}$ polaritonic loss rates. Minimizing the numerator of Eq. (6.6) leads to the determination of the

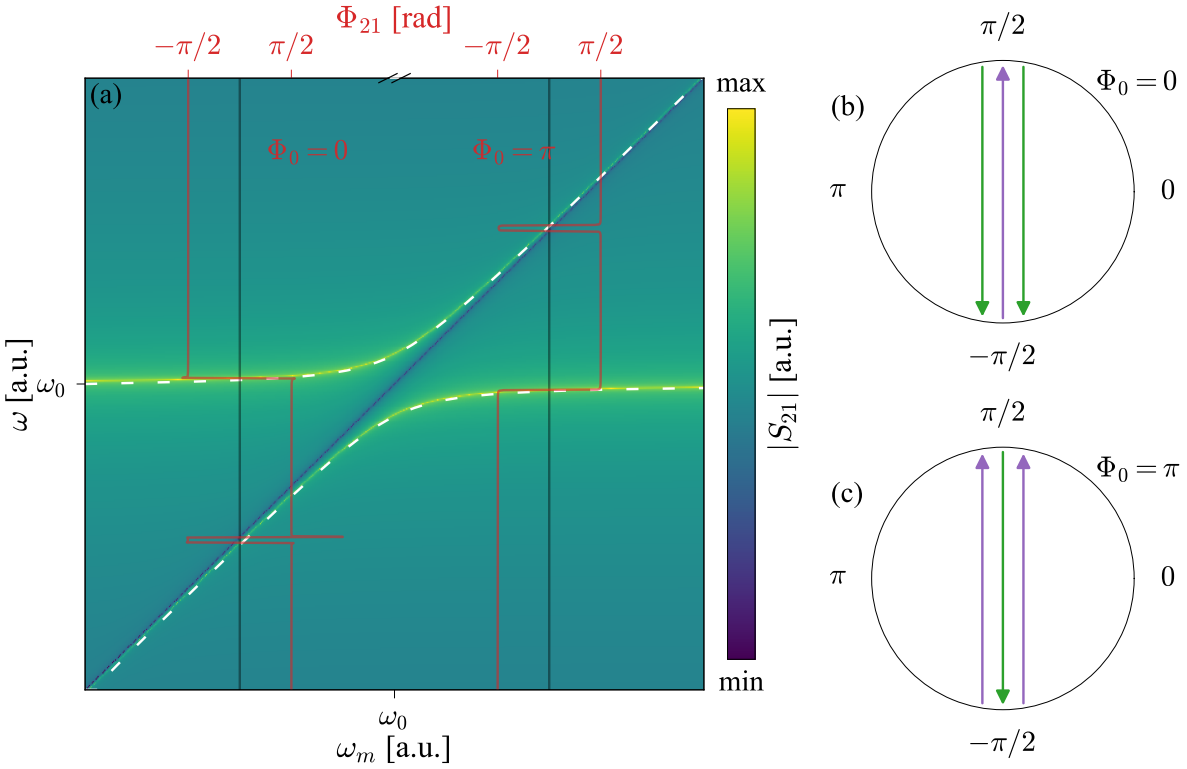

FIGURE 6.3: (a) Transmission spectrum of a system composed of a cavity photon and a magnon, sketched in Fig. 6.2 (a), using Eq. (6.6), and the polariton frequency dependence in dashed white line using Eq. (6.7). The phase of the S_{21} parameter for both cases $\Phi_0 = 0$ and $\Phi_0 = 1$ is presented with red lines, arbitrarily at $\omega_m = 0.5\omega_0$ and $\omega_m = 1.5\omega_0$, respectively. The phase-jumps of both the polariton resonances and the antiresonance for the two cases $\Phi_0 = 0$ and $\Phi_0 = 1$ are respectively represented in (b) and (d), respectively. The arrow of the middle represents the antiresonance phase-jump, while the two others shows the polariton resonance phase-jumps. In green is represented the negative phase-jump (from $\pi/2$ to $-\pi/2$), while in purple is represented the positive phase-jump (from $-\pi/2$ to $\pi/2$).

antiresonance frequency ω_{ar} arising from the interaction between a photon and a magnon:

$$\omega_{ar} = \omega_m. \tag{6.8}$$

For this case, regardless of the coupling phase between the cavity photon and the ports, the antiresonance frequency will always coincide with the magnon frequency, which is the externally non-excited oscillator, as highlighted in the transmission spectra of the system depicted in Fig. 6.3 (a).

Note that Eq. (6.6) can be expressed as a sum of Lorentzians:

$$S_{21} = -i\frac{\sqrt{\gamma_{00}\gamma_{01}}}{\tilde{\omega}_+ - \tilde{\omega}_-}\left(\frac{\tilde{\omega}_m - \tilde{\omega}_-}{\omega - \tilde{\omega}_-} + \frac{\tilde{\omega}_+ - \tilde{\omega}_m}{\omega - \tilde{\omega}_+}\right)e^{i\Phi_0}. \tag{6.9}$$

The terms within the parentheses correspond to the resonances of the lower and upper polaritons. Numerators and the shared factor term (except for $e^{i\Phi_0}$) are all positive. As

a result, the phase of both resonances shift from $\pi/2$ to $-\pi/2$ when $\Phi_0 = 0$ (referred to as negative phase-jump in all subsequent discussions, indicated by the green arrows in Fig. 6.3 (b)), and from $-\pi/2$ to $\pi/2$ when $\Phi_0 = \pi$ (positive phase-jump, represented by the purple arrows in Fig. 6.3 (c)). The phases for both cases are shown with red lines in Fig. 6.3 (a), arbitrarily at $\omega_m = 0.5\omega_0$ for $\Phi_0 = 0$, and at $\omega_m = 1.5\omega_0$ for $\Phi_0 = \pi$. The common phase factor $e^{i\Phi_0}$ for both polaritons indicates that these resonances undergo the same phase-jump.

To emphasize the phase-jump of the antiresonance, the transmission can be rewritten in a different manner:

$$S_{21} = -i\frac{\sqrt{\gamma_{00}\gamma_{01}}\tilde{\Delta}_m e^{i\Phi_0}}{(\omega - \tilde{\omega}_-)(\omega - \tilde{\omega}_+)}. \tag{6.10}$$

In a frequency range between the two polariton frequencies, the given equation characterizes the antiresonance. In this frequency range, all terms maintain the same sign except for $\Delta_m = \mathcal{R}\{\tilde{\Delta}_m\}$, which influences the phase-jump. To ensure a meaningful comparison of the phase in Eq. (6.9), it is crucial that all terms remain positive (excluding Δ_m and $e^{i\Phi_0}$); otherwise, the phase-jump would be affected. However, $\omega - \omega_+$ is negative around the antiresonance frequency. Therefore, to render all terms positive in the expression of the transmission, Eq. (6.10) becomes:

$$S_{21} = -i\frac{\sqrt{\gamma_{00}\gamma_{01}}\tilde{\Delta}_m e^{i\Phi_{\mathrm{ar}}}}{(\omega - \tilde{\omega}_-)(\tilde{\omega}_+ - \omega)}, \tag{6.11}$$

where $\Phi_{\mathrm{ar}} = \Phi_0 + \pi$ represents the phase factor of the antiresonance, and its phase factor is π-dephased compared to the phase factors of the polaritons, meaning that the phase-jump is positive when $\Phi_0 = 0$, and negative when $\Phi_0 = \pi$, as depicted in Fig. 6.3 (b) and (c) with the purple and green arrows, respectively. In this scenario, it has been shown that the phase-jumps does not impact the behavior of the antiresonance; the antiresonance frequency will always lie between the two polaritonic frequencies.

In the next subsection, we will demonstrate that, according to the scenario depicted in Fig. 6.2 (b); the antiresonance frequency can be explicitly dependent on the phase-jumps involved in the system. Furthermore, in the final subsection illustrated in Fig. 6.2 (c), we will demonstrate that antiresonance coupling can exist and, depending on the different phase-jumps involved in the system, this coupling will exhibit either level repulsion or attraction. It is important to note that the specific path the phase takes during the phase-jump - whether it passes through 0 or π - is not crucial for the antiresonance coupling. What matters is the sign of the phase-jump: whether it is negative (indicated by the green arrow) or positive (indicated by the purple arrow) for both the resonances and the antiresonance.

6.3.2 Two photon modes

The system illustrated in Fig. 6.2 (b) comprises two photonic modes $\hat{c}_0$ and $\hat{c}_1$ with frequencies ω_0 and ω_1, respectively. These two photon modes interact with two ports, $\hat{b}_0$ and $\hat{b}_1$, characterized by external coupling strengths denoted as κ_{00} and κ_{01} with respect to mode $\hat{c}_0$, and κ_{10} and κ_{11} with respect to mode $\hat{c}_1$. From Eq. (3.65) and Eq. (4.65), the

TABLE 6.1: Antiresonance behavior

	$\boldsymbol{\Phi = 0}$	$\boldsymbol{\Phi = \pi}$
$\boldsymbol{\delta > 1}$	$\omega_{\mathrm{ar}} \in [\omega_0; \omega_1]$	$\omega_{\mathrm{ar}} \in [0; \omega_0]$
$\boldsymbol{\delta < 1}$		$\omega_{\mathrm{ar}} \in [\omega_1; +\infty[$

transmission of such a system reads:

$$S_{21} = -i \frac{\sqrt{\gamma_{00}\gamma_{01}}\tilde{\Delta}_1 e^{i\Phi_0} + \sqrt{\gamma_{10}\gamma_{11}}\tilde{\Delta}_0 e^{i\Phi_1} - \frac{i}{2}\Gamma_1^2}{\tilde{\Delta}_0\tilde{\Delta}_1 + \frac{|\Gamma|^2}{4}}, \tag{6.12}$$

where $\tilde{\Delta}_1 = \omega - \tilde{\omega}_1$, $\tilde{\omega}_1 = \omega_1 - \frac{i}{2}(\gamma_{10} + \gamma_{11})$, $\Phi_1 = \phi_{11} - \phi_{10}$, $\Gamma = \sqrt{\gamma_{00}\gamma_{10}}e^{i(\phi_{10}-\phi_{00})} + \sqrt{\gamma_{01}\gamma_{11}}e^{i(\phi_{11}-\phi_{01})}$, and $\Gamma_1^2 = \sqrt{\gamma_{00}\gamma_{11}}\Gamma e^{i(\phi_{11}-\phi_{00})} + \sqrt{\gamma_{01}\gamma_{10}}\Gamma^* e^{i(\phi_{01}-\phi_{10})}$.
The complex resonance frequencies of the transmission read:

$$\tilde{\omega}_\pm = \frac{1}{2}\left[\tilde{\omega}_0 + \tilde{\omega}_1 \pm \sqrt{(\tilde{\omega}_1 - \tilde{\omega}_0)^2 - |\Gamma|^2}\right]. \tag{6.13}$$

In the context of a cavity exhibiting non-degenerate modes, the following hypothesis applies:

$$|\tilde{\omega}_1 - \tilde{\omega}_0| \gg |\Gamma|. \tag{6.14}$$

This inequality reflects the condition that the frequency difference between the two modes is significantly larger than the magnitude of Γ, interpreted as an indirect coupling mediated by the common coupling to the probes between the two photonic modes. In this approximation, the complex resonance frequencies are equal to the complex photon mode frequencies:

$$\tilde{\omega}_- = \tilde{\omega}_0, \qquad \tilde{\omega}_+ = \tilde{\omega}_1. \tag{6.15}$$

The antiresonance frequency of such a system is given by:

$$\omega_{\mathrm{ar}} = \frac{\omega_1 + \delta e^{i\Phi}\omega_0}{1 + \delta e^{i\Phi}}, \tag{6.16}$$

where $\delta = \sqrt{\gamma_{10}\gamma_{11}/\gamma_{00}\gamma_{01}}$ represents the external dissipation ratio between the mode $\hat{c}_1$ and $\hat{c}_0$ at the two probes, and $\Phi = \Phi_1 - \Phi_0 = \phi_{00} + \phi_{11} - \phi_{01} - \phi_{10}$ represents the phase factor difference between the two photonic modes.

We highlight three distinct antiresonance frequency regimes based on the values of δ and Φ, summarized in Table 6.1, and discussed just below.

Considering the hypothesis given in Eq. (6.14), the transmission from Eq. (6.12) can also be expressed as a sum of Lorentzians:

$$S_{21} = -i\left(\frac{\sqrt{\gamma_{00}\gamma_{01}}e^{i\Phi_0} + \frac{i}{2}\Gamma_2}{\omega - \tilde{\omega}_0} + \frac{\sqrt{\gamma_{10}\gamma_{11}}e^{i\Phi_1} - \frac{i}{2}\Gamma_2}{\omega - \tilde{\omega}_1}\right), \tag{6.17}$$

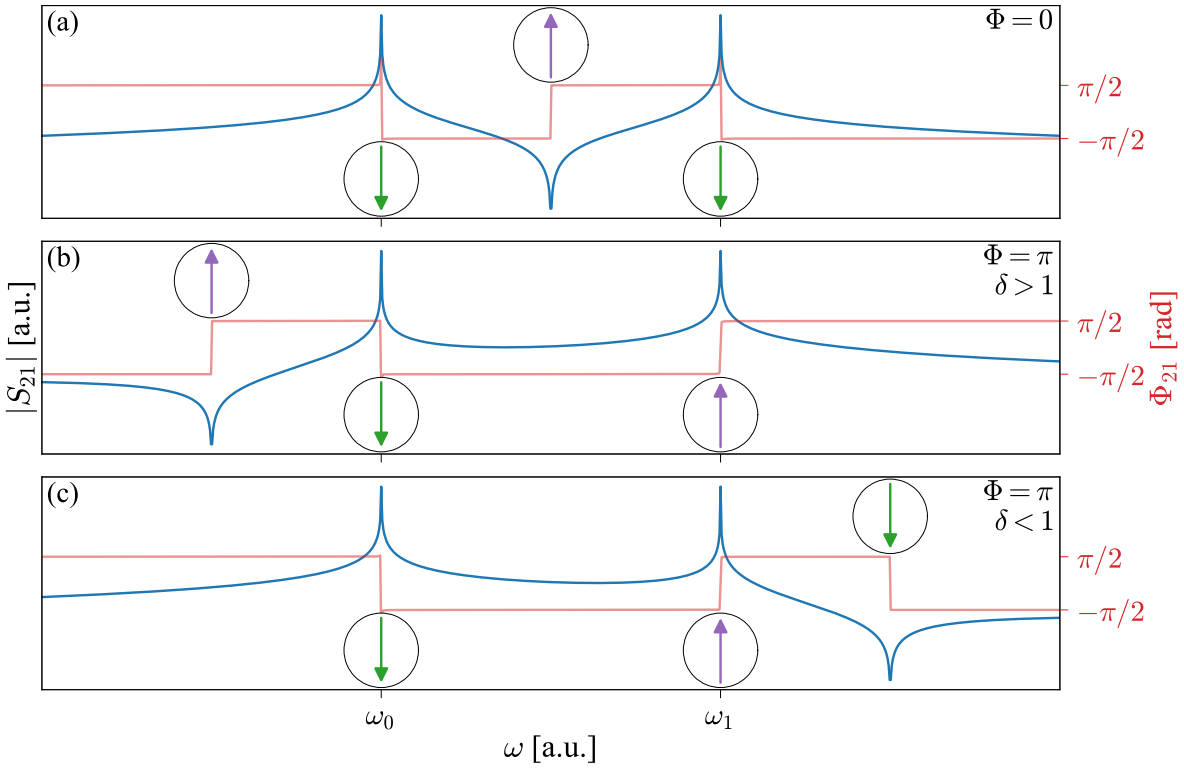

FIGURE 6.4: Three cases of the frequency dependence of the antiresonance of the system composed of two cavity photons, sketched in Fig. 6.2 (b). δ and Φ are defined in Eq. (6.16). The magnitude of the transmission in shown in blue, while the phase is represented in red. Green arrows represent the negative phase-jumps (from $\pi/2$ to $-\pi/2$), while purples arrows represent the positive phase-jumps (from $-\pi/2$ to $\pi/2$).

where $\Gamma_2 = \dfrac{\Gamma_1^2}{\tilde{\omega}_1 - \tilde{\omega}_0}$, is negligible far from the antiresonance frequency. By neglecting Γ_2, the two terms represent isolated photon modes.

When $\Phi = 0$, the antiresonance frequency ω_{ar} is situated between the two photon mode frequencies ω_0 and ω_1, as depicted in Fig. 6.4 (a) in blue. This corresponds to the scenario where the two Lorentzians in Eq. (6.17) share the same phase factor, i.e. $\Phi_0 = \Phi_1$, therefore the same phase-jump, as illustrated in Fig. 6.4 (a) with the green arrows. Thereby, the two Lorentzian are π-dephased and destruct themselves for frequencies between ω_0 and ω_1. This aligns with the case discussed in Sec. 6.3.1 in Eq. (6.9); when two eigenmodes share the phase factor, the antiresonance frequency lies between their respective eigenfrequencies.

When $\Phi = \pi$, the antiresonance frequency ω_{ar} is either less than ω_0 or higher than ω_1, but it is not situated between the two photon mode frequencies. This corresponds to the scenario where the phase factor of the two Lorentzians in Eq. (6.17) are π-dephased, therefore opposed phase-jumps, as highlighted by their respective green and purple arrows in Fig. 6.4 (b) and (c). Two cases arise: when $\delta > 1$, indicating that the photon mode $\hat{c}_1$ is more coupled with the probes than the photon mode $\hat{c}_0$, and the antiresonance frequency ω_{ar} is lower than ω_0, as illustrated in Fig. 6.4 (b); when $\delta < 1$, indicating that the photon mode $\hat{c}_0$ is more coupled with the probes than the photon mode $\hat{c}_1$, and ω_{ar} is higher than

ω_1, as shown in Fig. 6.4 (c).

As in the previous section, the transmission can be rewritten to emphasize the phase of the antiresonance:

$$S_{21} = -i\frac{\sqrt{\gamma_{00}\gamma_{01}}|1+\delta|(\omega-\omega_{\mathrm{ar}})e^{i\Phi_{\mathrm{ar}}} + \frac{i}{2}\Gamma_3^2}{(\omega-\omega_-)(\omega-\omega_+)}, \tag{6.18}$$

where $\Gamma_3^2 = \sqrt{\gamma_{00}\gamma_{01}}(\gamma_{10}+\gamma_{11}) + \sqrt{\gamma_{10}\gamma_{11}}(\gamma_{00}+\gamma_{01}) - \Gamma_1^2$, is negligible far from the antiresonance frequency, and $\Phi_{\mathrm{ar}} = \Phi_0 + \arg(1+\delta e^{i\Phi})$.

When $\Phi = 0$, the term $\omega - \omega_+$ becomes negative because the antiresonance frequency is situated between the two photon frequencies, and $\Phi_{\mathrm{ar}} \to \Phi_{\mathrm{ar}} + \pi$.

Similar to the case of a system composed of one photon and one magnon, as discussed in Sec. 6.3.1, $\Phi_{\mathrm{ar}} = \pi$ when $\Phi_0 = \Phi_1 = 0$, and $\Phi_{\mathrm{ar}} = 0$ when $\Phi_0 = \Phi_1 = \pi$. This indicates an opposing phase-jump of the antiresonance compared to the phase-jumps of the two resonances (indicated by a purple arrow in Fig. 6.4 (a)).

In the case where $\Phi = \pi$, i.e. $\Phi_1 = \Phi_0 + \pi$, the antiresonance has the same phase-jump as the second photon mode, i.e. $\Phi_{\mathrm{ar}} = \Phi_1$, as illustrated in Fig. 6.4 (b) by their shared purple arrows. Conversely, when $\delta < 1$, the antiresonance has the same phase-jump as the first photon mode, i.e. $\Phi_{\mathrm{ar}} = \Phi_0$, as depicted in Fig. 6.4 (c) by their shared green arrows. Understanding the phase-jump of the resonances and antiresonance is highly valuable in cavity engineering, as demonstrated in the following sections.

To conclude on the occurrence of antiresonances, we have explored two simplified scenarios involving only two internal modes. In a real cavity containing an infinity of modes, obtaining an analytical expression for the antiresonance frequency becomes a complex task. Nevertheless, it is feasible to obtain a reasonable approximation of the antiresonance frequency in a real cavity by considering the nearest and most attractive modes numerically, as will be shown later.

6.4 Coupling behavior

Here, we clarify all the contributions and conditions required to observe either antiresonance level repulsion or level attraction between two cavity photon modes and one magnon mode. The system is illustrated in Fig. 6.2 (c). From Eq. (3.65) and Eq. (4.65), the transmission of such a system reads:

$$S_{21} = -i\frac{\sqrt{\gamma_{00}\gamma_{01}}(\tilde{\Delta}_1\tilde{\Delta}_m - g_1^2)e^{i\Phi_0} + \sqrt{\gamma_{10}\gamma_{11}}(\tilde{\Delta}_0\tilde{\Delta}_m - g_0^2)e^{i\Phi_1} + \Gamma_4 g_0 g_1 - \frac{i}{2}\Gamma_5^2\tilde{\Delta}_m}{\tilde{\Delta}_0\tilde{\Delta}_1\tilde{\Delta}_m - g_0^2\tilde{\Delta}_1 - g_1^2\tilde{\Delta}_0 + \frac{|\Gamma|^2}{4}\tilde{\Delta}_m + \frac{i}{2}(\Gamma+\Gamma^*)g_0 g_1}, \tag{6.19}$$

where $\Gamma_4 = \sqrt{\gamma_{00}\gamma_{11}}e^{i(\phi_{11}-\phi_{00})} + \sqrt{\gamma_{01}\gamma_{10}}e^{i(\phi_{01}-\phi_{10})}$,
and $\Gamma_5^2 = \sqrt{\gamma_{00}\gamma_{11}}\Gamma^* e^{i(\phi_{11}-\phi_{00})} + \sqrt{\gamma_{01}\gamma_{10}}\Gamma e^{i(\phi_{01}-\phi_{10})}$.
Under the assumption outlined in Eq. (6.14), the system features three resonance frequencies given by:

$$\Omega_- = \omega_0^-, \qquad \Omega_0 = \omega_0^+ + \omega_1^- - \omega_m, \qquad \Omega_+ = \omega_1^+, \tag{6.20}$$

where $\omega_0^{\pm} = \omega_{\pm}(\tilde{\omega}_0)$, and $\omega_1^{\pm} = \omega_{\pm}(\tilde{\omega}_1)$, from Eq. (6.7).
The minima in transmission of the system are determined by the following antiresonance frequencies:

$$\omega_{\mathrm{ar}}^{\pm} = \frac{1}{2}\left[\omega_{\mathrm{ar}} + \omega_{\mathrm{m}} \pm \sqrt{(\omega_{\mathrm{ar}} - \omega_{\mathrm{m}})^2 + 4|g_{\mathrm{ar}}|^2 e^{i\Phi_{\mathrm{ar}}}}\right], \tag{6.21}$$

where ω_{ar} is defined in Eq. (6.16). The effective coupling strength between the two antiresonances reads as:

$$g_{\mathrm{ar}} = \sqrt{\frac{g_1^2 + \delta e^{i\Phi} g_0^2 + C g_0 g_1}{1 + \delta e^{i\Phi}}}, \tag{6.22}$$

where $C = \sqrt{\gamma_{11}/\gamma_{01}} e^{i(\phi_{11} - \phi_{01})} + \sqrt{\gamma_{10}/\gamma_{00}} e^{i(\phi_{00} - \phi_{10})}$, g_0 and g_1 are the coupling strengths of each cavity mode to the magnon, and δ and Φ are the same as in Eq. (6.16). When $\Phi = \pi$, g_{ar} can be either real or imaginary, depending on the values of δ, g_0, g_1, and C. In Eq. (6.21), we chose to explicitly introduce the effective coupling phase Φ_{ar}, justifying the absolute value of the effective coupling strength. This choice implies that Φ_{ar} is equal to 0 (π) when g_{ar} is real (imaginary), leading to level repulsion (attraction).

Drawing an analogy with the resonance frequencies of a single photon coupled with a magnon described in Eq. (6.7), we can derive the Hamiltonian that governs the antiresonance:

$$\frac{\hat{\mathcal{H}}_{\mathrm{ar}}}{\hbar} = \omega_{\mathrm{ar}} \hat{c}_{\mathrm{ar}}^{\dagger} \hat{c}_{\mathrm{ar}} + \omega_m \hat{m}^{\dagger} \hat{m} + g_{\mathrm{ar}} (\hat{c}_{\mathrm{ar}}^{\dagger} \hat{m} + e^{i\Phi_{\mathrm{ar}}} \hat{c}_{\mathrm{ar}} \hat{m}^{\dagger}), \tag{6.23}$$

where $\hat{c}_{\mathrm{ar}}^{\dagger}$ ($\hat{c}_{\mathrm{ar}}$) represents the effective creation (annihilation) operator of the cavity antiresonance with an eigenfrequency of ω_{ar}. Note that the eigenfrequencies resulting from the diagonalization of this Hamiltonian correspond to the antiresonance frequencies in Eq. (6.21). From here, we demonstrate that antiresonance coupling arises from interferences at a port due to multiple internal modes [230]. As explained by Gardin et al. (2024) [155] for level attraction due to interferences in two-tone driving, the Hamiltonian in Eq. (6.23) does not adequately describe the system. Indeed, while this Hamiltonian successfully captures the antiresonance coupling, it falls short in describing the entire spectrum, particularly the resonances. Although the dissipative coupling is typically modeled using a non-Hermitian Hamiltonian, the level attraction observed here remains a hallmark of a Hermitian Hamiltonian, representing the coherent coupling of internal modes. This level attraction at the antiresonance arises from interference between the different cavity modes, all of which are coupled to the same probes. This indicates that the observed level attraction for the antiresonance is not due to dissipative coupling, as previously suggested by [95]. By retrieving this Hamiltonian for the description of the antiresonance, we can understand why, in certain circumstances, level attraction has been misinterpreted as dissipative coupling.

It is worth noting that while the effective Hamiltonian in Eq. (6.23) and the frequencies of the effective antiresonances in Eq. (6.21) have been previously introduced based on phenomenological considerations, the effective coupling strength g_{ar} lacked a clear physical explanation [95]. The transmission spectrum of the antiresonance exhibits a level repulsion when the coupling strength g_{ar} is real. Conversely, the transmission spectrum shows a level attraction when g_{ar} is imaginary.

In the case where only one photonic mode is coupled with the magnon mode and the phase-jump of the two modes are opposed, i.e. $\Phi_1 = \Phi_0 + \pi$, the spectrum will exhibit

TABLE 6.2: Effective coupling behavior

	$g_1 = 0$	$g_0 = 0$
$\delta > 1$	$g_{\mathrm{ar}} = \dfrac{g_0}{\sqrt{1-\delta^{-1}}} \in \mathbb{R}$	$g_{\mathrm{ar}} = i\dfrac{g_1}{\sqrt{\delta-1}} \in i\mathbb{R}$
$\delta < 1$	$g_{\mathrm{ar}} = i\dfrac{g_0}{\sqrt{\delta^{-1}-1}} \in i\mathbb{R}$	$g_{\mathrm{ar}} = \dfrac{g_1}{\sqrt{1-\delta}} \in \mathbb{R}$

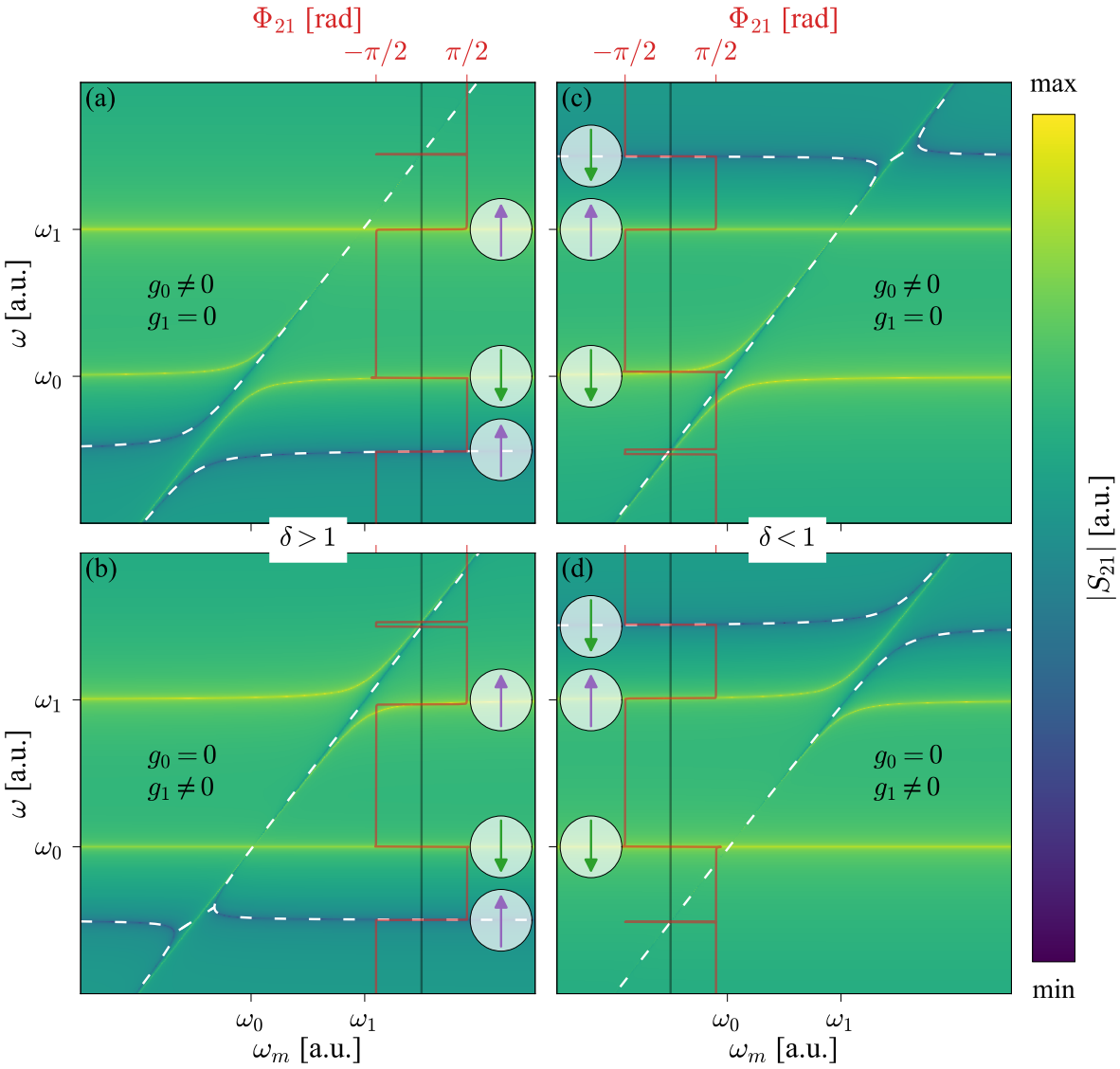

FIGURE 6.5: Transmission spectra of the system sketched in Fig. 6.2 (c) considering the 4 different cases related in Table 6.2 and using Eq. (6.19) showing either an effective level repulsion or level attraction between the antiresonances, where δ and Φ are defined in Eq. (6.16), and the effective antiresonance frequency dependences in dashed white lines using Eq. (6.21). The phase of the S_{21} parameter is presented with red lines, at arbitrary ω_m values. $\Phi = \pi$ in all four cases. Green arrows represent the negative phase-jumps (from $\pi/2$ to $-\pi/2$), while purples arrows represent the positive phase-jumps (from $-\pi/2$ to $\pi/2$).

either a repulsive or an attractive signature, and this is determined by the value of δ. The various situations based on the values of g_0, g_1, and δ, when $\Phi = \pi$ are illustrated in Table 6.2.

As mentioned earlier, when $\delta > 1$, $\omega_{\text{ar}} \leq \omega_0$. In this case, the phase-jump of the lower cavity mode and the cavity antiresonance $\hat{c}_{\text{ar}}$ are opposed, as depicted in Fig. 6.5 (a) and (b), where their arrows are green and purple, respectively. As a result, the lower CMP resulting from the hybridization of the magnon and the lower cavity mode exhibits level repulsion with the antiresonance mode, as depicted in Fig. 6.5 (a). In this case, the coupling strength g_{ar} is real, as provided in Table 6.2. However, the upper cavity mode and the cavity antiresonance exhibit the same phase-jump, represented by purple arrows. Consequently, the lower CMP resulting from the hybridization of the magnon and the upper cavity mode exhibits level attraction with the antiresonance modes, as shown in Fig. 6.5 (b). Here, g_{ar} is imaginary, as also indicated in Table 6.2.

Conversely, when δ is less than 1, $\omega_{\text{ar}} \geq \omega_1$. In this scenario, the phase-jumps of the upper cavity mode and the cavity antiresonance are opposed (purple and green arrows, respectively), while the lower cavity mode and the cavity antiresonance exhibit the same phase-jump, as illustrated in Fig. 6.5 (c) and (d) by green arrows. This leads to level attraction at the antiresonance coupling when the magnon is coupled to the lower cavity mode, as depicted in Fig. 6.5 (c), and to level repulsion at the antiresonance coupling when the magnon is coupled to the upper cavity mode, as shown in Fig. 6.5 (d). Their respective coupling strengths are imaginary and real, as noted in Table 6.2.

In summary, when there is an opposed phase-jump between a cavity mode and an antiresonance mode, it leads to level repulsion in the coupling between the antiresonance and the CMP resulting from the hybridization of the cavity mode and a magnon. Conversely, when there is a similar phase-jump between a cavity mode and an antiresonance mode, it results in level attraction in the coupling between the antiresonance and the CMP.

As mentioned earlier, in contrast to this two-mode cavity, a real cavity is characterized by an infinite amount of modes coupled to the same magnon mode. This results in a highly complex system, making it challenging to derive a straightforward analytic equation with easy interpretability. Nevertheless, the analysis of the phase of the resonances and the cavity antiresonance proves to be valuable for engineering cavities and predicting the coupling behavior of the antiresonance.

6.5 Simulation

6.5.1 Model comparison

This section, focusing on FEM simulation on COMSOL Multiphysics®, aims to put into practice the concepts from the previous section applied not only to just two-mode cavity but to a cylindrical cavity exhibiting seven modes in the Ku-band coupled to one magnon mode, represented by a YIG sphere placed at different locations.

It has previously been concluded that proximity to a node of the RF H-field of a cavity antiresonance was an essential condition for observing the level attraction of an antiresonance [95]. In this study, level attraction was observed exclusively in the

experimental measurements. The simulations were based on CST Studio®, where the H-field distribution is a combination from both probes excited, which does not accurately represent the real field distribution within the measurement setup, where ports are excited alternately, one at a time. Additionally, the simulations did not account for the magnetic properties of the YIG, treating it only as a dielectric, and did not analyze the antiresonance behavior as a function of the YIG's position within the cavity. Moreover, the level attraction was attributed to the Lenz effect produced by the cavity, generating a microwave current that hinders the dynamics of the magnetization. It was concluded that the CMP solely repulsively interacted with the antiresonances. Consequently, in an antinode of the RF H-field of a cavity antiresonance, the strong repulsive coupling would prevent the manifestation of the Lenz effect. However, CMP can in fact exert either repulsive or attractive influence on the coupling with the antiresonance. This behavior depends on the phase-jumps of both the antiresonance and the hybridized cavity mode.

A plausible initial approach to modeling a cavity with infinite modes involves considering the minimum number of modes necessary to achieve the same antiresonance frequency. Identifying the phase-jump of an antiresonance provides insights into whether a cavity mode, through the CMP resulting from its coupling with a magnon, behaves repulsively or attractively with the antiresonance.

6.5.2 Cavity features

In this study, a cylindrical cavity described in [95] is utilized, featuring a height of 35 mm and a radius of 12.5 mm. Positioned at each side of the cavity are two electrical probes, arranged in parallel as displayed in Fig. 6.6 (a). These probes are situated at 10 mm from the cavity's bottom. A YIG sphere, having a radius of 0.5 mm, is positioned at two distinct locations: position A (x, y, z = 11.9, 0, 0.6 mm from the bottom center of the cavity), inducing level repulsion; and position B (x, y, z = 0, 0, 0.6 mm), inducing level attraction.

In Fig. 6.6 (c) and (d), the amplitude and the phase of the transmission are respectively depicted. Seven cavity modes were considered in the input-output model to match the same $|S_{21}|$ trace from the Frequency Domain (FD) simulations. To accomplish this, we first solve for the eigenmodes of the system to extract various parameters, including the phases of the E-field located at each probe, the quality factor, and the cavity mode frequencies, as detailed in Table 6.3, following the procedure described in Sec. 4.1.3. It is worth noting that our assumption involved equal coupling of a cavity mode with each probe, resulting in equal external coupling strengths between an internal mode and ports. As depicted in the inset of Fig. 6.6 (c), there is a frequency shift of $\Delta = 11$ MHz observed for the antiresonance around 13.59 GHz between the FD simulation and the input-output model, corresponding to the frequencies of 13.589 GHz and 13.600 GHz respectively.

Note that we need to consider a sufficient number of modes to approach the FD simulation closely as illustrated in Fig. 6.6 (b), which shows the dependence of the mismatch between FD simulation and input-output as function of the number of modes considered. For instance, when only the TM_{012} and TE_{212} modes are considered, the discrepancy between the simulation and the model is 758 MHz. However, this mismatch decreases to 329 MHz when the TE_{211} mode is included in the model considerations. Therefore, when considering seven modes, the discrepancy is minimized to 11 MHz. The

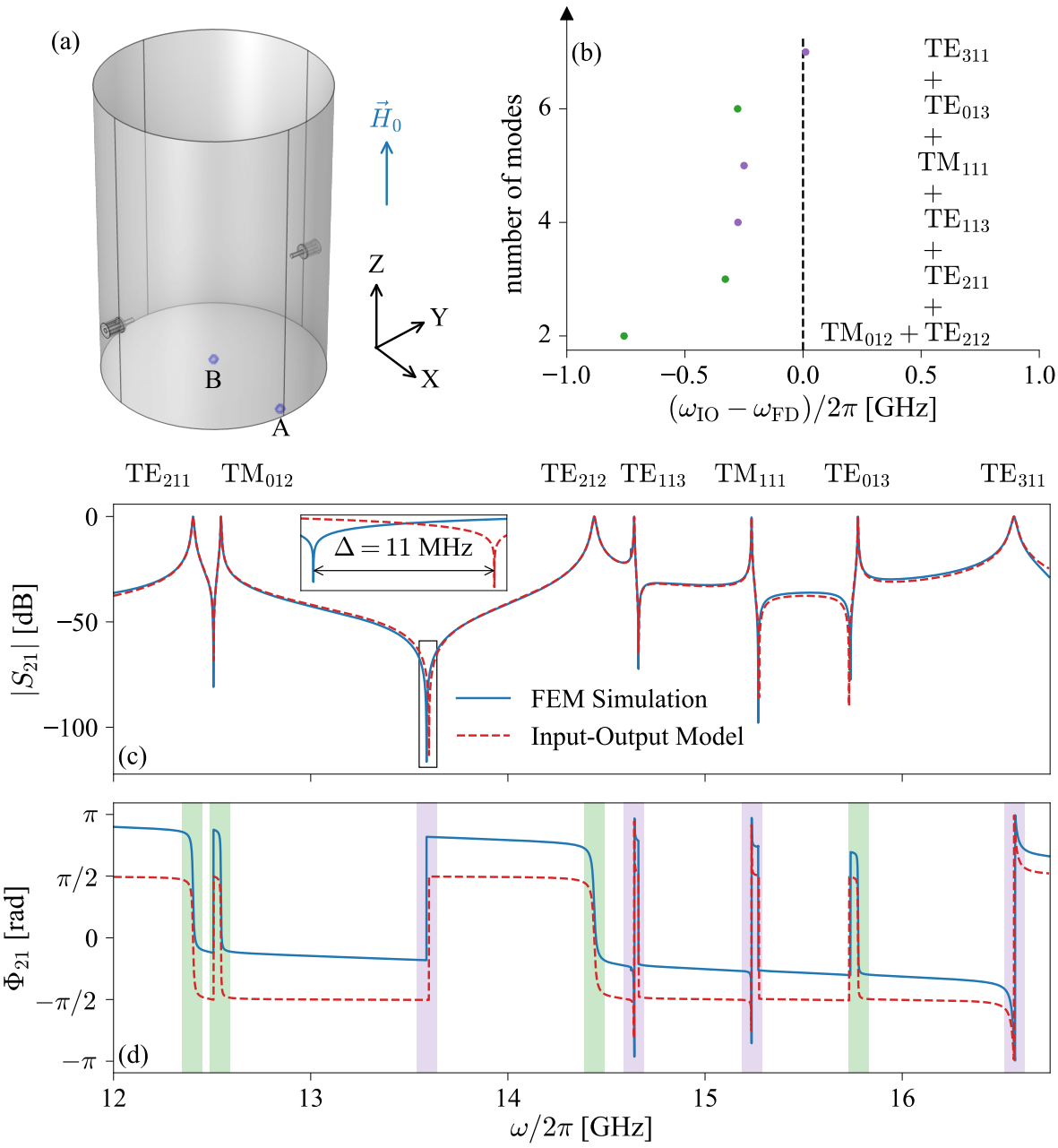

FIGURE 6.6: (a) Schematic of the cylindrical cavity, whith A the YIG position to observe effective repulsive coupling, and B the YIG position to observe effective attractive coupling; (b) Graph illustrating the convergence of the antiresonance frequency between the FEM simulation frequency ω_{FD} and the input-output model frequency ω_{IO} based on the number of considered modes; (c) $|S_{21}|$, and (d) Φ_{21} versus the frequency of the empty cavity, where the input-output model in dashed red line is compared to the FEM simulation in solid blue line. Green dots in (b) and areas in (d) represent modes exhibiting a negative phase-jump (from $\pi/2$ to $-\pi/2$). Purple dots in (b) and areas in (d) depict modes exhibiting a positive phase-jump (from $-\pi/2$ to $\pi/2$), as observed for the phase-jump of the antiresonance at 13.59 GHz in the same color in (d).

TABLE 6.3: Cavity Modes characteristics

Coupling	Φ_{21}-jump	Mode	$\omega/2\pi$ [GHz]	Q	$g_A/2\pi$ [MHz]	$g_B/2\pi$ [MHz]
repulsive	- (green area)	TE_{211}	12.4	1525	13.5	0.0
		TM_{012}	12.5	4441	39.3	0.0
		TE_{212}	14.4	912	30.1	0.0
		TM_{013}	15.8	9228	43.3	0.0
attractive	+ (purple area)	TE_{113}	14.6	7501	3.6	50.0
		TM_{111}	15.2	12023	3.2	72.2
		TE_{311}	16.6	739	2.5	4.5

input-output model demonstrates consistent phase, resembling the FEM simulation, except for a constant phase shift proportional to the frequency in the FEM simulation, as shown in Fig. 6.6 (d). As demonstrated in Sec. 4.1.4.b, this frequency shift can be compensated by introducing a second-order polynomial phase correction to the transmission parameter. Importantly, this adjustment does not affect the underlying physics. Since the same phase is applied to all terms in the expression for S_{21}, the magnitude - representing its absolute value - remains unchanged. Moreover, the phase-jump considerations, which are essential for characterizing the nature of different antiresonance couplings, are also preserved. As mentioned in Sec. 6.3.1, the specific path the phase takes during the phase-jump is not important; what matters is whether the phase-jump is considered positive or negative. In the model, a positive phase-jump indicates a shift from $\pi/2$ to $-\pi/2$, while a negative phase-jump corresponds to a shift from $-\pi/2$ to $\pi/2$. However, due to the polynomial phase shift, it is no longer practical to rely on the simulated phase itself. Nevertheless, the phase-jump consistently alternates between positive and negative, meaning that we must count the number of phase-jumps between the antiresonance and the resonance for proper interpretation. Furthermore, with the inclusion of more than 7 modes, the model fails to converge for the antiresonance frequency and cannot accurately match the frequency obtained from FEM simulations. This phenomenon may be attributed to the first Markov approximation, where the external coupling is assumed to be independent of frequency [234, 235]. Consequently, there is a significant influence from far-detuned modes on the antiresonance frequency. However, this shifts the antiresonance frequency without altering its phase-jump, which remains the key feature for predicting whether the effective antiresonance coupling would be repulsive or attractive.

Around the antiresonance at a frequency of 13.59 GHz, the phase undergoes a positive phase-jump, from $-\pi/2$ to $\pi/2$. On the contrary, the resonances may exhibit a positive or negative phase-jumps, depicted in purple or green areas respectively in Fig. 6.6 (d), and are summarized in Table 6.3, where the YIG sphere has been placed at either position A or B in simulations. As mentioned earlier, a resonance with the same phase-jump contributes attractively, while a resonance with an opposite phase-jump acts repulsively with the antiresonance.

The $TM_{\theta rz}$ and $TE_{\theta rz}$ modes are characterized by the number of field nodes in the θ (spanning 180°), r, and z directions, where r represents the radial direction and θ symbolizes the azimuthal direction in the xy-plane. Referring to Fig. 6.6, for a specified r value (in this case, equal to 1), only the θ number will determine the coupling phase

dependence associated with each mode since the probes are oriented in the radial direction. In this scenario, modes with an odd θ number induce a repulsive effect, while modes with an even θ number generate an attractive influence.

The H-field and E-field distributions of the repulsive mode TE_{212} is illustrated in Fig. 6.7 (a) and (c), while the field distributions of the attractive mode TE_{113} is depicted in Fig. 6.7 (b) and (d). For each mode in the Ku-band, we calculated the coupling strengths [110] for two distinct locations of the YIG sphere, A and B, as summarized in Table 6.3. Here, we present only two modes to illustrate the main message of the chapter: regarding the field distribution of modes that act repulsively or attractively to the generated antiresonance permit in determining the optimal positioning of the YIG sphere as function of the needs, level attraction or repulsion behavior with the antiresonance. The conclusion of the field distribution of the two illustrated mode also applies for the other repulsive and attractive modes, as shown in Appendix 6.B.

At the bottom right side in the xz-plane of the cavity (position A), the YIG sphere is positioned at an anti-node of the H-field for the repulsive modes and at a node of the H-field for the attractive modes. In contrast, at the bottom center position (position B), the YIG sphere is placed at a node of the H-field for the repulsive modes and at an anti-node of the H-field for the attractive modes. More generally, we observe that the repulsive modes exhibit a minimum in the H-field at position B, while the attractive modes show a minimum in the H-field at position A. This indicates that by carefully positioning the YIG sphere within the cavity, we can selectively minimize the impact of either the repulsive or attractive mode.

The modes are either even (for repulsive modes) or odd (for attractive modes) along the azimuthal direction, determining the sign of the probed E-field in transmission. This relationship is depicted in Fig. 6.7, which shows the E-field distribution in the xy-plane. In Fig. 6.7 (e) and (f), the FD simulation of the transmission spectrum versus the magnon frequency and the applied RF frequency reveals the effective level repulsion of the antiresonance when the YIG sphere is positioned at position A, and the effective level attraction of the antiresonance when the YIG sphere is positioned at position B, respectively. Both types of coupling are effectively replicated by the input-output model, depicted in white dashed lines in Fig. 6.7 (e) and (f). Note that the effective antiresonance frequencies were obtained by fitting the resulting spectra from the input-output model. These frequencies are illustrated in Sec. 6.A.

Despite the similarity in coupling behavior, there exists a notable disparity in the coupling strengths between the simulation and the model. Specifically, the effective repulsive (attractive) coupling strength is of 26 MHz (15 MHz) in the simulation, contrasting with 14 MHz (24 MHz) in the model when the YIG sphere is positioned at location A (B). This discrepancy may arise from the approximations made for the external coupling strength and the neglected internal photonic damping rates. Additionally, limitations in mode truncation may contribute to an inadequate value. Nevertheless, our findings demonstrate that modes can exhibit either repulsive or attractive effective coupling, and by strategically engineering cavities to spatially separate the modes, it becomes possible to control the coupling behavior when positioning the YIG sphere at different locations.

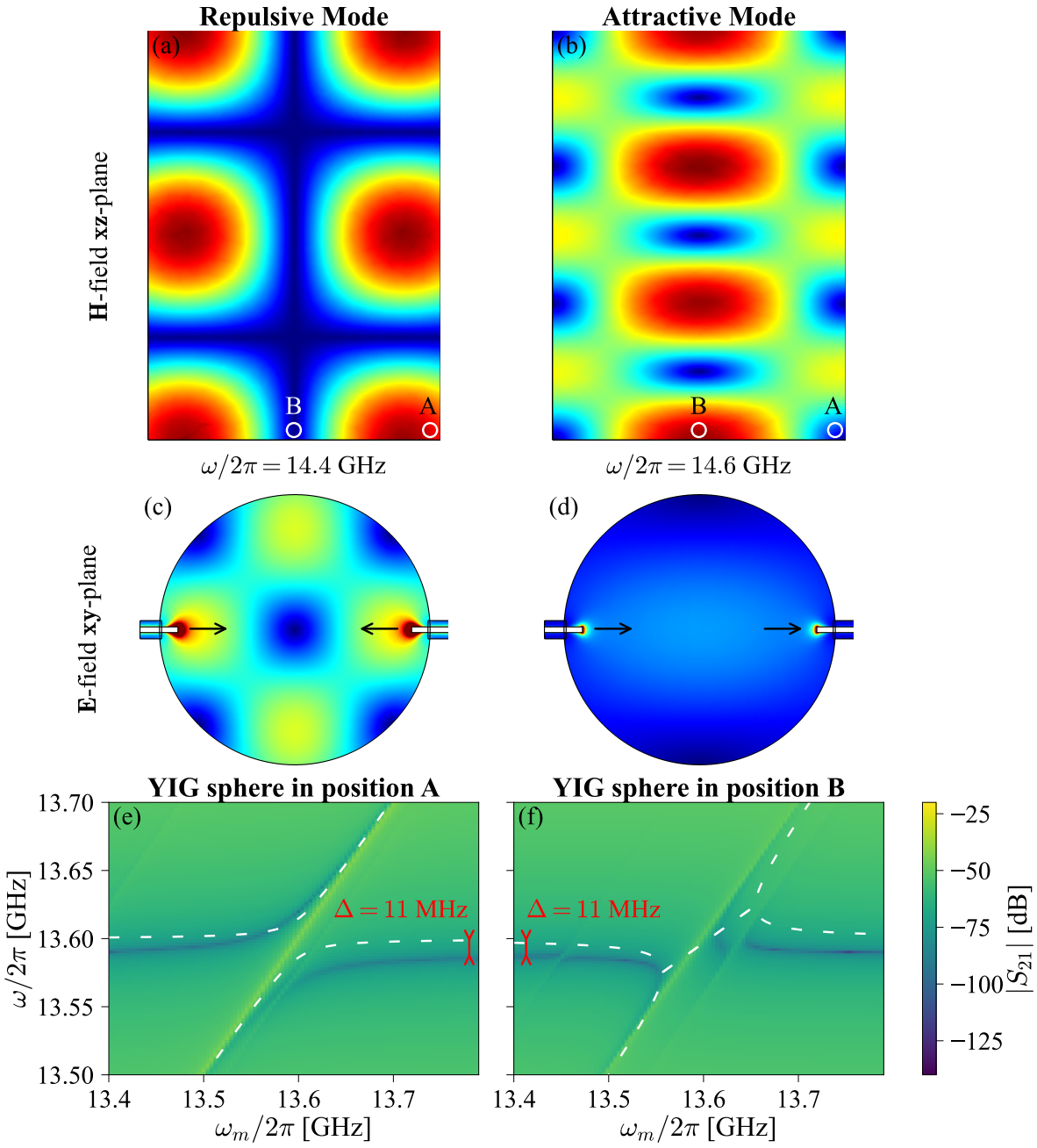

FIGURE 6.7: Norm of the H-field in the xz-plane for (a) TE_{212} and (b) TE_{113}. Norm of the E-field in the xy-plane at the height of the probes for (c) TE_{212}, and (d) TE_{113}. In (a)-(d), the circles illustrate the positions (A or B) of the YIG sphere mentioned in Fig. 6.6, and the black arrows in (c) and (d) indicate the polarization of the E-field at the probe locations. The transmission spectra from FD simulation are shown in (e) when the YIG sphere is placed at position A, and in (f) when the sphere is placed at position B. Utilizing the parameter values from Table 6.3, including the mode frequencies, the phase of the E-field polarization at each probe, the quality factors, and the coupling strengths of the 7 modes, the white dashed line in (e) and (f) represents the antiresonance frequency obtained by fitting the resulting spectra from the input-output model sketched in Fig. 6.12 in Appendix 6.A.

6.6 Conclusion

This study has provided valuable insights into the intricate interaction between cavity modes and magnons within quasi-closed cavities. Through the incorporation of the input-output formalism enhanced with a crucial phase factor in external couplings, we have not only successfully replicated antiresonance behavior in simulations but also provided explanations for the intriguing phenomena of antiresonances, encompassing both their level repulsion and level attraction, as observed in the transmission spectrum. Furthermore, we provided and demonstrated the physical underpinnings of the effective antiresonance coupling g_{ar}. Understanding the phase-jumps of the antiresonance and the different mode families (e.g. characterized by their symmetries), enables the prediction of the behavior of g_{ar} regarding the coupling of mode families.

The reconfigured model introduced here carries promising implications for cavity design, offering a versatile tool to tailor these structures for a wide range of applications, from metrology [214, 215] to RF devices [236, 237] and the domain of quantum devices [87, 238–240].

6.7 Further Work

In this section, we compare the model developed using input-output theory, as presented in this chapter, with measurements performed on the double re-entrant cavity. We aim to verify the statement from [95], which claims that the RF magnetic field in the cavity only acts repulsively with a cavity antiresonance. To justify this statement, it has been considered the RF magnetic field distribution in the cavity at the antiresonance frequency, as presented in Sec. 6.5.2. It has been concluded that positioning the YIG sphere in an intense field would produce level repulsion, while positioning the YIG sphere at a field minimum would produce level attraction. This was explained by the negative back-action due to the Lenz effect being dominant when the YIG sphere is at a field minimum (the spin precession induces an RF h-field, which impede the the spin precession).

In this chapter, we analytically demonstrate that no Lenz effect occurs. The antiresonance arises from interferences between different pathways, i.e. cavity modes, that the RF field takes. Consequently, the RF coupling depends on the phase-jump of the different cavity modes and their coupling strengths with the magnon.

Considering COMSOL Multiphysics® simulations, measurements, and modeling, we will show that the field distribution at the antiresonance frequency provides no insights into the coupling nature of the antiresonance. Only an analysis of the different modes on each side of the antiresonance can yield a correct interpretation.

6.7.1 Antiresonance creation

The first step is to design a cavity that presents an antiresonance distinct from a simple cylindrical cavity. For this purpose, we used a double re-entrant cavity, previously described in Chapter 5. To create an antiresonance at a sufficiently low frequency, we used a dielectric with a relative permittivity $\varepsilon_{\mathrm{r}} = 10$ and dimensions $6.2{\times}3.8{\times}0.6$ mm^3, positioned between the two posts. To understand how antiresonances can occur, FD

simulations were performed on the cavity for eight different dielectric widths, ranging from 520 µm to 580 µm. The transmissions for each dielectric width are depicted as solid black lines in Fig. 6.8 (a). As shown, two antiresonances occur and repel each other in frequency as the dielectric width increases. To understand which variables cause these antiresonance

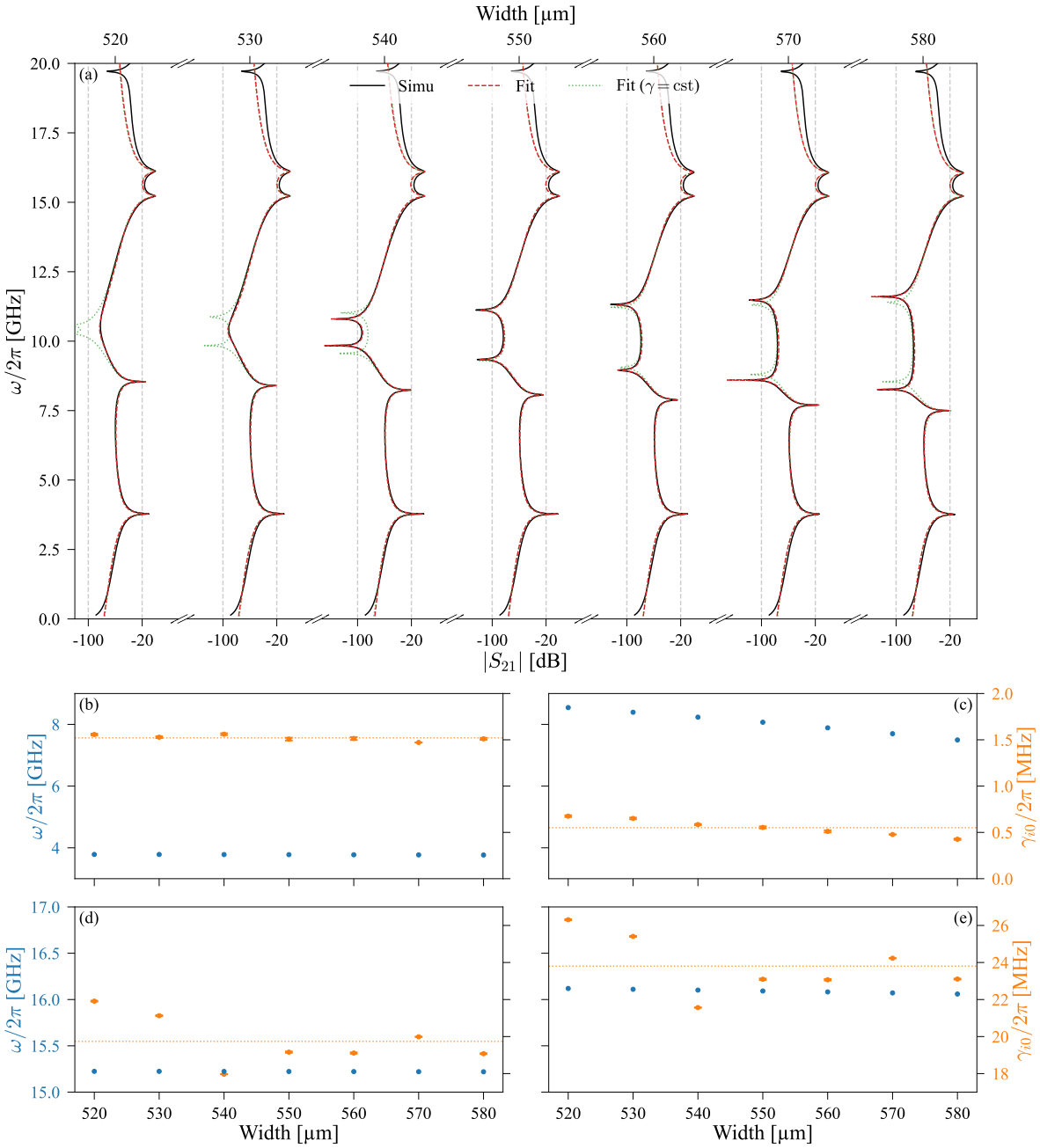

FIGURE 6.8: (a) Transmission of the dielectric-loaded cavity at different dielectric widths: FD simulation in solid black lines; input-output model with fitted γ_{i0} values in dashed red lines; and input-output model with the mean over dielectric widths of the fitted γ_{i0} values in dotted green line. (b)-(e) show the mode frequencies in blue and the fitted $\gamma_{i0}/2\pi$ values in orange versus the dielectric width for the first four modes. The mean values of $\gamma_{i0}/2\pi$ over the dielectric widths are represented by the dotted orange lines for each mode.

dynamics, each of the transmissions was fitted using the input-output model. In the FD simulations, the cavity boundaries were considered perfect electric conductors, meaning that intrinsic dissipation rates associated with electric losses are null. The fitted variables are the external dissipation rates γ_{ij}, associated with the external coupling strengths κ_{ij}. In this cavity, two probes are considered, and their coupling to one mode is assumed to be equal, i.e., $\gamma_{i0} = \gamma_{i1}$, where i represents the considered cavity mode, and 0 or 1 represents the first or second probe in the cavity.

The fitted values of the external dissipation rates are illustrated in Fig. 6.8 for (b) γ_{00}, (c) γ_{10}, (d) γ_{20}, and (e) γ_{30} with respect to the dielectric width. Note that the mode frequencies ω_i are depicted in Fig. 6.8 (b)-(e) and are known from eigenmodes simulations. The external coupling phases ϕ_{ij} lead to the same phase jumps for the first and third modes, and are opposed to the second and fourth modes.

The dashed red line in Fig. 6.8 (a) represents the transmission of the input-output model with the values given in Fig. 6.8 (b)-(e), accurately reproducing the resonances and antiresonances in the frequency range from 3.5 to 16.5 GHz. We observe that only the frequency of the second mode depends on the dielectric width, decreasing slightly from 8.54 to 7.50 GHz as the width increases from 520 to 580 µm. Additionally, the external dissipation rates of the first mode remain relatively constant, while those of the second mode decrease. However, the external dissipation rates of the last two modes vary with respect to the dielectric width without a clear trend.

To understand the role of the second mode's frequency decrease and the variation in external dissipation rates, all transmissions were plotted as dotted green lines in Fig. 6.8 (a) using the input-output model, assuming constant γ values equal to their mean values across different dielectric widths. We also observe the attraction of the two antiresonances with decreasing dielectric width, which is primarily due to the increasing frequency of the second mode. However, without the γ variations of the last two modes, the attraction of the two antiresonances is not sufficient to match the simulation results.

In the following subsection, we will focus on the second antiresonance, higher in frequency. This analysis will demonstrate that the field distribution at the antiresonance frequency does not provide insights into the antiresonance coupling behavior.

6.7.2 Coupling analysis

The measured transmission of the dielectric-loaded cavity without a YIG sphere is depicted in Fig. 6.9 (a) as a solid black line, where the second antiresonance frequency is at 11.46 GHz. Unlike the FD simulations, intrinsic losses of the modes were considered. Consequently, the number of unknown variables increased to eight: four external dissipation rates γ_{i0} as previously; and four intrinsic dissipation rates γ_i^{int} associated with each cavity mode.

Fits were performed iteratively on the external dissipation rates, followed by the intrinsic dissipation rates until convergence, within the frequency range of 3.3 to 15.7 GHz. The results are shown as dashed grey lines in Fig. 6.9 (a). The fitted transmission, depicted by the dashed red line, shows excellent agreement with the measured transmission. The fitted values are detailed in Table 6.4.

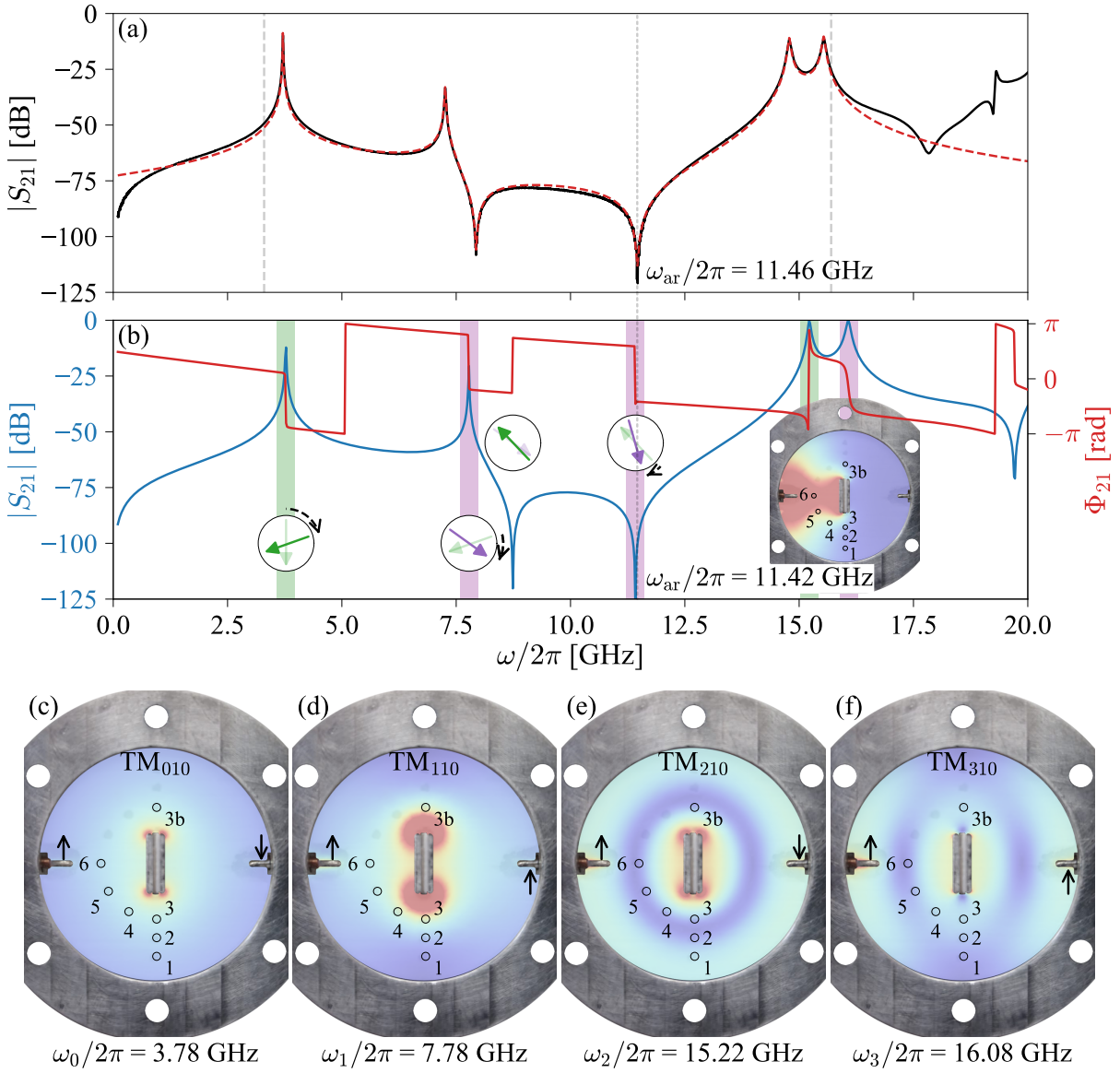

FIGURE 6.9: (a) Transmission of the dielectric-loaded cavity: Measurement in solid black line; and input-output model with fitted γ_{i0} and γ_i^{int} values in dashed red line. The fit was made in the frequency range from 3.5 to 16.5 GHz depicted by the dashed grey lines. (b) FD simulation of the transmission of the dielectric-loaded cavity with a dielectric width of 566 µm. The magnitude is depicted in blue, and the phase in red. The modes with the same phase-jump are illustrated in the green areas and arrows, while the modes and the considered antiresonance with the opposite phase-jump are shown in the purple areas and arrows. The dotted grey line indicates the measured considered antiresonance frequency. The inset shows the RF magnetic field in the cavity at the antiresonance frequency. (c)-(f) depict the RF magnetic fields of the first four modes and the different YIG positions.

In Fig. 6.9 (b), the simulated transmission is depicted by a solid blue line for a dielectric width of 566 µm. While the frequencies of the cavity modes do not match the measurements exactly, the second antiresonance at 11.42 GHz is very close to the measured

TABLE 6.4: Fitted values of the external dissipation rates γ_{i0} and the internal dissipation rates γ_i^{int} for the first four modes.

modes	$\boldsymbol{\gamma_{i0}}$ **[MHz]**	$\boldsymbol{\gamma_i^{\text{int}}}$ **[MHz]**
$\mathbf{TM_{010}}$	1.186 ± 0.006	3.4 ± 0.7
$\mathbf{TM_{110}}$	0.2334 ± 0.0007	20.2 ± 0.7
$\mathbf{TM_{210}}$	7.56 ± 0.03	38.1 ± 1.3
$\mathbf{TM_{310}}$	8.89 ± 0.04	40.2 ± 1.7

value of 11.46 GHz, indicated by the dotted grey line. The phase Φ_{21} is shown as a solid red line, indicating that the first and third modes share the same phase-jump, represented by the green area and arrow, and are opposed to the second and fourth modes, represented by the purple area and arrow. In the representations with the arrows, the total phase shift is considered, referring to the shift discussed Sec. 4.1.4.b. As shown, this shift does not alter the "nature" of the phase-jump we need to consider; that is, the specific phase values before and after the phase-jump are irrelevant. Instead, what matters is the number of phase-jumps separating a resonance from the antiresonance. Depending on whether this number is even or odd, the phase-jumps will be categorized as either the same or opposed, which in turn determines whether the coupling is attractive or repulsive.

The second antiresonance exhibits the same phase-jump as the second and fourth modes, implying that these modes contribute attractively to the antiresonance coupling, while the other two modes contribute repulsively.

In the inset of Fig. 6.9 (b), the RF magnetic field distribution at the antiresonance frequency is shown, with various placements of the YIG sphere, numbered from 1 to 6, and an additional position 3b for a second YIG sphere, which will be discussed later. According to the conclusions in [95], position 1 of the YIG sphere would exhibit attractive coupling of the antiresonance or, at the very least, a less repulsive coupling compared to position 6, because the magnetic field is minimized at position 1 and maximized at position 6.

In Fig. 6.9 (c)-(f), the first four modes are illustrated: TM_{010} at 3.78 GHz, TM_{110} at 7.78 GHz, TM_{210} at 15.22 GHz, and TM_{310} at 16.08 GHz. For the measurements, the mode frequencies are $\omega_0/2\pi = 3.71$ GHz, $\omega_1/2\pi = 7.26$ GHz, $\omega_2/2\pi = 14.78$ GHz, and $\omega_3/2\pi = 15.54$ GHz. Interpreting the antiresonance coupling based solely on the RF magnetic field distribution of these modes is challenging.

However, some observations can be made regarding the magnetic field distribution at specific positions. At position 1, the two "attractive modes" (TM_{110} and TM_{310}) have minimized field intensity, whereas their field is significantly higher at position 3. For the "repulsive modes" (TM_{010} and TM_{210}), the field intensity is relatively constant between positions 1 and 3. This suggests that the antiresonance coupling strength would be more attractive or less repulsive at position 3 compared to position 1. Similarly, at position 6, the field intensity for the "attractive modes" is less than at position 3, while the field for the "repulsive modes" remains constant, implying that position 6 is less attractive or more repulsive than position 3.

It is important to note that the field distributions in Fig. 6.9 (c)-(f) are not normalized, and their values were saturated to better observe the field variations. Crucially, it is not merely the mode with the higher field intensity at the YIG position that determines the

TABLE 6.5: Coupling strength values in MHz of the first four modes at the 6 YIG sphere positions from EM simulations.

modes \ positions	1	2	3	4	5	6
$\mathbf{TM_{010}}$	32.14	40.19	52.41	48.89	43.95	42.40
$\mathbf{TM_{110}}$	3.05	8.93	23.45	20.03	16.84	16.41
$\mathbf{TM_{210}}$	82.15	44.06	32.43	32.76	20.34	3.93
$\mathbf{TM_{310}}$	25.06	58.58	82.53	78.36	46.19	5.79

antiresonance coupling behavior. As demonstrated in Eq. (6.22), the internal coupling strengths are effectively "weighted" by the external dissipation rates, meaning that the coupling behavior at the antiresonance is influenced by the interplay of these factors rather than by field intensity alone.

To investigate the coupling behavior at various YIG sphere positions, the coupling strengths for each mode were computed using eigenmodes simulations. These computed values are summarized in Table 6.5 and were incorporated into the input-output model alongside the dissipation rates provided in Table 6.4. From the measurements, the gyromagnetic ratio of the YIG spheres was estimated to be $\gamma = 28.74 \pm 0.20$ GHz.T^{-1}.

The transmission spectra from the input-output model for all YIG positions are illustrated in the first column of Fig. 6.10. The Gilbert damping rate was arbitrarily set to $\alpha = 2.10^{-3}$ to align with the measurement observations. Note that no fitting was performed on α as it does not affect the coupling behavior. The increase in damping rate could be attributed to the excitation of multiple magnon modes, driven by the inhomogeneous RF magnetic field concentrated on the YIG [241]. These spectra align with the previous interpretation of the modes' field distributions. Specifically, at position 1, the antiresonance coupling exhibits level repulsion, whereas at position 3, it shows level attraction. Furthermore, position 6 also demonstrates no coupling, meaning that the coupling effectively decreased by compensation between "attractive modes" and "repulsive modes".

The second column of Fig. 6.10 presents the measured transmission spectra for all YIG positions. It is evident that interpreting the antiresonance coupling behavior based on the field distribution at the antiresonance frequency did not accurately predict the coupling behavior. In particular, it was anticipated that position 1 would exhibit a weaker repulsive coupling compared to position 6; however, the measurements reveal the opposite trend.

The third column in Fig. 6.10 depicts the measured phases Φ_{21} for all YIG positions. Although the coupling behavior is not always clear from certain transmission measurements - where coupling with higher magnon modes obscures the antiresonance polaritons around the coupling frame - the phase jump in the phase spectra helps track the polariton frequencies. The dotted black line in the third column represents the fitted antiresonance polaritons according to the input-output model.

We observe that the evolution of the antiresonance coupling across different YIG positions is consistent between the input-output model and the measurements. Specifically, positions 1, 3, 4, and 5 exhibit the same coupling strength and nature. However, for positions 2 and 6, where the coupling strengths are respectively very low or does not

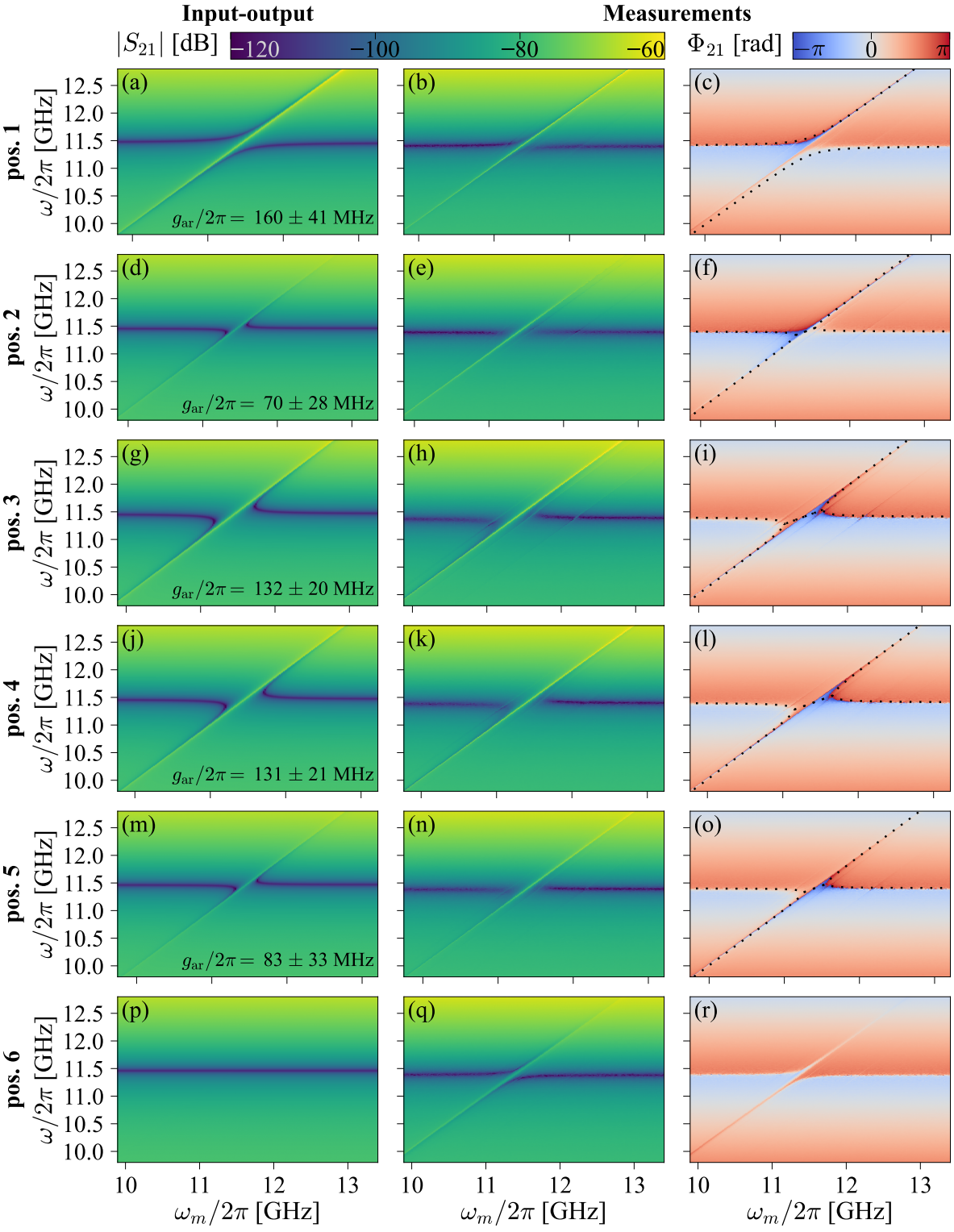

FIGURE 6.10: Transmission spectra at the 6 YIG sphere positions, showing the magnitude for the input-output model in the first column, the measurements in the second column, and the phase of the measurements in the third column. The antiresonance polariton frequencies from the input-output transmission spectra are indicated by dotted black lines in the third column.

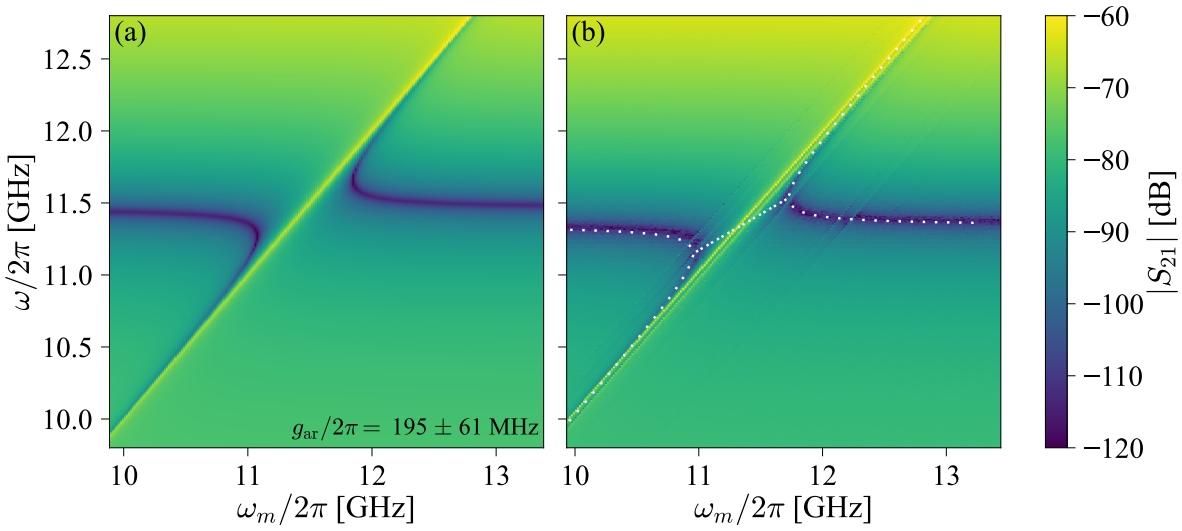

FIGURE 6.11: Transmission spectra with two YIG spheres positioned at 3 and 3b for (a) the input-output model and (b) measurements. In (b), the antiresonance polariton frequencies from the input-output model are indicated by a dotted white line.

occur, the coupling behavior differs, and the measurements indicate level repulsion. This discrepancy can be attributed to the fact that the resonance coupling strengths were extracted from EM simulations, which used different mode frequencies than those measured. Consequently, the coupling strength may vary slightly, leading to different antiresonance coupling behaviors at low coupling strengths.

In Fig. 6.11, we present the transmission spectra of (a) the input-output model and (b) the measurement with two YIG spheres placed at positions 3 and 3b. For the model, the coupling strengths of each mode at position 3b are assumed to be the same as those at position 3, based on symmetry considerations of the cavity. The effective antiresonance coupling strength in the model is $g_{ar}/2\pi = 195 \pm 61$ MHz, and the antiresonance polariton frequencies fit well with the measurements, as indicated by the dotted white line in Fig. 6.11(b). This demonstrates that by considering the field distribution of the cavity modes, we can tune the antiresonance as desired and increase the coupling strength, regardless of the coupling nature.

Appendices of Chapter 6

6.A Model fitting

In Fig. 6.12, the transmission spectra generated by the input-output model for two distinct positions of the YIG sphere (A and B) are illustrated in (a) and (b) respectively. To generate these spectra, the model was provided with necessary parameter values, including the mode frequencies, the phase of the E-field polarization at each probe, the quality factors, and the coupling strengths of the 7 modes as detailed in Table 6.3. Due to the complexity of obtaining an analytical solution for the polariton frequencies, the antiresonance frequencies were determined by fitting the two spectra.

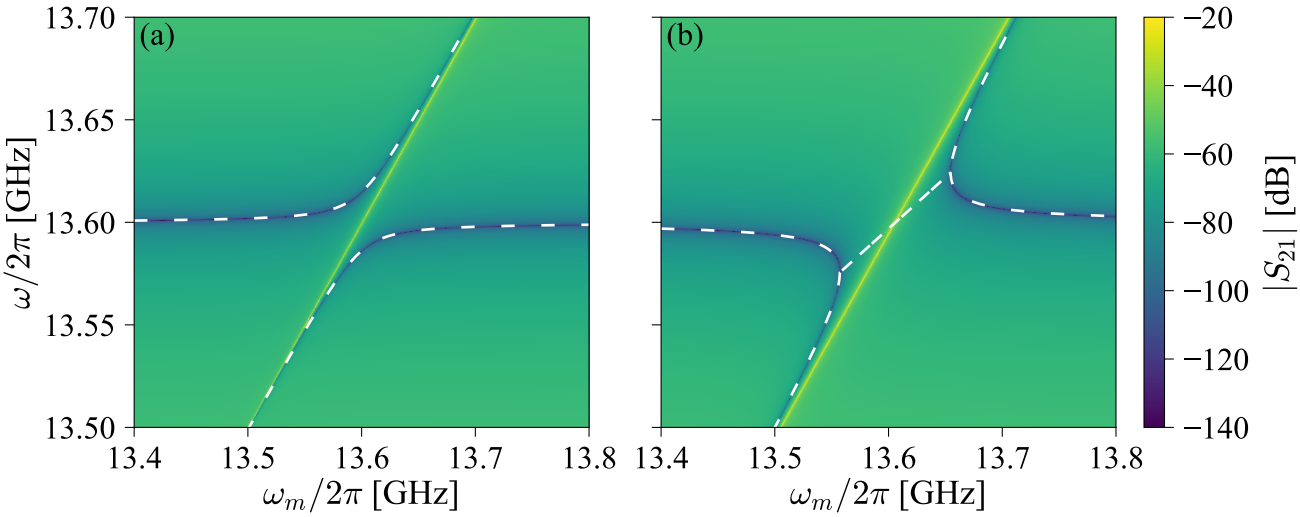

FIGURE 6.12: Transmission spectra generated by the input-output model for two different positions of the YIG sphere: (a) when positioned at A, and (b) when positioned at B. The parameter values injected into the model, including mode frequencies, the phase of the E-field polarization at each probe, quality factors, and coupling strengths of the 7 modes, are detailed in Table 6.3. The antiresonance frequencies, indicated to the dashed white lines, were determined by fitting the spectra.

6.B Field Distribution of cavity modes

Fig. 6.13 illustrates the magnitudes of the H- and E-fields for the seven considered cavity modes in the input-output model, as discussed in Sec. 6.5.2.

For $r = 1$, the repulsive modes exhibit an even θ number, leading to a minimum in the H-field at position B. Additionally, the E-field polarization at the two probes is π-dephased, a condition necessary for observing level repulsion in the effective coupling of the antiresonance at 13.59 GHz with the coupled magnon-photon mode.

Conversely, with $r = 1$, the attractive modes exhibit an odd θ number, resulting in a minimum of the H-field at position A. Furthermore, the E-field polarization at the two probes is in phase, a condition for observing level attraction in the effective coupling of the antiresonance at 13.59 GHz with the coupled magnon-photon mode.

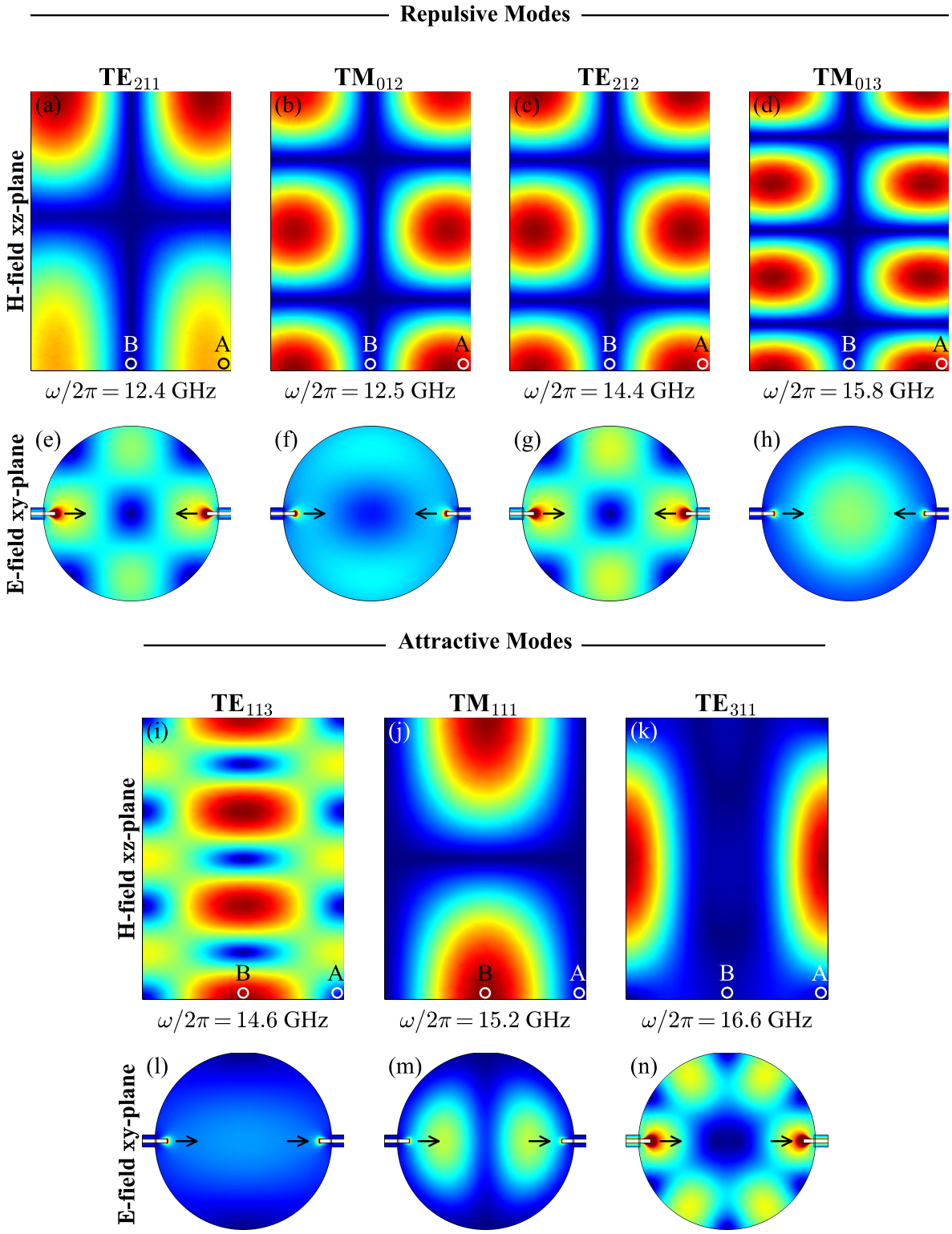

FIGURE 6.13: Norm of the H-field in the xz-plane for (a)-(d) repulsive modes and (i)-(k) attractive modes. Norm of the E-field in the xy-plane at the height of the probes for (e)-(h) repulsive modes, and (l)-(n) attractive modes. The circles illustrate the positions (A or B) of the YIG sphere mentioned in Fig. 6.6, and the black arrows in (e)-(h) and (l)-(n) indicate the polarization of the E-field at the probe locations.

7 Conclusion & Outlook

In this thesis, we explore the dynamic field of spincavitronics, with a particular emphasis on the robust interplay between cavity modes and magnons in three-dimensional (3D) cavities. The exploration of cavity magnon polaritons has demonstrated that strong coupling between magnons and photons can result in innovative hybrid states with significant applications across quantum technologies and communication systems.

The origins of spincavitronics can be traced back to key contributions made in the early 2010s, with the prediction of strong magnon-photon coupling by Soykal and Flatté (2010) [52], followed by experimental confirmations from Huebl et al. (2013) [53], Tabuchi et al. (2014) [54], and Zhang et al. (2014) [55] that marked significant advancements in our understanding of these interactions. These pioneering studies underscored the versatility of magnons, characterized by their broad frequency tunability and long coherence times, thereby positioning them as promising candidates for quantum memory applications. Their role in quantum magnonics further opens new avenues for enhancing quantum computing and communication technologies.

A significant aspect of this research is the characterization of the ultra-strong coupling regime, wherein the coupling strength surpasses 10% of the cavity frequency. The USC regime not only enhances performance across various applications but also enables the observation of novel phenomena, highlighting its potential for exploring new states of matter and deepening our understanding of light-matter interactions. Mechanisms to achieve the USC regime, whether by coupling multiple dipoles or optimizing the coupling strength of a single dipole to a cavity mode, provide an expanded toolkit for experimental and theoretical investigations in cavity magnonics.

Our experimental findings validate the critical importance of optimizing parameters, such as the filling factor, in realizing USC, alongside conventional factors like resonator frequency and spin density. The utilized reconfigurable double-post reentrant cavity design permits to explore the transition from strong coupling to the USC regime, marking a substantial advancement in our comprehension of magnon-photon interactions. Notably, our results suggest that commonly utilized models, such as the Dicke and Hopfield models, may not fully encapsulate the complexities observed in our data, necessitating further refinement of theoretical frameworks. The incorporation of a magnon frequency shift related to the filling factor introduces a new dimension in modeling magnon-photon interactions, warranting additional research to elucidate the underlying physics.

Moreover, we highlighted in this thesis the critical role of level attraction in systems exhibiting strong coupling between magnons and antiresonance cavity modes. The emergence of singularities, such as exceptional points and bound states in the continuum, offers exciting prospects for applications in sensing technologies and quantum information processing. Level attraction has the potential to enhance device sensitivity, enabling robust energy transfer against external perturbations. Through the application of input-output theory, we elucidate the fundamental principles governing the coupling behaviors of antiresonances in quasi-closed systems.

Overall, the studies presented in this thesis contribute significantly to our understanding of cavity magnon polaritons, examining the dynamics of strong and ultra-strong coupling regimes while unveiling new opportunities for the advancement of quantum technologies and radiofrequency applications. The implications for cavity design and optimization extend from metrology to advanced quantum devices, highlighting the versatility and promise of spincavitronics for future technological developments.

Outlook:

Our investigation into USC between an Yttrium Iron Garnet (YIG) slab and a 3D cavity reveals a coupling ratio of 59% at room temperature, a milestone in magnon-photon coupling. However, the observed magnon frequency shift, previously unreported, requires elucidation. Future theoretical work should focus on understanding this phenomenon, particularly the nonlinearities that may arise due to the coupling strength, which are only observable in the USC regime.

Our recent advancements in cavity design have demonstrated enhanced coupling ratios beyond those reported previously, providing deeper insights into the quadratic evolution of magnon frequency shifts relative to coupling ratios. Future machining of these cavities aims to produce new experimental data approaching the deep strong coupling regime, a frontier not yet achieved in magnon-photon hybrid systems at room temperature.

The level attraction of antiresonances within quasi-closed cavities has been insufficiently explored thus far, here we relate the future direction in the exploration of level attraction of antiresonances in quasi-closed cavities:

(i) Our study demonstrates that excessive mode incorporation can lead to discrepancies between measurements or simulations and the developed model. Specifically, the first Markov condition in the input-output derivation assumes a constant external coupling strength over frequency, implying that cavity modes distant from the antiresonance may exert influence. For one-dimensional cavities, such as Fabry-Pérot cavities, it has been shown that coupling strength follows a cardinal sinusoidal function. A proper generalization for 3D cavities could resolve the aforementioned discrepancies.

(ii) The literature presents several models aimed at interpreting observations of level attractions, particularly for open cavities. However, these models often incorporate phase factors to align with experimental results, lacking deeper physical justification. Future work could clarify and develop a more physically grounded model.

(iii) A primary objective in leveraging level attraction within a system is to achieve exceptional points. While level attraction exists in 3D cavities, we posit that EPs

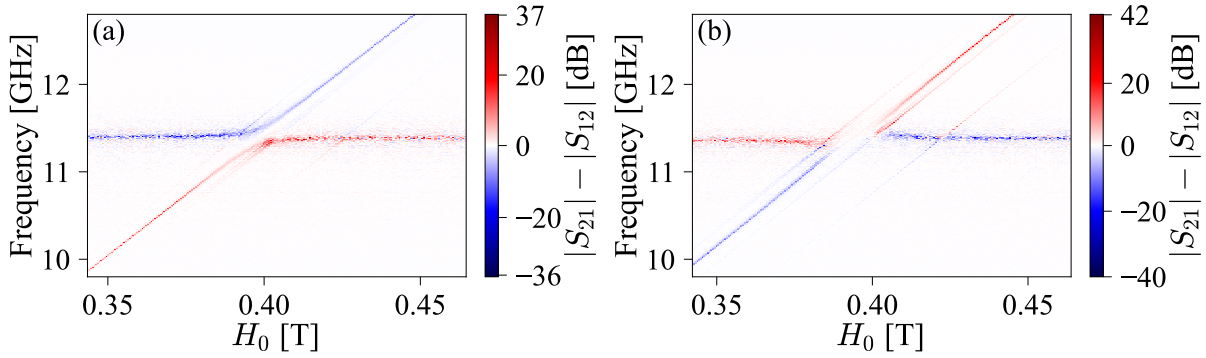

FIGURE 7.1: Non-reciprocity of the antiresonances between transmission probes as a function of the applied magnetic field and input microwave frequency for two YIG positions in the dielectric-loaded double re-entrant cavity, where the antiresonance coupling is (a) repulsive, and (b) attractive.

can be generated by modulating magnon dissipation, as is customary. Future investigations will explore tuning dissipation through the spin Hall effect [242].

(iv) Our recent measurements of double reentrant cavities, as discussed in our exploration of level attraction, reveal significant potential for non-reciprocity in 3D cavities, as depicted in Fig. 7.1. We attribute this phenomenon to the combination of internal coupling phases (highlighted in [157]), and external coupling phases elucidated in our study.

Ultimately, enhancing our model to incorporate models describing the ultra-strong coupling regime may yield higher tunability of antiresonances and increased non-reciprocity. Moreover, the cavity designs can be adapted for integration on a printed circuit board (PCB) using substrate integrated waveguide (SIW) technology [243, 244], which serves as the integrated analog of a 3D cavity. In this case, the dimensions must account for the substrate and dielectric permittivities, enabling operation within the same frequency range while maintaining comparable magnon-photon coupling performance. However, additional losses are introduced by the dielectric material and the metallic vias, which serve as cavity walls, leading to a reduction in the quality factor.

Bibliography

[1] S Das Sarma. "Spintronics: Fundamentals and Applications". In: *Rev. Mod. Phys.* 76.2 (2004).

[2] Mark Johnson and R. H. Silsbee. "Interfacial Charge-Spin Coupling: Injection and Detection of Spin Magnetization in Metals". In: *Physical Review Letters* 55.17 (Oct. 1985), pp. 1790–1793. ISSN: 0031-9007. DOI: 10.1103/PhysRevLett.55.1790.

[3] M. N. Baibich et al. "Giant Magnetoresistance of (001)Fe/(001)Cr Magnetic Superlattices". In: *Physical Review Letters* 61.21 (Nov. 1988), pp. 2472–2475. ISSN: 0031-9007. DOI: 10.1103/PhysRevLett.61.2472.

[4] G. Binasch et al. "Enhanced Magnetoresistance in Layered Magnetic Structures with Antiferromagnetic Interlayer Exchange". In: *Physical Review B* 39.7 (Mar. 1989), pp. 4828–4830. DOI: 10.1103/PhysRevB.39.4828.

[5] S. A. Wolf et al. "Spintronics: A Spin-Based Electronics Vision for the Future". In: *Science* 294.5546 (Nov. 2001), pp. 1488–1495. ISSN: 0036-8075, 1095-9203. DOI: 10.1126/science.1065389.

[6] Lihui Bai et al. "Spin Pumping in Electrodynamically Coupled Magnon-Photon Systems". In: *Physical Review Letters* 114.22 (June 2015), p. 227201. ISSN: 0031-9007, 1079-7114. DOI: 10.1103/PhysRevLett.114.227201.

[7] V. Castel et al. "Platinum Thickness Dependence of the Inverse Spin-Hall Voltage from Spin Pumping in a Hybrid Yttrium Iron Garnet/Platinum System". In: *Applied Physics Letters* 101.13 (Sept. 2012), p. 132414. ISSN: 0003-6951, 1077-3118. DOI: 10.1063/1.4754837.

[8] V. Castel et al. "Frequency and Power Dependence of Spin-Current Emission by Spin Pumping in a Thin-Film YIG/Pt System". In: *Physical Review B* 86.13 (Oct. 2012), p. 134419. ISSN: 1098-0121, 1550-235X. DOI: 10.1103/PhysRevB.86.134419.

[9] H. Maier-Flaig et al. "Spin Pumping in Strongly Coupled Magnon-Photon Systems". In: *Physical Review B* 94.5 (Aug. 2016), p. 054433. ISSN: 2469-9950, 2469-9969. DOI: 10.1103/PhysRevB.94.054433.

[10] O. Mosendz et al. "Quantifying Spin Hall Angles from Spin Pumping: Experiments and Theory". In: *Physical Review Letters* 104.4 (Jan. 2010), p. 046601. ISSN: 0031-9007, 1079-7114. DOI: 10.1103/PhysRevLett.104.046601.

[11] O. Mosendz et al. "Detection and Quantification of Inverse Spin Hall Effect from Spin Pumping in Permalloy/Normal Metal Bilayers". In: *Physical Review B* 82.21 (Dec. 2010), p. 214403. ISSN: 1098-0121, 1550-235X. DOI: 10.1103/PhysRevB.82.214403.

[12] J. E. Hirsch. "Spin Hall Effect". In: *Physical Review Letters* 83.9 (Aug. 1999), pp. 1834–1837. ISSN: 0031-9007, 1079-7114. DOI: 10.1103/PhysRevLett.83.1834.

[13] Y. Kajiwara et al. “Transmission of Electrical Signals by Spin-Wave Interconversion in a Magnetic Insulator”. In: *Nature* 464.7286 (Mar. 2010), pp. 262–266. ISSN: 0028-0836, 1476-4687. DOI: 10.1038/nature08876.

[14] Fumihiro Matsukura, Yoshinori Tokura, and Hideo Ohno. “Control of Magnetism by Electric Fields”. In: *Nature Nanotechnology* 10.3 (Mar. 2015), pp. 209–220. ISSN: 1748-3387, 1748-3395. DOI: 10.1038/nnano.2015.22.

[15] G Bihlmayer, O Rader, and R Winkler. “Focus on the Rashba Effect”. In: *New Journal of Physics* 17.5 (May 2015), p. 050202. ISSN: 1367-2630. DOI: 10.1088/1367-2630/17/5/050202.

[16] Qiming Shao et al. “Roadmap of Spin–Orbit Torques”. In: *IEEE Transactions on Magnetics* 57.7 (July 2021), pp. 1–39. ISSN: 0018-9464, 1941-0069. DOI: 10.1109/TMAG.2021.3078583.

[17] Jairo Sinova et al. “Spin Hall Effects”. In: *Reviews of Modern Physics* 87.4 (Oct. 2015), pp. 1213–1260. ISSN: 0034-6861, 1539-0756. DOI: 10.1103/RevModPhys.87.1213.

[18] Weinan Lin et al. “Interface-Based Tuning of Rashba Spin-Orbit Interaction in Asymmetric Oxide Heterostructures with 3d Electrons”. In: *Nature Communications* 10.1 (July 2019), p. 3052. ISSN: 2041-1723. DOI: 10.1038/s41467-019-10961-z.

[19] Shaohua Yan et al. “Developments and Applications of Tunneling Magnetoresistance Sensors”. In: *Tsinghua Science and Technology* 27.3 (June 2022), pp. 443–454. ISSN: 1007-0214. DOI: 10.26599/TST.2021.9010061.

[20] S.D. Bader and S.S.P. Parkin. “Spintronics”. In: *Annual Review of Condensed Matter Physics* 1.1 (Aug. 2010), pp. 71–88. ISSN: 1947-5454, 1947-5462. DOI: 10.1146/annurev-conmatphys-070909-104123.

[21] Andrew D. Kent and Daniel C. Worledge. “A New Spin on Magnetic Memories”. In: *Nature Nanotechnology* 10.3 (Mar. 2015), pp. 187–191. ISSN: 1748-3387, 1748-3395. DOI: 10.1038/nnano.2015.24.

[22] Xuyang Liu et al. “Overview of Spintronic Sensors With Internet of Things for Smart Living”. In: *IEEE Transactions on Magnetics* 55.11 (Nov. 2019), pp. 1–22. ISSN: 0018-9464, 1941-0069. DOI: 10.1109/TMAG.2019.2927457.

[23] Hyun Seok Choi et al. “Spin Nano–Oscillator–Based Wireless Communication”. In: *Scientific Reports* 4.1 (June 2014), p. 5486. ISSN: 2045-2322. DOI: 10.1038/srep05486.

[24] Atsufumi Hirohata et al. “Review on Spintronics: Principles and Device Applications”. In: *Journal of Magnetism and Magnetic Materials* 509 (Sept. 2020), p. 166711. ISSN: 03048853. DOI: 10.1016/j.jmmm.2020.166711.

[25] *Spin Waves*. Boston, MA: Springer US, 2009. ISBN: 978-0-387-77864-8 978-0-387-77865-5. DOI: 10.1007/978-0-387-77865-5.

[26] B. Flebus et al. “Recent Advances in Magnonics”. In: *Journal of Applied Physics* 133.16 (Apr. 2023), p. 160401. ISSN: 0021-8979, 1089-7550. DOI: 10.1063/5.0153424.

[27] Anjan Barman et al. “The 2021 Magnonics Roadmap”. In: *Journal of Physics: Condensed Matter* 33.41 (Oct. 2021), p. 413001. ISSN: 0953-8984, 1361-648X. DOI: 10.1088/1361-648X/abec1a.

[28] A A Serga, A V Chumak, and B Hillebrands. “YIG Magnonics”. In: *Journal of Physics D: Applied Physics* 43.26 (July 2010), p. 264002. ISSN: 0022-3727, 1361-6463. DOI: 10.1088/0022-3727/43/26/264002.

[29] Benedetta Flebus et al. "The 2024 Magnonics Roadmap". In: *Journal of Physics: Condensed Matter* 36.36 (Sept. 2024), p. 363501. ISSN: 0953-8984, 1361-648X. DOI: 10.1088/1361-648X/ad399c.

[30] B. Lenk et al. "The Building Blocks of Magnonics". In: *Physics Reports* 507.4-5 (Oct. 2011), pp. 107–136. ISSN: 03701573. DOI: 10.1016/j.physrep.2011.06.003.

[31] Alexander Khitun, Mingqiang Bao, and Kang L Wang. "Magnonic Logic Circuits". In: *Journal of Physics D: Applied Physics* 43.26 (July 2010), p. 264005. ISSN: 0022-3727, 1361-6463. DOI: 10.1088/0022-3727/43/26/264005.

[32] Philipp Pirro et al. "Advances in Coherent Magnonics". In: *Nature Reviews Materials* 6.12 (July 2021), pp. 1114–1135. ISSN: 2058-8437. DOI: 10.1038/s41578-021-00332-w.

[33] A. V. Chumak et al. "Magnon Spintronics". In: *Nature Physics* 11.6 (June 2015), pp. 453–461. ISSN: 1745-2473, 1745-2481. DOI: 10.1038/nphys3347.

[34] V V Kruglyak, S O Demokritov, and D Grundler. "Magnonics". In: *Journal of Physics D: Applied Physics* 43.26 (July 2010), p. 264001. ISSN: 0022-3727, 1361-6463. DOI: 10.1088/0022-3727/43/26/264001.

[35] A. V. Chumak et al. "Advances in Magnetics Roadmap on Spin-Wave Computing". In: *IEEE Transactions on Magnetics* 58.6 (June 2022), pp. 1–72. ISSN: 0018-9464, 1941-0069. DOI: 10.1109/TMAG.2022.3149664.

[36] D. S. Dovzhenko et al. "Light–Matter Interaction in the Strong Coupling Regime: Configurations, Conditions, and Applications". In: *Nanoscale* 10.8 (2018), pp. 3589–3605. ISSN: 2040-3364, 2040-3372. DOI: 10.1039/C7NR06917K.

[37] Richard P. Feynman. *QED: The Strange Theory of Light and Matter*. Expanded ed. Princeton Science Library. Princeton, NJ: Princeton Univ. Press, 2006. ISBN: 978-0-691-12575-6 978-0-691-12717-0.

[38] Marina Litinskaya. "Polaritons". In: *Reference Module in Materials Science and Materials Engineering*. Elsevier, 2019, B9780128035818012340. ISBN: 978-0-12-803581-8. DOI: 10.1016/B978-0-12-803581-8.01234-0.

[39] Daniel F. Walls and Gerard J. Milburn. *Quantum Optics*. 2. ed. Berlin Heidelberg: Springer, 2008. ISBN: 978-3-540-28573-1.

[40] Babak Zare Rameshti et al. "Cavity Magnonics". In: *Physics Reports* 979 (Sept. 2022), pp. 1–61. ISSN: 03701573. DOI: 10.1016/j.physrep.2022.06.001.

[41] Michael Harder and Can-Ming Hu. "Cavity Spintronics: An Early Review of Recent Progress in the Study of Magnon–Photon Level Repulsion". In: *Solid State Physics*. Vol. 69. Elsevier, 2018, pp. 47–121. ISBN: 978-0-12-815242-3. DOI: 10.1016/bs.ssp.2018.08.001.

[42] S. Haroche and J.-M. Raimond. *Exploring the Quantum: Atoms, Cavities and Photons*. Oxford Graduate Texts. Oxford ; New York: Oxford University Press, 2006. ISBN: 978-0-19-850914-1.

[43] Fei Ge, Xiao Han, and Jialiang Xu. "Strongly Coupled Systems for Nonlinear Optics". In: *Laser & Photonics Reviews* 15.4 (Apr. 2021), p. 2000514. ISSN: 1863-8880, 1863-8899. DOI: 10.1002/lpor.202000514.

[44] Huakang Yu et al. "Plasmon-Enhanced Light–Matter Interactions and Applications". In: *npj Computational Materials* 5.1 (Apr. 2019), p. 45. ISSN: 2057-3960. DOI: 10.1038/s41524-019-0184-1.

[45] D. Ballarini et al. "All-Optical Polariton Transistor". In: *Nature Communications* 4.1 (Apr. 2013), p. 1778. ISSN: 2041-1723. DOI: 10.1038/ncomms2734.

[46] Morten Kjaergaard et al. "Superconducting Qubits: Current State of Play". In: *Annual Review of Condensed Matter Physics* 11.1 (Mar. 2020), pp. 369–395. ISSN: 1947-5454, 1947-5462. DOI: 10.1146/annurev-conmatphys-031119-050605.

[47] P. Krantz et al. "A Quantum Engineer's Guide to Superconducting Qubits". In: *Applied Physics Reviews* 6.2 (June 2019), p. 021318. ISSN: 1931-9401. DOI: 10.1063/1.5089550.

[48] Alex Krasnok et al. *Superconducting Microwave Cavities and Qubits for Quantum Information Systems*. June 2023.

[49] Stefano Pirandola et al. "Advances in Quantum Teleportation". In: *Nature Photonics* 9.10 (Oct. 2015), pp. 641–652. ISSN: 1749-4885, 1749-4893. DOI: 10.1038/nphoton.2015.154. arXiv: 1505.07831 [cond-mat, physics:physics, physics:quant-ph].

[50] Nilakantha Meher and S. Sivakumar. "A Review on Quantum Information Processing in Cavities". In: *The European Physical Journal Plus* 137.8 (Aug. 2022), p. 985. ISSN: 2190-5444. DOI: 10.1140/epjp/s13360-022-03172-x. arXiv: 2204.01322 [quant-ph].

[51] H. J. Kimble. "The Quantum Internet". In: *Nature* 453.7198 (June 2008), pp. 1023–1030. ISSN: 0028-0836, 1476-4687. DOI: 10.1038/nature07127.

[52] Ö. O. Soykal and M. E. Flatté. "Strong Field Interactions between a Nanomagnet and a Photonic Cavity". In: *Physical Review Letters* 104.7 (Feb. 2010), p. 077202. ISSN: 0031-9007, 1079-7114. DOI: 10.1103/PhysRevLett.104.077202.

[53] Hans Huebl et al. "High Cooperativity in Coupled Microwave Resonator Ferrimagnetic Insulator Hybrids". In: *Physical Review Letters* 111.12 (Sept. 2013), p. 127003. ISSN: 0031-9007, 1079-7114. DOI: 10.1103/PhysRevLett.111.127003.

[54] Yutaka Tabuchi et al. "Hybridizing Ferromagnetic Magnons and Microwave Photons in the Quantum Limit". In: *Physical Review Letters* 113.8 (Aug. 2014), p. 083603. ISSN: 0031-9007, 1079-7114. DOI: 10.1103/PhysRevLett.113.083603.

[55] Xufeng Zhang et al. "Strongly Coupled Magnons and Cavity Microwave Photons". In: *Physical Review Letters* 113.15 (Oct. 2014), p. 156401. ISSN: 0031-9007, 1079-7114. DOI: 10.1103/PhysRevLett.113.156401.

[56] Dany Lachance-Quirion et al. "Hybrid Quantum Systems Based on Magnonics". In: *Applied Physics Express* 12.7 (June 2019), p. 070101. ISSN: 1882-0786. DOI: 10.7567/1882-0786/ab248d.

[57] Brian Julsgaard et al. "Quantum Memory for Microwave Photons in an Inhomogeneously Broadened Spin Ensemble". In: *Physical Review Letters* 110.25 (June 2013), p. 250503. ISSN: 0031-9007, 1079-7114. DOI: 10.1103/PhysRevLett.110.250503.

[58] Cécile Grezes et al. "Towards a Spin-Ensemble Quantum Memory for Superconducting Qubits". In: *Comptes Rendus Physique* 17.7 (Aug. 2016), pp. 693–704. ISSN: 16310705. DOI: 10.1016/j.crhy.2016.07.006.

[59] Steven D. Bass and Michael Doser. *Quantum Sensing for Particle Physics*. May 2023. arXiv: 2305.11518 [hep-ex, physics:hep-ph, physics:physics, physics:quant-ph]. URL: http://arxiv.org/abs/2305.11518.

[60] R Barbieri et al. "Axion to Magnon Conversion. A Scheme for the Detection of Galactic Axions". In: *Physics Letters B* 226.3-4 (Aug. 1989), pp. 357–360. ISSN: 03702693. DOI: 10.1016/0370-2693(89)91209-4.

[61] Wei-Jiang Wu et al. *Microwave-to-Optics Conversion Using Magnetostatic Modes and a Tunable Optical Cavity*. Mar. 2024. arXiv: 2403.00345 [physics, physics:quant-ph]. URL: http://arxiv.org/abs/2403.00345.

[62] B. Rameev. "MW-Magnon Systems for Quantum Transduction Applications". In: *2023 Photonics & Electromagnetics Research Symposium (PIERS)*. July 2023, pp. 2086–2092. DOI: 10.1109/PIERS59004.2023.10221301.

[63] R. Hisatomi et al. "Bidirectional Conversion between Microwave and Light via Ferromagnetic Magnons". In: *Physical Review B* 93.17 (May 2016), p. 174427. ISSN: 2469-9950, 2469-9969. DOI: 10.1103/PhysRevB.93.174427.

[64] Hana K. Warner et al. *Coherent Control of a Superconducting Qubit Using Light*. Oct. 2023. arXiv: 2310.16155 [quant-ph]. URL: http://arxiv.org/abs/2310.16155.

[65] A. Metelmann and A. A. Clerk. "Nonreciprocal Photon Transmission and Amplification via Reservoir Engineering". In: *Physical Review X* 5.2 (June 2015), p. 021025. ISSN: 2160-3308. DOI: 10.1103/PhysRevX.5.021025.

[66] Xunwei Xu et al. "Nonreciprocal Transition between Two Nondegenerate Energy Levels". In: *Photonics Research* 9.5 (May 2021), pp. 879–886. ISSN: 2327-9125. DOI: 10.1364/PRJ.412904.

[67] Yi-Pu Wang et al. "Nonreciprocity and Unidirectional Invisibility in Cavity Magnonics". In: *Physical Review Letters* 123.12 (Sept. 2019), p. 127202. ISSN: 0031-9007, 1079-7114. DOI: 10.1103/PhysRevLett.123.127202.

[68] S. Barzanjeh et al. "Mechanical On-Chip Microwave Circulator". In: *Nature Communications* 8.1 (Oct. 2017), p. 953. ISSN: 2041-1723. DOI: 10.1038/s41467-017-01304-x.

[69] N. R. Bernier et al. "Nonreciprocal Reconfigurable Microwave Optomechanical Circuit". In: *Nature Communications* 8.1 (Sept. 2017), p. 604. ISSN: 2041-1723. DOI: 10.1038/s41467-017-00447-1.

[70] Christophe Caloz et al. "Electromagnetic Nonreciprocity". In: *Physical Review Applied* 10.4 (Oct. 2018), p. 047001. ISSN: 2331-7019. DOI: 10.1103/PhysRevApplied.10.047001.

[71] F. Lecocq et al. "Nonreciprocal Microwave Signal Processing with a Field-Programmable Josephson Amplifier". In: *Physical Review Applied* 7.2 (Feb. 2017), p. 024028. ISSN: 2331-7019. DOI: 10.1103/PhysRevApplied.7.024028.

[72] G. A. Peterson et al. "Demonstration of Efficient Nonreciprocity in a Microwave Optomechanical Circuit". In: *Physical Review X* 7.3 (July 2017), p. 031001. ISSN: 2160-3308. DOI: 10.1103/PhysRevX.7.031001.

[73] Kejie Fang et al. "Generalized Non-Reciprocity in an Optomechanical Circuit via Synthetic Magnetism and Reservoir Engineering". In: *Nature Physics* 13.5 (May 2017), pp. 465–471. ISSN: 1745-2473, 1745-2481. DOI: 10.1038/nphys4009.

[74] Anton Frisk Kockum et al. "Ultrastrong Coupling between Light and Matter". In: *Nature Reviews Physics* 1.1 (Jan. 2019), pp. 19–40. ISSN: 2522-5820. DOI: 10.1038/s42254-018-0006-2.

[75] Anton Frisk Kockum et al. "Deterministic Quantum Nonlinear Optics with Single Atoms and Virtual Photons". In: *Physical Review A* 95.6 (June 2017), p. 063849. ISSN: 2469-9926, 2469-9934. DOI: 10.1103/PhysRevA.95.063849.

[76] Zongping Gong, Ryusuke Hamazaki, and Masahito Ueda. "Discrete Time-Crystalline Order in Cavity and Circuit QED Systems". In: *Physical Review Letters* 120.4 (Jan. 2018), p. 040404. ISSN: 0031-9007, 1079-7114. DOI: 10.1103/PhysRevLett.120.040404.

[77] P. Forn-Díaz et al. "Ultrastrong Coupling Regimes of Light-Matter Interaction". In: *Reviews of Modern Physics* 91.2 (June 2019), p. 025005. ISSN: 0034-6861, 1539-0756. DOI: 10.1103/RevModPhys.91.025005.

[78] G. Romero et al. "Ultrafast Quantum Gates in Circuit QED". In: *Physical Review Letters* 108.12 (Mar. 2012), p. 120501. ISSN: 0031-9007, 1079-7114. DOI: 10.1103/PhysRevLett.108.120501.

[79] Roberto Stassi et al. "Quantum Nonlinear Optics without Photons". In: *Physical Review A* 96.2 (Aug. 2017), p. 023818. ISSN: 2469-9926, 2469-9934. DOI: 10.1103/PhysRevA.96.023818.

[80] Xufeng Zhang et al. "Optomagnonic Whispering Gallery Microresonators". In: *Physical Review Letters* 117.12 (Sept. 2016), p. 123605. ISSN: 0031-9007, 1079-7114. DOI: 10.1103/PhysRevLett.117.123605.

[81] Benjamin Askenazi et al. "Mid-Infrared Ultra-Strong Light-Matter Coupling for THz Thermal Emission". In: *ACS Photonics* ().

[82] G. Scalari et al. "Ultrastrong Light-Matter Coupling at Terahertz Frequencies with Split Ring Resonators and Inter-Landau Level Transitions". In: *Journal of Applied Physics* 113.13 (Apr. 2013), p. 136510. ISSN: 0021-8979, 1089-7550. DOI: 10.1063/1.4795543.

[83] Fumiki Yoshihara et al. "Superconducting Qubit–Oscillator Circuit beyond the Ultrastrong-Coupling Regime". In: *Nature Physics* 13.1 (Jan. 2017), pp. 44–47. ISSN: 1745-2481. DOI: ApproachingDeep-Strong.

[84] I.A. Golovchanskiy et al. "Approaching Deep-Strong On-Chip Photon-To-Magnon Coupling". In: *Physical Review Applied* 16.3 (Sept. 2021), p. 034029. ISSN: 2331-7019. DOI: 10.1103/PhysRevApplied.16.034029.

[85] Chi Zhang et al. "Ultra-Strong Magnon-Photon Coupling Induced in the Photonic Crystals with an YGaGeIG Defect". In: *Applied Physics Letters* 115.2 (July 2019), p. 022407. ISSN: 0003-6951, 1077-3118. DOI: 10.1063/1.5089523.

[86] Vahram L. Grigoryan and Ke Xia. "Cavity-Mediated Dissipative Spin-Spin Coupling". In: *Physical Review B* 100.1 (July 2019), p. 014415. ISSN: 2469-9950, 2469-9969. DOI: 10.1103/PhysRevB.100.014415.

[87] Florentin Reiter, David Reeb, and Anders S. Sørensen. "Scalable Dissipative Preparation of Many-Body Entanglement". In: *Physical Review Letters* 117.4 (July 2016), p. 040501. ISSN: 0031-9007, 1079-7114. DOI: 10.1103/PhysRevLett.117.040501.

[88] Lihui Bai et al. "Cavity Mediated Manipulation of Distant Spin Currents Using a Cavity-Magnon-Polariton". In: *Physical Review Letters* 118.21 (May 2017), p. 217201. ISSN: 0031-9007, 1079-7114. DOI: 10.1103/PhysRevLett.118.217201.

[89] Bimu Yao et al. "The Microscopic Origin of Magnon-Photon Level Attraction by Traveling Waves: Theory and Experiment". In: *Physical Review B* 100.21 (Dec. 2019), p. 214426. DOI: 10.1103/PhysRevB.100.214426.

[90] Biswanath Bhoi et al. "Abnormal Anticrossing Effect in Photon-Magnon Coupling". In: *Physical Review B* 99.13 (Apr. 2019), p. 134426. ISSN: 2469-9950, 2469-9969. DOI: 10.1103/PhysRevB.99.134426.

[91] J. W. Rao et al. "Interactions between a Magnon Mode and a Cavity Photon Mode Mediated by Traveling Photons". In: *Physical Review B* 101.6 (Feb. 2020), p. 064404. ISSN: 2469-9950, 2469-9969. DOI: 10.1103/PhysRevB.101.064404.

[92] J. Qian et al. "Manipulation of the Zero-Damping Conditions and Unidirectional Invisibility in Cavity Magnonics". In: *Applied Physics Letters* 116.19 (May 2020), p. 192401. ISSN: 0003-6951, 1077-3118. DOI: 10.1063/5.0006363.

[93] Bimu Yao et al. "Coherent Control of Magnon Radiative Damping with Local Photon States". In: *Communications Physics* 2.1 (Dec. 2019), pp. 1–8. ISSN: 2399-3650. DOI: 10.1038/s42005-019-0264-z.

[94] Y. Yang et al. "Control of the Magnon-Photon Level Attraction in a Planar Cavity". In: *Physical Review Applied* 11.5 (May 2019), p. 054023. ISSN: 2331-7019. DOI: 10.1103/PhysRevApplied.11.054023.

[95] J W Rao et al. "Level Attraction and Level Repulsion of Magnon Coupled with a Cavity Anti-Resonance". In: *New Journal of Physics* 21.6 (June 2019), p. 065001. ISSN: 1367-2630. DOI: 10.1088/1367-2630/ab2482.

[96] Guillaume Bourcin et al. "Strong to Ultrastrong Coherent Coupling Measurements in a YIG/Cavity System at Room Temperature". In: *Physical Review B* 107.21 (June 2023), p. 214423. ISSN: 2469-9950, 2469-9969. DOI: 10.1103/PhysRevB.107.214423.

[97] Guillaume Bourcin et al. "Level Attraction in a Quasiclosed Cavity: Antiresonance in Magnonic Devices". In: *Physical Review Applied* 22.6 (Dec. 2024), p. 064036. DOI: 10.1103/PhysRevApplied.22.064036.

[98] Richard P. Feynman. *The Feynman Lectures on Physics. Volume 2: Mainly Electromagnetism and Matter*. The new millennium edition, paperback first published. New York: Basic Books, 2011. ISBN: 978-0-465-02494-0 978-0-465-02416-2.

[99] Claude Cohen-Tannoudji, Bernard Diu, and Franck Laloë. "Mécanique quantique - Tome I". In: ().

[100] Walther Gerlach and Otto Stern. "Das magnetische Moment des Silberatoms". In: *Zeitschrift für Physik* 9.1 (Dec. 1922), pp. 353–355. ISSN: 0044-3328. DOI: 10.1007/BF01326984.

[101] James D. Bjorken, Sidney D. Drell, and J. E. Mansfield. "*Relativistic Quantum Mechanics*". In: *Physics Today* 18.3 (Mar. 1965), pp. 81–82. ISSN: 0031-9228, 1945-0699. DOI: 10.1063/1.3047288.

[102] H. N. Russell and F. A. Saunders. "New Regularities in the Spectra of the Alkaline Earths". In: *The Astrophysical Journal* 61 (Jan. 1925), p. 38. ISSN: 0004-637X, 1538-4357. DOI: 10.1086/142872.

[103] David McMahon. *Quantum Field Theory Demystified*. McGraw-Hill "Demystified" Series. New York, N.Y: McGraw-Hill, 2008. ISBN: 978-0-07-154382-8.

[104] Isabella Rahel Boventer. "Cavity Magnon-Polariton Spectroscopy". PhD thesis. Johannes Gutenberg-Universität Mainz, 2019. DOI: StudyoftheCavity-Magnon-Polariton.

[105] Pierre Weiss. "L'hypothèse du champ moléculaire et la propriété ferromagnétique". In: *Journal de Physique Théorique et Appliquée* 6.1 (1907), pp. 661–690. ISSN: 0368-3893. DOI: 10.1051/jphystap:019070060066100.

[106] Neil William Ashcroft and N. David Mermin. *Physique des solides*. EDP Sciences, Jan. 2002. ISBN: 978-2-7598-0178-7. DOI: 10.1051/978-2-7598-0178-7.

[107] Hidekazu Kurebayashi et al. "Controlled Enhancement of Spin-Current Emission by Three-Magnon Splitting". In: *Nature Materials* 10.9 (Sept. 2011), pp. 660–664. ISSN: 1476-1122, 1476-4660. DOI: 10.1038/nmat3053.

[108] B. Heinrich et al. “Spin Pumping at the Magnetic Insulator (YIG)/Normal Metal (Au) Interfaces”. In: *Physical Review Letters* 107.6 (Aug. 2011), p. 066604. ISSN: 0031-9007, 1079-7114. DOI: 10.1103/PhysRevLett.107.066604.

[109] Babak Zare Rameshti, Yunshan Cao, and Gerrit E. W. Bauer. “Magnetic Spheres in Microwave Cavities”. In: *Physical Review B* 91.21 (June 2015), p. 214430. ISSN: 1098-0121, 1550-235X. DOI: 10.1103/PhysRevB.91.214430.

[110] Jeremy Bourhill et al. “Universal Characterization of Cavity–Magnon Polariton Coupling Strength Verified in Modifiable Microwave Cavity”. In: *Journal of Applied Physics* 128.7 (Aug. 2020), p. 073904. ISSN: 0021-8979. DOI: OntheTheoryofFerromagnetic.

[111] Alberto Sposito. “Pulsed Laser Deposition of Thin Film Magneto-Optic Materials and Lasing Waveguides”. In: ().

[112] Eva Pavarini et al., eds. *Correlated Electrons: From Models to Materials: Lecture Notes of the Autumn School Correlated Electrons 2012: At Forschungszentrum Jülich, 3-7 September 2012*. Schriften Des Forschungszentrums Jülich. Reihe Modeling and Simulation Band 2. Jülich: Forschungszentrum Jülich, Zentralbibliothek, Verl, 2012. ISBN: 978-3-89336-796-2.

[113] T. Holstein and H. Primakoff. “Field Dependence of the Intrinsic Domain Magnetization of a Ferromagnet”. In: *Physical Review* 58.12 (Dec. 1940), pp. 1098–1113. ISSN: 0031-899X. DOI: 10.1103/PhysRev.58.1098.

[114] Takehiko Oguchi. “Theory of Spin-Wave Interactions in Ferro- and Antiferromagnetism”. In: *Physical Review* 117.1 (Jan. 1960), pp. 117–123. ISSN: 0031-899X. DOI: 10.1103/PhysRev.117.117.

[115] D. Polder. “VIII. On the Theory of Ferromagnetic Resonance”. In: *The London, Edinburgh, and Dublin Philosophical Magazine and Journal of Science* 40.300 (Jan. 1949), pp. 99–115. ISSN: 1941-5982, 1941-5990. DOI: 10.1080/14786444908561215.

[116] L. R. Walker. “Resonant Modes of Ferromagnetic Spheroids”. In: *Journal of Applied Physics* 29.3 (Mar. 1958), pp. 318–323. ISSN: 0021-8979, 1089-7550. DOI: 10.1063/1.1723117.

[117] Ernst Schlömann. “A Sum Rule Concerning the Inhomogeneous Demagnetizing Field in Nonellipsoidal Samples”. In: *Journal of Applied Physics* 33.9 (Sept. 1962), pp. 2825–2826. ISSN: 0021-8979, 1089-7550. DOI: 10.1063/1.1702557.

[118] Charles Kittel. “On the Theory of Ferromagnetic Resonance Absorption”. In: *Physical Review* 73.2 (Jan. 1948), pp. 155–161. ISSN: 0031-899X. DOI: 10.1103/PhysRev.73.155.

[119] R. I. Joseph and E. Schlömann. “Demagnetizing Field in Nonellipsoidal Bodies”. In: *Journal of Applied Physics* 36.5 (May 1965), pp. 1579–1593. ISSN: 0021-8979, 1089-7550. DOI: 10.1063/1.1703091.

[120] Farhan Rana. “Quantum Optics Lectures ECE5310, Cornell University.” In: (2009). URL: https://bpb-us-w2.wpmucdn.com/sites.coecis.cornell.edu/dist/4/81/files/2017/03/ece5310_handout5-2062ta5.pdf.

[121] M. Harder et al. “Coherent and Dissipative Cavity Magnonics”. In: *Journal of Applied Physics* 129.20 (May 2021), p. 201101. ISSN: 0021-8979, 1089-7550. DOI: SignaturesoftheUltrastrong.

[122] Y. Kaluzny et al. “Observation of Self-Induced Rabi Oscillations in Two-Level Atoms Excited Inside a Resonant Cavity: The Ringing Regime of Superradiance”. In: *Physical Review Letters* 51.13 (Sept. 1983), pp. 1175–1178. ISSN: 0031-9007. DOI: 10.1103/PhysRevLett.51.1175.

[123] D. Meschede, H. Walther, and G. Müller. "One-Atom Maser". In: *Physical Review Letters* 54.6 (Feb. 1985), pp. 551–554. ISSN: 0031-9007. DOI: 10.1103/PhysRevLett.54.551.

[124] R. J. Thompson, G. Rempe, and H. J. Kimble. "Observation of Normal-Mode Splitting for an Atom in an Optical Cavity". In: *Physical Review Letters* 68.8 (Feb. 1992), pp. 1132–1135. ISSN: 0031-9007. DOI: 10.1103/PhysRevLett.68.1132.

[125] Peter Lodahl, Sahand Mahmoodian, and Søren Stobbe. "Interfacing Single Photons and Single Quantum Dots with Photonic Nanostructures". In: *Reviews of Modern Physics* 87.2 (May 2015), pp. 347–400. ISSN: 0034-6861, 1539-0756. DOI: 10.1103/RevModPhys.87.347.

[126] Xiu Gu et al. "Microwave Photonics with Superconducting Quantum Circuits". In: *Physics Reports* 718–719 (Nov. 2017), pp. 1–102. ISSN: 03701573. DOI: 10.1016/j.physrep.2017.10.002.

[127] Aji A. Anappara et al. "Signatures of the Ultrastrong Light-Matter Coupling Regime". In: *Physical Review B* 79.20 (May 2009), p. 201303. ISSN: 1098-0121, 1550-235X. DOI: 10.1103/PhysRevB.79.201303.

[128] J. Casanova et al. "Deep Strong Coupling Regime of the Jaynes-Cummings Model". In: *Physical Review Letters* 105.26 (Dec. 2010), p. 263603. ISSN: 0031-9007, 1079-7114. DOI: 10.1103/PhysRevLett.105.263603.

[129] Andreas Bayer et al. "Terahertz Light–Matter Interaction beyond Unity Coupling Strength". In: *Nano Letters* 17.10 (Oct. 2017), pp. 6340–6344. ISSN: 1530-6984, 1530-6992. DOI: SuperconductingQubitâĂŞOscillatorCircuitbeyond.

[130] Neereja M. Sundaresan et al. "Beyond Strong Coupling in a Multimode Cavity". In: *Physical Review X* 5.2 (June 2015), p. 021035. ISSN: 2160-3308. DOI: 10.1103/PhysRevX.5.021035.

[131] Dmitry O. Krimer et al. "Route from Spontaneous Decay to Complex Multimode Dynamics in Cavity QED". In: *Physical Review A* 89.3 (Mar. 2014), p. 033820. ISSN: 1050-2947, 1094-1622. DOI: 10.1103/PhysRevA.89.033820.

[132] D. J. Egger and F. K. Wilhelm. "Multimode Circuit Quantum Electrodynamics with Hybrid Metamaterial Transmission Lines". In: *Physical Review Letters* 111.16 (Oct. 2013), p. 163601. ISSN: 0031-9007, 1079-7114. DOI: 10.1103/PhysRevLett.111.163601.

[133] J.B. Khurgin. "Excitonic Radius in the Cavity Polariton in the Regime of Very Strong Coupling". In: *Solid State Communications* 117.5 (Jan. 2001), pp. 307–310. ISSN: 00381098. DOI: 10.1016/S0038-1098(00)00469-5.

[134] D. Meiser and P. Meystre. "Superstrong Coupling Regime of Cavity Quantum Electrodynamics". In: *Physical Review A* 74.6 (Dec. 2006), p. 065801. ISSN: 1050-2947, 1094-1622. DOI: 10.1103/PhysRevA.74.065801.

[135] Xufeng Zhang et al. "Superstrong Coupling of Thin Film Magnetostatic Waves with Microwave Cavity". In: *Journal of Applied Physics* 119.2 (Jan. 2016), p. 023905. ISSN: 0021-8979, 1089-7550. DOI: 10.1063/1.4939134.

[136] I. I. Rabi. "Space Quantization in a Gyrating Magnetic Field". In: *Physical Review* 51.8 (Apr. 1937), pp. 652–654. ISSN: 0031-899X. DOI: 10.1103/PhysRev.51.652.

[137] Qiong-Tao Xie et al. "Anisotropic Rabi Model". In: *Physical Review X* 4.2 (June 2014), p. 021046. ISSN: 2160-3308. DOI: 10.1103/PhysRevX.4.021046.

[138] Mark P. Silverman. *More Than One Mystery*. New York, NY: Springer New York, 1995. ISBN: 978-0-387-94376-3 978-1-4612-2504-1. DOI: 10.1007/978-1-4612-2504-1.

[139] E.T. Jaynes and F.W. Cummings. "Comparison of Quantum and Semiclassical Radiation Theories with Application to the Beam Maser". In: *Proceedings of the IEEE* 51.1 (1963), pp. 89–109. ISSN: 0018-9219. DOI: 10.1109/PROC.1963.1664.

[140] Michael Tavis and Frederick W. Cummings. "Exact Solution for an N -Molecule—Radiation-Field Hamiltonian". In: *Physical Review* 170.2 (June 1968), pp. 379–384. ISSN: 0031-899X. DOI: 10.1103/PhysRev.170.379.

[141] Barry M. Garraway. "The Dicke Model in Quantum Optics: Dicke Model Revisited". In: *Philosophical Transactions of the Royal Society A: Mathematical, Physical and Engineering Sciences* 369.1939 (Mar. 2011), pp. 1137–1155. DOI: 10.1098/rsta.2010.0333.

[142] R. H. Dicke. "Coherence in Spontaneous Radiation Processes". In: *Physical Review* 93.1 (Jan. 1954), pp. 99–110. ISSN: 0031-899X. DOI: 10.1103/PhysRev.93.99.

[143] J. J. Hopfield. "Theory of the Contribution of Excitons to the Complex Dielectric Constant of Crystals". In: *Physical Review* 112.5 (Dec. 1958), pp. 1555–1567. ISSN: 0031-899X. DOI: 10.1103/PhysRev.112.1555.

[144] Clive Emary and Tobias Brandes. "Quantum Chaos Triggered by Precursors of a Quantum Phase Transition: The Dicke Model". In: *Physical Review Letters* 90.4 (Jan. 2003), p. 044101. ISSN: 0031-9007, 1079-7114. DOI: 10.1103/PhysRevLett.90.044101.

[145] Clive Emary and Tobias Brandes. "Chaos and the Quantum Phase Transition in the Dicke Model". In: *Physical Review E* 67.6 (June 2003), p. 066203. DOI: 10.1103/PhysRevE.67.066203.

[146] Alberto Ghirri et al. *Ultra Strong Magnon-Photon Coupling Achieved by Magnetic Films in Contact with Superconducting Resonators*. Feb. 2023. arXiv: 2302.00804 [cond-mat]. URL: http://arxiv.org/abs/2302.00804.

[147] Niclas S. Mueller et al. "Deep Strong Light–Matter Coupling in Plasmonic Nanoparticle Crystals". In: *Nature* 583.7818 (July 2020), pp. 780–784. ISSN: 1476-4687. DOI: 10.1038/s41586-020-2508-1.

[148] Salvatore Savasta, Omar Di Stefano, and Franco Nori. "Thomas–Reiche–Kuhn (TRK) Sum Rule for Interacting Photons". In: *Nanophotonics* 10.1 (Dec. 2020), pp. 465–476. ISSN: 2192-8614, 2192-8606. DOI: 10.1515/nanoph-2020-0433.

[149] Dominik Lentrodt and Jörg Evers. "*Ab Initio* Few-Mode Theory for Quantum Potential Scattering Problems". In: *Physical Review X* 10.1 (Jan. 2020), p. 011008. ISSN: 2160-3308. DOI: 10.1103/PhysRevX.10.011008.

[150] C. W. Gardiner and M. J. Collett. "Input and Output in Damped Quantum Systems: Quantum Stochastic Differential Equations and the Master Equation". In: *Physical Review A* 31.6 (June 1985), pp. 3761–3774. ISSN: 0556-2791. DOI: 10.1103/PhysRevA.31.3761.

[151] Cristiano Ciuti and Iacopo Carusotto. "Input-Output Theory of Cavities in the Ultrastrong Coupling Regime: The Case of Time-Independent Cavity Parameters". In: *Physical Review A* 74.3 (Sept. 2006), p. 033811. ISSN: 1050-2947, 1094-1622. DOI: 10.1103/PhysRevA.74.033811.

[152] H. Y. Yuan, Weichao Yu, and Jiang Xiao. "Loop Theory for Input-Output Problems in Cavities". In: *Physical Review A* 101.4 (Apr. 2020), p. 043824. ISSN: 2469-9926, 2469-9934. DOI: 10.1103/PhysRevA.101.043824.

[153] Isabella Boventer et al. "Steering between Level Repulsion and Attraction: Broad Tunability of Two-Port Driven Cavity Magnon-Polaritons". In: *New Journal of Physics* 21.12 (Dec. 2019), p. 125001. ISSN: 1367-2630. DOI: 10.1088/1367-2630/ab5c12.

[154] Isabella Boventer et al. "Control of the Coupling Strength and Linewidth of a Cavity Magnon-Polariton". In: *Physical Review Research* 2.1 (Feb. 2020), p. 013154. ISSN: 2643-1564. DOI: 10.1103/PhysRevResearch.2.013154.

[155] Alan Gardin et al. *Level Attraction from Interference in Two-Tone Driving*. Apr. 2024. arXiv: 2404.17108 [physics, physics:quant-ph]. URL: http://arxiv.org/abs/2404.17108.

[156] Graeme Flower et al. "Experimental Implementations of Cavity-Magnon Systems: From Ultra Strong Coupling to Applications in Precision Measurement". In: *New Journal of Physics* 21.9 (Sept. 2019), p. 095004. ISSN: 1367-2630. DOI: 10.1088/1367-2630/ab3e1c.

[157] Alan Gardin et al. "Manifestation of the Coupling Phase in Microwave Cavity Magnonics". In: *Physical Review Applied* 19.5 (May 2023), p. 054069. DOI: 10.1103/PhysRevApplied.19.054069.

[158] George B. Arfken, Hans J. Weber, and Frank E. Harris. *Mathematical Methods for Physicists*. Elsevier, 2013. ISBN: 978-0-12-384654-9. DOI: 10.1016/B978-0-12-384654-9.00030-X.

[159] COMSOL. *COMSOL Multiphysics Reference Manual*. URL: https://doc.comsol.com/5.5/doc/com.comsol.help.comsol/COMSOL_ReferenceManual.pdf.

[160] COMSOL. *COMSOL RF Module Users Guide*. URL: https://doc.comsol.com/5.4/doc/com.comsol.help.rf/RFModuleUsersGuide.pdf.

[161] Alan Gardin et al. *Engineering Synthetic Gauge Fields through the Coupling Phases in Cavity Magnonics*. Apr. 2024. arXiv: 2312.04915 [physics, physics:quant-ph]. URL: http://arxiv.org/abs/2312.04915.

[162] *RF Cable EZ 47 M17*. URL: https://ezform.com/products/coaxial-cables/semi-rigid/ez-47-m17/.

[163] D. M. Pozar. *Microwave Engineering, 3Rd Ed.* Wiley India Pvt. Limited, 2009. ISBN: 978-81-265-1049-8. URL: https://books.google.fr/books?id=UZgvwJ3Eex8C.

[164] Christian Ngô and Hélène Ngô. *Physique quantique : Introduction - Cours et exercices corrigés*. Dunod, Oct. 2000. ISBN: 978-2-10-005362-9.

[165] *Metallisation Des Plastiques Materiaux et Traitements de Surface 2 Ed 2e26 (2e Édition) - Montfort-Windel - Centre Technique Des Industries Mecaniques - Grand Format - Librairie Des Sciences-Politiques PARIS*. URL: https://www.librairie-sciencespo.fr/livre/9782854006230-metallisation-des-plastiques-materiaux-et-traitements-de-surface-2-ed-2e26-2e-edition-montfort-windel/.

[166] Luiz Alberto Cesar Teixeira and Marcela Costa Santini. "Surface Conditioning of ABS for Metallization without the Use of Chromium Baths". In: *Journal of Materials Processing Technology* 170.1 (Dec. 2005), pp. 37–41. ISSN: 0924-0136. DOI: 10.1016/j.jmatprotec.2005.04.075.

[167] Glenn O. Mallory and Juan B. Hajdu. *Electroless Plating: Fundamentals and Applications*. William Andrew, 1990. ISBN: 978-0-936569-07-9.

[168] Milan Paunovic and Mordechay Schlesinger. "Fundamentals of Electrochemical Deposition". In: ().

[169] Vincent Castel et al. "Strong Coupling of Magnons to Microwave Photons in Three-Dimensional Printed Resonators". In: *IEEE Magnetics Letters* 10 (2019), pp. 1–5. ISSN: 1949-307X, 1949-3088. DOI: 10.1109/LMAG.2019.2892927.

[170] Russell Messier. "Electrodeposition—the Materials Science of Coatings and Substrates. By Jack W. Dini, Noyes Publications, Park Ridge, NJ 1993, 367 Pp., Hardcover, US $ 78, ISBN 0-8155-1320-8". In: *Advanced Materials* 6.1 (1994), pp. 88–89. ISSN: 1521-4095. DOI: 10.1002/adma.19940060127.

[171] M. Pellaton et al. "3D Printed Microwave Cavity for Atomic Clock Applications: Proof of Concept". In: *Electronics Letters* 54.11 (2018), pp. 691–693. ISSN: 1350-911X. DOI: 10.1049/el.2017.4176.

[172] Nicolò Crescini et al. "Coherent Coupling between Multiple Ferrimagnetic Spheres and a Microwave Cavity in the Quantum-Limit". In: *Physical Review B* 104.6 (Aug. 2021), p. 064426. ISSN: 2469-9950, 2469-9969. DOI: 10.1103/PhysRevB.104.064426. arXiv: 2007.08908 [cond-mat, physics:quant-ph].

[173] National Instruments. *Introduction to Network Analyzer Measurements: Fundamentals and Background*. URL: https://download.ni.com/evaluation/rf/Introduction_to_Network_Analyzer_Measurements.pdf.

[174] Andrej Rumiantsev and Nick Ridler. "VNA Calibration". In: *IEEE Microwave Magazine* 9.3 (June 2008), pp. 86–99. ISSN: 1557-9581. DOI: 10.1109/MMM.2008.919925.

[175] Tibault Reveyrand et al. "SOLT and SOLR Calibration Methods Using a Single Multiport "Thru" Standard Connection". In: *2020 95th ARFTG Microwave Measurement Conference (ARFTG)*. Los Angeles, CA, USA: IEEE, Aug. 2020, pp. 1–4. ISBN: 978-1-72810-951-0. DOI: 10.1109/ARFTG47271.2020.9241365.

[176] Nikola Janju˘sevic. "UVNA-63 Application Note Error Correction". In: ().

[177] Test Equipment Solutions Ltd. *Rohde&Schwarz ZNB40 Datasheet*. URL: https://www.testequipmenthq.com/datasheets/Rohde-Schwarz-ZNB40-Datasheet.pdf.

[178] Lake Shore Cryotronics, Inc. *Lake Shore Gaussmeter Model 455 DSP Datasheet*. URL: https://www.lakeshore.com/docs/default-source/product-downloads/manuals/455_manual.pdf?sfvrsn=f1b42767_1.

[179] Danfysik. *Danfysik SYSTEM 9700 Magnet Power Supply Datasheet*. URL: https://danfysik.dk/images/downloadcenter/SYSTEM_9700.pdf.

[180] Lake Shore Cryotronics, Inc. *Lake Shore EM7-HV Datasheet*. URL: https://www.lakeshore.com/docs/default-source/product-downloads/catalog/electromagnets_l.pdf?sfvrsn=5954b507_1.

[181] John R. Wolberg. *Data Analysis Using the Method of Least Squares: Extracting the Most Information from Experiments; with ... 68 Tables*. Berlin Heidelberg: Springer, 2006. ISBN: 978-3-540-25674-8.

[182] Luigi Garziano et al. "Multiphoton Quantum Rabi Oscillations in Ultrastrong Cavity QED". In: *Physical Review A* 92.6 (Dec. 2015), p. 063830. ISSN: 1050-2947, 1094-1622. DOI: 10.1103/PhysRevA.92.063830.

[183] Vincenzo Macrì et al. "Spontaneous Scattering of Raman Photons from Cavity-QED Systems in the Ultrastrong Coupling Regime". In: *Physical Review Letters* 129.27 (Dec. 2022), p. 273602. DOI: 10.1103/PhysRevLett.129.273602.

[184] Cristiano Ciuti, Gérald Bastard, and Iacopo Carusotto. "Quantum Vacuum Properties of the Intersubband Cavity Polariton Field". In: *Physical Review B* 72.11 (Sept. 2005), p. 115303. ISSN: 1098-0121, 1550-235X. DOI: 10.1103/PhysRevB.72.115303.

[185] Simone De Liberato, Cristiano Ciuti, and Iacopo Carusotto. "Quantum Vacuum Radiation Spectra from a Semiconductor Microcavity with a Time-Modulated Vacuum Rabi Frequency". In: *Physical Review Letters* 98.10 (Mar. 2007), p. 103602. ISSN: 0031-9007, 1079-7114. DOI: 10.1103/PhysRevLett.98.103602.

[186] Adrian Auer and Guido Burkard. "Entangled Photons from the Polariton Vacuum in a Switchable Optical Cavity". In: *Physical Review B* 85.23 (June 2012), p. 235140. ISSN: 1098-0121, 1550-235X. DOI: 10.1103/PhysRevB.85.235140.

[187] Fuyang Tay et al. "Landau Polaritons in the Ultrastrong and Superstrong Coupling Regime in a Multimode Terahertz Photonic-Crystal Cavity". In: *2023 48th International Conference on Infrared, Millimeter, and Terahertz Waves (IRMMW-THz)*. Montreal, QC, Canada: IEEE, Sept. 2023, pp. 1–2. ISBN: 9798350336603. DOI: 10.1109/IRMMW-THz57677.2023.10298925.

[188] V. M. Muravev et al. "Observation of Hybrid Plasmon-Photon Modes in Microwave Transmission of Coplanar Microresonators". In: *Physical Review B* 83.7 (Feb. 2011), p. 075309. ISSN: 1098-0121, 1550-235X. DOI: 10.1103/PhysRevB.83.075309.

[189] Xinwei Li et al. "Vacuum Bloch–Siegert Shift in Landau Polaritons with Ultra-High Cooperativity". In: *Nature Photonics* 12.6 (June 2018), pp. 324–329. ISSN: 1749-4885, 1749-4893. DOI: 10.1038/s41566-018-0153-0.

[190] T. Niemczyk et al. "Circuit Quantum Electrodynamics in the Ultrastrong-Coupling Regime". In: *Nature Physics* 6.10 (Oct. 2010), pp. 772–776. ISSN: 1745-2473, 1745-2481. DOI: 10.1038/nphys1730.

[191] P. Forn-Díaz et al. "Observation of the Bloch-Siegert Shift in a Qubit-Oscillator System in the Ultrastrong Coupling Regime". In: *Physical Review Letters* 105.23 (Nov. 2010), p. 237001. ISSN: 0031-9007, 1079-7114. DOI: 10.1103/PhysRevLett.105.237001.

[192] J. Q. You and Franco Nori. "Superconducting Circuits and Quantum Information". In: *Physics Today* 58.11 (Nov. 2005), pp. 42–47. ISSN: 0031-9228, 1945-0699. DOI: 10.1063/1.2155757.

[193] N. Crescini et al. "Cavity Magnon Polariton Based Precision Magnetometry". In: *Applied Physics Letters* 117.14 (Oct. 2020), p. 144001. ISSN: 0003-6951, 1077-3118. DOI: 10.1063/5.0024369.

[194] Nicolò Crescini, Giovanni Carugno, and Giuseppe Ruoso. "Phase-Modulated Cavity Magnon Polaritons as a Precise Magnetic Field Probe". In: *Physical Review Applied* 16.3 (Sept. 2021), p. 034036. ISSN: 2331-7019. DOI: 10.1103/PhysRevApplied.16.034036.

[195] Qing-Kun Wan, Hai-Long Shi, and Xi-Wen Guan. "Quantum-Enhanced Metrology in Cavity Magnonics". In: *Physical Review B* 109.4 (Jan. 2024), p. L041301. DOI: 10.1103/PhysRevB.109.L041301.

[196] Maxim Goryachev et al. "High-Cooperativity Cavity QED with Magnons at Microwave Frequencies". In: *Physical Review Applied* 2.5 (Nov. 2014), p. 054002. ISSN: 2331-7019. DOI: 10.1103/PhysRevApplied.2.054002.

[197] J. Bourhill et al. "Ultrahigh Cooperativity Interactions between Magnons and Resonant Photons in a YIG Sphere". In: *Physical Review B* 93.14 (Apr. 2016), p. 144420. ISSN: 2469-9950, 2469-9969. DOI: 10.1103/PhysRevB.93.144420.

[198] Igor A. Golovchanskiy et al. "Ultrastrong Photon-to-Magnon Coupling in Multilayered Heterostructures Involving Superconducting Coherence via Ferromagnetic Layers". In: *Science Advances* 7.25 (June 2021), eabe8638. DOI: 10.1126/sciadv.abe8638.

[199] Yunshan Cao et al. "Exchange Magnon-Polaritons in Microwave Cavities". In: *Physical Review B* 91.9 (Mar. 2015), p. 094423. ISSN: 1098-0121, 1550-235X. DOI: 10.1103/PhysRevB.91.094423.

[200] Maxim Goryachev and Michael E Tobar. "The 3D Split-Ring Cavity Lattice: A New Metastructure for Engineering Arrays of Coupled Microwave Harmonic Oscillators". In: *New Journal of Physics* 17.2 (Jan. 2015), p. 023003. ISSN: 1367-2630. DOI: 10.1088/1367-2630/17/2/023003.

[201] W. W. Hansen. "A Type of Electrical Resonator". In: *Journal of Applied Physics* 9.10 (Oct. 1938), pp. 654–663. ISSN: 0021-8979, 1089-7550. DOI: 10.1063/1.1710371.

[202] K. Fujisawa. "General Treatment of Klystron Resonant Cavities". In: *IEEE Transactions on Microwave Theory and Techniques* 6.4 (Oct. 1958), pp. 344–358. ISSN: 0018-9480. DOI: 10.1109/TMTT.1958.1125205.

[203] J-M. Le Floch et al. "Rigorous Analysis of Highly Tunable Cylindrical Transverse Magnetic Mode Re-Entrant Cavities". In: *Review of Scientific Instruments* 84.12 (Dec. 2013), p. 125114. ISSN: 0034-6748, 1089-7623. DOI: 10.1063/1.4848935.

[204] Li-Shan Xie et al. "First-Principles Study of Exchange Interactions of Yttrium Iron Garnet". In: *Physical Review B* 95.1 (Jan. 2017), p. 014423. ISSN: 2469-9950, 2469-9969. DOI: 10.1103/PhysRevB.95.014423.

[205] Janine Keller et al. "Landau Polaritons in Highly Non-Parabolic 2D Gases in the Ultra-Strong Coupling Regime". In: *Physical Review B* 101.7 (Feb. 2020), p. 075301. ISSN: 2469-9950, 2469-9969. DOI: 10.1103/PhysRevB.101.075301. arXiv: 1708.07773.

[206] Zhi-Bo Yang et al. "Bistability of Squeezing and Entanglement in Cavity Magnonics". In: *Physical Review Research* 3.2 (May 2021), p. 023126. ISSN: 2643-1564. DOI: 10.1103/PhysRevResearch.3.023126.

[207] M. X. Bi et al. "Bistability of Cavity Magnon Polaritons beyond the Holstein–Primakoff Transformation". In: *Journal of Applied Physics* 130.24 (Dec. 2021), p. 243902. ISSN: 0021-8979, 1089-7550. DOI: 10.1063/5.0073446.

[208] Zhi-Bo Yang et al. "Steady Entangled-State Generation via Cross-Kerr Effect in a Ferrimagnetic Crystal". In: *Physical Review A* 106.1 (July 2022), p. 012419. ISSN: 2469-9926, 2469-9934. DOI: 10.1103/PhysRevA.106.012419. arXiv: 2205.11865 [cond-mat, physics:quant-ph].

[209] Wei-Jiang Wu et al. *Observation of Magnon Cross-Kerr Effect in Cavity Magnonics*. Dec. 2021. DOI: 10.48550/arXiv.2112.13807. arXiv: 2112.13807 [cond-mat, physics:quant-ph].

[210] GuoQiang Zhang, YiPu Wang, and JianQiang You. "Theory of the Magnon Kerr Effect in Cavity Magnonics". In: *Science China Physics, Mechanics & Astronomy* 62.8 (Mar. 2019), p. 987511. ISSN: 1869-1927. DOI: 10.1007/s11433-018-9344-8.

[211] Ş. K. Özdemir et al. "Parity–Time Symmetry and Exceptional Points in Photonics". In: *Nature Materials* 18.8 (Aug. 2019), pp. 783–798. ISSN: 1476-1122, 1476-4660. DOI: 10.1038/s41563-019-0304-9.

[212] H. Xu et al. "Topological Energy Transfer in an Optomechanical System with Exceptional Points". In: *Nature* 537.7618 (Sept. 2016), pp. 80–83. ISSN: 0028-0836, 1476-4687. DOI: 10.1038/nature18604.

[213] Jan Wiersig. "Enhancing the Sensitivity of Frequency and Energy Splitting Detection by Using Exceptional Points: Application to Microcavity Sensors for Single-Particle Detection". In: *Physical Review Letters* 112.20 (May 2014), p. 203901. ISSN: 0031-9007, 1079-7114. DOI: 10.1103/PhysRevLett.112.203901.

[214] Xufeng Zhang et al. "Experimental Observation of an Exceptional Surface in Synthetic Dimensions with Magnon Polaritons". In: *Physical Review Letters* 123.23 (Dec. 2019), p. 237202. ISSN: 0031-9007, 1079-7114. DOI: 10.1103/PhysRevLett.123.237202.

[215] Yunshan Cao and Peng Yan. "Exceptional Magnetic Sensitivity of P T -Symmetric Cavity Magnon Polaritons". In: *Physical Review B* 99.21 (June 2019), p. 214415. ISSN: 2469-9950, 2469-9969. DOI: 10.1103/PhysRevB.99.214415.

[216] Y. Yang et al. "Unconventional Singularity in Anti-Parity-Time Symmetric Cavity Magnonics". In: *Physical Review Letters* 125.14 (Oct. 2020), p. 147202. ISSN: 0031-9007, 1079-7114. DOI: 10.1103/PhysRevLett.125.147202.

[217] S.-A. Biehs and G. S. Agarwal. "Enhancement of Synthetic Magnetic Field Induced Nonreciprocity via Bound States in the Continuum in Dissipatively Coupled Systems". In: *Physical Review B* 108.3 (July 2023), p. 035423. DOI: 10.1103/PhysRevB.108.035423.

[218] H. Y. Yuan et al. "Steady Bell State Generation via Magnon-Photon Coupling". In: *Physical Review Letters* 124.5 (Feb. 2020), p. 053602. ISSN: 0031-9007, 1079-7114. DOI: 10.1103/PhysRevLett.124.053602.

[219] Dan C Marinescu and Gabriela M Marinescu. "Classical and Quantum Information". In: ().

[220] Yi-Pu Wang and Can-Ming Hu. "Dissipative Couplings in Cavity Magnonics". In: *Journal of Applied Physics* 127.13 (Apr. 2020), p. 130901. ISSN: 0021-8979. DOI: 10.1063/1.5144202.

[221] Weichao Yu et al. "Prediction of Attractive Level Crossing via a Dissipative Mode". In: *Physical Review Letters* 123.22 (Nov. 2019), p. 227201. ISSN: 0031-9007, 1079-7114. DOI: 10.1103/PhysRevLett.123.227201.

[222] M. Harder et al. "Level Attraction Due to Dissipative Magnon-Photon Coupling". In: *Physical Review Letters* 121.13 (Sept. 2018), p. 137203. ISSN: 0031-9007, 1079-7114. DOI: 10.1103/PhysRevLett.121.137203.

[223] Jie Zhao et al. "Observation of Anti- P T -Symmetry Phase Transition in the Magnon-Cavity-Magnon Coupled System". In: *Physical Review Applied* 13.1 (Jan. 2020), p. 014053. ISSN: 2331-7019. DOI: 10.1103/PhysRevApplied.13.014053.

[224] Peng-Chao Xu et al. "Cavity-Mediated Dissipative Coupling of Distant Magnetic Moments: Theory and Experiment". In: *Physical Review B* 100.9 (Sept. 2019), p. 094415. DOI: 10.1103/PhysRevB.100.094415.

[225] N. R. Bernier et al. "Level Attraction in a Microwave Optomechanical Circuit". In: *Physical Review A* 98.2 (Aug. 2018), p. 023841. ISSN: 2469-9926, 2469-9934. DOI: 10.1103/PhysRevA.98.023841.

[226] Jonathan Kohler et al. "Negative-Mass Instability of the Spin and Motion of an Atomic Gas Driven by Optical Cavity Backaction". In: *Physical Review Letters* 120.1 (Jan. 2018), p. 013601. ISSN: 0031-9007, 1079-7114. DOI: 10.1103/PhysRevLett.120.013601.

[227] Christoffer B. Møller et al. "Quantum Back-Action-Evading Measurement of Motion in a Negative Mass Reference Frame". In: *Nature* 547.7662 (July 2017), pp. 191–195. ISSN: 0028-0836, 1476-4687. DOI: 10.1038/nature22980.

[228] Eugene S. Polzik and Klemens Hammerer. "Trajectories without Quantum Uncertainties". In: *Annalen der Physik* 527.1-2 (Jan. 2015). ISSN: 0003-3804, 1521-3889. DOI: 10.1002/andp.201400099.

[229] Vahram L. Grigoryan, Ka Shen, and Ke Xia. "Synchronized Spin-Photon Coupling in a Microwave Cavity". In: *Physical Review B* 98.2 (July 2018), p. 024406. ISSN: 2469-9950, 2469-9969. DOI: 10.1103/PhysRevB.98.024406.

[230] J. W. Rao et al. "Interferometric Control of Magnon-Induced Nearly Perfect Absorption in Cavity Magnonics". In: *Nature Communications* 12.1 (Mar. 2021), p. 1933. ISSN: 2041-1723. DOI: 10.1038/s41467-021-22171-7.

[231] Alexandre Le Boité. "Theoretical Methods for Ultrastrong Light–Matter Interactions". In: *Advanced Quantum Technologies* 3.7 (July 2020), p. 1900140. ISSN: 2511-9044, 2511-9044. DOI: 10.1002/qute.201900140.

[232] Jeremy Bourhill et al. "Generation of Circulating Cavity Magnon Polaritons". In: *Physical Review Applied* 19.1 (Jan. 2023), p. 014030. ISSN: 2331-7019. DOI: 10.1103/PhysRevApplied.19.014030.

[233] Xufeng Zhang et al. "Broadband Nonreciprocity Enabled by Strong Coupling of Magnons and Microwave Photons". In: *Physical Review Applied* 13.4 (Apr. 2020), p. 044039. ISSN: 2331-7019. DOI: 10.1103/PhysRevApplied.13.044039.

[234] Heng-Na Xiong et al. "Exact Non-Markovian Cavity Dynamics Strongly Coupled to a Reservoir". In: *Physical Review A* 82.1 (July 2010), p. 012105. ISSN: 1050-2947, 1094-1622. DOI: 10.1103/PhysRevA.82.012105.

[235] G. M. Moy, J. J. Hope, and C. M. Savage. "The Born and Markov Approximations for Atom Lasers". In: *Physical Review A* 59.1 (Jan. 1999), pp. 667–675. ISSN: 1050-2947, 1094-1622. DOI: 10.1103/PhysRevA.59.667. arXiv: quant-ph/9801046.

[236] Hilary M. Hurst and Benedetta Flebus. "Non-Hermitian Physics in Magnetic Systems". In: *Journal of Applied Physics* 132.22 (Dec. 2022), p. 220902. ISSN: 0021-8979, 1089-7550. DOI: 10.1063/5.0124841.

[237] Xin Wang et al. "Nonreciprocal Double-Carrier Frequency Combs in Cavity Magnonics". In: *Chaos, Solitons & Fractals* 176 (Nov. 2023), p. 114137. ISSN: 0960-0779. DOI: 10.1016/j.chaos.2023.114137.

[238] G. S. Agarwal. "Generation of Pair Coherent States and Squeezing via the Competition of Four-Wave Mixing and Amplified Spontaneous Emission". In: *Physical Review Letters* 57.7 (Aug. 1986), pp. 827–830. ISSN: 0031-9007. DOI: 10.1103/PhysRevLett.57.827.

[239] Fabio Benatti, Roberto Floreanini, and Marco Piani. "Environment Induced Entanglement in Markovian Dissipative Dynamics". In: *Physical Review Letters* 91.7 (Aug. 2003), p. 070402. ISSN: 0031-9007, 1079-7114. DOI: 10.1103/PhysRevLett.91.070402.

[240] M. J. Kastoryano, F. Reiter, and A. S. Sørensen. "Dissipative Preparation of Entanglement in Optical Cavities". In: *Physical Review Letters* 106.9 (Feb. 2011), p. 090502. ISSN: 0031-9007, 1079-7114. DOI: 10.1103/PhysRevLett.106.090502.

[241] Vincent Castel et al. "Thermal Control of the Magnon-Photon Coupling in a Notch Filter Coupled to a Yttrium Iron Garnet/Platinum System". In: *Physical Review B* 96.6 (Aug. 2017), p. 064407. ISSN: 2469-9950, 2469-9969. DOI: 10.1103/PhysRevB.96.064407.

[242] Justin T. Hou et al. "Electrical Manipulation of Dissipation in Microwave Photon–Magnon Hybrid System through the Spin Hall Effect". In: *Applied Physics Letters* 124.7 (Feb. 2024), p. 072401. ISSN: 0003-6951, 1077-3118. DOI: 10.1063/5.0182270.

[243] Dominic Deslandes and Ke Wu. "Design Consideration and Performance Analysis of Substrate Integrated Waveguide Components". In: *32nd European Microwave Conference, 2002*. Milan, Italy: IEEE, Oct. 2002, pp. 1–4. DOI: 10.1109/EUMA.2002.339426.

[244] Ke Wu, D. Deslandes, and Y. Cassivi. "The Substrate Integrated Circuits - a New Concept for High-Frequency Electronics and Optoelectronics". In: *6th International Conference on Telecommunications in Modern Satellite, Cable and Broadcasting Service, 2003. TELSIKS 2003.* Nis, Yugoslavia: IEEE, 2003, P–III. ISBN: 978-0-7803-7963-3. DOI: 10.1109/TELSKS.2003.1246173.

Résumé

Chapitre 1 - Introduction:

La spincavitronique, ou magnonique en cavité, est un domaine de recherche récent qui se concentre sur le couplage fort entre les magnons, qui sont des quasi-particules associées aux ondes de spin dans les matériaux ferromagnétiques, et les photons à l'intérieur d'une cavité électromagnétique. Ce couplage donne lieu à des états hybrides, appelés polaritons magnons-cavité (CMP). Ce domaine, qui a commencé à prendre forme au début des années 2010, se situe à l'interface de plusieurs disciplines : la spintronique, qui explore les propriétés des spins dans les systèmes électroniques, la magnonique, qui étudie les ondes de spin, et l'électrodynamique quantique en cavité (QED), où les interactions entre la matière et la lumière sont étudiées dans des environnements confinés. Ce cadre théorique et expérimental ouvre de nouvelles perspectives pour le développement de dispositifs quantiques avancés, particulièrement en matière de communication et de traitement de l'information.

Un des régimes les plus intéressants dans ce domaine est le régime de couplage ultra-fort (USC), où la force de couplage dépasse 10% de la fréquence de la cavité. Ce régime permet d'explorer des phénomènes encore plus complexes, comme les excitations virtuelles, et pourrait donner lieu à des états exotiques tels que les cristaux temporels discrets. Le régime USC améliore également les performances des dispositifs fonctionnant dans le régime de couplage fort, notamment en accélérant les temps de réponse et de contrôle dans les systèmes. Ce régime est particulièrement crucial pour des applications quantiques avancées, comme la conversion de fréquence, les portes logiques quantiques, et même la détection de matière noire. Pour atteindre ce régime, différentes approches sont étudiées, comme l'optimisation du couplage entre un grand nombre de dipôles ou un seul dipôle avec le mode de la cavité. Cependant, l'obtention de ce régime à température ambiante reste un défi. Des progrès ont été réalisés à des températures très basses, mais des résultats significatifs à température ambiante sont encore rares.

Dans la première étude de cette thèse, un système hybride reconfigurable a été développé pour étudier la transition entre le régime de couplage fort et celui de couplage ultra-fort, à température ambiante et dans une plage de fréquences allant de 0,1 à 15 GHz. Grâce à cette configuration, un couplage allant de 12% à 59% de la fréquence de la cavité a été atteint. Nos résultats suggèrent également qu'il est nécessaire d'incorporer un terme supplémentaire dans l'équation de résonance ferromagnétique pour décrire avec précision l'hybridation observée dans le régime USC. Cette étude constitue une contribution majeure à la compréhension des dynamiques dans ce régime, et ouvre la voie à la mise au point d'un modèle cohérent pour décrire ces systèmes complexes, ce qui pourrait avoir des implications importantes pour le développement de nouvelles technologies quantiques.

Un autre aspect clé de ce domaine est le phénomène d'attraction des niveaux dans les systèmes quantiques, qui présente des applications prometteuses dans le développement

de dispositifs de communication moderne. L'attraction des niveaux, en permettant un couplage non-hermitien entre les magnons et les photons, favorise des transmissions de photons non-réciproques, essentielles pour des dispositifs comme les circulateurs et les amplificateurs de signaux unidirectionnels, qui sont des éléments cruciaux dans les technologies de communication. De plus, le couplage dissipatif entre magnons et photons permet des applications telles que la mémoire quantique à gradient de magnon, un développement prometteur pour améliorer le stockage et la gestion de l'information dans les technologies de calcul quantique. L'attraction des niveaux pourrait également jouer un rôle important dans les dispositifs de détection de précision et en métrologie, en facilitant l'interaction longue distance entre les magnons, utile pour les technologies basées sur les spins.

Les premières prédictions théoriques du couplage fort magnon-photon ont été faites en 2010, et dès 2013, des démonstrations expérimentales ont confirmé ces prédictions à des températures extrêmement basses. Depuis, des expériences réussies ont été réalisées à température ambiante, notamment avec des sphères de YIG (grenat d'yttrium et de fer), ouvrant la voie à des avancées dans la magnonique quantique. Grâce à la longue durée de cohérence des magnons, ces systèmes sont envisagés comme de possibles mémoires quantiques, empêchant ainsi la perte d'information due à la décohérence des qubits supraconducteurs. En outre, ces systèmes sont prometteurs pour la détection non-destructive de champs magnétiques statiques ou micro-ondes faibles, ainsi que pour la recherche sur la matière noire.

Dans ce contexte, la spincavitronique pourrait également permettre le développement d'un transducteur quantique bidirectionnel entre les micro-ondes et la lumière optique dans les circuits supraconducteurs. Cela permettrait de transférer de l'information quantique d'un qubit supraconducteur vers la lumière optique via un transducteur de magnons, ouvrant la voie à des communications quantiques longue distance. Ces dispositifs nécessitent cependant d'améliorer encore la force de couplage entre qubits et magnons. En parallèle, des applications potentielles de la spincavitronique dans le domaine des radiofréquences apparaissent, comme des filtres réglables, des amplificateurs à faible bruit ou encore des isolateurs et circulateurs, essentiels pour les technologies de communication modernes.

Enfin, l'observation du phénomène d'attraction des niveaux dans des cavités 3D, bien que prometteuse, reste encore mal comprise. Peu d'études ont été réalisées sur ce sujet, et les modèles actuels sont largement phénoménologiques, sans offrir une description physique complète des systèmes. Dans ce travail, nous avons proposé un modèle physique qui explique l'apparition et le couplage des anti-résonances dans les cavités 3D, soutenu par des simulations et des mesures expérimentales. Ces résultats apportent une nouvelle compréhension des mécanismes de couplage dans ces systèmes hybrides, contribuant à leur développement pour des applications futures dans la communication quantique et les technologies de détection à haute précision.

Chapitre 2:

Dans ce deuxième chapitre, les bases du magnétisme dans les matériaux sont posées en explorant le concept de moment angulaire, depuis les orbites électroniques jusqu'au

phénomène quantique du spin. Une première partie se concentre sur la description quantique du moment angulaire en présence d'un champ magnétique statique, avec une analyse à travers une interprétation semi-classique, suivis de l'introduction de l'énergie de Zeeman et du phénomène de précession de Larmor. Une attention particulière est portée à l'équation du mouvement d'un moment angulaire sous l'effet d'un champ magnétique.

La deuxième section présente une vue d'ensemble des différents types de matériaux magnétiques : diamagnétiques, paramagnétiques, ferromagnétiques et antiferromagnétiques. Une attention spéciale est accordée au YIG, un matériau artificiel utilisé dans des dispositifs à radiofréquences (RF) en raison de ses propriétés magnétiques uniques et de sa pertinence dans les études de couplage magnon-photon. Le YIG est présenté comme un matériau de référence dans le domaine de la magnonique en raison de ses faibles pertes et de sa grande stabilité, ce qui en fait un choix privilégié pour des applications dans des dispositifs RF.

Enfin, le chapitre se termine par une analyse des ondes de spin dans les ferromagnétiques, qui émergent de deux interactions principales : l'interaction d'échange et l'interaction dipolaire. Les ondes de spin d'échange, gouvernées par l'interaction d'échange entre les spins voisins, et les ondes de spin dipolaires, résultant des interactions dipolaires à longue portée, sont examinées en détail. Ces phénomènes sont essentiels pour comprendre le comportement des matériaux ferromagnétiques dans des conditions dynamiques et leurs applications dans le domaine de la spincavitronique.

Chapitre 3:

Le troisième chapitre débute par la quantification du champ électromagnétique au sein d'une cavité pour établir l'Hamiltonien de la cavité, base essentielle pour les analyses ultérieures. Cette étape permet de décrire les interactions fondamentales entre la lumière et la matière dans un cadre quantique. L'approche classique de l'électrodynamique est d'abord exposée, suivie de sa version quantique, dans le but d'introduire la modélisation des interactions lumière-matière.

Ensuite, une analogie est développée entre le couplage lumière-matière et la physique de deux oscillateurs couplés. Ce modèle simplifié, illustré par des pendules couplés via des ressorts ou des amortisseurs, permet de mieux comprendre les principales caractéristiques des différents régimes de couplage. Ces analogies mécaniques aident à conceptualiser les interactions complexes qui se produisent dans des systèmes quantiques réels. Le chapitre poursuit en définissant et en discutant ces régimes de couplage, avec une attention particulière portée aux systèmes à deux niveaux, qui sont fondamentaux dans la compréhension de l'électrodynamique quantique en cavité. Les systèmes collectifs à deux niveaux, où de nombreux dipôles interagissent simultanément avec un champ électromagnétique, sont également abordés, afin de comprenre l'interaction entre la lumière et les quasi-particules associées au comportement collectif des systèmes de plusieurs particules (magnons, phonons, excitons, plasmons, ...).

Le chapitre explore ensuite comment ces systèmes interagissent avec leur environnement, notamment à travers le formalisme d'entrée-sortie. Ce formalisme est essentiel pour modéliser des cavités quasi-fermées ou ouvertes, où les photons, venant de l'environnement

extérieur, peuvent intéragir avec le système, influençant ainsi les propriétés des systèmes étudiés. L'interaction avec l'environnement est un facteur crucial dans la description réaliste des systèmes quantiques, car elle permet de prendre en compte les pertes et les interférences avec l'extérieur.

Enfin, le chapitre se termine par la dérivation du modèle de couplage photon-magnon dans des cavités micro-ondes, une interaction centrale dans le domaine de la spincavitronique. Ce couplage permet d'explorer les interactions entre les photons et les magnons dans des matériaux magnétiques comme le YIG. Cette dernière section est d'une grande importance pour comprendre le comportement des systèmes hybrides.

Le chapitre offre ainsi une vue d'ensemble des modèles théoriques qui sous-tendent le couplage lumière-matière et leur application aux systèmes réels, en s'appuyant sur des concepts de physique classique et quantique pour guider le lecteur vers une compréhension approfondie des phénomènes complexes dans ce domaine.

Chapitre 4:

Le quatrième chapitre présente les différentes étapes méthodologiques utilisées dans les études de cette thèse. Il commence par discuter des simulations réalisées pour étudier les propriétés des cavités électromagnétiques, en se concentrant sur les considérations physiques des simulations, en particulier l'utilisation de conducteurs électriques parfaits pour les parois de la cavité et la configuration de la grille de maillage. Il est discuté des paramètres liés au couplage magnon-photon pouvant être extrait des simulations avec le solveur des modes propres, tels que le facteur de forme, la fréquence et les pertes dans le système. Les simulations prennent en compte les propriétés magnétiques du YIG pour le solveur en domaine fréquentiel, afin de modéliser les interactions entre les magnons et les photons au sein de la cavité, et d'en extraire les paramètres S, que ce soit l'intensité ou la phase.

Ensuite, le chapitre décrit les différentes techniques de fabrication utilisées pour concevoir les cavités. Cela inclut des méthodes traditionnelles de fraisage mécanique ainsi que des techniques plus récentes comme l'impression 3D en plastique. La métallisation, un processus clé pour garantir la conductivité des parois des cavités imprimées en 3D, est également abordée en détail. Ces approches permettent de créer des cavités capables de supporter les expérimentations sur le couplage photon-magnon.

La dernière section se concentre sur l'instrumentation et les mesures expérimentales. Elle détaille le fonctionnement de l'analyseur de réseau vectoriel, l'instrument principal utilisé pour les mesures des paramètres électromagnétiques de la cavité. Cette section décrit aussi l'agencement expérimental dans le laboratoire et l'automatisation des mesures, qui permet d'améliorer l'efficacité des campagnes de tests. L'ensemble de ce chapitre fournit ainsi une vue d'ensemble des outils et méthodes utilisés pour la simulation, la conception, et la mesure des cavités dans le cadre de ces recherches.

Chapitre 5:

Le cinquième chapitre présente une étude expérimentale du passage du régime de couplage fort (SC) au régime de couplage ultra-fort (USC) dans des cavités réentrantes tridimensionnelles reconfigurables en fréquence, couplées à un parallélépipède macroscopique de YIG à température ambiante. Le taux de couplage observé, défini comme le rapport entre la force de couplage et la fréquence de la cavité, varie de 12% à 59%. Les résultats montrent que certaines considérations spécifiques doivent être prises en compte lors de l'analyse des branches polaritoniques dans ces dispositifs, où le champ RF est fortement concentré dans le matériau magnétique. Ces observations concordent parfaitement avec les simulations électromagnétiques par éléments finis effectuées dans le domaine fréquentiel.

Le chapitre débute par un rappel du régime USC, qui se produit lorsque la force de couplage dépasse 10% fois la fréquence de la cavité. Ce régime, tout comme le régime SC, présente un grand intérêt pour diverses applications, telles que l'amélioration des dispositifs de spintronique et de communication quantique. Dans le régime USC, des phénomènes nouveaux émergent, comme ceux dûs aux excitations virtuelles, ce qui ouvre la voie à des processus d'ordre supérieur, tels que la génération de sous-harmoniques ou l'absorption multi-photonique.

L'atteinte du régime USC peut se faire de deux façons principales : soit en couplant un grand nombre de dipôles à un même mode de cavité, soit en optimisant les degrés de liberté pour améliorer la force de couplage entre un seul dipôle et la cavité. Depuis sa première démonstration expérimentale en 2009, plusieurs systèmes ont été étudiés dans ce contexte, notamment les polaritons inter-sous-bandes, les circuits supraconducteurs et les polaritons magnons-cavités (CMPs). Ces derniers ont récemment montré un grand potentiel dans des domaines tels que la métrologie, les mémoires quantiques et la détection de matière noire.

Dans cette étude, nous avons conçu un système hybride reconfigurable permettant de suivre la transition du SC au USC à température ambiante, dans une gamme de fréquences de 0,1 à 15 GHz. Les cavités réentrantes à double plots utilisées, qui concentrent le champ magnétique RF dans le matériau YIG, ont permis d'observer cette transition, et de révéler la nécessité d'ajouter un terme supplémentaire à la fréquence de résonance ferromagnétique (FMR) dans les modèles standards pour ces conditions de couplages afin de décrire avec précision la fréquence des polaritons.

La cavité a été conçu afin d'optimiser certains paramètres tels que le facteur de remplissage, qui est cruciale pour atteindre le régime USC. Les distances entre les éléments de la cavité ont été ajustées pour permettre une transition progressive entre les régimes SC et USC, offrant ainsi une meilleure compréhension des mécanismes en jeu dans le couplage magnon-photon.

Les résultats obtenus montrent un excellent accord entre les mesures expérimentales et les simulations électromagnétiques. Cependant, les modèles standards utilisés pour décrire le couplage dans ces systèmes, comme les modèles de Dicke et de Hopfield, se sont révélés inadéquats pour expliquer les données expérimentales. Un décalage de fréquence dans la résonance magnonique, dépendant du facteur de remplissage, a permis de mieux ajuster les résultats, une observation qui reste à expliquer théoriquement. Bien que son origine

physique ne soit pas encore claire, il constitue une piste prometteuse pour de futures recherches sur ces systèmes hybrides.

En conclusion, cette étude démontre un couplage ultra-fort magnon-photon à température ambiante, ouvrant ainsi de nouvelles perspectives pour les applications en spintronique et dans les dispositifs RF. Nous avons montré que l'optimisation du facteur de remplissage est essentielle pour atteindre le régime USC et que les modèles existants doivent être adaptés pour prendre en compte des effets spécifiques observés dans ce contexte. Enfin, cette étude jette les bases pour de futures investigations visant à mieux comprendre la physique du couplage USC magnon-photon, avec des applications potentielles dans des domaines aussi variés que les technologies quantiques et les dispositifs RF.

Chapitre 6:

Dans le chapitre 6, nous proposons une description analytique approfondie du couplage effectif associé à une anti-résonance au sein d'un système hybride constitué d'une cavité photonique quasi-fermée et d'un matériau ferrimagnétique. Alors que le phénomène d'attraction de niveaux entre un système résonant dans une cavité ouverte est bien compris, les fondements physiques de ce phénomène dans les cavités quasi-fermées restent flous. En nous appuyant sur la théorie de l'entrée-sortie, nous parvenons à distinguer entre les aspects répulsifs et attractifs de ce couplage. Notre modèle suggère qu'en comprenant le saut de phase aux résonances et l'anti-résonance étudiée, nous pouvons prédire la nature du couplage effectif de l'anti-résonance en fonction de la position du matériau ferrimagnétique dans la cavité.

L'attraction de niveaux d'énergies des états hybrides a suscité un intérêt croissant au cours de la dernière décennie, ouvrant de nouvelles perspectives pour le développement de dispositifs à micro-ondes et quantiques. L'attraction de niveaux est particulièrement prometteuse car elle peut donner lieu à deux types distincts de singularités : les points exceptionnels (EP) et les états liés dans le continuum (BIC). Les EP permettent des applications tels que le transfert topologique d'énergie, et peuvent améliorer la sensibilité des dispositifs de détection. Quant aux Bics, ils permettent aux modes hybridés de ne pas dissiper d'énergie, offrant ainsi une durée de vie exceptionnellement longue, ce qui est avantageux pour des applications dans des dispositifs à lumière lente, la détection et la mémoire quantique.

De plus, l'attraction de niveaux entre photons et magnons peut mener à une rupture spontanée de la symétrie parité-temps (PT), favorisant ainsi la formation d'états de Bell à haute fidélité. Ces états de Bell sont cruciaux pour les applications en information quantique, y compris la téléportation et la cryptographie quantique. La robustesse de cette intrication est essentielle pour éviter les instabilités causées par les perturbations environnementales.

Aussi, un Hamiltonien non-Hermitien peuvent afficher une transmission non-réciproque des photons, ce qui est essentiel pour des dispositifs tels que des circulateurs et des amplificateurs de signal unidirectionnels. L'attraction de niveaux peut se manifester dans des systèmes dissipatifs, où le Hamiltonien effectif est non-Hermitien, ou dans des systèmes

cohérents, par le biais d'interactions entre systèmes ayant des énergies effectives positives et négatives, ou d'interférences.

Notre analyse se concentre sur le couplage entre une anti-résonance le magnon à l'aide de la théorie d'entrée-sortie. Cette approche nous permet de mieux comprendre les paramètres qui régissent le comportement du couplage, qu'il soit répulsif ou attractif. Nous présentons la matrice S générale dérivée de cette théorie et explorons différents systèmes simples composées de un ou deux modes photonique et un magnon afin de comprendre l'émergence et la nature de couplage des anti-résonances. Nous mettons en avant le saut de phase, qui est un élément clé du comportement du couplage effectif de l'anti-résonance.

Nous avons également validé notre modèle par des simulations utilisant la méthode des éléments finis (FEM), confirmant ainsi la possibilité de contrôler précisément le comportement du couplage en positionnant une sphère de YIG à différentes emplacements dans une cavité quasi-fermée.

En conclusion, cette étude apporte des éclaircissements sur l'interaction complexe entre les modes de cavité et les magnons dans les cavités quasi-fermées. Grâce à l'incorporation d'un formalisme d'entrée-sortie, enrichi d'un facteur de phase crucial, nous avons non seulement reproduit le comportement des anti-résonances dans nos simulations, mais également fourni des explications la nauture des couplages des anti-résonances, permettant à la fois d'expliquer la répulsion et l'attraction des niveaux d'énergie observées dans le spectre de transmission. La compréhension des sauts de phase de l'anti-résonance et des différents modes de cavité nous permet de prédire le comportement de l'intéraction entre les anti-résonances de cavité et le magnon.

Chapitre 7 - Conclusion:

Dans cette thèse, nous explorons le domaine dynamique de la spincavitronique, en mettant particulièrement l'accent sur l'interaction robuste entre les modes de cavité et les magnons dans des cavités tridimensionnelles (3D). L'exploration des intéractions magnon-photon a démontré que leur couplage fort peut donner lieu à des états hybrides jusqu'alors peu explorés, avec des applications significatives dans les technologies quantiques et les systèmes de communication.

Les origines de la spincavitronique remontent à des contributions clés faites au début des années 2010, notamment la prédiction d'un couplage fort entre les magnons et les photons en 2010, suivie de confirmations expérimentales en 2013 et 2014, qui ont marqué des avancées significatives dans notre compréhension de ces interactions. Ces études pionnières ont souligné la polyvalence des magnons, caractérisés par leur large capacité de réglage de fréquence et leurs longs temps de cohérence, les positionnant ainsi comme des candidats prometteurs pour les applications de mémoire quantique. Leur rôle dans la magnonique quantique ouvre également de nouvelles perspectives pour améliorer les technologies de calcul et de communication quantiques.

Un aspect important de cette recherche est la caractérisation du régime de couplage ultra-fort (USC), où la force de couplage dépasse 10% de la fréquence de la cavité. Le régime USC améliore non seulement les performances dans diverses applications, mais permet

également l'observation de phénomènes nouveaux, soulignant son potentiel pour explorer de nouveaux états de la matière et approfondir notre compréhension des interactions lumière-matière. Les mécanismes pour atteindre le régime USC, que ce soit par le couplage de plusieurs dipôles ou l'optimisation de la force de couplage d'un seul dipôle à un mode de cavité, offrent un large champ de possibilités pour les investigations expérimentales et théoriques en spincavitronique.

Nos résultats expérimentaux valident l'importance cruciale de l'optimisation des paramètres, tels que le facteur de remplissage, pour réaliser l'USC, en plus des facteurs conventionnels comme la fréquence du résonateur et la densité de spins. Le design de cavité réentrante à double plots reconfigurable utilisé permet d'explorer la transition du régime SC au régime USC, marquant un progrès substantiel dans notre compréhension des interactions magnons-photons. Nos résultats suggèrent également que les modèles couramment utilisés, tels que les modèles de Dicke et de Hopfield, peuvent ne pas saisir pleinement les complexités observées dans nos données, nécessitant un raffinement supplémentaire des cadres théoriques. L'incorporation d'un décalage de fréquence des magnons lié au facteur de remplissage introduit une nouvelle dimension dans la modélisation des interactions magnons-photons, nécessitant des recherches supplémentaires pour élucider la physique sous-jacente.

De plus, nous avons souligné dans cette thèse le rôle crucial de l'attraction de niveaux d'énergie des modes hybridés dans les systèmes couplés entre les magnons et les anti-résonances de cavité. L'émergence de singularités, telles que les points exceptionnels et les états liés dans le continuum, offre des perspectives intéressantes pour les applications dans les technologies de détection et le traitement de l'information quantique. L'attraction de niveaux a le potentiel d'améliorer la sensibilité des dispositifs, permettant un transfert d'énergie robuste face aux perturbations extérieures. Grâce à l'application de la théorie d'entrée-sortie, nous élucideons les principes fondamentaux régissant les comportements de couplage des anti-résonances dans des systèmes quasi-fermés.

Dans l'ensemble, les études présentées dans cette thèse contribuent de manière significative à notre compréhension des polaritons magnon-photons, examinant la dynamique des régimes de couplage fort et ultra-fort. Les implications pour la conception et l'optimisation des cavités s'étendent de la métrologie aux dispositifs quantiques avancés, soulignant la polyvalence et le potentiel de la spincavitronique pour les développements technologiques futurs.

Notre investigation sur l'USC à température ambiante est une étape importante dans la compréhension du couplage magnons-photons. Le décalage de fréquence des magnons observé, auparavant non rapporté, nécessite des éclaircissements. Les travaux théoriques futurs devraient se concentrer sur la compréhension de ce phénomène, en particulier des non-linéarités qui peuvent surgir en raison de la force de couplage, qui ne sont observables que dans le régime USC.

Nos avancées récentes en matière de conception de cavités ont démontré des rapports de couplage améliorés au-delà de ceux rapportés précédemment, offrant une déscription précise sur l'évolution quadratique des décalages de fréquence des magnons par rapport aux rapports de couplage. Les futurs travaux de fabrication de ces cavités visent à produire de nouvelles données expérimentales s'approchant du régime de couplage deep-strong

(DSC), une frontière encore non atteinte dans les systèmes hybrides magnons-photons à température ambiante.

L'attraction de niveaux des anti-résonances au sein de cavités quasi-fermées a été insuffisamment explorée jusqu'à présent ; nous relions ici les directions futures dans l'exploration de l'attraction de niveaux des modes hybrides avec des anti-résonances dans les cavités quasi-fermées :

(i) Notre étude démontre qu'une incorporation excessive de modes peut entraîner des écarts entre les mesures ou les simulations et le modèle développé. En particulier, la première condition de Markov dans la dérivation d'entrée-sortie suppose une force de couplage externe constante en fonction de la fréquence, impliquant que les modes de cavité éloignés de l'anti-résonance peuvent exercer une influence conséquente. Pour les cavités unidimensionnelles, telles que les cavités Fabry-Pérot, il a été démontré que la force de couplage suit une fonction sinusoidale cardinale. Une généralisation appropriée pour les cavités 3D pourrait résoudre les écarts mentionnés ci-dessus.

(ii) La littérature présente plusieurs modèles visant à interpréter les observations d' attractions de niveaux, en particulier pour les cavités ouvertes. Cependant, ces modèles intègrent souvent des facteurs de phase pour s'aligner avec les résultats expérimentaux, manquant d'une justification physique. Les travaux futurs pourraient clarifier et développer un modèle plus physiquement.

(iii) Un objectif principal en exploitant l'attraction de niveaux dans un système est d'atteindre des points exceptionnels. Bien que l'attraction de niveaux existe dans les cavités 3D, nous posons l'hypothèse que des EP peuvent être générés dans ces cavité avec les anti-résonances, en modulant la dissipation des magnons, comme c'est généralement le cas. Les futures investigations exploreront le réglage de la dissipation à travers l'effet Hall de spin.

(iv) Nos récentes mesures de cavités doubles réentrantes, telles que discutées dans notre étude de l'attraction de niveaux, révèlent un potentiel significatif pour la non-réciprocité dans les cavités 3D. Nous attribuons ce phénomène à la combinaison des phases de couplage internes et externes élucidées dans notre étude.

Pour conclure, l'amélioration de notre modèle pour intégrer des modèles décrivant le régime de couplage ultra-fort pourrait permettre un meilleur contrôle de la fréquence des anti-résonances et une non-réciprocité accrue. De plus, les conceptions de cavité peuvent être adaptées pour une intégration sur un circuit imprimé (PCB) en utilisant la technologie des guides d'ondes intégrés au substrat (SIW), qui constitue l'analogue intégré d'une cavité 3D. Dans ce cas, les dimensions doivent tenir compte du substrat et des permittivités diélectriques, permettant une opération dans la même gamme de fréquences tout en maintenant des performances de couplage magnon-photon comparables. Cependant, des pertes supplémentaires sont introduites par le matériau diélectrique et les vias métalliques, qui servent de parois à la cavité, ce qui entraîne une réduction du facteur de qualité.

COLLEGES BRETAGNE LOIRE SCIENCES POUR L'INGENIEUR ET LE NUMERIQUE

IMT Atlantique
Bretagne-Pays de la Loire
École Mines-Télécom

Titre : Spincavitronique : Repulsion et attraction des niveaux d'énergie dans des systèmes couplés de cavité micro-ondes et YIG macroscopique.

Mots clés : spincavitronique, CMPS, USC, répulsion des niveaux, attraction des niveaux

Résumé : Cette thèse explore le domaine de la spincavitronique, en se concentrant sur le couplage fort entre les magnons et les photons dans des cavités tridimensionnelles (3D), conduisant à la formation de polaritons magnons-cavité (CMPs). Nous étudions la transition entre les régimes de couplage fort et ultra-fort, atteignant des forces de couplage de 12 % à 58 % de la fréquence de la cavité à température ambiante. Les magnons, avec leurs fréquences ajustables et leurs longs temps de cohérence, sont des candidats prometteurs pour la mémoire quantique et d'autres technologies quantiques, avec des applications dans le calcul et la communication quantiques. Nos recherches approfondissent la compréhension des interactions magnon-photon, avec des implications pour l'optimisation des systèmes hybrides quantiques. Ce travail présente également une étude du phénomène d'attraction de niveaux entre magnons et modes photoniques d'antirésonance dans des cavités 3D. Ce phénomène permet la transmission non réciproque des photons, essentielle pour des dispositifs tels que les circulateurs et les systèmes de mémoire quantique. Nous développons un modèle physique pour expliquer ces antirésonances, validé par des mesures expérimentales et des simulations. Ces résultats ouvrent de nouvelles perspectives pour l'utilisation des mécanismes d'attraction de niveaux dans les technologies de détection et d'information quantique.

Title : Spincavitronics : Repulsive and Attractive Energy Levels in YIG Bulk-Microwave Cavity Coupled Systems

Keywords : spincavitronics, CMP, USC, level repulsion, level attraction

Abstract : This thesis investigates the field of spincavitronics, focusing on the strong coupling between magnons and photons in three-dimensional (3D) cavities, leading to the formation of cavity magnon polaritons (CMPs). We explore the transition between the strong coupling and ultra-strong coupling regimes, achieving coupling strengths between 12% and 58% of the cavity frequency at room temperature. Magnons, with their tunable frequencies and long coherence times, are promising candidates for quantum memory and other quantum technologies, offering applications in quantum computing and long-distance quantum communication. Our research contributes to the development of a deeper understanding of magnon-photon interactions, with implications for improving the coupling strength and optimizing hybrid quantum systems. Additionally, this work presents a detailed study of the level attraction phenomenon between magnons and antiresonant photonic modes in 3D cavities. This phenomenon enables non-reciprocal photon transmission, which is essential for the design of advanced communication devices such as circulators and quantum memory systems. We develop a physical model to explain the emergence of these antiresonances, supported by experimental validation and simulations. These insights open new pathways for applying level attraction mechanisms in sensing technologies and quantum information processing, demonstrating the versatility of spincavitronics for future advancements in both quantum technologies and radiofrequency applications.